

1 SEARCH FOR PRODUCTION OF A HIGGS BOSON AND A SINGLE TOP  
2 QUARK IN MULTILEPTON FINAL STATES IN  $pp$  COLLISIONS AT  $\sqrt{s} = 13$   
3 TeV.

4 by

5 Jose Andres Monroy MontaÑez

6 A DISSERTATION

7 Presented to the Faculty of

8 The Graduate College at the University of Nebraska

In Partial Fulfilment of Requirements

10 For the Degree of Doctor of Philosophy

11 Major: Physics and Astronomy

12 Under the Supervision of Kenneth Bloom and Aaron Dominguez

13 Lincoln, Nebraska

14 July, 2018

15 SEARCH FOR PRODUCTION OF A HIGGS BOSON AND A SINGLE TOP  
16 QUARK IN MULTILEPTON FINAL STATES IN pp COLLISIONS AT  $\sqrt{s} = 13$   
17 TeV.

18 Jose Andres Monroy Montañez, Ph.D.

19 University of Nebraska, 2018

20 Adviser: Kenneth Bloom and Aaron Dominguez

# <sup>21</sup> Table of Contents

<sup>22</sup>	<b>Table of Contents</b>	<b>iii</b>
<sup>23</sup>	<b>List of Figures</b>	<b>vii</b>
<sup>24</sup>	<b>List of Tables</b>	<b>x</b>
<sup>25</sup>	<b>1 Theoretical approach</b>	<b>1</b>
<sup>26</sup>	1.1 Introduction . . . . .	1
<sup>27</sup>	1.2 Standard model of particle physics . . . . .	2
<sup>28</sup>	1.2.1 Fermions . . . . .	4
<sup>29</sup>	1.2.1.1 Leptons . . . . .	5
<sup>30</sup>	1.2.1.2 Quarks . . . . .	7
<sup>31</sup>	1.2.2 Fundamental interactions . . . . .	11
<sup>32</sup>	1.2.3 Gauge invariance. . . . .	15
<sup>33</sup>	1.2.4 Gauge bosons . . . . .	17
<sup>34</sup>	1.3 Electroweak unification and the Higgs mechanism . . . . .	18
<sup>35</sup>	1.3.1 Spontaneous symmetry breaking (SSB) . . . . .	26
<sup>36</sup>	1.3.2 Higgs mechanism . . . . .	30
<sup>37</sup>	1.3.3 Masses of the gauge bosons . . . . .	33
<sup>38</sup>	1.3.4 Masses of the fermions . . . . .	34

39	1.3.5	The Higgs field . . . . .	35
40	1.3.6	Production of Higgs bosons at LHC . . . . .	36
41	1.3.7	Higgs boson decay channels . . . . .	40
42	1.4	Experimental status of the anomalous Higgs-fermion coupling . . . .	42
43	1.5	Associated production of a Higgs boson and a single top quark . . . .	44
44	1.6	CP-mixing in $tH$ processes . . . . .	49
45	<b>2</b>	<b>The CMS experiment at the LHC</b>	<b>54</b>
46	2.1	Introduction . . . . .	54
47	2.2	The LHC . . . . .	55
48	2.3	The CMS experiment . . . . .	65
49	2.3.1	CMS coordinate system . . . . .	68
50	2.3.2	Tracking system . . . . .	70
51	2.3.3	Silicon strip tracker . . . . .	73
52	2.3.4	Electromagnetic calorimeter . . . . .	74
53	2.3.5	Hadronic calorimeter . . . . .	76
54	2.3.6	Superconducting solenoid magnet . . . . .	77
55	2.3.7	Muon system . . . . .	79
56	2.3.8	CMS trigger system . . . . .	80
57	2.3.9	CMS computing . . . . .	81
58	<b>3</b>	<b>Event generation, simulation and reconstruction</b>	<b>86</b>
59	3.1	Event generation . . . . .	87
60	3.2	Monte Carlo Event Generators. . . . .	91
61	3.3	CMS detector simulation. . . . .	92
62	3.4	Event reconstruction. . . . .	94
63	3.4.1	Particle-Flow Algorithm. . . . .	94

64	3.4.1.1	Missing transverse energy. . . . .	109
65	3.4.2	Event reconstruction examples . . . . .	110
66	<b>5</b>	<b>Statistical methods</b>	<b>113</b>
67	5.1	Multivariate analysis . . . . .	113
68	5.1.1	Decision trees . . . . .	117
69	5.1.2	Boosted decision trees (BDT). . . . .	119
70	5.1.3	Overtraining . . . . .	122
71	5.1.4	Variable ranking . . . . .	122
72	5.1.5	BDT output example. . . . .	123
73	5.2	Statistical inference. . . . .	124
74	5.2.1	Nuisance parameters. . . . .	124
75	5.2.2	Maximum likelihood estimation method . . . . .	125
76	5.3	Upper limits . . . . .	127
77	5.4	Asymptotic limits . . . . .	131
78	<b>6</b>	<b>Search for production of a Higgs boson and a single top quark in multilepton final states in pp collisions at <math>\sqrt{s} = 13</math> TeV</b>	<b>133</b>
80	6.1	Introduction . . . . .	133
81	6.2	$tHq$ signature . . . . .	135
82	6.3	Background processes . . . . .	137
83	6.4	Data and MC Samples . . . . .	139
84	6.4.1	Full 2016 dataset and MC samples . . . . .	139
85	6.4.2	Triggers . . . . .	140
86	6.5	Object Identification . . . . .	144
87	6.5.1	Jets and $b$ -jet tagging. . . . .	144
88	6.5.2	Missing Energy MET. . . . .	145

89	6.5.3 Lepton reconstruction and identification . . . . .	146
90	6.5.4 Lepton selection efficiency . . . . .	154
91	6.6 Event selection . . . . .	156
92	6.7 Background predictions . . . . .	157
93	6.8 Signal discrimination . . . . .	159
94	6.8.1 Classifiers response . . . . .	161
95	6.9 Additional discriminating variables . . . . .	165
96	<b>Bibliography</b>	<b>167</b>
97	<b>References</b>	<b>169</b>

## <sup>98</sup> List of Figures

99	1.1 Standard Model of particle physics. . . . .	3
100	1.2 Transformations between quarks . . . . .	11
101	1.3 Fundamental interactions in nature. . . . .	12
102	1.4 SM interactions diagrams . . . . .	13
103	1.5 Neutral current processes . . . . .	19
104	1.6 Spontaneous symmetry breaking mechanism . . . . .	27
105	1.7 SSB Potential form . . . . .	28
106	1.8 Potential for complex scalar field . . . . .	29
107	1.9 SSB mechanism for complex scalar field . . . . .	30
108	1.10 Proton-Proton collision . . . . .	36
109	1.11 Proton PDFs . . . . .	37
110	1.12 Higgs boson production mechanism Feynman diagrams . . . . .	38
111	1.13 Higgs boson production cross section and decay branching ratios . . . . .	39
112	1.14 $\kappa_t$ - $\kappa_V$ plot of the coupling modifiers. ATLAS and CMS combination. . .	42
113	1.15 Higgs boson production in association with a top quark . . . . .	45
114	1.16 Cross section for $tHq$ process as a function of $\kappa_t$ . . . . .	48
115	1.17 Cross section for $tHW$ process as a function of $\kappa_{Htt}$ . . . . .	48
116	1.18 NLO cross section for $tX_0$ and $t\bar{t}X_0$ . . . . .	52

117	1.19 NLO cross section for $tWX_0, t\bar{t}X_0$ .	53
118	2.1 CERN accelerator complex . . . . .	55
119	2.2 LHC protons source. First acceleration stage.	56
120	2.3 The LINAC2 accelerating system at CERN.	57
121	2.4 LHC layout and RF cavities module.	58
122	2.5 LHC dipole magnet.	60
123	2.6 Integrated luminosity delivered by LHC and recorded by CMS during 2016	62
124	2.7 LHC interaction points . . . . .	63
125	2.8 Multiple $pp$ collision bunch crossing at CMS.	65
126	2.9 Layout of the CMS detector . . . . .	66
127	2.10 CMS detector transverse slice . . . . .	67
128	2.11 CMS detector coordinate system . . . . .	69
129	2.12 CMS tracking system schematic view.	70
130	2.13 CMS pixel detector . . . . .	71
131	2.14 SST Schematic view. . . . .	73
132	2.15 CMS ECAL schematic view . . . . .	75
133	2.16 CMS HCAL schematic view . . . . .	77
134	2.17 CMS solenoid magnet . . . . .	78
135	2.18 CMS Muon system schematic view . . . . .	79
136	2.19 CMS Level-1 trigger architecture . . . . .	81
137	2.20 WLCG structure . . . . .	82
138	2.21 Data flow from CMS detector through hardware Tiers . . . . .	84
139	3.1 Event generation process. . . . .	87
140	3.2 Particle flow algorithm. . . . .	95
141	3.3 Stable cones identification . . . . .	103

142	3.4	Jet reconstruction.	105
143	3.5	Jet energy corrections.	106
144	3.6	Secondary vertex in a b-hadron decay.	108
145	3.7	HIG-13-004 Event 1 reconstruction.	110
146	3.8	$e\mu$ event reconstruction.	111
147	3.9	Recorded event reconstruction.	112
148	5.1	Scatter plots-MVA event classification.	115
149	5.2	Scalar test statistical.	116
150	5.3	Decision tree.	117
151	5.4	Decision tree output example.	120
152	5.5	BDT output example.	123
153	5.6	$t_r$ p.d.f. assuming each $H_0$ and $H_1$	128
154	5.7	Illustration of the $CL_s$ limit.	130
155	5.8	Example of Brazilian flag plot	131
156	6.1	$tHq$ event signature	136
157	6.2	$t\bar{t}$ and $t\bar{t}W$ events signature	138
158	6.3	Tight vs loose lepton selection efficiencies in the 2lss channel.	154
159	6.4	Tight vs loose lepton selection efficiencies in the 3l channel.	155
160	6.5	Input variables to the BDT for signal discrimination normalized.	160
161	6.6	Input variables to the BDT for signal discrimination not normalized.	162
162	6.7	BDT input variables. Discrimination against $t\bar{t}$ .	163
163	6.8	BDT input variables. Discrimination against $t\bar{t}V$ .	164
164	6.9	Correlation matrices for the BDT input variables.	165
165	6.10	MVA classifiers performance.	165
166	6.11	Additional discriminating variables distributions.	167

# <sup>167</sup> List of Tables

168	1.1	Fermions of the SM. . . . .	4
169	1.2	Fermion masses. . . . .	5
170	1.3	Lepton properties. . . . .	7
171	1.4	Quark properties. . . . .	8
172	1.5	Fermion weak isospin and weak hypercharge multiplets. . . . .	9
173	1.6	Fundamental interactions features. . . . .	14
174	1.7	SM gauge bosons. . . . .	18
175	1.8	Higgs boson properties. . . . .	36
176	1.9	Predicted branching ratios for a SM Higgs boson with $m_H = 125 \text{ GeV}/c^2$ . . . . .	41
177	1.10	Predicted SM cross sections for $tH$ production at $\sqrt{s} = 13 \text{ TeV}$ . . . . .	46
178	1.11	Predicted enhancement of the $tHq$ and $tHW$ cross sections at LHC . . . . .	49
179	6.1	Signal samples and their cross section and branching fraction. . . . .	140
180	6.2	$\kappa_V$ and $\kappa_t$ combinations. . . . .	141
181	6.3	List of background samples used in this analysis (CMSSW 80X). . . . .	142
182	6.4	Leading-order $t\bar{t}W$ and $t\bar{t}Z$ samples used in the signal BDT training. . . . .	142
183	6.5	Table of high-level triggers that we consider in the analysis. . . . .	143
184	6.6	Trigger efficiency scale factors and associated uncertainties. . . . .	144
185	6.7	Effective areas, for electrons and muons. . . . .	150

186	6.8 Requirements on each of the three muon selections.	153
187	6.9 Criteria for each of the three electron selections.	153
188	6.10 MVA input discriminating variables	161
189	6.11 TMVA input variables ranking for BDTA_GRAD method	166
190	6.12 TMVA configuration used in the BDT training.	166
191	6.13 ROC-integral for all the testing cases.	168

<sup>192</sup> **Chapter 1**

<sup>193</sup> **Theoretical approach**

<sup>194</sup> **1.1 Introduction**

<sup>195</sup> The physical description of the universe is a challenge that physicists have faced by  
<sup>196</sup> making theories that refine existing principles and proposing new ones in an attempt  
<sup>197</sup> to embrace emerging facts and phenomena.

<sup>198</sup> At the end of 1940s Julian Schwinger [1] and Richard P. Feynman [2], based on  
<sup>199</sup> the work of Sin-Itiro Tomonaga [3], developed an electromagnetic theory consistent  
<sup>200</sup> with special relativity and quantum mechanics that describes how matter and light  
<sup>201</sup> interact; the so-called *quantum electrodynamics* (QED) was born.

<sup>202</sup> QED has become the blueprint for developing theories that describe the universe.  
<sup>203</sup> It was the first example of a quantum field theory (QFT), which is the theoretical  
<sup>204</sup> framework for building quantum mechanical models that describes particles and their  
<sup>205</sup> interactions. QFT is composed of a set of mathematical tools that combines classical  
<sup>206</sup> fields, special relativity and quantum mechanics, while keeping the quantum point  
<sup>207</sup> particles and locality ideas.

<sup>208</sup> This chapter gives an overview of the standard model of particle physics, starting

209 with a description of the particles and their interactions, followed by a description of  
 210 the electroweak interaction, the Higgs boson and the associated production of Higgs  
 211 boson and a single top quark ( $tH$ ). The description contained in this chapter is based  
 212 on References [4–6].

## 213 1.2 Standard model of particle physics

214 The *standard model of particle physics (SM)* describes particle physics at the funda-  
 215 mental level in terms of a collection of interacting particles and fields. The full picture  
 216 of the SM is composed of three fields<sup>1</sup> whose excitations are interpreted as particles  
 217 called mediators or force-carriers, a set of fields whose excitations are interpreted as  
 218 elementary particles interacting through the exchange of those mediators, and a field  
 219 that gives the mass to elementary particles. Figure 1.1 shows a scheme of the SM  
 220 particles’ organization. In addition, for each of the particles in the scheme there exists  
 221 an antiparticle with the same mass and opposite quantum numbers. The existence of  
 222 antiparticles is a prediction of the relativistic quantum mechanics from the solution  
 223 of the Dirac equation for which a negative energy solution is also possible. In some  
 224 cases a particle is its own anti-particle, like photon or Higgs boson.

225 The mathematical formulation of the SM is based on group theory and the use of  
 226 Noether’s theorem [8] which states that for a physical system modeled by a Lagrangian  
 227 that is invariant under a group of transformations a conservation law is expected. For  
 228 instance, a system described by a time-independent Lagrangian is invariant (symmet-  
 229 ric) under time changes (transformations) with the total energy conservation law as  
 230 the expected conservation law. In QED, the charge operator ( $Q$ ) is the generator of

---

<sup>1</sup> The formal and complete treatment of the SM is out of the scope of this document, however a plenty of textbooks describing it at several levels are available in the literature. The treatment in References [5, 6] is quite comprehensive and detailed. Note that gravitational field is not included in the standard model formulation

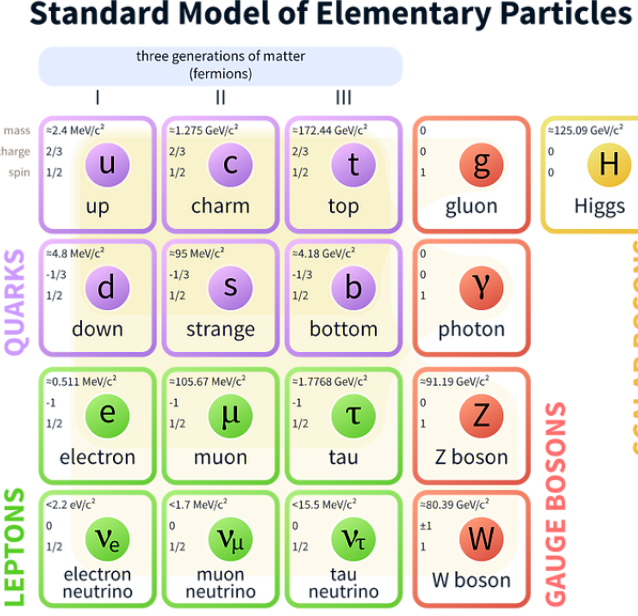


**Figure 1.1:** Schematic representation of the Standard Model of particle physics. The SM is a theoretical model intended to describe three of the four fundamental forces of the universe in terms of a set of particles and their interactions. [7].

231 the  $U(1)$  symmetry which according to the Noether's theorem means that there is a  
 232 conserved quantity; this conserved quantity is the electric charge and thus the law  
 233 conservation of electric charge is established.

234 In the SM, the symmetry group  $SU(3)_C \otimes SU(2)_L \otimes U(1)_Y$  describes three of the  
 235 four fundamental interactions in nature (see Section 1.2.2): strong interaction (SI),  
 236 weak interaction (WI) and electromagnetic interactions (EI) in terms of symmetries  
 237 associated to physical quantities:

- 238     • Strong:  $SU(3)_C$  associated to color charge
- 239     • Weak:  $SU(2)_L$  associated to weak isospin and chirality
- 240     • Electromagnetic:  $U(1)_Y$  associated to weak hypercharge and electric charge
- 241 It will be shown that the electromagnetic and weak interactions are combined in

242 the so-called electroweak interaction where chirality, hypercharge, weak isospin and  
 243 electric charge are the central concepts.

244 **1.2.1 Fermions**

245 The basic constituents of the ordinary matter at the lowest level, which form the set  
 246 of elementary particles in the SM formulation, are quarks and leptons. All of them  
 247 have spin 1/2, therefore they are classified as fermions since they obey Fermi-Dirac  
 248 statistics. There are six *flavors* of quarks and three of leptons organized in three  
 249 generations, or families, as shown in Table 1.1.

		Generation		
		1st	2nd	3rd
Leptons	Type	Charged	Electron (e)	Moun( $\mu$ )
	Neutral	Neutral	Electron neutrino ( $\nu_e$ )	Muon neutrino ( $\nu_\mu$ )
Quarks	Up-type	Up (u)	Charm (c)	Top (t)
	Down-type	Down (d)	Strange (s)	Bottom (b)

**Table 1.1:** Fermions of the SM. There are six flavors of quarks and three of leptons, organized in three generations, or families, composed of two pairs of closely related particles. The close relationship is motivated by the fact that each pair of particles is a member of an  $SU(2)_L$  doublet that has an associated invariance under isospin transformations. WI between leptons is limited to the members of the same generation; WI between quarks is not limited but greatly favored, to same generation members.

250

251 There is a mass hierarchy between generations (see Table 1.2), where the higher  
 252 generation particles decays to the lower one, which can explain why the ordinary  
 253 matter is made of particles from the first generation. In the SM, neutrinos are modeled  
 254 as massless particles so they are not subject to this mass hierarchy; however, today it  
 255 is known that neutrinos are massive so the hierarchy could be restated. The reason  
 256 behind this mass hierarchy is one of the most important open questions in particle  
 257 physics, and it becomes more puzzling when noticing that the mass difference between

258 first and second generation fermions is small compared to the mass difference with  
 259 respect to the third generation.

Lepton	Mass (MeV/c <sup>2</sup> )	Quark	Mass (MeV/c <sup>2</sup> )
e	0.51	u	2.2
$\mu$	105.65	c	$1.28 \times 10^3$
$\tau$	1776.86	t	$173.1 \times 10^3$
$\nu_e$	Unknown	d	4.7
$\nu_\mu$	Unknown	s	96
$\tau_\mu$	Unknown	b	$4.18 \times 10^3$

**Table 1.2:** Fermion masses [9]. Generations differ by mass in a way that has been interpreted as a mass hierarchy. Approximate values with no uncertainties are used, for comparison purpose.

260

261        Usually, the second and third generation fermions are produced in high energy  
 262 processes, like the ones recreated in particle accelerators.

263 **1.2.1.1 Leptons**

264 A lepton is an elementary particle that is not subject to the SI. As seen in Table 1.1,  
 265 there are two types of leptons, the charged ones (electron, muon and tau) and the  
 266 neutral ones (the three neutrinos). The electric charge (Q) is the property that gives  
 267 leptons the ability to participate in the EI. From the classical point of view, Q plays  
 268 a central role determining, among others, the strength of the electric field through  
 269 which the electromagnetic force is exerted. It is clear that neutrinos are not affected  
 270 by EI because they don't carry electric charge.

271        Another feature of the leptons that is fundamental in the mathematical description  
 272 of the SM is the chirality, which is closely related to spin and helicity. Helicity  
 273 defines the handedness of a particle by relating its spin and momentum such that  
 274 if they are parallel then the particle is right-handed; if spin and momentum are

275 antiparallel the particle is said to be left-handed. The study of parity conservation  
 276 (or violation) in  $\beta$ -decay has shown that only left-handed electrons/neutrinos or right-  
 277 handed positrons/anti-neutrinos are created [10]; the inclusion of that feature in the  
 278 theory was achieved by using projection operators for helicity, however, helicity is  
 279 frame dependent for massive particles which makes it not Lorentz invariant and then  
 280 another related attribute has to be used: *chirality*.

281 Chirality is a purely quantum attribute which makes it not so easy to describe in  
 282 graphical terms but it defines how the wave function of a particle transforms under  
 283 certain rotations. As with helicity, there are two chiral states, left-handed chiral (L)  
 284 and right-handed chiral (R). In the highly relativistic limit where  $E \approx p \gg m$  helicity  
 285 and chirality converge, becoming exactly the same for massless particles.

286 In the following, when referring to left-handed (right-handed) it will mean left-  
 287 handed chiral (right-handed chiral). The fundamental fact about chirality is that  
 288 while EI and SI are not sensitive to chirality, in WI left-handed and right-handed  
 289 fermions are treated asymmetrically, such that only left-handed fermions and right-  
 290 handed anti-fermions are allowed to couple to WI mediators, which is a violation of  
 291 parity. The way to translate this statement in a formal mathematical formulation is  
 292 based on the isospin symmetry group  $SU(2)_L$ .

293 Each generation of leptons is seen as a weak isospin doublet.<sup>2</sup> The left-handed  
 294 charged lepton and its associated left-handed neutrino are arranged in doublets of  
 295 weak isospin  $T=1/2$  while their right-handed partners are singlets:

$$\begin{pmatrix} \nu_l \\ l \end{pmatrix}_L, l_R := \begin{pmatrix} \nu_e \\ e \end{pmatrix}_L, \begin{pmatrix} \nu_\mu \\ \mu \end{pmatrix}_L, \begin{pmatrix} \nu_\tau \\ \tau \end{pmatrix}_L, e_R, \mu_R, \tau_R, \nu_{eR}, \nu_{\mu R}, \nu_{\tau R} \quad (1.1)$$

296 The isospin third component refers to the eigenvalues of the weak isospin operator

---

<sup>2</sup> The weak isospin is an analogy of the isospin symmetry in strong interaction where neutron and proton are affected equally by strong force but differ in their charge.

which for doublets is  $T_3 = \pm 1/2$ , while for singlets it is  $T_3 = 0$ . The physical meaning of this doublet-singlet arrangement falls in that the WI couples the two particles in the doublet by exchanging the interaction mediator while the singlet member is not involved in WI. The main properties of the leptons are summarized in Table 1.3.

Although all three flavor neutrinos have been observed, their masses remain unknown and only some estimations have been made [11]. The main reason is that the flavor eigenstates are not the same as the mass eigenstates which implies that when a neutrino is created its mass state is a linear combination of the three mass eigenstates and experiments can only probe the squared difference of the masses. The Pontecorvo-Maki-Nakagawa-Sakata (PMNS) mixing matrix encodes the relationship between flavor and mass eigenstates.

Lepton	$Q(e)$	$T_3$	$L_e$	$L_\mu$	$L_\tau$	Lifetime (s)
Electron (e)	-1	-1/2	1	0	0	Stable
Electron neutrino( $\nu_e$ )	0	1/2	1	0	0	Unknown
Muon ( $\mu$ )	-1	-1/2	0	1	0	$2.19 \times 10^{-6}$
Muon neutrino ( $\nu_\mu$ )	0	1/2	0	1	0	Unknown
Tau ( $\tau$ )	-1	-1/2	0	0	1	$290.3 \times 10^{-15}$
Tau neutrino ( $\nu_\tau$ )	0	1/2	0	0	1	Unknown

**Table 1.3:** Lepton properties [9]. Q: electric charge,  $T_3$ : weak isospin. Only left-handed leptons and right-handed anti-leptons participate in the WI. Anti-particles with inverted  $T_3$ , Q and lepton number complete the leptons set but are not listed. Right-handed leptons and left-handed anti-leptons, neither listed, form weak isospin singlets with  $T_3 = 0$  and do not take part in the weak interaction.

308

### 309 1.2.1.2 Quarks

Quarks are the basic constituents of protons and neutrons. The way quarks join to form bound states, called *hadrons*, is through the SI. Quarks are affected by all the fundamental interactions which means that they carry all the four types of charges: color, electric charge, weak isospin and mass.

Flavor	$Q(e)$	$I_3$	$T_3$	B	C	S	T	$B'$	Y	Color
Up (u)	2/3	1/2	1/2	1/3	0	0	0	0	1/3	r,b,g
Charm (c)	2/3	0	1/2	1/3	1	0	0	0	4/3	r,b,g
Top(t)	2/3	0	1/2	1/3	0	0	1	0	4/3	r,b,g
Down(d)	-1/3	-1/2	-1/2	1/3	0	0	0	0	1/3	r,b,g
Strange(s)	-1/3	0	-1/2	1/3	0	-1	0	0	-2/3	r,b,g
Bottom(b)	-1/3	0	-1/2	1/3	0	0	0	-1	-2/3	r,b,g

**Table 1.4:** Quark properties [9]. Q: electric charge,  $I_3$ : isospin,  $T_3$ : weak isospin, B: baryon number, C: charmness, S: strangeness, T: topness,  $B'$ : bottomness, Y: hypercharge. Anti-quarks posses the same mass and spin as quarks but all charges (color, flavor numbers) have opposite sign.

314

315     Table 1.4 summarizes the features of quarks, among which the most remarkable  
 316    is their fractional electric charge. Note that fractional charge is not a problem, given  
 317    that quarks are not found isolated, but serves to explain how composed particles are  
 318    formed out of two or more valence quarks<sup>3</sup>.

319     Color charge is responsible for the SI between quarks and is the symmetry ( $SU(3)_C$ )  
 320    that defines the formalism to describe SI. There are three colors: red (r), blue (b)  
 321    and green (g) and their corresponding three anti-colors; thus each quark carries one  
 322    color unit while anti-quarks carries one anti-color unit. As explained in Section 1.2.2,  
 323    quarks are not allowed to be isolated due to the color confinement effect, hence, their  
 324    features have been studied indirectly by observing their bound states created when

- 325       • one quark with a color charge is attracted by an anti-quark with the correspond-  
 326       ing anti-color charge forming a colorless particle called a *meson*.  
  
 327       • three quarks (anti-quarks) with different color (anti-color) charges are attracted  
 328       among them forming a colorless particle called a *baryon (anti-baryon)*.

---

<sup>3</sup> Hadrons can contain an indefinite number of virtual quarks and gluons, known as the quark and gluon sea, but only the valence quarks determine hadrons' quantum numbers.

329        In practice, when a quark is left alone isolated a process called *hadronization* occurs  
 330 where the quark emits gluons (see Section 1.2.4) which eventually will generate new  
 331 quark-antiquark pairs and so on; those quarks will recombine to form hadrons that  
 332 will decay into leptons. This proliferation of particles looks like a *jet* coming from  
 333 the isolated quark. More details about the hadronization process and jet structure  
 334 will be given in chapter3.

335        In the first version of the quark model (1964), M. Gell-Mann [12] and G. Zweig  
 336 [13, 14] developed a consistent way to classify hadrons according to their properties.  
 337 Only three quarks (u, d, s) were involved in a scheme in which all baryons have baryon  
 338 number  $B=1$  and therefore quarks have  $B=1/3$ ; non-baryons have  $B=0$ . Baryon  
 339 number is conserved in SI and EI which means that single quarks cannot be created  
 340 but in pairs  $q - \bar{q}$ .

341        The scheme organizes baryons in a two-dimensional space ( $I_3$  - Y); Y (hyper-  
 342 charge) and  $I_3$  (isospin) are quantum numbers related by the Gell-Mann-Nishijima  
 343 formula [15, 16]:

$$Q = I_3 + \frac{Y}{2} \quad (1.2)$$

344 where  $Y = B + S + C + T + B'$  are the quantum numbers listed in Table 1.4.

345        There are six quark flavors organized in three generations (see Table 1.1) fol-  
 346 lowing a mass hierarchy which, again, implies that higher generations decay to first  
 347 generation quarks.

	Quarks			$T_3$	$Y_W$	Leptons			$T_3$	$Y_W$
Doublets	$(\frac{u}{d'})_L$	$(\frac{c}{s'})_L$	$(\frac{t}{b'})_L$	$(\frac{1/2}{-1/2})$	$1/3$	$(\nu_e)_L$	$(\nu_\mu)_L$	$(\nu_\tau)_L$	$(\frac{1/2}{-1/2})$	-1
Singlets	$u_R$	$c_R$	$t_R$	0	$4/3$	$\nu_{eR}$	$\nu_{\mu R}$	$\nu_{\tau R}$	0	-2

**Table 1.5:** Fermion weak isospin and weak hypercharge multiplets. Weak hypercharge is calculated through the Gell-Mann-Nishijima formula 1.2 but using the weak isospin and charge for quarks.

348

349 Isospin doublets of quarks are also defined (see Table 1.5), and same as for neutrinos,  
 350 the WI eigenstates are not the same as the mass eigenstates which means that  
 351 members of different quark generations are connected by the WI mediator; thus, up-  
 352 type quarks are coupled not to down-type quarks (the mass eigenstates) directly but  
 353 to a superposition of down-type quarks ( $q'_d$ ; *the weak eigenstates*) via WI according  
 354 to:

355

$$\begin{aligned} q'_d &= V_{CKM} q_d \\ \begin{pmatrix} d' \\ s' \\ b' \end{pmatrix} &= \begin{pmatrix} V_{ud} & V_{us} & V_{ub} \\ V_{cd} & V_{cs} & V_{cb} \\ V_{td} & V_{ts} & V_{tb} \end{pmatrix} \begin{pmatrix} d \\ s \\ b \end{pmatrix} \end{aligned} \quad (1.3)$$

356 where  $V_{CKM}$  is known as Cabibbo-Kobayashi-Maskawa (CKM) mixing matrix [17,18]  
 357 given by

$$\begin{pmatrix} |V_{ud}| & |V_{us}| & |V_{ub}| \\ |V_{cd}| & |V_{cs}| & |V_{cb}| \\ |V_{td}| & |V_{ts}| & |V_{tb}| \end{pmatrix} = \begin{pmatrix} 0.97427 \pm 0.00015 & 0.22534 \pm 0.00065 & 0.00351^{+0.00015}_{-0.00014} \\ 0.22520 \pm 0.00065 & 0.97344 \pm 0.00016 & 0.0412^{+0.0011}_{-0.0005} \\ 0.00867^{+0.00029}_{-0.00031} & 0.0404^{+0.0011}_{-0.0005} & 0.999146^{+0.000021}_{-0.000046} \end{pmatrix}. \quad (1.4)$$

358 The weak decays of quarks are represented in the diagram of Figure 1.2; again  
 359 the CKM matrix plays a central role since it contains the probabilities for the differ-  
 360 ent quark decay channels, in particular, note that quark decays are greatly favored  
 361 between generation members.

362 CKM matrix is a  $3 \times 3$  unitary matrix parametrized by three mixing angles and  
 363 the *CP-mixing phase*; the latter is the parameter responsible for the Charge-Parity

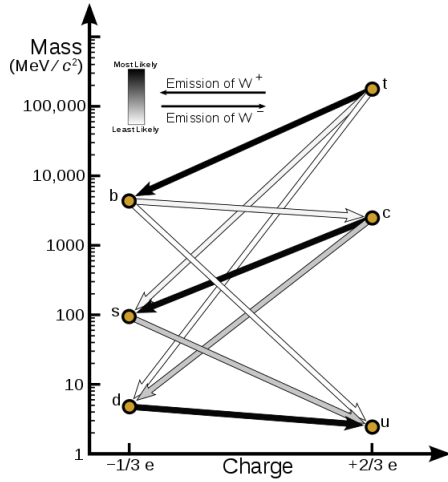


**Figure 1.2:** Transformations between quarks through the exchange of a WI. Higher generations quarks decay to first generation quarks by emitting a W boson. The arrow color indicates the likelihood of the transition according to the grey scale in the top left side which represent the CKM matrix parameters [19].

364 symmetry violation (CP-violation) in the SM. The fact that the top quark decays  
 365 almost all the time to a bottom quark is exploited in this thesis when making the  
 366 selection of the signal events by requiring the presence of a jet tagged as a jet coming  
 367 from a  $b$  quark in the final state.

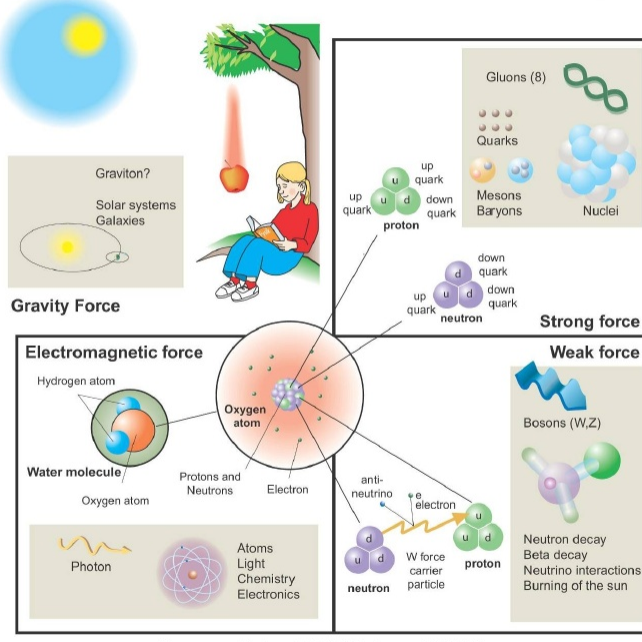
### 368 1.2.2 Fundamental interactions

369 Even though there are many manifestations of force in nature, like the ones repre-  
 370 sented in Figure 1.3, we can classify all of them in four fundamental interactions:

- 371 • *Electromagnetic interaction (EI)* affects particles that are *electrically charged*,  
 372 like electrons and protons. Figure 1.4a. shows a graphical representation, known  
 373 as *Feynman diagram*, of electron-electron scattering.
- 374 • *Strong interaction (SI)* described by Quantum Chromodynamics (QCD). Hadrons  
 375 like the proton and the neutron have internal structure given that they are com-

## Fundamental interactions.

Illustration: Typoform



Summer School KPI 15 August 2009

**Figure 1.3:** Fundamental interactions in nature. Despite the many manifestations of forces in nature, we can track all of them back to one of the fundamental interactions. The most common forces are gravity and electromagnetic given that all of us are subject and experience them in everyday life.

posed of two or more valence quarks<sup>4</sup>. Quarks have fractional electric charge which means that they are subject to electromagnetic interaction and in the case of the proton they should break apart due to electrostatic repulsion; however, quarks are held together inside the hadrons against their electrostatic repulsion by the *Strong Force* through the exchange of *gluons*. The analog to the electric charge is the *color charge*. Electrons and photons are elementary particles as quarks but they don't carry color charge, therefore they are not subject to SI. A Feynman diagram for gluon exchange between quarks is shown in Figure 1.4b.

- *Weak interaction (WI)* described by the weak theory (WT), is responsible, for instance, for the radioactive decay in atoms and the deuterium production

<sup>4</sup> Particles made of four and five quarks are exotic states not so common.

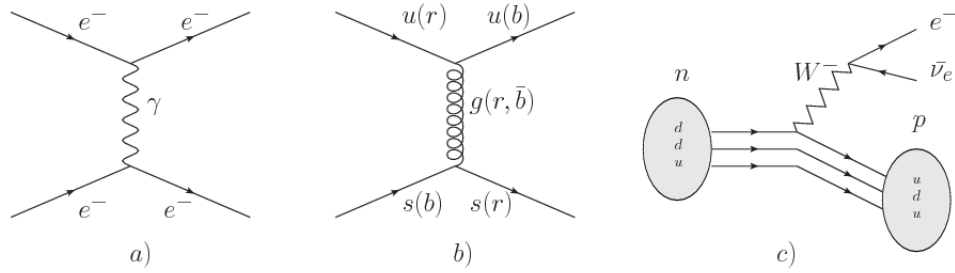


**Figure 1.4:** Feynman diagrams representing the interactions in SM; a) EI:  $e$ - $e$  scattering; b) SI: gluon exchange between quarks ; c) WI:  $\beta$ -decay

within the sun. Quarks and leptons are the particles affected by the weak interaction; they possess a property called *flavor charge* (see 1.2.1) which can be changed by emitting or absorbing one weak force mediator. There are three mediators of the *weak force* known as  $Z$  boson in the case of electrically neutral flavor changes and  $W^\pm$  bosons in the case of electrically charged flavor changes. The *weak isospin* is the WI analog to electric charge in EI, and color charge in SI, and defines how quarks and leptons are affected by the weak force. Figure 1.4c. shows the Feynman diagram of  $\beta$ -decay where a neutron ( $n$ ) is transformed in a proton ( $p$ ) by emitting a  $W^-$  particle.

- *Gravitational interaction (GI)* described by General Theory of Relativity (GR). It is responsible for the structure of galaxies and black holes as well as the expansion of the universe. As a classical theory, in the sense that it can be formulated without even appeal to the concept of quantization, it implies that the space-time is a continuum and predictions can be made without limitation to the precision of the measurement tools. The latter represents a direct contradiction of the quantum mechanics principles. Gravity is deterministic while quantum mechanics is probabilistic; despite that, efforts to develop a quantum theory of gravity have predicted the *graviton* as mediator of the gravitational

404 force<sup>5</sup>.

Interaction	Acts on	Relative strength	Range (m)	Mediators
Electromagnetic (QED)	Electrically charged particles	$10^{-2}$	Infinite	Photon
Strong (QCD)	Quarks and gluons	1	$10^{-15}$	Gluon
Weak (WI)	Leptons and quarks	$10^{-6}$	$10^{-18}$	$W^\pm, Z$
Gravitational (GI)	Massive particles	$10^{-39}$	Infinite	Graviton

Table 1.6: Fundamental interactions features [20].

405

406 Table 1.6 summarizes the main features of the fundamental interactions. The  
 407 strength of the interactions is represented by the coupling constants which depend  
 408 on the energy scale at which the interaction is evaluated, therefore, it is the relative  
 409 strength of the fundamental forces that reveals the meaning of strong and weak; in  
 410 a context where the relative strength of the SI is 1, the EI is about hundred times  
 411 weaker and WI is about million times weaker than the SI. A good description on how  
 412 the relative strength and range of the fundamental interactions are calculated can  
 413 be found in References [20, 21]. In the everyday life, only EI and GI are explicitly  
 414 experienced due to the range of these interactions; i.e., at the human scale distances  
 415 only EI and GI have appreciable effects, in contrast to SI which at distances greater  
 416 than  $10^{-15}$ m become negligible. Is it important to clarify that the weakness of the  
 417 WI is attributed to the fact that its mediators are highly massive which affects the  
 418 propagators of the interaction, as a result, the effect of the coupling constant is  
 419 reduced.

---

<sup>5</sup> Actually a wide variety of theories have been developed in an attempt to describe gravity; some famous examples are string theory and supergravity.

420 **1.2.3 Gauge invariance.**

421 QED was built successfully on the basis of the classical electrodynamics theory (CED)  
 422 of Maxwell and Lorentz, following theoretical and experimental requirements imposed  
 423 by

- 424     • Lorentz invariance: independence on the reference frame.
- 425     • Locality: interacting fields are evaluated at the same space-time point to avoid  
     426       action at a distance.
- 427     • Renormalizability: physical predictions are finite and well defined.
- 428     • Particle spectrum, symmetries and conservation laws already known must emerge  
     429       from the theory.
- 430     • Local gauge invariance.

431     The gauge invariance requirement reflects the fact that the fundamental fields  
 432     cannot be directly measured but associated fields which are the observables. Electric  
 433     (**E**) and magnetic (**B**) fields in CED are associated with the electric scalar potential  
 434      $V$  and the vector potential **A**. In particular, **E** can be obtained by measuring the  
 435     change in the space of the scalar potential ( $\Delta V$ ); however, two scalar potentials  
 436     differing by a constant  $f$  correspond to the same electric field. The same happens  
 437     in the case of the vector potential **A**; thus, different configurations of the associated  
 438     fields result in the same set of values of the observables. The freedom in choosing one  
 439     particular configuration is known as *gauge freedom*; the transformation law connecting  
 440     two configurations is known as *gauge transformation* and the fact that the observables  
 441     are not affected by a gauge transformation is called *gauge invariance*.

442     When the gauge transformation:

$$\begin{aligned} \mathbf{A} &\rightarrow \mathbf{A} - \Delta f \\ V &\rightarrow V - \frac{\partial f}{\partial t} \end{aligned} \tag{1.5}$$

443 is applied to Maxwell equations, they are still satisfied and the fields remain invariant.  
 444 Thus, CED is invariant under gauge transformations and is called a *gauge theory*.  
 445 The set of all gauge transformations form the *symmetry group* of the theory, which  
 446 according to the group theory, has a set of *group generators*. The number of group  
 447 generators determine the number of *gauge fields* of the theory.

448 As mentioned in the first lines of Section 1.2, QED has one symmetry group ( $U(1)$ )  
 449 with one group generator (the  $Q$  operator) and one gauge field (the electromagnetic  
 450 field  $A^\mu$ ). In CED there is not a clear definition, beyond the historical convention,  
 451 of which fields are the fundamental and which are the associated, but in QED the  
 452 fundamental field is  $A^\mu$ . When a gauge theory is quantized, the gauge fields are  
 453 quantized and their quanta are called *gauge bosons*. The word boson characterizes  
 454 particles with integer spin which obey Bose-Einstein statistics.

455 As will be detailed in Section 1.3, interactions between particles in a system can  
 456 be obtained by considering first the Lagrangian density of free particles in the sys-  
 457 tem, which of course is incomplete because the interaction terms have been left out,  
 458 and demanding global phase transformation invariance. Global phase transforma-  
 459 tion means that a gauge transformation is performed identically to every point  
 460 in the space<sup>6</sup> and the Lagrangian remains invariant. Then, the global transforma-  
 461 tion is promoted to a local phase transformation (this time the gauge transforma-  
 462 tion depends on the position in space) and again invariance is required.

---

<sup>6</sup> Here space corresponds to the 4-dimensional space i.e. space-time.

463 Due to the space dependence of the local transformation, the Lagrangian density is  
 464 not invariant anymore. In order to reinstate the gauge invariance, the gauge covariant  
 465 derivative is introduced in the Lagrangian and with it the gauge field responsible for  
 466 the interaction between particles in the system. The new Lagrangian density is gauge  
 467 invariant, includes the interaction terms needed to account for the interactions and  
 468 provides a way to explain the interaction between particles through the exchange of  
 469 the gauge boson.

470 This recipe was used to build QED and the theories that aim to explain the  
 471 fundamental interactions.

#### 472 1.2.4 Gauge bosons

473 The importance of the gauge bosons comes from the fact that they are the force  
 474 mediators or force carriers. The features of the gauge bosons reflect those of the fields  
 475 they represent and they are extracted from the Lagrangian density used to describe  
 476 the interactions. In Section 1.3, it will be shown how the gauge bosons of the EI and  
 477 WI emerge from the electroweak Lagrangian. The SI gauge bosons features are also  
 478 extracted from the SI Lagrangian but it is not detailed in this document. The main  
 479 features of the SM gauge bosons will be briefly presented below and summarized in  
 480 Table 1.7.

481 • **Photon.** EI occurs when the photon couples to (is exchanged between) parti-  
 482 cles carrying electric charge; however, The photon itself does not carry electric  
 483 charge, therefore, there is no coupling between photons. Given that the photon  
 484 is massless the EI is of infinite range, i.e., electrically charged particles interact  
 485 even if they are located far away one from each other; this also implies that  
 486 photons always move with the speed of light.

- 487     • **Gluon.** SI is mediated by gluons which just as photons are massless. They  
 488       carry one unit of color charge and one unit of anticolor charge, hence, gluons  
 489       can couple to other gluons. As a result, the range of the SI is not infinite  
 490       but very short due to the attraction between gluons, giving rise to the *color*  
 491       *confinement* which explains why color charged particles cannot be isolated but  
 492       live within composite particles, like quarks inside protons.
- 493     • **W, Z.**  $W^\pm$  and Z, are massive which explains their short-range. Given that  
 494       the WI is the only interaction that can change the flavor of the interacting  
 495       particles, the W boson is the responsible for the nuclear transmutation where  
 496       a neutron is converted into a proton or vice versa with the involvement of an  
 497       electron and a neutrino (see Figure 1.4c). The Z boson is the responsible for the  
 498       neutral weak processes like neutrino elastic scattering where no electric charge  
 499       but momentum transference is involved. WI gauge bosons carry isospin charge  
 500       which makes interaction between them possible.

Interaction	Mediator	Electric charge (e)	Color charge	Weak Isospin	mass (GeV/c <sup>2</sup> )
Electromagnetic	Photon ( $\gamma$ )	0	No	0	0
Strong	Gluon (g)	0	Yes -octet	No	0
Weak	$W^\pm$	$\pm 1$	No	$\pm 1$	$80.385 \pm 0.015$
	Z	0	No	0	$91.188 \pm 0.002$

Table 1.7: SM gauge bosons main features [9].

501

### 502    1.3 Electroweak unification and the Higgs 503       mechanism

504    Physicists dream of building a theory that contains all the interactions in one single  
 505       interaction, i.e., showing that at some scale in energy all the four fundamental inter-

actions are unified and only one interaction emerges in a *Theory of everything*. The first sign of the feasibility of such unification came from success in the construction of the CED. Einstein spent years trying to reach that full unification, which by 1920 only involved electromagnetism and gravity, with no success; however, a new partial unification was achieved in the 1960's, when S.Glashow [22], A.Salam [23] and S.Weinberg [24] independently proposed that electromagnetic and weak interactions are two manifestations of a more general interaction called *electroweak interaction* (EWI). EWI was developed by following the useful prescription provided by QED and the gauge invariance principles.

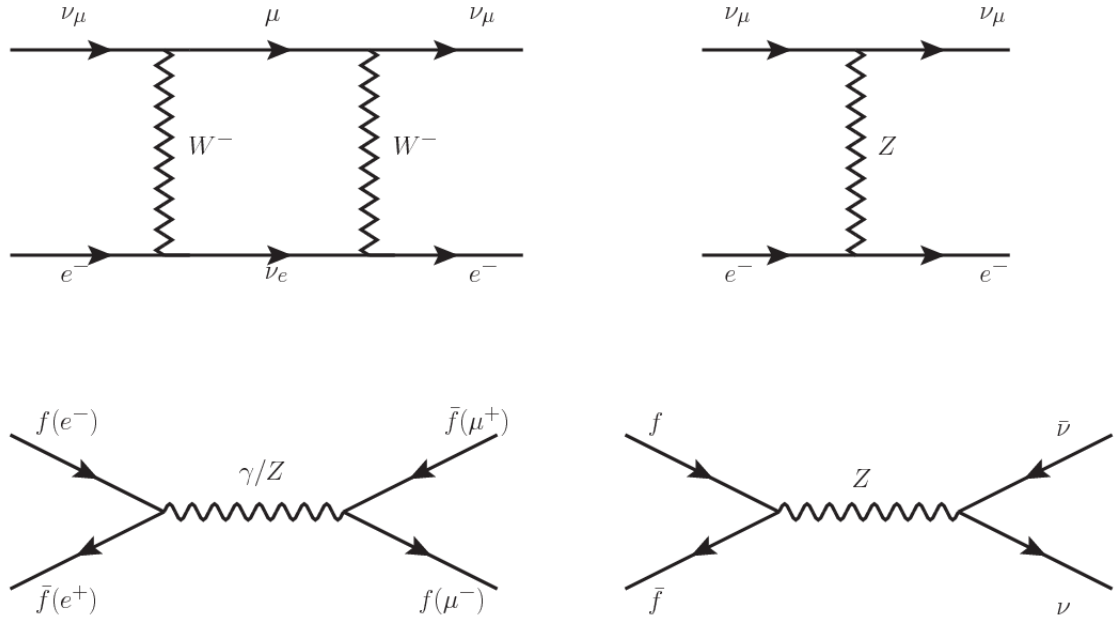


**Figure 1.5:** Top:  $\nu_\mu - e^-$  scattering going through charged currents (left) and neutral currents (right). Bottom: neutral current processes for charged fermions (left) and involving neutrinos (right). While neutral current processes involving only charged fermions can proceed through EI or WI, those involving neutrinos can only proceed via WI.

The *classic* weak theory developed by Fermi, did not have the concept of the W boson but instead it was treated as a point interaction with the dimensionful constant  $G_F$  associated with it. It works really well at low energies very far off the W mass

shell. When going up in energy, the theory of weak interactions involving the W boson is capable of explaining the  $\beta$ -decay and in general the processes mediated by  $W^\pm$  bosons. However, there were some processes like the  $\nu_\mu - e$  scattering which would require the exchange of two W bosons (see Figure 1.5 top diagrams) giving rise to divergent loop integrals and then non-finite predictions. The EWI theory, by including neutral currents involving fermions via the exchange of a neutral bosons Z, overcomes those divergences and the predictions become realistic.

Neutral weak interaction vertices conserve flavor in the same way as the electromagnetic vertices do, but additionally, the Z boson can couple to neutrinos which implies that processes involving charged fermions can proceed through EI or WI but processes involving neutrinos can proceed only through WI.

The prescription to build a gauge theory of the WI consists of proposing a free field Lagrangian density that includes the particles involved; next, by requesting invariance under global phase transformations first and generalizing to local phase transformations invariance later, the conserved currents are identified and interactions are generated by introducing gauge fields. Given that the goal is to include the EI and WI in a single theory, the group symmetry considered should be a combination of  $SU(2)_L$  and  $U(1)_{em}$ , however the latter cannot be used directly because the EI treats left and right-handed particles indistinctly in contrast to the former. Fortunately, the weak hypercharge, which is a combination of the weak isospin and the electric charge (Eqn. 1.2) is suitable to be used since it is conserved by the EI and WI. Thus, the symmetry group to be considered is

$$G \equiv SU(2)_L \otimes U(1)_Y \quad (1.6)$$

The following treatment applies to any of the fermion generations, but for sim-

541 plicity the first generation of leptons will be considered [5, 6, 25, 26].

542 Given the first generation of leptons

$$\psi_1 = \begin{pmatrix} \nu_e \\ e^- \end{pmatrix}_L, \quad \psi_2 = \nu_{eR}, \quad \psi_3 = e_R^- \quad (1.7)$$

543 the charged fermionic currents are given by

$$J_\mu \equiv J_\mu^+ = \bar{\nu}_{eL} \gamma_\mu e_L, \quad J_\mu^\dagger \equiv J_\mu^- = \bar{e}_L \gamma_\mu \nu_{eL} \quad (1.8)$$

544 and the free Lagrangian is given by

$$\mathcal{L}_0 = \sum_{j=1}^3 i\bar{\psi}_j(x) \gamma^\mu \partial_\mu \psi_j(x). \quad (1.9)$$

545 Mass terms are included directly in the QED free Lagrangians since they preserve  
 546 the invariance under the symmetry transformations involved which treat left and right  
 547 handed particles similarly, however mass terms of the form

$$m_W^2 W_\mu^\dagger(x) W^\mu(x) + \frac{1}{2} m_Z^2 Z_\mu(x) Z^\mu(x) - m_e \bar{\psi}_e(x) \psi_e(x) \quad (1.10)$$

548 which represent the mass of  $W^\pm$ , Z and electrons, are not invariant under G trans-  
 549 formations, therefore the gauge fields described by the EWI are in principle massless.

550 Experiments have shown that the EWI gauge fields are not massless [27–30];  
 551 however, they have to acquire mass through a mechanism compatible with the gauge  
 552 invariance; that mechanism is known as the *Higgs mechanism* and will be considered  
 553 later in this Section. The global transformations in the combined symmetry group G  
 554 can be written as

$$\begin{aligned}
\psi_1(x) &\xrightarrow{G} \psi'_1(x) \equiv U_Y U_L \psi_1(x), \\
\psi_2(x) &\xrightarrow{G} \psi'_2(x) \equiv U_Y \psi_2(x), \\
\psi_3(x) &\xrightarrow{G} \psi'_3(x) \equiv U_Y \psi_3(x)
\end{aligned} \tag{1.11}$$

555 where  $U_L$  represent the  $SU(2)_L$  transformation acting only on the weak isospin dou-  
 556 blet and  $U_Y$  represent the  $U(1)_Y$  transformation acting on all the weak isospin mul-  
 557 tiplets. Explicitly

$$U_L \equiv \exp\left(i \frac{\sigma_i}{2} \alpha^i\right), \quad U_Y \equiv \exp(i y_i \beta) \quad (i = 1, 2, 3) \tag{1.12}$$

558 with  $\sigma_i$  the Pauli matrices and  $y_i$  the weak hypercharges. In order to promote the  
 559 transformations from global to local while keeping the invariance, it is required that  
 560  $\alpha^i = \alpha^i(x)$ ,  $\beta = \beta(x)$  and the replacement of the ordinary derivatives by the covariant  
 561 derivatives

$$\begin{aligned}
D_\mu \psi_1(x) &\equiv \left[ \partial_\mu + ig\sigma_i W_\mu^i(x)/2 + ig'y_1 B_\mu(x) \right] \psi_1(x) \\
D_\mu \psi_2(x) &\equiv \left[ \partial_\mu + ig'y_2 B_\mu(x) \right] \psi_2(x) \\
D_\mu \psi_3(x) &\equiv \left[ \partial_\mu + ig'y_3 B_\mu(x) \right] \psi_3(x)
\end{aligned} \tag{1.13}$$

562 introducing in this way four gauge fields,  $W_\mu^i(x)$  and  $B_\mu(x)$ , in the process. The  
 563 covariant derivatives (Eqn. 1.13) are required to transform in the same way as fermion  
 564 fields  $\psi_i(x)$  themselves, therefore, the gauge fields transform as:

$$\begin{aligned} B_\mu(x) &\xrightarrow{G} B'_\mu(x) \equiv B_\mu(x) - \frac{1}{g'} \partial_\mu \beta(x) \\ W_\mu^i(x) &\xrightarrow{G} W_\mu^{i\prime}(x) \equiv W_\mu^i(x) - \frac{i}{g} \partial_\mu \alpha_i(x) - \varepsilon_{ijk} \alpha_i(x) W_\mu^j(x). \end{aligned} \quad (1.14)$$

565 The G invariant version of the Lagrangian density 1.9 can be written as

$$\mathcal{L}_0 = \sum_{j=1}^3 i \bar{\psi}_j(x) \gamma^\mu D_\mu \psi_j(x) \quad (1.15)$$

566 where free massless fermion and gauge fields and fermion-gauge boson interactions  
 567 are included. The EWI Lagrangian density must additionally include kinetic terms  
 568 for the gauge fields ( $\mathcal{L}_G$ ) which are built from the field strengths, according to

$$B_{\mu\nu}(x) \equiv \partial_\mu B_\nu - \partial_\nu B_\mu \quad (1.16)$$

$$W_{\mu\nu}^i(x) \equiv \partial_\mu W_\nu^i(x) - \partial_\nu W_\mu^i(x) - g \varepsilon^{ijk} W_\mu^j W_\nu^k \quad (1.17)$$

569 the last term in Eqn. 1.17 is added in order to hold the gauge invariance; therefore,

$$\mathcal{L}_G = -\frac{1}{4} B_{\mu\nu}(x) B^{\mu\nu}(x) - \frac{1}{4} W_{\mu\nu}^i(x) W_i^{\mu\nu}(x) \quad (1.18)$$

570 which contains not only the free gauge fields contributions, but also the gauge fields  
 571 self-interactions and interactions among them.

572 The three weak isospin conserved currents resulting from the  $SU(2)_L$  symmetry  
 573 are given by

$$J_\mu^i(x) = \frac{1}{2} \bar{\psi}_1(x) \gamma_\mu \sigma^i \psi_1(x) \quad (1.19)$$

574 while the weak hypercharge conserved current resulting from the  $U(1)_Y$  symmetry is  
 575 given by

$$J_\mu^Y = \sum_{j=1}^3 \bar{\psi}_j(x) \gamma_\mu y_j \psi_j(x) \quad (1.20)$$

576 In order to evaluate the electroweak interactions modeled by an isos triplet field  
 577  $W_\mu^i$  that couples to isospin currents  $J_\mu^i$  with strength  $g$  and additionally the singlet  
 578 field  $B_\mu$  which couples to the weak hypercharge current  $J_\mu^Y$  with strength  $g'/2$ . The  
 579 interaction Lagrangian density to be considered is

$$\mathcal{L}_I = -g J^{i\mu}(x) W_\mu^i(x) - \frac{g'}{2} J^{Y\mu}(x) B_\mu(x) \quad (1.21)$$

580 Note that the weak isospin currents are not the same as the charged fermionic cur-  
 581 rents that were used to describe the WI (Eqn. 1.8), since the weak isospin eigenstates  
 582 are not the same as the mass eigenstates, but they are closely related

$$J_\mu = \frac{1}{2}(J_\mu^1 + iJ_\mu^2), \quad J_\mu^\dagger = \frac{1}{2}(J_\mu^1 - iJ_\mu^2). \quad (1.22)$$

583 The same happens with the gauge fields  $W_\mu^i$  which are related to the mass eigen-  
 584 states  $W^\pm$  by

$$W_\mu^+ = \frac{1}{\sqrt{2}}(W_\mu^1 - iW_\mu^2), \quad W_\mu^- = \frac{1}{\sqrt{2}}(W_\mu^1 + iW_\mu^2). \quad (1.23)$$

585 The fact that there are three weak isospin conserved currents is an indication that  
 586 in addition to the charged fermionic currents, which couple charged to neutral leptons,  
 587 there should be a neutral fermionic current that does not involve electric charge  
 588 exchange; therefore, it couples neutral fermions or fermions of the same electric charge.  
 589 The third weak isospin current contains a term that is similar to the electromagnetic

590 current ( $j_\mu^{em}$ ), indicating that there is a relation between them and resembling the  
 591 Gell-Mann-Nishijima formula 1.2 adapted to electroweak interactions

$$Q = T_3 + \frac{Y_W}{2}. \quad (1.24)$$

592 Just as  $Q$  generates the  $U(1)_{em}$  symmetry, the weak hypercharge generates the  
 593  $U(1)_Y$  symmetry as said before. It is possible to write the relationship in terms of  
 594 the currents as

$$j_\mu^{em} = J_\mu^3 + \frac{1}{2} J_\mu^Y. \quad (1.25)$$

595 The neutral gauge fields  $W_\mu^3$  and  $B_\mu$  cannot be directly identified with the  $Z$   
 596 and the photon fields since the photon interacts similarly with left and right-handed  
 597 fermions; however, they are related through a linear combination given by

$$\begin{aligned} A_\mu &= B_\mu \cos \theta_W + W_\mu^3 \sin \theta_W \\ Z_\mu &= -B_\mu \sin \theta_W + W_\mu^3 \cos \theta_W \end{aligned} \quad (1.26)$$

where  $\theta_W$  is known as the *Weinberg angle*. The interaction Lagrangian is now given by

$$\begin{aligned} \mathcal{L}_I = -\frac{g}{\sqrt{2}}(J^\mu W_\mu^+ + J^{\mu\dagger} W_\mu^-) - &\left(g \sin \theta_W J_\mu^3 + g' \cos \theta_W \frac{J_\mu^Y}{2}\right) A^\mu \\ &- \left(g \cos \theta_W J_\mu^3 - g' \sin \theta_W \frac{J_\mu^Y}{2}\right) Z^\mu \end{aligned} \quad (1.27)$$

598 the first term is the weak charged current interaction, while the second term is the

599 electromagnetic interaction under the condition

$$g \sin \theta_W = g' \cos \theta_W = e, \quad \frac{g'}{g} = \tan \theta_W \quad (1.28)$$

600 contained in the Eqn.1.25; the third term is the neutral weak current.

601

602 Note that the neutral fields transformation given by the Eqn. 1.26 can be written  
 603 in terms of the coupling constants  $g$  and  $g'$  as:

$$A_\mu = \frac{g' W_\mu^3 + g B_\mu}{\sqrt{g^2 + g'^2}}, \quad Z_\mu = \frac{g W_\mu^3 - g' B_\mu}{\sqrt{g^2 + g'^2}}. \quad (1.29)$$

604 So far, the Lagrangian density describing the non-massive EWI is:

$$\mathcal{L}_{nmEWI} = \mathcal{L}_0 + \mathcal{L}_G \quad (1.30)$$

605 where fermion and gauge fields have been considered massless because their regular  
 606 mass terms are manifestly non invariant under  $G$  transformations; therefore, masses  
 607 have to be generated in a gauge invariant way. The mechanism by which this goal is  
 608 achieved is known as the *Higgs mechanism* and is closely connected to the concept of  
 609 *spontaneous symmetry breaking*.

### 610 1.3.1 Spontaneous symmetry breaking (SSB)

611 Figure 1.6 left shows a steel nail (top) which is subject to an external force; the form  
 612 of the potential energy is also shown (bottom).

613 Before reaching the critical force value, the system has rotational symmetry with  
 614 respect to the nail axis; however, after the critical force value is reached the nail buck-

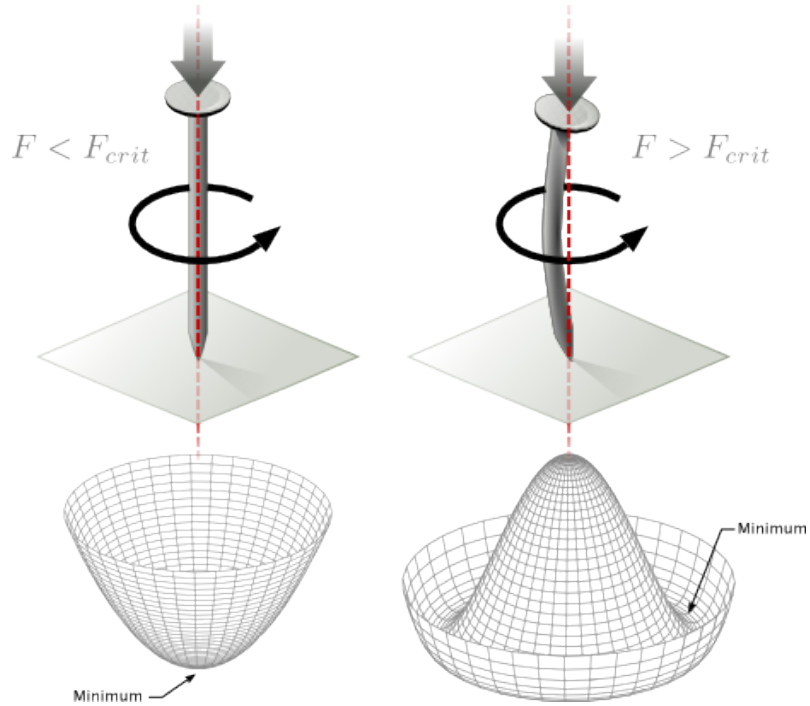


**Figure 1.6:** Spontaneous symmetry breaking mechanism. The steel nail, subject to an external force (top left), has rotational symmetry with respect to its axis. When the external force overcomes a critical value the nail buckles (top right) choosing a minimal energy state (ground state) and thus *breaking spontaneously the rotational symmetry*. The potential energy (bottom) changes but holds the rotational symmetry; however, an infinite number of asymmetric ground states are generated and circularly distributed in the bottom of the potential [31].

615 les (top right). The form of the potential energy (bottom right) changes appearing a  
 616 set of infinity minima but preserving its rotational symmetry. Right before the nail  
 617 buckles there is no indication of the direction the nail will bend because any of the  
 618 directions are equivalent, but once the nail bends, choosing a direction, an arbitrary  
 619 minimal energy state (ground state) is selected and it does not share the system's  
 620 rotational symmetry. This mechanism for reaching an asymmetric ground state is  
 621 known as *spontaneous symmetry breaking*.

622 The lesson from this analysis is that the way to introduce the SSB mechanism  
 623 into a system is by adding the appropriate potential to it.

624 Figure 1.7 shows a plot of the potential  $V(\phi)$  in the case of a scalar field  $\phi$

$$V(\phi) = \mu^2 \phi^\dagger \phi + \lambda (\phi^\dagger \phi)^2 \quad (1.31)$$

625     If  $\mu^2 > 0$  the potential has only one minimum at  $\phi = 0$  and describes a scalar field  
 626    with mass  $\mu$ . If  $\mu^2 < 0$  the potential has a local maximum at  $\phi = 0$  and two minima  
 627    at  $\phi = \pm\sqrt{-\mu^2/\lambda}$  which enables the SSB mechanism to work.

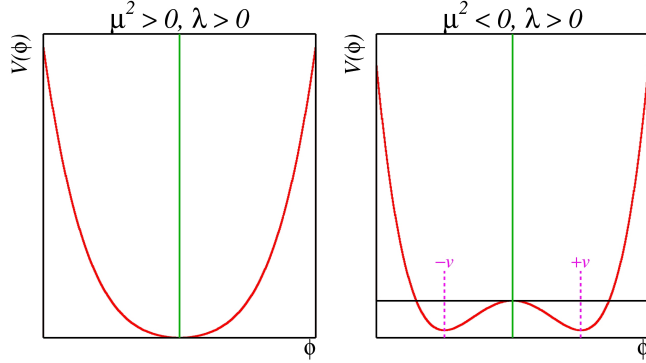


**Figure 1.7:** Shape of the potential  $V(\phi)$  for  $\lambda > 0$  and:  $\mu^2 > 0$  (left) and  $\mu^2 < 0$  (right). The case  $\mu^2 < 0$  corresponds to the potential suitable for introducing the SSB mechanism by choosing one of the two ground states which are connected via reflection symmetry. [31].

628     In the case of a complex scalar field  $\phi(x)$

$$\phi(x) = \frac{1}{\sqrt{2}}(\phi_1 + i\phi_2) \quad (1.32)$$

629    the Lagrangian (invariant under global  $U(1)$  transformations) is given by

$$\mathcal{L} = (\partial_\mu \phi)^\dagger (\partial^\mu \phi) - V(\phi), \quad V(\phi) = \mu^2 \phi^\dagger \phi + \lambda (\phi^\dagger \phi)^2 \quad (1.33)$$

630    where an appropriate potential has been added in order to introduce the SSB.

631     As seen in Figure 1.8, the potential has now an infinite number of minima circularly  
 632    distributed along the  $\xi$ -direction which makes possible the occurrence of the SSB by  
 633    choosing an arbitrary ground state; for instance,  $\xi = 0$ , i.e.  $\phi_1 = v, \phi_2 = 0$

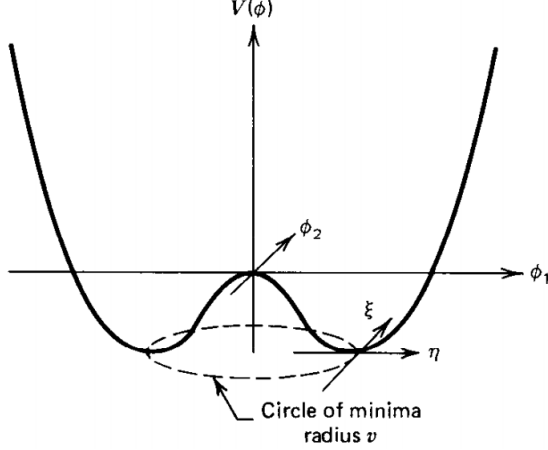


**Figure 1.8:** Potential for complex scalar field. There is a circle of minima of radius  $v$  along the  $\xi$ -direction [6].

$$\phi_0 = \frac{v}{\sqrt{2}} \exp(i\xi) \xrightarrow{\text{SSB}} \phi_0 = \frac{v}{\sqrt{2}} \quad (1.34)$$

634 As usual, excitations over the ground state are studied by making an expansion  
635 about it; thus, the excitations can be parametrized as:

$$\phi(x) = \frac{1}{\sqrt{2}}(v + \eta(x) + i\xi(x)) \quad (1.35)$$

636 which when substituted into Eqn. 1.33 produces a Lagrangian in terms of the new  
637 fields  $\eta$  and  $\xi$

$$\mathcal{L}' = \frac{1}{2}(\partial_\mu \xi)^2 + \frac{1}{2}(\partial_\mu \eta)^2 + \mu^2 \eta^2 - V(\phi_0) - \lambda v \eta (\eta^2 + \xi^2) - \frac{\lambda}{4}(\eta^2 + \xi^2)^2 \quad (1.36)$$

638 where the last two terms represent the interactions and self-interaction between the  
639 two fields  $\eta$  and  $\xi$ . The particular feature of the SSB mechanism is revealed when  
640 looking to the first three terms of  $\mathcal{L}'$ . Before the SSB, only the massless  $\phi$  field is

641 present in the system; after the SSB there are two fields of which the  $\eta$ -field has  
 642 acquired mass  $m_\eta = \sqrt{-2\mu^2}$  while the  $\xi$ -field is still massless (see Figure 1.9).

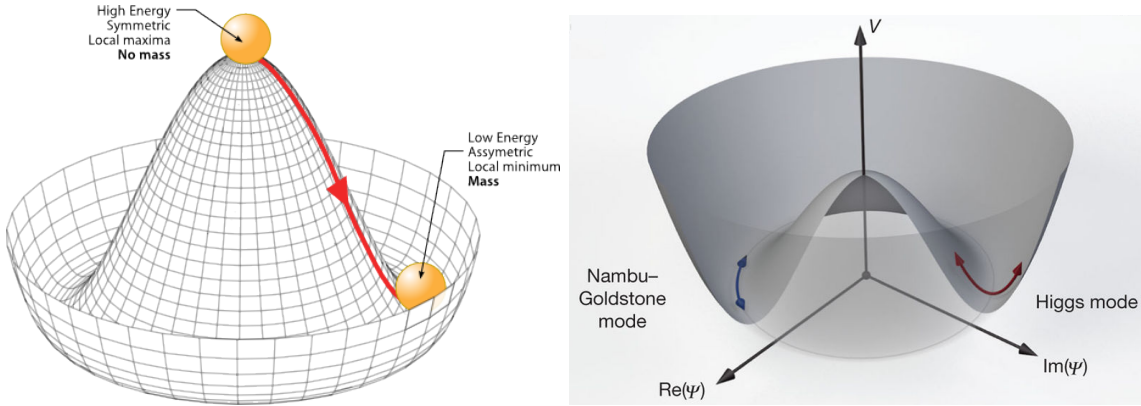


**Figure 1.9:** SSB mechanism for a complex scalar field [31, 32].

643 Thus, the SSB mechanism serves as a method to generate mass but as a side ef-  
 644 fect a massless field is introduced in the system. This fact is known as the Goldstone  
 645 theorem and states that a massless scalar field appears in the system for each con-  
 646 tinuous symmetry spontaneously broken. Another version of the Goldstone theorem  
 647 states that “if a Lagrangian is invariant under a continuous symmetry group  $G$ , but  
 648 the vacuum is only invariant under a subgroup  $H \subset G$ , then there must exist as many  
 649 massless spin-0 particles (Nambu-Goldstone bosons) as broken generators.” [26] The  
 650 Nambu-Goldstone boson can be understood considering that the potential in the  $\xi$ -  
 651 direction is flat so excitations in that direction are not energy consuming and thus  
 652 represent a massless state.

### 653 1.3.2 Higgs mechanism

654 When the SSB mechanism is introduced in the formulation of the EWI in an attempt  
 655 to generate the mass of the so far massless gauge bosons and fermions, an interesting  
 656 effect is revealed. In order to keep the  $G$  symmetry group invariance and generate

657 the mass of the EW gauge bosons, a G invariant Lagrangian density ( $\mathcal{L}_S$ ) has to be  
 658 added to the non massive EWI Lagrangian (Eqn. 1.30)

$$\mathcal{L}_S = (D_\mu \phi)^\dagger (D^\mu \phi) - \mu^2 \phi^\dagger \phi - \lambda (\phi^\dagger \phi)^2, \quad \lambda > 0, \mu^2 < 0 \quad (1.37)$$

$$D_\mu \phi = \left( i\partial_\mu - g \frac{\sigma_i}{2} W_\mu^i - g' \frac{Y}{2} B_\mu \right) \phi \quad (1.38)$$

659  $\phi$  has to be an isospin doublet of complex scalar fields so it preserves the G invariance;  
 660 thus  $\phi$  can be defined as:

$$\phi = \begin{pmatrix} \phi^+ \\ \phi^0 \end{pmatrix} \equiv \frac{1}{\sqrt{2}} \begin{pmatrix} \phi_1 + i\phi_2 \\ \phi_3 + i\phi_4 \end{pmatrix}. \quad (1.39)$$

661 The minima of the potential are defined by

$$\phi^\dagger \phi = \frac{1}{2} (\phi_1^2 + \phi_2^2 + \phi_3^2 + \phi_4^2) = -\frac{\mu^2}{2\lambda}. \quad (1.40)$$

662 The choice of the ground state is critical. By choosing a ground state, invariant  
 663 under  $U(1)_{em}$  gauge symmetry, the photon will remain massless and the  $W^\pm$  and  $Z$   
 664 bosons masses will be generated which is exactly what is needed. In that sense, the  
 665 best choice corresponds to a weak isospin doublet with  $T_3 = -1/2$ ,  $Y_W = 1$  and  $Q = 0$   
 666 which defines a ground state with  $\phi_1 = \phi_2 = \phi_4$  and  $\phi_3 = v$ :

$$\phi_0 \equiv \frac{1}{\sqrt{2}} \begin{pmatrix} 0 \\ v \end{pmatrix}, \quad v^2 \equiv -\frac{\mu^2}{\lambda}. \quad (1.41)$$

667 where the vacuum expectation value  $v$  is fixed by the Fermi coupling  $G_F$  according  
 668 to  $v = (\sqrt{2}G_F)^{1/2} \approx 246$  GeV.

669 The G symmetry has been broken and three Nambu-Goldstone bosons will appear.

670 The next step is to expand  $\phi$  about the chosen ground state as:

$$\phi(x) = \frac{1}{\sqrt{2}} \exp\left(\frac{i}{v} \sigma_i \theta^i(x)\right) \begin{pmatrix} 0 \\ v + H(x) \end{pmatrix} \approx \frac{1}{\sqrt{2}} \begin{pmatrix} \theta_1(x) + i\theta_2(x) \\ v + H(x) - i\theta_3(x) \end{pmatrix} \quad (1.42)$$

671 to describe fluctuations from the ground state  $\phi_0$ . The fields  $\theta_i(x)$  represent the  
 672 Nambu-Goldstone bosons while  $H(x)$  is known as *Higgs field*. The fundamental fea-  
 673 ture of the parametrization used is that the dependence on the  $\theta_i(x)$  fields is factored  
 674 out in a global phase that can be eliminated by taking the physical *unitary gauge*  
 675  $\theta_i(x) = 0$ . Therefore the expansion about the ground state is given by:

$$\phi(x) \frac{1}{\sqrt{2}} \begin{pmatrix} 0 \\ v + H(x) \end{pmatrix} \quad (1.43)$$

676 which when substituted into  $\mathcal{L}_S$  (Eqn. 1.37) results in a Lagrangian containing the  
 677 now massive three gauge bosons  $W^\pm, Z$ , one massless gauge boson (photon) and  
 678 the new Higgs field ( $H$ ). The three degrees of freedom corresponding to the Nambu-  
 679 Goldstone bosons are now integrated into the massive gauge bosons as their lon-  
 680 gitudinal polarizations which were not available when they were massless particles.  
 681 The effect by which vector boson fields acquire mass after an spontaneous symmetry  
 682 breaking, but without an explicit gauge invariance breaking is known as the *Higgs*  
 683 *mechanism*.

684 The mechanism was proposed by three independent groups: F.Englert and R.Brout  
 685 in August 1964 [33], P.Higgs in October 1964 [34] and G.Guralnik, C.Hagen and  
 686 T.Kibble in November 1964 [35]; however, its importance was not realized until  
 687 S.Glashow [22], A.Salam [23] and S.Weinberg [24], independently, proposed that elec-  
 688 tromagnetic and weak interactions are two manifestations of a more general interac-  
 689 tion called *electroweak interaction* in 1967.

690 **1.3.3 Masses of the gauge bosons**

691 The masses of the gauge bosons are extracted by evaluating the kinetic part of La-  
 692 grangian  $\mathcal{L}_S$  in the ground state (known also as the vacuum expectation value), i.e.,

$$\left| \left( \partial_\mu - ig \frac{\sigma_i}{2} W_\mu^i - i \frac{g'}{2} B_\mu \right) \phi_0 \right|^2 = \left( \frac{1}{2} v g \right)^2 W_\mu^+ W^{-\mu} + \frac{1}{8} v^2 (W_\mu^3, B_\mu) \begin{pmatrix} g^2 & -gg' \\ -gg' & g'^2 \end{pmatrix} \begin{pmatrix} W^{3\mu} \\ B^\mu \end{pmatrix} \quad (1.44)$$

693 comparing with the typical mass term for a charged boson  $M_W^2 W^+ W^-$

$$M_W = \frac{1}{2} v g. \quad (1.45)$$

The second term in the right side of the Eqn.1.44 comprises the masses of the neutral bosons, but it needs to be written in terms of the gauge fields  $Z_\mu$  and  $A_\mu$  in order to be compared to the typical mass terms for neutral bosons, therefore using Eqn. 1.29

$$\begin{aligned} \frac{1}{8} v^2 [g^2 (W_\mu^3)^2 - 2gg' W_\mu^3 B^\mu + g'^2 B_\mu^2] &= \frac{1}{8} v^2 [g W_\mu^3 - g' B_\mu]^2 + 0[g' W_\mu^3 + g B_\mu]^2 \quad (1.46) \\ &= \frac{1}{8} v^2 [\sqrt{g^2 + g'^2} Z_\mu]^2 + 0[\sqrt{g^2 + g'^2} A_\mu]^2 \end{aligned}$$

694 and then

$$M_Z = \frac{1}{2} v \sqrt{g^2 + g'^2}, \quad M_A = 0 \quad (1.47)$$

695 **1.3.4 Masses of the fermions**

696 The lepton mass terms can be generated by introducing a gauge invariant Lagrangian  
 697 term describing the Yukawa coupling between the lepton field and the Higgs field

$$\mathcal{L}_{Yl} = -G_l \left[ (\bar{\nu}_l, \bar{l})_L \begin{pmatrix} \phi^+ \\ \phi^0 \end{pmatrix} l_R + \bar{l}_R (\phi^-, \bar{\phi}^0) \begin{pmatrix} \nu_l \\ l \end{pmatrix} \right], \quad l = e, \mu, \tau. \quad (1.48)$$

698 After the SSB and replacing the usual field expansion about the ground state  
 699 (Eqn.1.41) into  $\mathcal{L}_{Yl}$ , the mass term arises

$$\mathcal{L}_{Yl} = -m_l (\bar{l}_L l_R + \bar{l}_R l_L) - \frac{m_l}{v} (\bar{l}_L l_R + \bar{l}_R l_L) H = -m_l \bar{l} l \left( 1 + \frac{H}{v} \right) \quad (1.49)$$

700

$$m_l = \frac{G_l}{\sqrt{2}} v \quad (1.50)$$

701 where the additional term represents the lepton-Higgs interaction. The quark masses  
 702 are generated in a similar way as lepton masses but for the upper member of the  
 703 quark doublet a different Higgs doublet is needed:

$$\phi_c = -i\sigma_2 \phi^* = \begin{pmatrix} -\bar{\phi}^0 \\ \phi^- \end{pmatrix}. \quad (1.51)$$

704 Additionally, given that the quark isospin doublets are not constructed in terms  
 705 of the mass eigenstates but in terms of the flavor eigenstates, as shown in Table 1.5,  
 706 the coupling parameters will be related to the CKM matrix elements; thus, the quark  
 707 Lagrangian is given by:

$$\mathcal{L}_{Yq} = -G_d^{i,j} (\bar{u}_i, \bar{d}'_i)_L \begin{pmatrix} \phi^+ \\ \phi^0 \end{pmatrix} d_{jR} - G_u^{i,j} (\bar{u}_i, \bar{d}'_i)_L \begin{pmatrix} -\bar{\phi}^0 \\ \phi^- \end{pmatrix} u_{jR} + h.c. \quad (1.52)$$

708 with  $i, j = 1, 2, 3$ . After SSB and expansion about the ground state, the diagonal form

709 of  $\mathcal{L}_{Yq}$  is:

$$\mathcal{L}_{Yq} = -m_d^i \bar{d}_i d_i \left(1 + \frac{H}{v}\right) - m_u^i \bar{u}_i u_i \left(1 + \frac{H}{v}\right) \quad (1.53)$$

710 Fermion masses depend on arbitrary couplings  $G_l$  and  $G_{u,d}$  and are not predicted  
711 by the theory.

### 712 1.3.5 The Higgs field

713 After the characterization of the fermions and gauge bosons as well as their interac-  
714 tions, it is necessary to characterize the Higgs field itself. The Lagrangian  $\mathcal{L}_S$  in Eqn.  
715 1.37 written in terms of the gauge bosons is given by

$$\mathcal{L}_S = \frac{1}{4} \lambda v^4 + \mathcal{L}_H + \mathcal{L}_{HV} \quad (1.54)$$

716

$$\mathcal{L}_H = \frac{1}{2} \partial_\mu H \partial^\mu H - \frac{1}{2} m_H^2 H^2 - \frac{1}{2v} m_H^2 H^3 - \frac{1}{8v^2} m_H^2 H^4 \quad (1.55)$$

717

$$\mathcal{L}_{HV} = m_H^2 W_\mu^+ W^{\mu-} \left(1 + \frac{2}{v} H + \frac{2}{v^2} H^2\right) + \frac{1}{2} m_Z^2 Z_\mu Z^\mu \left(1 + \frac{2}{v} H + \frac{2}{v^2} H^2\right) \quad (1.56)$$

718 The mass of the Higgs boson is deduced as usual from the mass term in the Lagrangian  
719 resulting in:

$$m_H = \sqrt{-2\mu^2} = \sqrt{2\lambda}v \quad (1.57)$$

720 however, it is not predicted by the theory either. The experimental measurement of  
721 the Higgs boson mass have been performed by the *Compact Muon Solenoid (CMS)*  
722 experiment and the *A Toroidal LHC Appartus (ATLAS)* experiments at the *Large  
723 Hadron Collider (LHC)*, [36–38], and is presented in Table 1.8.

724

Property	Value
Electric charge	0
Color charge	0
Spin	0
Weak isospin	-1/2
Weak hypercharge	1
Parity	1
Mass (GeV/c <sup>2</sup> )	125.09±0.21 (stat.)±0.11 (syst.)

**Table 1.8:** Higgs boson properties. Higgs mass is not predicted by the theory and the value here corresponds to the experimental measurement.

### 1.3.6 Production of Higgs bosons at LHC

726 At the LHC, Higgs bosons are produced as a result of the collision of two counter-  
 727 rotating protons beams. A detailed description of the LHC machine will be presented  
 in chapter 2.

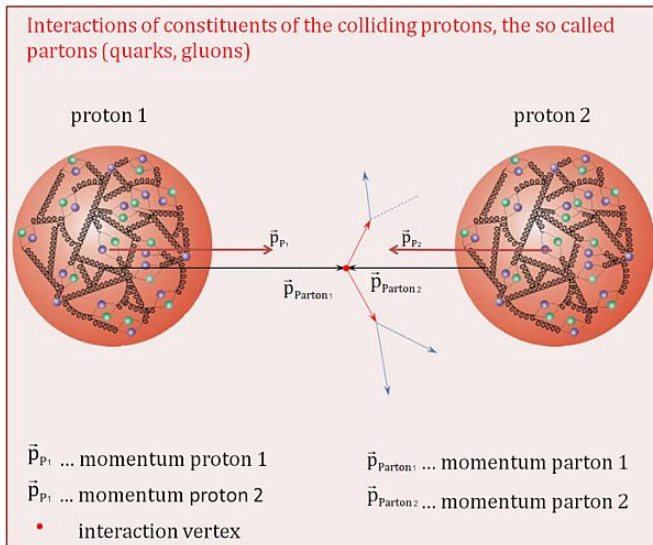


**Figure 1.10:** Proton-proton collision. Protons are composed of 3 valence quarks, a sea of quarks and gluons; therefore in a proton-proton collision, quarks and gluons are those who collide. [39].

728

729 Protons are composed of quarks and these quarks are bound by gluons; however,  
730 what is commonly called the quark content of the proton makes reference to the  
731 valence quarks. In fact, a proton is not just a rigid entity with three balls in it all  
732 tied up with springs, but the gluons exchanged by the valence quarks tend to split

733 spontaneously into quark-antiquark pairs or more gluons, creating *sea of quarks and*  
 734 *gluons* as represented in Figure 1.10.

735 In a proton-proton ( $pp$ ) collision, the proton's constituents, quarks and gluons, are  
 736 those that collide. The  $pp$  cross section depends on the momentum of the colliding  
 737 particles, reason for which it is needed to know how the momentum is distributed  
 738 inside the proton. Quarks and gluons are known as partons, hence, the functions  
 739 that describe how the proton momentum is distributed among partons inside it are  
 740 called *parton distribution functions (PDFs)*; PDFs are determined from experimental  
 741 data obtained in experiments where the internal structure of hadrons is tested, and  
 742 depend on the momentum transfer  $Q$  and the fraction of momentum  $x$  carried by an  
 743 specific parton. Figure 1.11 shows the proton PDFs ( $xf(x, Q^2)$ ) for two values of  $Q$ .

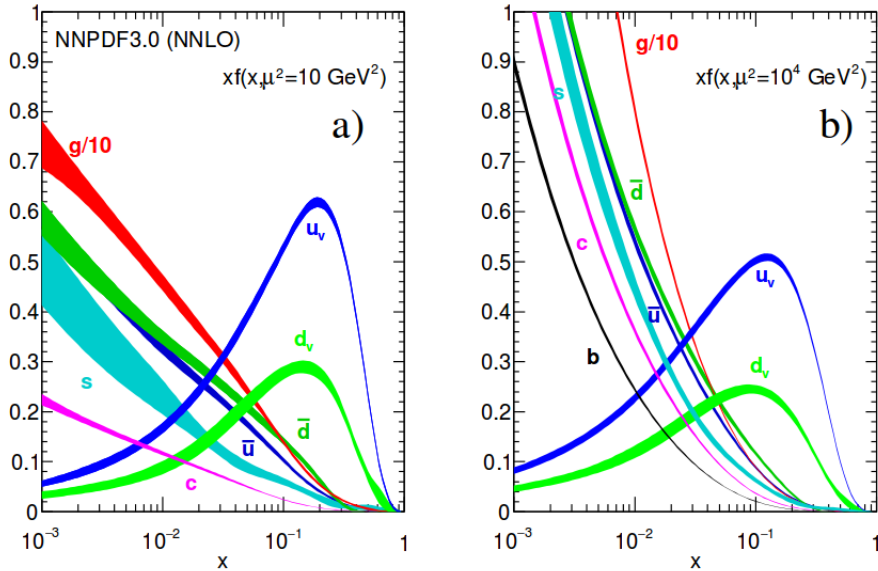


**Figure 1.11:** Proton PDFs for two values of  $Q^2$ : left.  $\mu^2 = Q^2 = 10 \text{ GeV}^2$ , right.  $\mu^2 = Q^2 = 10^4 \text{ GeV}^2$ .  $u_v$  and  $d_v$  correspond to the  $u$  and  $d$  valence quarks,  $s, c, b, \bar{u}, \bar{d}$  correspond to sea quarks, and  $g$  corresponds to gluons. Note that gluons carry a high fraction of the proton's momentum. [9]

744 In physics, a common approach to study complex systems consists of starting  
 745 with a simpler version of them, for which a well known description is available, and

adding an additional *perturbation* which represents a small deviation from the known behavior. If the perturbation is small enough, the physical quantities associated with the perturbed system are expressed as a series of corrections to those of the simpler system. The perturbation series corresponds to an expansion in power series of a small parameter, therefore, the more terms are considered in the series (the higher order in the perturbation series), the more precise is the description of the complex system. If the perturbation does not get progressively smaller, the strategy cannot be applied and new methods have to be employed.

High energy systems, like the Higgs production at LHC explored in this thesis, usually can be treated perturbatively with the expansion made in terms of the coupling constants. The overview presented here will be oriented specifically to the Higgs boson production mechanisms in  $pp$  collisions at LHC.

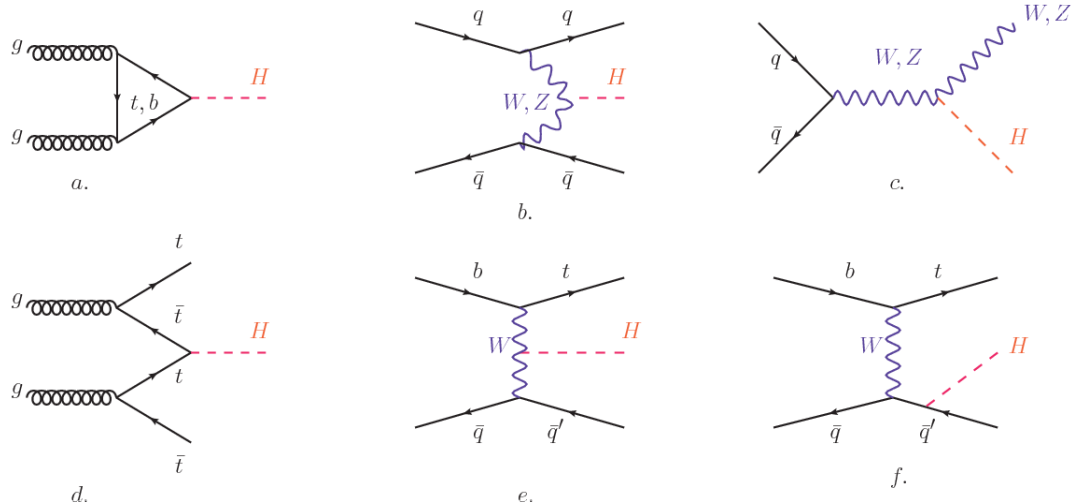


**Figure 1.12:** Main Higgs boson production mechanism Feynman diagrams. a. gluon-gluon fusion, b. vector boson fusion (VBF), c. Higgs-strahlung, d. Associated production with a top or bottom quark pair, e-f. associated production with a single top quark.

Figure 1.12 shows the Feynman diagrams for the leading order (first order) Higgs production processes at LHC; note that in these diagrams the incoming particles are not the protons themselves but the partons from the protons that actually participate

in the interaction, hence, theorists typically calculate the cross section for the parton interaction, and then convolute that cross section with the information from the PDFs to get a production cross section that is actually measured in experiments. The cross section for Higgs production as a function of the center of mass-energy ( $\sqrt{s}$ ) for  $pp$  collisions is showed in Figure 1.13 left. The tags NLO (next to leading order), NNLO (next to next to leading order) and N3LO (next to next to next to leading order) make reference to the order at which the perturbation series have been considered while the tags QCD and EW correspond to the strong and electroweak coupling constants respectively.

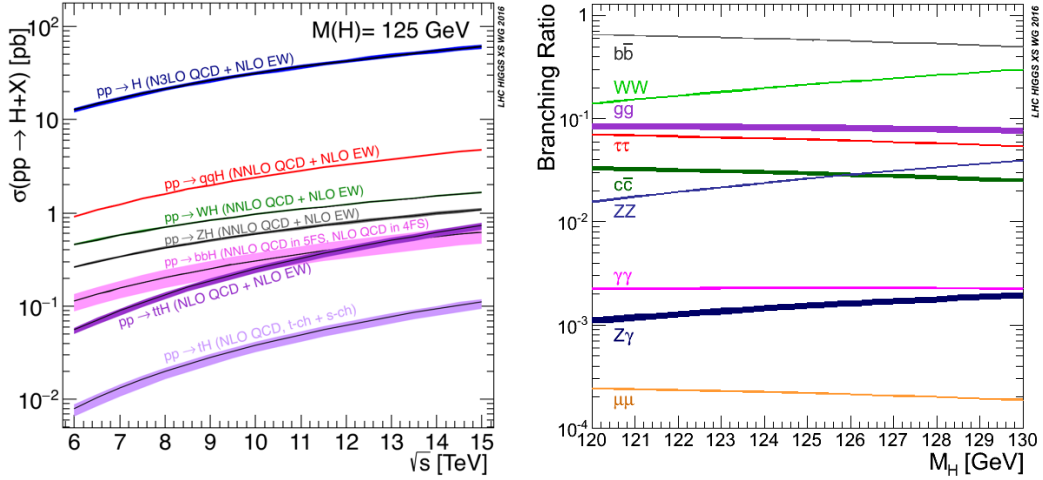


**Figure 1.13:** Higgs boson production cross sections (left) and decay branching ratios (right) for the main mechanisms. The VBF is indicated as  $qqH$  [40].

The main production mechanism is the gluon fusion (Figure 1.12a and  $pp \rightarrow H$  in Figure 1.13) given that gluons carry the highest fraction of momentum of the protons in  $pp$  colliders (as shown in Figure ??). Since the Higgs boson does not couple to gluons, the mechanism proceeds through the exchange of a virtual top-quark loop. Note that in this process the Higgs boson is produced alone, turning out to be problematic for some Higgs decays, because such absence of anything produced in

776 association with the Higgs represent a trouble for triggering, however, this mechanism  
 777 is experimentally clean when combined with the two-photon or the four-lepton decay  
 778 channels (see Section 1.3.7).

779 Vector boson fusion (Figure 1.12b and  $pp \rightarrow qqH$  in Figure 1.13) has the second  
 780 largest production cross section. The scattering of two fermions is mediated by a weak  
 781 gauge boson which later emits a Higgs boson. In the final state, the two fermions tend  
 782 to be located in the central region of the detector; this kind of features are generally  
 783 used as a signature when analyzing the datasets provided by the experiments<sup>7</sup>.

784 In the Higgs-strahlung mechanism (Figure 1.12c and  $pp \rightarrow WH, pp \rightarrow ZH$  in  
 785 Figure 1.13) two fermions annihilate to form a weak gauge boson. If the initial  
 786 fermions have enough energy, the emergent boson might emit a Higgs boson.

787 The associated production with a top or bottom quark pair and the associated  
 788 production with a single top quark (Figure 1.12d-f and  $pp \rightarrow bbH, pp \rightarrow t\bar{t}H, pp \rightarrow tH$   
 789 in Figure 1.13) have a smaller cross section than the main three mechanisms above,  
 790 but they provide a good opportunity to test the Higgs-top coupling. The analysis  
 791 reported in this thesis is developed using these production mechanisms. A detailed  
 792 description of the  $tH$  mechanism will be given in Section 1.5.

### 793 1.3.7 Higgs boson decay channels

794 When a particle can decay through several modes, also known as channels, the prob-  
 795 ability of decaying through a given channel is quantified by the *branching ratio (BR)*  
 796 of the decay channel; thus, the BR is defined as the ratio of number of decays go-  
 797 ing through that given channel to the total number of decays. In regard to the  
 798 Higgs boson decay, the BR can be predicted with accuracy once the Higgs mass is  
 799 known [41, 42]. In Figure 1.13 right, a plot of the BR as a function of the Higgs mass

---

<sup>7</sup> More details about how to identify events of interest in this analysis will be given in chapter 6.

is presented; the largest predicted BR corresponds to the  $b\bar{b}$  pair decay channel (see Table 1.9) given that it is the heaviest particle pair whose on-shell<sup>8</sup> production is kinematically allowed in the decay.

Decay channel	Branching ratio	Rel. uncertainty
$H \rightarrow b\bar{b}$	$5.84 \times 10^{-1}$	$+3.2\% - 3.3\%$
$H \rightarrow W^+W^-$	$2.14 \times 10^{-1}$	$+4.3\% - 4.2\%$
$H \rightarrow \tau^+\tau^-$	$6.27 \times 10^{-2}$	$+5.7\% - 5.7\%$
$H \rightarrow ZZ$	$2.62 \times 10^{-2}$	$+4.3\% - 4.1\%$
$H \rightarrow \gamma\gamma$	$2.27 \times 10^{-3}$	$+5.0\% - 4.9\%$
$H \rightarrow Z\gamma$	$1.53 \times 10^{-3}$	$+9.0\% - 8.9\%$
$H \rightarrow \mu^+\mu^-$	$2.18 \times 10^{-4}$	$+6.0\% - 5.9\%$

**Table 1.9:** Predicted branching ratios and the relative uncertainty for some decay channels of a SM Higgs boson with  $m_H = 125\text{GeV}/c^2$  [9]; the uncertainties are driven by theoretical uncertainties for the different Higgs boson partial widths and by parametric uncertainties associated to the strong coupling and the masses of the quarks which are the input parameters. Further details on these calculations can be found in Reference [43]

803

804 Decays to other lepton and quark pairs, like electron, strange, up, and down  
 805 quark pairs not listed in the table, are also possible but their likelihood is too small  
 806 to measure since they are very lightweight, hence, their interaction with the Higgs  
 807 boson is very weak. On other hand, the decay to top quark pairs is heavily suppressed  
 808 due to the top quark mass ( $\approx 173\text{ GeV}/c^2$ ).

809 Decays to gluons proceed indirectly through a virtual top quark loop while the  
 810 decays to photons proceed through a virtual W boson loop, therefore, their branching  
 811 ratio is smaller compared to direct interaction decays. Same is true for the decay to  
 812 a photon and a Z boson.

---

<sup>8</sup> In general, on-shell or real particles are those which satisfy the energy-momentum relation ( $E^2 - |\vec{p}|^2 c^2 = m^2 c^4$ ); off-shell or virtual particles does not satisfy it which is possible under the uncertainty principle of quantum mechanics. Usually, virtual particles correspond to internal propagators in Feynman diagrams.

813        In the case of decays to pairs of W and Z bosons, the decay proceed with one of  
 814        the bosons being on-shell and the other being off-shell. The likelihood of the process  
 815        diminish depending on how far off-shell are the virtual particles involved, hence, the  
 816        branching ratio for W boson pairs is bigger than for Z boson pairs since Z boson mass  
 817        is bigger than W boson mass.

818        Note that the decay to a pair of virtual top quarks is possible, but the probability  
 819        is way too small.

820        **1.4 Experimental status of the anomalous**  
 821        **Higgs-fermion coupling**

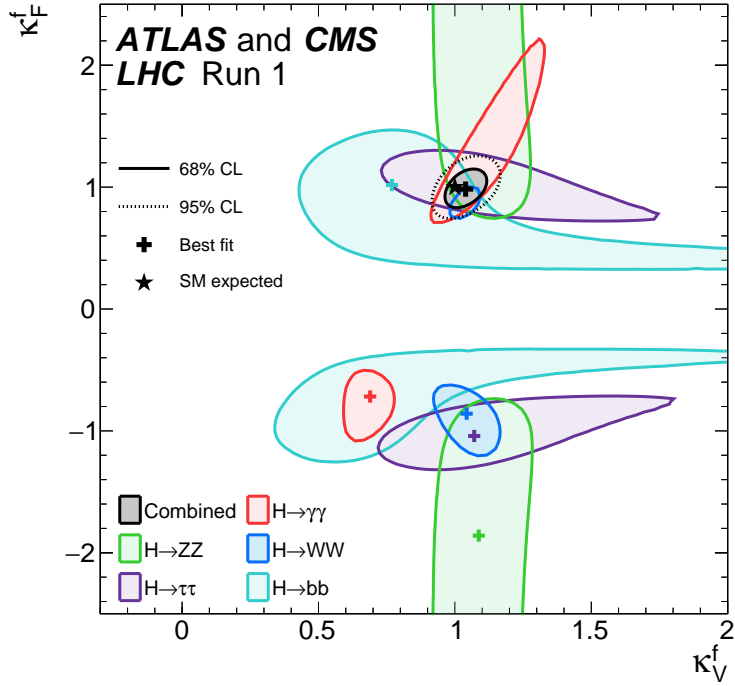


**Figure 1.14:** Combination of the ATLAS and CMS fits for coupling modifiers  $\kappa_t - \kappa_V$ ; also shown the individual decay channels combination and their global combination. No assumptions have been made on the sign of the coupling modifiers [44].

822       ATLAS and CMS have performed analyses of the anomalous Higgs-fermion cou-  
 823 pling by making likelihood scans for the two coupling modifiers,  $\kappa_f$  and  $\kappa_V$ , under  
 824 the assumption that  $\kappa_Z = \kappa_W \equiv \kappa_V$  and  $\kappa_t = \kappa_\tau = \kappa_b \equiv \kappa_f$ . Figure 1.14 shows the  
 825 result of the combination of ATLAS and CMS fits; also the individual decay channels  
 826 combination and the global combination results are shown. Note that from this plot  
 827 there is limited information on the sign of the coupling since the only information  
 828 available about the sign of the coupling comes from decays rather than production.

829       While all the channels are compatible for positive values of the modifiers, for  
 830 negative values of  $\kappa_f$  there is no compatibility. The best fit for individual channels  
 831 is compatible with negative values of  $\kappa_f$  except for the  $H \rightarrow bb$  channel. The best  
 832 fit for the combination yields  $\kappa_f \geq 0$ , in contrast to the yields from the individual  
 833 channels; the reason of this yield resides in the  $H \rightarrow \gamma\gamma$  coupling.  $H \rightarrow \gamma\gamma$  decay  
 834 proceeds through a loop of either top quarks or W bosons, hence, this channel is  
 835 sensitive to  $\kappa_t$  thanks to the interference of these two amplitude contributions; under  
 836 the assumption that no beyond SM particles take part in the loops, a flipped sign  
 837 of  $\kappa_t$  will increase the  $H \rightarrow \gamma\gamma$  branching fraction by a factor of  $\sim 2.4$  which is not  
 838 supported by measurements; thus, this large asymmetry between the positive and  
 839 negative coupling ratios in the  $H \rightarrow \gamma\gamma$  channel drives the yield of the global fit and  
 840 would mean that the anomalous H-t coupling is excluded as stated in Reference [44],  
 841 but there is a caveat, this exclusion holds only if no new particles contribute to the  
 842 loop in the main diagram for that decay.

843       Although the  $H \rightarrow bb$  channel is expected to be the most sensitive channel and  
 844 its best fit value of  $\kappa_t$  is positive, and then the global fit yield is still supported,  
 845 the contributions from all the other decay channels, small compared to the  $H \rightarrow bb$ ,  
 846 indicate that the anomalous H-t coupling cannot be excluded completely, motivating  
 847 to look at  $tH$  processes which can help with both, the limited information on the sign

848 of the H-t coupling and the access to information from the Higgs boson production  
 849 rather than from its decays.

850 It will be shown in Section 1.5 that the same interference effect enhance the  
 851  $tH$  production rate and could reveal evidence of direct production of heavy new par-  
 852 ticles as predicted in composite and little Higgs models [45], or new physics related  
 853 to Higgs boson mediated flavor changing neutral currents [46] as well as probes the  
 854 CP-violating phase of the H-t coupling [47, 48].

## 855 1.5 Associated production of a Higgs boson and a 856 single top quark

857 The production of Higgs boson in association with a top quark has been extensively  
 858 studied [47, 49–52]. While measurements of the main Higgs production mechanisms  
 859 rates are sensitive to the strength of the Higgs coupling to W boson or top quark,  
 860 they are not sensitive to the relative sign between the two couplings. In this thesis,  
 861 the Higgs boson production mechanism explored is the associated production with a  
 862 single top quark ( $tH$ ) which offers sensitivity to the relative sign of the Higgs couplings  
 863 to W boson and to top quark. The description given here is based on Reference [51]

A process where two incoming particles interact and produce a final state with two particles can proceed in three called channels (see, for instance, Figure 1.15 omitting the red line). The t-channel represents processes where an intermediate particle is emitted by one of the incoming particles and absorbed by the other. The s-channel represents processes where the two incoming particles merge into an intermediate particle which eventually will split into the particles in the final state. The third channel, u-channel, is similar to the t-channel but the two outgoing particles interchange their

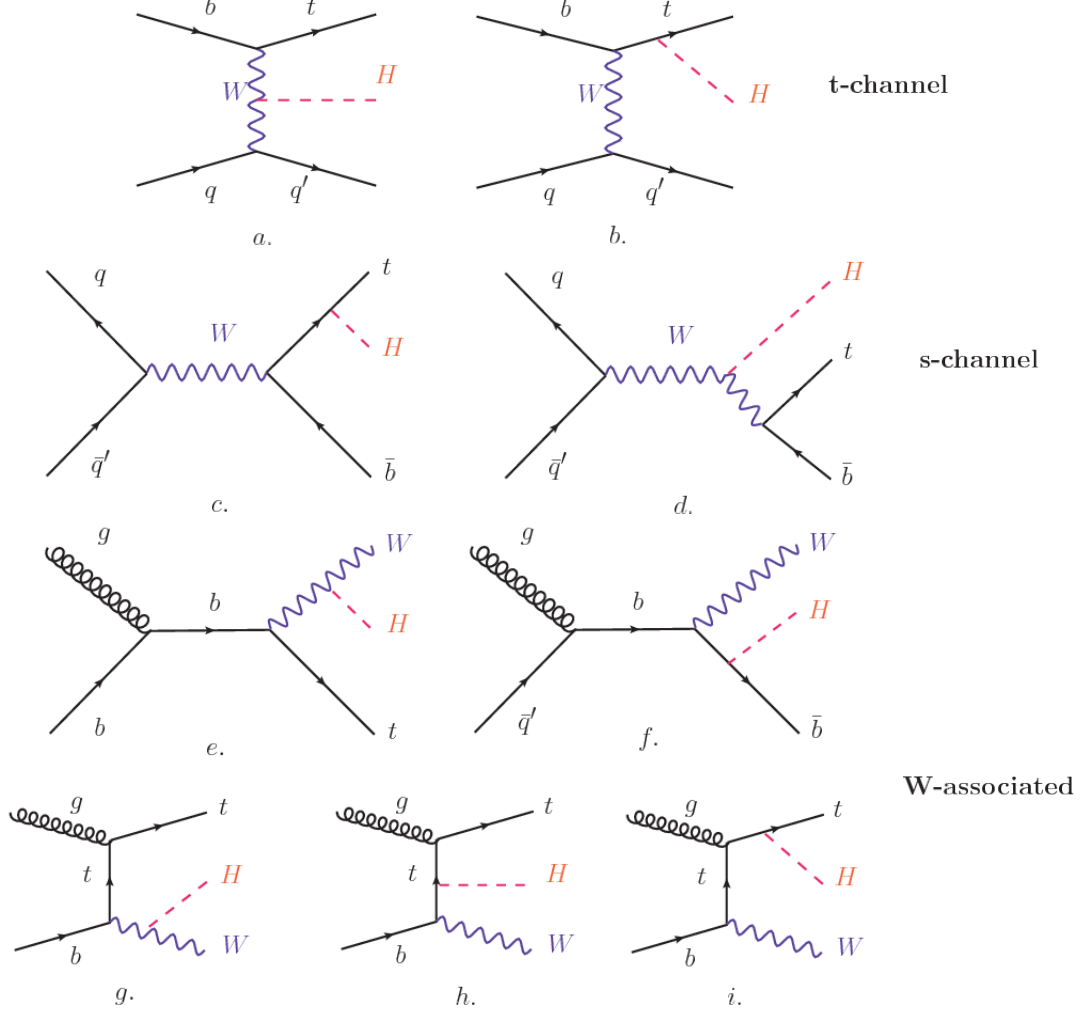


**Figure 1.15:** Associated Higgs boson production with a top quark mechanism Feynman diagrams. a.,b. t-channel ( $tHq$ ), c.,d. s-channel ( $tHb$ ), e-i. W-associated.

roles. These three channels are connected to the so-called Mandelstam variables

$$s = (p_1 + p_2)^2 = (p'_1 + p'_2)^2 \rightarrow \text{square of the center mass-energy.} \quad (1.58)$$

$$t = (p_1 - p'_1)^2 = (p'_2 - p_2)^2 \rightarrow \text{square of the four-momentum transfer.} \quad (1.59)$$

$$u = (p_1 - p'_2)^2 = (p'_1 - p_2)^2 \rightarrow \text{square of the crossed four-momentum transfer.} \quad (1.60)$$

$$s + t + u = m_1^2 + m_2^2 + m'_1^2 + m'_2^2 \quad (1.61)$$

which relate the momentum, energy and the angles of the incoming and outgoing particles in an scattering process of two particles to two particles. The importance of the Mandelstam variables reside in that they form a minimum set of variables needed to describe the kinematics of this scattering process; they are Lorentz invariant which makes them very useful when doing calculations.

The  $tH$  production, where Higgs boson can be radiated either from the top quark or from the W boson, is represented by the leading order Feynman diagrams in Figure 1.15. The cross section for the  $tH$  process is calculated, as usual, summing over the contributions from the different Feynman diagrams; therefore it depends on the interference between the contributions. In the SM, the interference for t-channel ( $tHq$  process) and W-associated ( $tHW$  process) production is destructive [49] resulting in the small cross sections presented in Table 1.10.

tH production channel	Cross section (fb)
t-channel ( $pp \rightarrow tHq$ )	$70.79^{+2.99}_{-4.80}$
W-associated ( $pp \rightarrow tHW$ )	$15.61^{+0.83}_{-1.04}$
s-channel( $pp \rightarrow tHb$ )	$2.87^{+0.09}_{-0.08}$

**Table 1.10:** Predicted SM cross sections for  $tH$  production at  $\sqrt{s} = 13$  TeV [53, 54].

876

The s-channel contribution can be neglected. It will be shown that a deviation from the SM destructive interference would result in an enhancement of the  $tH$  cross section compared to that in SM, which could be used to get information about the sign of the Higgs-top coupling [51, 52]. In order to describe  $tH$  production processes, Feynman diagram 1.15b will be considered; there, the W boson is radiated by a quark in the proton and eventually it will interact with the b quark. In the high energy regime, the effective W approximation [55] is used to describe the process as the

884 emission of an approximately on-shell W and its hard scattering with the b quark;  
 885 i.e.  $Wb \rightarrow th$ . The scattering amplitude for the process is given by

$$\mathcal{A} = \frac{g}{\sqrt{2}} \left[ (\kappa_t - \kappa_V) \frac{m_t \sqrt{s}}{m_W v} A \left( \frac{t}{s}, \varphi; \xi_t, \xi_b \right) + \left( \kappa_V \frac{2m_W s}{v t} + (2\kappa_t - \kappa_V) \frac{m_t^2}{m_W v} \right) B \left( \frac{t}{s}, \varphi; \xi_t, \xi_b \right) \right], \quad (1.62)$$

886 where  $\kappa_V \equiv g_{HVV}/g_{HVV}^{SM}$  and  $\kappa_t \equiv g_{Ht}/g_{Ht}^{SM} = y_t/y_t^{SM}$  are scaling factors that quantify  
 887 possible deviations of the couplings from the SM values, Higgs-Vector boson (H-  
 888 W) and Higgs-top (H-t) respectively, from the SM couplings;  $s = (p_W + p_b)^2$ ,  $t =$   
 889  $(p_W - p_H)^2$ ,  $\varphi$  is the Higgs azimuthal angle around the  $z$  axis taken parallel to the  
 890 direction of motion of the incoming W; A and B are functions describing the weak  
 891 interaction in terms of the chiral states  $(\xi_t, \xi_b)$  of the quarks  $b$  and  $t$ . Terms that  
 892 vanish in the high energy limit have been neglected as well as the Higgs and  $b$  quark  
 893 masses<sup>9</sup>.

894 The scattering amplitude grows with energy like  $\sqrt{s}$  for  $\kappa_V \neq \kappa_t$ , in contrast to  
 895 the SM ( $\kappa_t = \kappa_V = 1$ ), where the first term in 1.62 cancels out and the amplitude  
 896 is constant for large  $s$ ; therefore, a deviation from the SM predictions represents an  
 897 enhancement in the  $tHq$  cross section. In particular, for a SM H-W coupling and a  
 898 H-t coupling of inverted sign with respect to the SM ( $\kappa_V = -\kappa_t = 1$ ) the  $tHq$  cross  
 899 section is enhanced by a factor greater 10 as seen in the Figure 1.16 taken from  
 900 Reference [51]; Reference [56] has reported similar enhancement results.

901 A similar analysis is valid for the W-associated channel but, in that case, the in-  
 902 terference is more complicated since there are more than two contributions and an ad-  
 903 ditional interference with the production of Higgs boson and a top pair process( $t\bar{t}H$ ).  
 904 The calculations are made using the so-called Diagram Removal (DR) technique where

---

<sup>9</sup> A detailed explanation of the structure and approximations used to derive  $\mathcal{A}$  can be found in Reference [51]

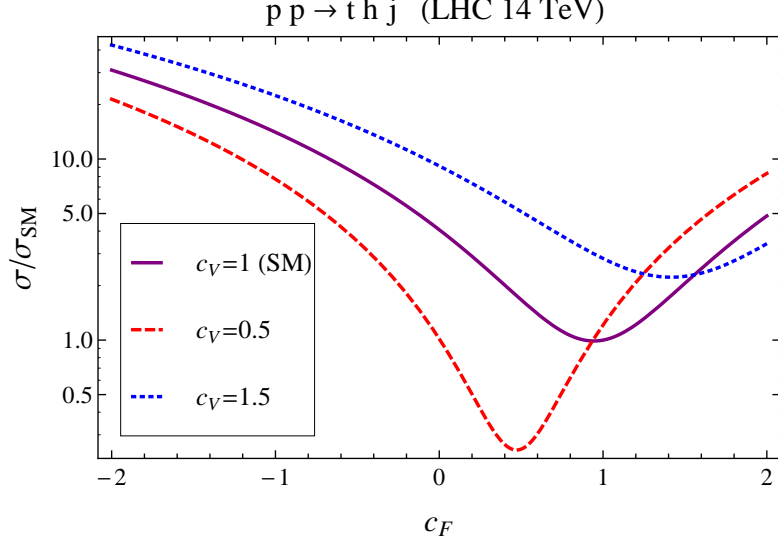


**Figure 1.16:** Cross section for  $tHq$  process as a function of  $\kappa_t$ , normalized to the SM, for three values of  $\kappa_V$ . In the plot  $c_f$  refers to the Higgs-fermion coupling which is dominated by the H-t coupling and represented here by  $\kappa_t$ . Solid, dashed and dotted lines correspond to  $c_V \rightarrow \kappa_V = 1, 0.5, 1.5$  respectively. Note that for the SM ( $\kappa_V = \kappa_t = 1$ ), the destructive effect of the interference is maximal.

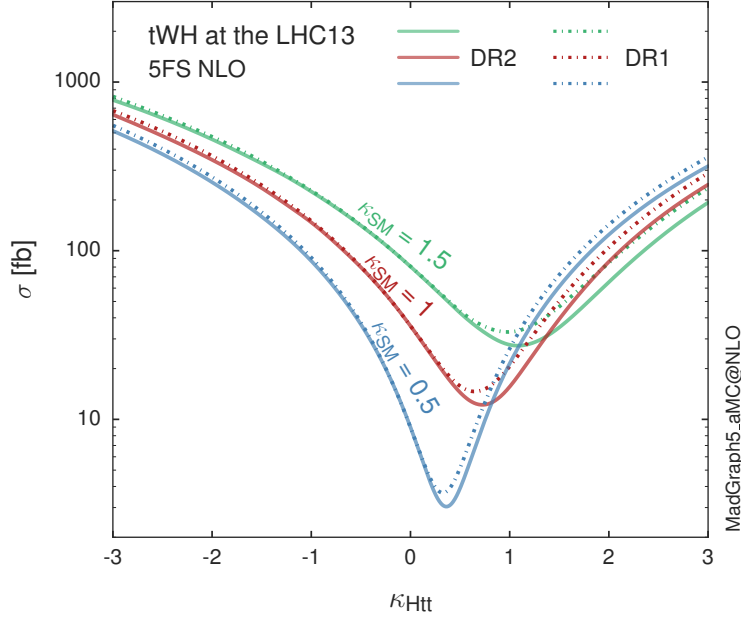


**Figure 1.17:** Cross section for  $tHW$  process as a function of  $\kappa_{Htt}$ , for three values of  $\kappa_{SM}$  at  $\sqrt{s} = 13$  TeV.  $\kappa_{Htt}^2 = \sigma_{Htt}/\sigma_{Htt}^{SM}$  is a simple re-scaling of the SM Higgs interactions.

905 interfering diagrams are removed (or added) from the calculations in order to evaluate  
 906 the impact of the removed contributions. DR1 was defined to neglect  $t\bar{t}H$  interfer-  
 907 ence while DR2 was defined to take  $t\bar{t}H$  interference into account [48]. As shown in  
 908 Figure 1.17, the  $tHW$  cross section is enhanced from about 15 fb (SM:  $\kappa_{Htt} = 1$ ) to  
 909 about 150 fb ( $\kappa_{Htt} = -1$ ). Differences between curves for DR1 and DR2 help to gauge  
 910 the impact of the interference with  $t\bar{t}H$ . Results of the calculations of the  $tHq$  and  
 911  $tHW$  cross sections at  $\sqrt{s} = 13$  TeV can be found in Reference [57] and a summary of  
 912 the results is presented in Table 1.11.

	$\sqrt{s}$ TeV	$\kappa_t = 1$	$\kappa_t = -1$
$\sigma^{LO}(tHq)(fb)$ [51]	8	$\approx 17.4$	$\approx 252.7$
	14	$\approx 80.4$	$\approx 1042$
$\sigma^{NLO}(tHq)(fb)$ [51]	8	$18.28^{+0.42}_{-0.38}$	$233.8^{+4.6}_{-0.0}$
	14	$88.2^{+1.7}_{-0.0}$	$982.8^{+28}_{-0.0}$
$\sigma^{LO}(tHq)(fb)$ [56]	14	$\approx 71.8$	$\approx 893$
$\sigma^{LO}(tHW)(fb)$ [56]	14	$\approx 16.0$	$\approx 139$
$\sigma^{NLO}(tHq)(fb)$ [57]	8	$18.69^{+8.62\%}_{-17.13\%}$	-
	13	$74.25^{+7.48\%}_{-15.35\%}$	$848^{+7.37\%}_{-13.70\%}$
	14	$90.10^{+7.34\%}_{-15.13\%}$	$1011^{+7.24\%}_{-13.39\%}$
$\sigma^{LO}(tHW)(fb)$ [48]	13	$15.77^{+15.91\%}_{-15.76\%}$	-
$\sigma^{NLO}DR1(tHW)(fb)$ [48]	13	$21.72^{+6.52\%}_{-5.24\%}$	$\approx 150$
$\sigma^{NLO}DR2(tHW)(fb)$ [48]	13	$16.28^{+7.34\%}_{-15.13\%}$	$\approx 150$

**Table 1.11:** Predicted enhancement of the  $tHq$  and  $tHW$  cross sections at LHC for  $\kappa_V = 1$  and  $\kappa_t = \pm 1$  at LO and NLO; the cross section enhancement of more than a factor of 10 is due to the flipping in the sign of the H-t coupling with respect to the SM one.

913

## 914 1.6 CP-mixing in $tH$ processes

915 In addition to the sensitivity to sign of the H-t coupling, the  $tHq$  and  $tHW$  processes  
 916 have been proposed as a tool to investigate the possibility of a H-t coupling that does

917 not conserve CP [47, 48, 58].

918 In this thesis, the sensitivity of  $tH$ processes to CP-mixing is also studied on the  
 919 basis of References [47, 48] using the effective field theory framework where a generic  
 920 particle ( $X_0$ ) of spin-0 and a general CP violating interaction with the top quark  
 921 ( $Htt$  coupling), can couple to scalar and pseudo-scalar fermionic densities. The H-W  
 922 interaction is assumed to be SM-like. The Lagrangian modeling the H-t interaction  
 923 is given by

$$\mathcal{L}_0^t = -\bar{\psi}_t (c_\alpha \kappa_{Htt} g_{Htt} + i s_\alpha \kappa_{Att} g_{Att} \gamma_5) \psi_t X_0, \quad (1.63)$$

924 where  $\alpha$  is the CP-mixing phase,  $c_\alpha \equiv \cos \alpha$  and  $s_\alpha \equiv \sin \alpha$ ,  $\kappa_{Htt}$  and  $\kappa_{Att}$  are real  
 925 dimensionless re-scaling parameters<sup>10</sup> used to parametrize the magnitude of the CP-  
 926 violating and CP-conserving parts of the amplitude. The model defines  $g_{Htt} =$   
 927  $g_{Att} = m_t/v = y_t/\sqrt{2}$  with  $v \sim 246$  GeV the Higgs vacuum expectation value. In  
 928 this parametrization, three special cases can be recovered

929 • CP-even coupling  $\rightarrow \alpha = 0^\circ$

930 • CP-odd coupling  $\rightarrow \alpha = 90^\circ$

931 • SM coupling  $\rightarrow \alpha = 0^\circ$  and  $\kappa_{Htt} = 1$

932 The loop induced  $X_0$  coupling to gluons can also be described in terms of the  
 933 parametrization above, according to

$$\mathcal{L}_0^g = -\frac{1}{4} \left( c_\alpha \kappa_{Hgg} g_{Hgg} G_{\mu\nu}^a G^{a,\mu\nu} + s_\alpha \kappa_{Agg} g_{Agg} G_{\mu\nu}^a \tilde{G}^{a,\mu\nu} \right) X_0. \quad (1.64)$$

934 where  $g_{Hgg} = -\alpha_s/3\pi v$  and  $g_{Agg} = \alpha_s/2\pi v$  and  $G_{\mu\nu}$  is the gluon field strength tensors.

935 Under the assumption that the top quark dominates the gluon-fusion process at LHC

---

<sup>10</sup> analog to  $\kappa_t$  and  $\kappa_V$

936 energies,  $\kappa_{Hgg} \rightarrow \kappa_{Htt}$  and  $\kappa_{Agg} \rightarrow \kappa_{Att}$ , so that the ratio between the gluon-gluon  
 937 fusion cross section for  $X_0$  and for the SM Higgs prediction can be written as

$$\frac{\sigma_{NLO}^{gg \rightarrow X_0}}{\sigma_{NLO,SM}^{gg \rightarrow H}} = c_\alpha^2 \kappa_{Htt}^2 + s_\alpha^2 \left( \kappa_{Att} \frac{g_{Agg}}{g_{Hgg}} \right)^2. \quad (1.65)$$

938 If the re-scaling parameters are set to

$$\kappa_{Htt} = 1, \quad \kappa_{Att} = \left| \frac{g_{Hgg}}{g_{Agg}} \right| = \frac{2}{3}. \quad (1.66)$$

939 the gluon-fusion SM cross section is reproduced for every value of the CP-mixing  
 940 angle  $\alpha$ ; therefore, by imposing that condition to the Lagrangian density 1.63, the  
 941 CP-mixing angle is not constrained by current data. Figure 1.18 shows the NLO cross  
 942 sections for t-channel  $tX_0$ (blue) and  $t\bar{t}X_0$  (red) associated production processes as a  
 943 function of the CP-mixing angle  $\alpha$ .  $X_0$  is a generic spin-0 particle with top quark  
 944 CP-violating coupling. Re-scaling factors  $\kappa_{Htt}$  and  $\kappa_{Att}$  have been set to reproduce  
 945 the SM gluon-fusion cross sections.

946 It is interesting to notice that the  $tX_0$  cross section is enhanced, by a factor of  
 947 about 10, when a continuous rotation in the scalar-pseudoscalar plane is applied; this  
 948 enhancement is similar to the enhancement produced when the H-t coupling is flipped  
 949 in sign with respect to the SM ( $y_t = -y_{t,SM}$  in the plot), as showed in Section 1.5. In  
 950 contrast, the degeneracy in the  $t\bar{t}X_0$  cross section is still present given that it depends  
 951 quadratically on the H-t coupling, but more interesting is to notice that  $t\bar{t}X_0$  cross  
 952 section is exceeded by  $tX_0$  cross section after  $\alpha \sim 60^\circ$ .

953 A similar parametrization can be used to investigate the  $tHW$  process sensitivity  
 954 to CP-violating H-t coupling. As said in 1.5, the interference in the W-associated  
 955 channel is more complicated because there are more than two contributions and also  
 956 there is interference with the  $t\bar{t}H$  production process.

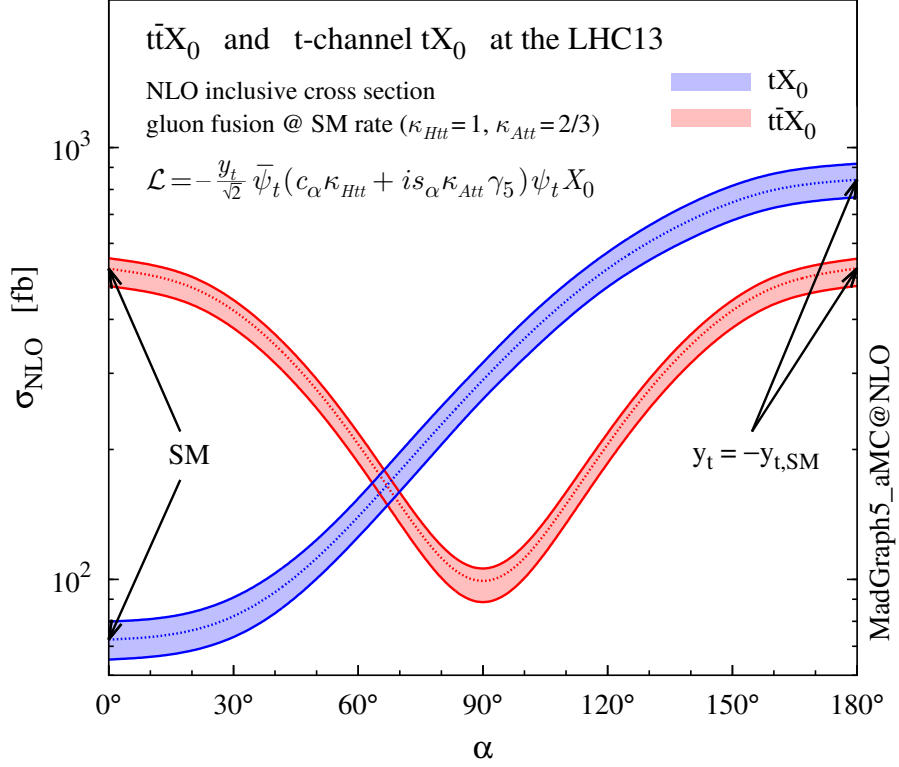


**Figure 1.18:** NLO cross sections for t-channel  $tX_0$ (blue) and  $t\bar{t}X_0$  (red) associated production processes as a function of the CP-mixing angle  $\alpha$ .  $X_0$  is a generic spin-0 particle with top quark CP-violating coupling [47].

957       Figure 1.19 shows the NLO cross sections for t-channel  $tX_0$ (blue),  $t\bar{t}X_0$  (red)  
958       associated production and for the combined  $tWX_0+t\bar{t}X_0+interference$  (orange) as  
959       a function of the CP-mixing angle. It is clear that the effect of the interference in the  
960       combined case is the lifting of the degeneracy present in the  $t\bar{t}X_0$  production. The  
961       constructive interference enhances the cross section from about 500 fb at SM ( $\alpha = 0$ )  
962       to about 600 fb ( $\alpha = 180^\circ \rightarrow y_t = -y_{t,SM}$ ).

963       An analysis combining  $tHq$  and  $tHW$ processes will be made in this thesis taking  
964       advantage of the sensitivity improvement.

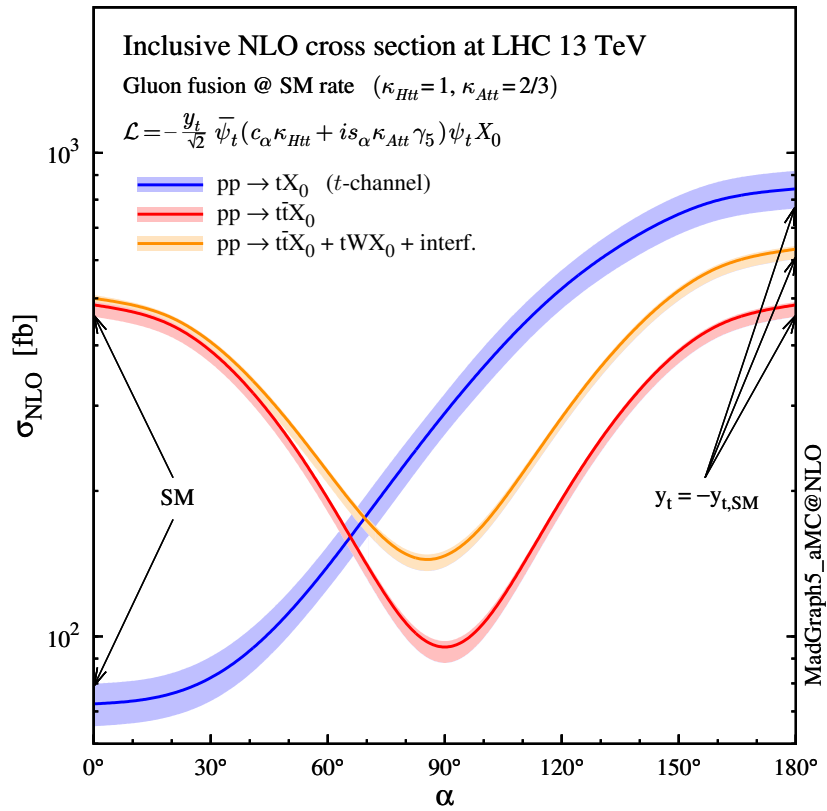


**Figure 1.19:** NLO cross sections for t-channel  $tX_0$ (blue),  $t\bar{t}X_0$  (red) associated production processes and combined  $tWX_0 + t\bar{t}X_0$  (including interference) production as a function of the CP-mixing angle  $\alpha$  [47].

965 **Chapter 2**

966 **The CMS experiment at the LHC**

967 **2.1 Introduction**

968 Located on the Swiss-French border, the European Council for Nuclear Research  
969 (CERN) is the largest scientific organization leading particle physics research. About  
970 13000 people in a broad range of roles including users, students, scientists, engineers,  
971 among others, contribute to the data taking and analysis, with the goal of unveiling  
972 the secrets of nature and revealing the fundamental structure of the universe. CERN  
973 is also the home of the Large Hadron Collider (LHC), the largest particle accelerator  
974 around the world, where protons (or heavy ions) traveling close to the speed of light,  
975 are made to collide. These collisions open a window to investigate how particles (and  
976 their constituents if they are composite) interact with each other, providing clues  
977 about the laws of nature. This chapter presents an overview of the LHC structure  
978 and operation. A detailed description of the CMS detector is offered, given that the  
979 data used in this thesis have been taken with this detector.

## 980 2.2 The LHC

981 With 27 km of circumference, the LHC is currently the most powerful circular accelerator  
 982 in the world. It is installed in the same tunnel where the Large Electron-Positron  
 983 (LEP) collider was located, taking advantage of the existing infrastructure. The LHC  
 984 is part of the CERN's accelerator complex composed of several successive accelerat-  
 985 ing stages before the particles are injected into the LHC ring where they reach their  
 986 maximum energy (see Figure 2.1).

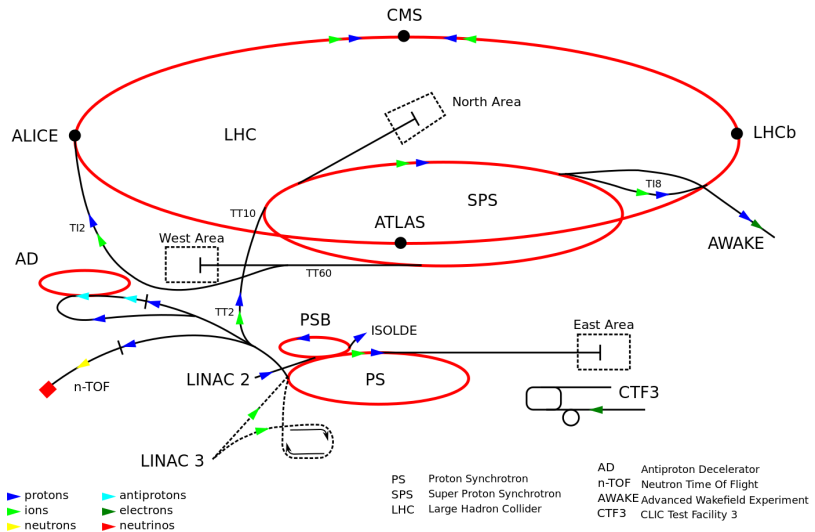


**Figure 2.1:** CERN accelerator complex. Blue arrows show the path followed by protons along the acceleration process [61].

987 The LHC runs in three collision modes depending on the particles being acceler-  
 988 ated

- 989 • Proton-Proton collisions ( $pp$ ) for multiple physics experiments.
- 990 • Lead-Lead collisions ( $Pb-Pb$ ) for heavy ion experiments.
- 991 • Proton-Lead collisions ( $p-Pb$ ) for quark-gluon plasma experiments.

992 In this thesis only  $pp$  collisions will be considered.

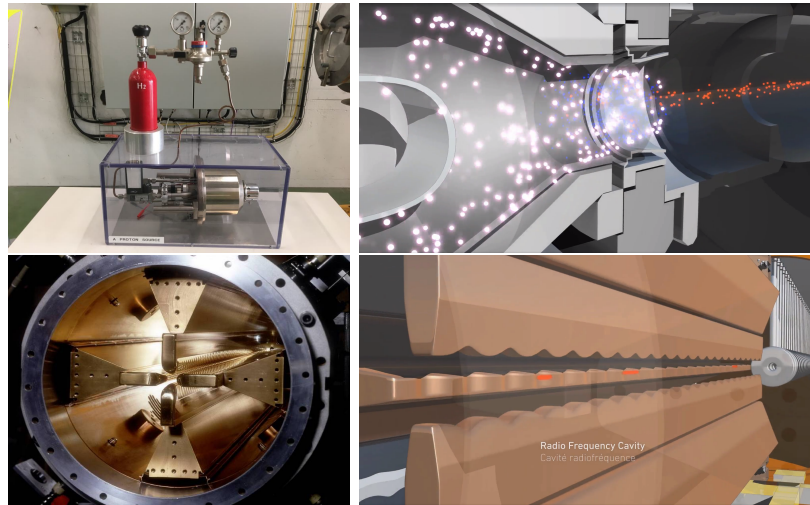


**Figure 2.2:** LHC protons source and the first acceleration stage. Top: the bottle contains hydrogen gas which is injected into the metal cylinder (white dots) to be broken down into electrons (blue dots) and protons (red dots); Bottom: the obtained protons are directed towards the radio frequency quadrupole which perform the first acceleration, focus the beam and create the bunches of protons. Left images are real pictures while right images are drawings [65, 66].

993      Collection of protons starts with hydrogen atoms taken from a bottle, containing  
 994      hydrogen gas, and injecting them in a metal cylinder; hydrogen atoms are broken  
 995      down into electrons and protons by an intense electric field (see Figure 2.2 top).  
 996      The resulting protons leave the metal cylinder towards a radio frequency quadrupole  
 997      (RFQ) that focus the beam, accelerates the protons and creates the packets of protons  
 998      called bunches. In the RFQ, an electric field is generated by a RF wave at a frequency  
 999      that matches the resonance frequency of the cavity where the electrodes are contained.  
 1000     The beam of protons traveling on the RFQ axis experiences an alternating electric  
 1001     field gradient that generates the focusing forces.

1002     In order to accelerate the protons, a longitudinal time-varying electric field com-  
 1003     ponent is added to the system; it is done by giving the electrodes a sine-like profile as  
 1004     shown in Figure 2.2 bottom. By matching the speed and phase of the protons with  
 1005     the longitudinal electric field the bunching is performed; protons synchronized with

1006 the RFQ (synchronous protons) do not feel an accelerating force, but those protons in  
 1007 the beam that have more (or less) energy than the synchronous proton (asynchronous  
 1008 protons) will feel a decelerating (accelerating) force; therefore, asynchronous protons  
 1009 will oscillate around the synchronous ones forming bunches of protons [63]. From the  
 1010 RFQ protons emerge with energy 750 keV in bunches of about  $1.15 \times 10^{11}$  protons [64].

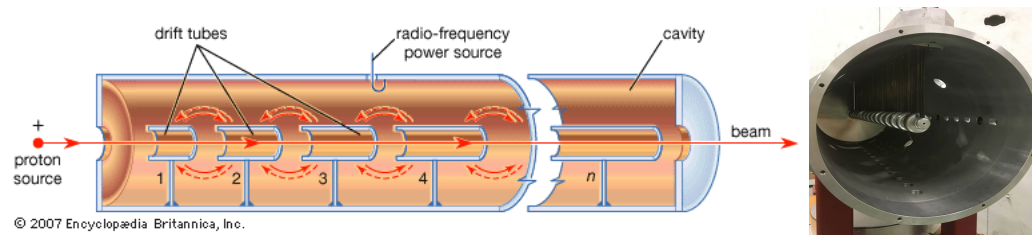


**Figure 2.3:** Left: drawing of the LINAC2 accelerating system at CERN. Electric fields generated by radio frequency (RF) create acceleration and deceleration zones inside the cavity; deceleration zones are blocked by drift tubes where quadrupole magnets focus the proton beam. Right: picture of a real RF cavity [67].

1011 Proton bunches coming from the RFQ go to the linear accelerator 2 (LINAC2)  
 1012 where they are accelerated to reach 50 MeV energy. In the LINAC2 stage, acceleration  
 1013 is performed using electric fields generated by radio frequency which create zones  
 1014 of acceleration and deceleration as shown in Figure 2.3. In the deceleration zones,  
 1015 the electric field is blocked using drift tubes where protons are free to drift while  
 1016 quadrupole magnets focus the beam.

1017 The beam coming from LINAC2 is injected into the proton synchrotron booster  
 1018 (PSB) to reach 1.4 GeV in energy. The next acceleration is provided at the proton  
 1019 synchrotron (PS) up to 26 GeV, followed by the injection into the super proton  
 1020 synchrotron (SPS) where protons are accelerated to 450 GeV. Finally, protons are  
 1021 injected into the LHC where they are accelerated to the target energy of 6.5 TeV.

1022 PSB, PS, SPS and LHC accelerate protons using the same RF acceleration tech-  
 1023 nique described before.

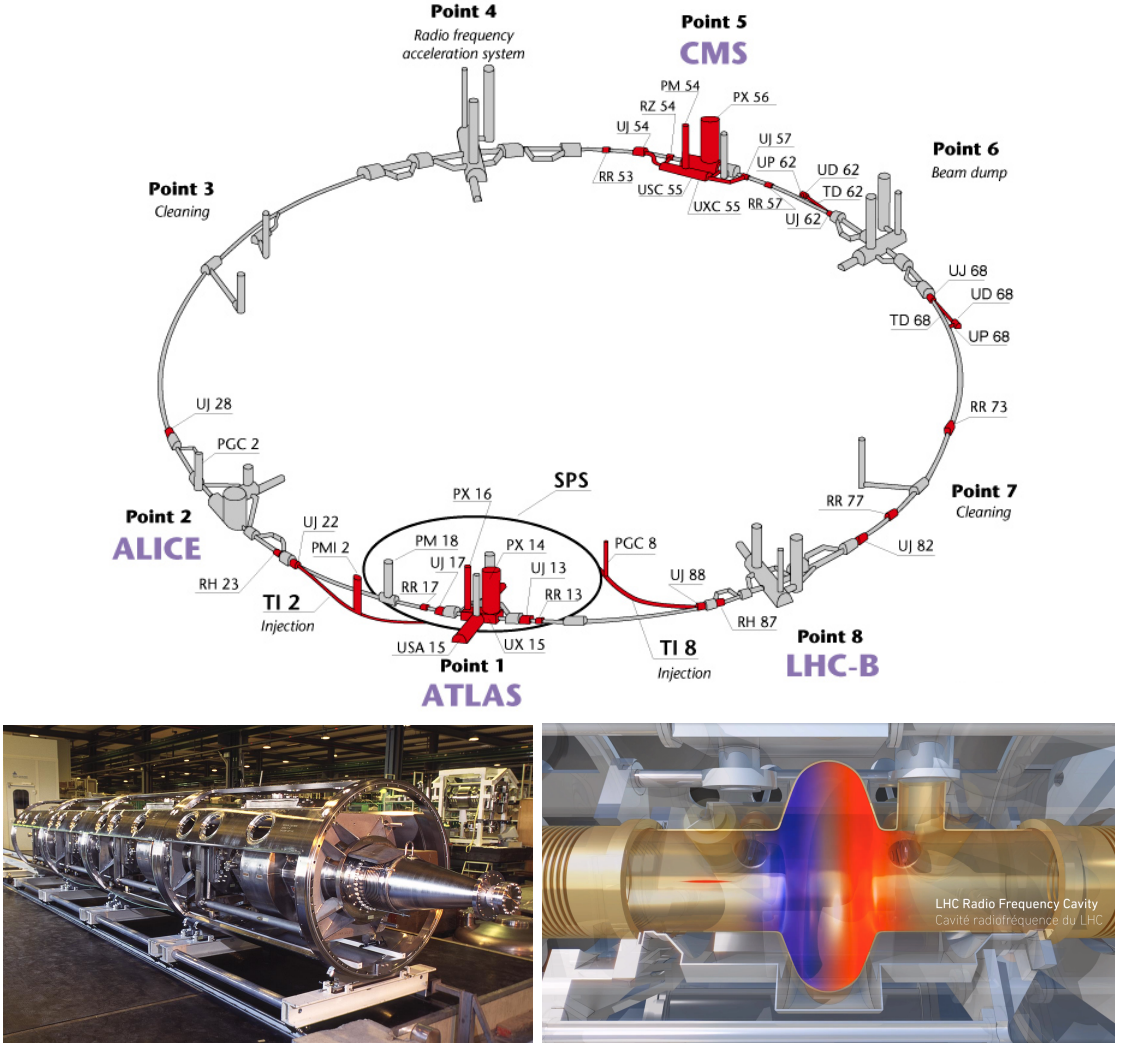


**Figure 2.4:** Top: LHC layout. The red zones indicate the infrastructure additions to the LEP installations, built to accommodate the ATLAS and CMS experiments which exceed the size of the former experiments located there [62]. Bottom: LHC RF cavities. A module (left picture) accommodates 4 cavities, each like the one in the right drawing, that accelerate protons and preserve the bunch structure of the beam. The color gradient pattern represents the strength of the electric field inside the cavity; red zone corresponds to the maximum of the oscillation electric field while the blue zone corresponds to the minimum. [66, 68]

1024        The LHC has a system of 16 RF cavities located in the so-called point 4, as  
 1025        shown in Figure 2.4 top, tuned at a frequency of 400 MHz. The bottom side of  
 1026        Figure 2.4 shows a picture of a RF module composed of 4 RF cavities working in a  
 1027        superconducting state at 4.5 K; also, a representation of the accelerating electric field

that accelerates the protons in the bunch is shown. The maximum of the oscillating electric field (red region) picks the proton bunches at the entrance of the cavity and keeps accelerating them through the whole cavity. The protons are carefully timed so that in addition to the acceleration effect the bunch structure of the beam is preserved.

While protons are accelerated in one section of the LHC ring, where the RF cavities are located, in the rest of their path they have to be kept in the curved trajectory defined by the LHC ring. Technically, LHC is not a perfect circle; RF, injection, beam dumping, beam cleaning and sections before and after the experimental points where protons collide are all straight sections. In total, there are 8 arcs 2.45 km long each and 8 straight sections 545 m long each. In order to curve the proton's trajectory in the arc sections, superconducting dipole magnets are used.

Inside the LHC ring, there are two proton beams traveling in opposite directions in two separated beam pipes; the beam pipes are kept at ultra-high vacuum ( $\sim 10^{-9}$  Pa) to ensure that there are no particles that interact with the proton beams. The superconducting dipole magnets used in LHC are made of a NbTi alloy, capable of transporting currents of about 12000 A when cooled at a temperature below 2K using liquid helium (see Figure 2.5).

Protons in the arc sections of LHC feel a centripetal force exerted by the dipole magnets; the magnitude of magnetic field needed to keep the protons in the LHC curved trayectomy can be found assuming that protons travel at  $v \approx c$ , using the standard values for proton mass and charge and the LHC radius, as

$$F_m = \frac{mv^2}{r} = qBv \rightarrow B = 8.33T \quad (2.1)$$

which is about 100000 times the Earth's magnetic field. A representation of the

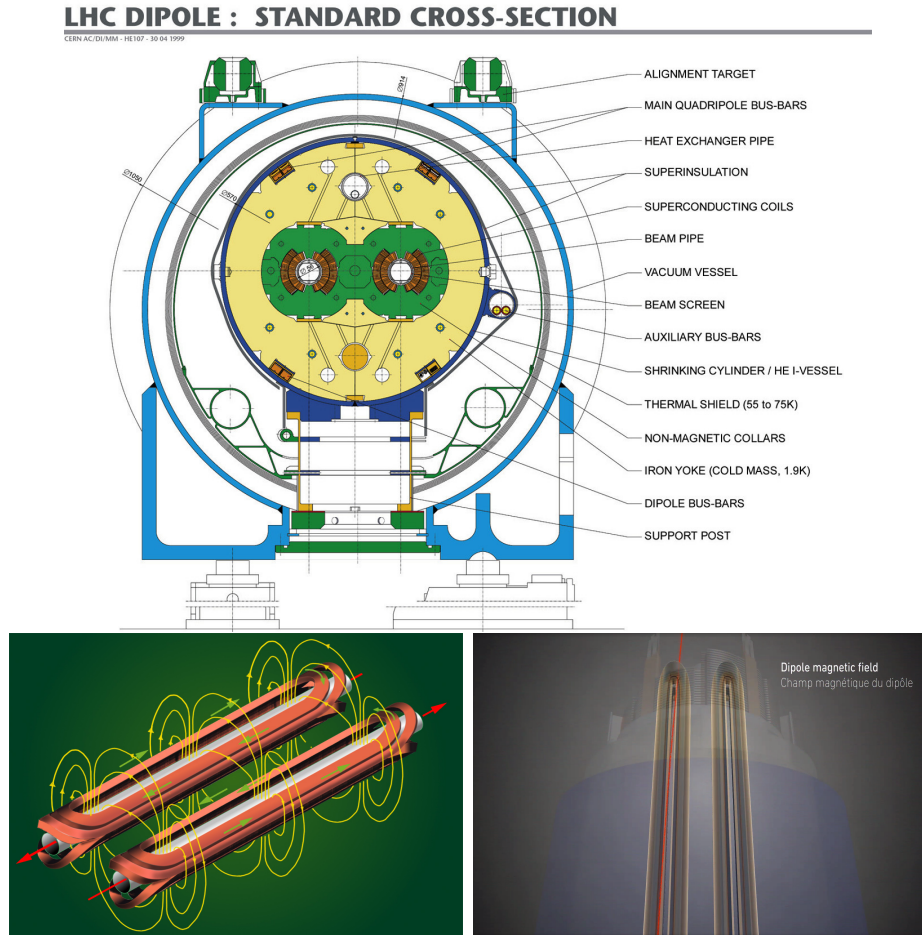


**Figure 2.5:** Top: LHC dipole magnet transverse view; cooling, shielding and mechanical support are indicated. Bottom left: Magnetic field generated by the dipole magnets; note that the direction of the field inside one beam pipe is opposite with respect to the other beam pipe which guarantee that both proton beams are curved in the same direction towards the center of the ring. The effect of the dipole magnetic field on the proton beam is represented on the bottom right side [66, 69, 70].

1051 magnetic field generated by the dipole magnets is shown on the bottom left side of  
 1052 Figure 2.5. The bending effect of the magnetic field on the proton beam is shown on  
 1053 the bottom right side of Figure 2.5. Note that the dipole magnets are not curved;  
 1054 the arc section of the LHC ring is composed of straight dipole magnets of about 15  
 1055 m. In total there are 1232 dipole magnets along the LHC ring.  
 1056 In addition to the bending of the beam trajectory, the beam has to be focused. The

focusing is performed by quadrupole magnets installed in a different straight section; in total 858 quadrupole magnets are installed along the LHC ring. Other effects like electromagnetic interaction among bunches, interaction with electron clouds from the beam pipe, the gravitational force on the protons, differences in energy among protons in the same bunch, among others, are corrected using sextupole and other magnetic multipoles.

The two proton beams inside the LHC ring are made of bunches with a cylindrical shape of about 7.5 cm long and about 1 mm in diameter; when bunches are close to the interaction point (IP), the beam is focused up to a diameter of about 16  $\mu\text{m}$  in order to maximize the probability of collisions between protons. The number of collisions per second is proportional to the cross section of the bunches with the *luminosity* ( $L$ ) as the proportionality factor, thus, the luminosity can be calculated using

$$L = fn \frac{N_1 N_2}{4\pi\sigma_x\sigma_y} \quad (2.2)$$

where  $f$  is the revolution frequency,  $n$  is the number of bunches per beam,  $N_1$  and  $N_2$  are the numbers of protons per bunch,  $\sigma_x$  and  $\sigma_y$  are the gaussian transverse sizes of the bunches. With the expected parameters, the LHC expected luminosity is about

$$f = \frac{v}{2\pi r_{LHC}} \approx \frac{3 \times 10^8 \text{ m/s}}{27 \text{ km}} \approx 11.1 \text{ kHz},$$

$$n = 2808$$

$$N_1 = N_2 \sim 1.5 \times 10^{11}$$

$$\sigma_x = \sigma_y = 16 \mu\text{m}$$

$$L = 1.28 \times 10^{34} \text{ cm}^{-2} \text{ s}^{-1} = 1.28 \times 10^{-5} \text{ fb}^{-1} \text{ s}^{-1} \quad (2.3)$$

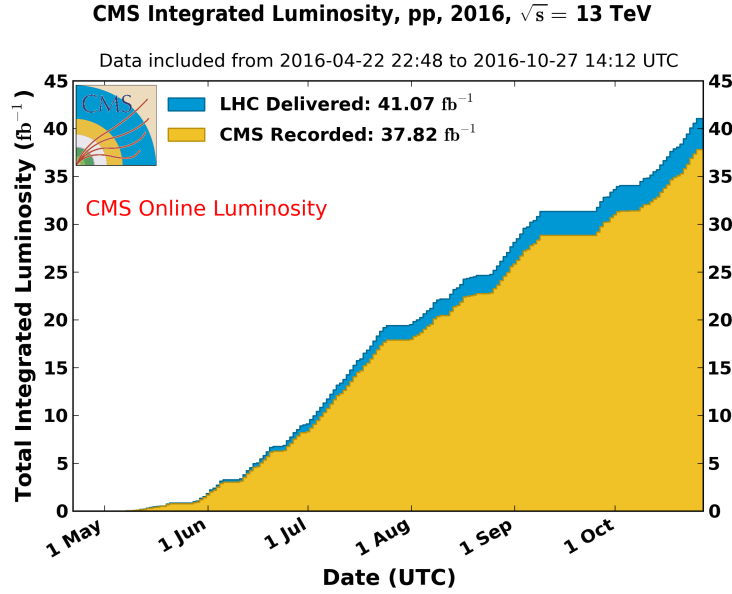


**Figure 2.6:** Integrated luminosity delivered by LHC and recorded by CMS during 2016. The difference between the delivered and the recorded luminosity is due to fails and issues occurred during the data taking in the CMS experiment [71].

1073        Luminosity is a fundamental aspect of LHC given that the bigger luminosity the  
 1074        bigger number of collisions, which means that for processes with a very small cross  
 1075        section the number of expected occurrences is increased and so the chances of being  
 1076        detected. The integrated luminosity, collected by the CMS experiment during 2016  
 1077        is shown in Figure 2.6; the data analyzed in this thesis corresponds to an integrated  
 1078        luminosity of  $35.9 \text{ fb}^{-1}$  at a center of mass-energy  $\sqrt{s} = 13 \text{ TeV}$ .

1079        One way to increase  $L$  is increasing the number of bunches in the beam. Cur-  
 1080        rently, the separation between two consecutive bunches in the beam is 7.5 m which  
 1081        corresponds to a time separation of 25 ns. In the full LHC ring the allowed number  
 1082        of bunches is  $n = 27\text{km}/7.5\text{m} = 3600$ ; however, there are some gaps in the bunch pat-  
 1083        tern intended for preparing the dumping and injection of the beam, thus, the proton  
 1084        beams are composed of 2808 bunches.

1085        Once the proton beams reach the desired energy, they are brought to cross each

1086 other producing  $pp$  collisions. The bunch crossing happens in precise places where  
 1087 the four LHC experiments are located, as seen in the top of Figure 2.7. In 2008  $pp$   
 1088 collisions of  $\sqrt{s} = 7$  TeV were performed; the energy was increased to 8 TeV in 2012  
 1089 and to 13 TeV in 2015.

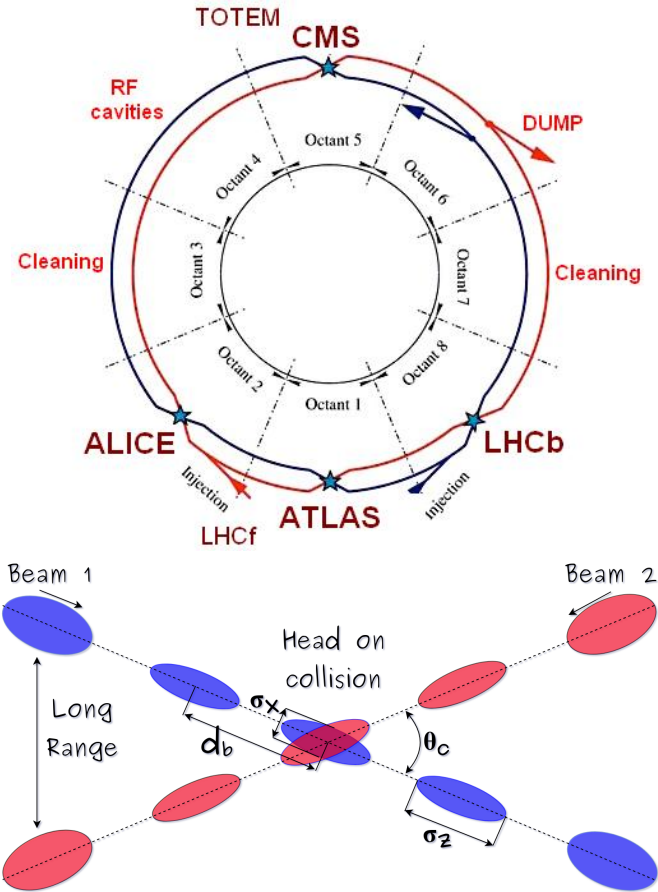


**Figure 2.7:** Top: LHC interaction points. Bunch crossing occurs where the LHC experiments are located [72]. Sections indicated as cleaning are dedicated to collimate the beam in order to protect the LHC ring from collisions with protons in very spreaded bunches. Bottom: bunch crossing scheme. Since the bunch crossing is not perfectly head-on, the luminosity is reduced in a factor of 17%; adapted from Reference [86].

1090 The CMS and ATLAS experiments are multi-purpose experiments, hence, they  
 1091 are enabled to explore physics in any of the LHC collision modes. LHCb experiment  
 1092 is optimized to explore bottom quark physics, while ALICE is optimized for heavy

1093 ion collisions searches; TOTEM and LHCf are dedicated to forward physics studies;  
 1094 MoEDAL (not indicated in the Figure) is intended for monopole or massive pseudo  
 1095 stable particles searches.

1096 At the IP there are two interesting details that need to be addressed. The first  
 1097 one is that the bunch crossing does not occur head-on but at a small crossing angle  $\theta_c$   
 1098 (280  $\mu$ rad in CMS and ATLAS) as shown in the bottom side of Figure 2.7, affecting  
 1099 the overlapping between bunches; the consequence is a reduction of about 17% in  
 1100 the luminosity (represented by a factor not included in eqn. 2.2). The second one  
 1101 is the occurrence of multiple  $pp$  collisions in the same bunch crossing; this effect is  
 1102 called *pileup* (PU). A fairly simple estimation of the PU follows from estimating the  
 1103 probability of collision between two protons, one from each of the bunches in the  
 1104 course of collision; it depends roughly on the ratio of proton size and the cross section  
 1105 of the bunch in the IP, i.e.,

$$P(pp\text{-}collision) \sim \frac{d_{proton}^2}{\sigma_x \sigma_y} = \frac{(1\text{fm})^2}{(16\mu\text{m})^2} \sim 4 \times 10^{-21} \quad (2.4)$$

1106 however, there are  $N = 1.15 \times 10^{11}$  protons in a bunch, thus the estimated number of  
 1107 collisions in a bunch crossing is

$$PU = N^2 * P(pp\text{-}collision) \sim 50pp \text{ collision per bunch crossing}, \quad (2.5)$$

1108 about 20 of which are inelastic. A multiple  $pp$  collision event in a bunch crossing at  
 1109 CMS is shown in Figure 2.8.

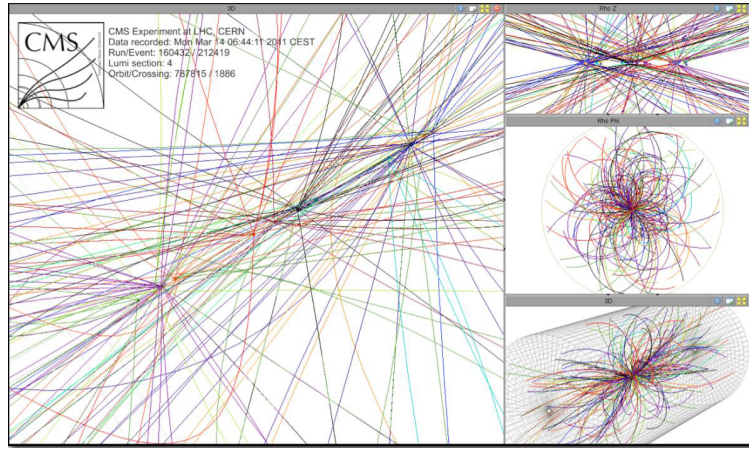


**Figure 2.8:** Multiple  $pp$  collision bunch crossing at CMS. [73].

## 1110 2.3 The CMS experiment

1111 CMS is a general-purpose detector designed to conduct research in a wide range  
 1112 of physics from the standard model to new physics like extra dimensions and dark  
 1113 matter. Located at Point 5 in the LHC layout as shown in Figure 2.4, CMS is  
 1114 composed of several detection systems distributed in a cylindrical structure; in total,  
 1115 CMS weights about 12500 tons in a very compact 21.6 m long and 14.6 m diameter  
 1116 cylinder. It was built in 15 separate sections at the ground level and lowered to the  
 1117 cavern individually to be assembled. A complete and detailed description of the CMS  
 1118 detector and its components is given in Reference [74] on which this section is based.  
 1119 Figure 2.9 shows the layout of the CMS detector. The detection system is composed  
 1120 of (from the innermost to the outermost)

- 1121     • Pixel detector.
- 1122     • Silicon strip tracker.
- 1123     • Preshower detector.
- 1124     • Electromagnetic calorimeter.

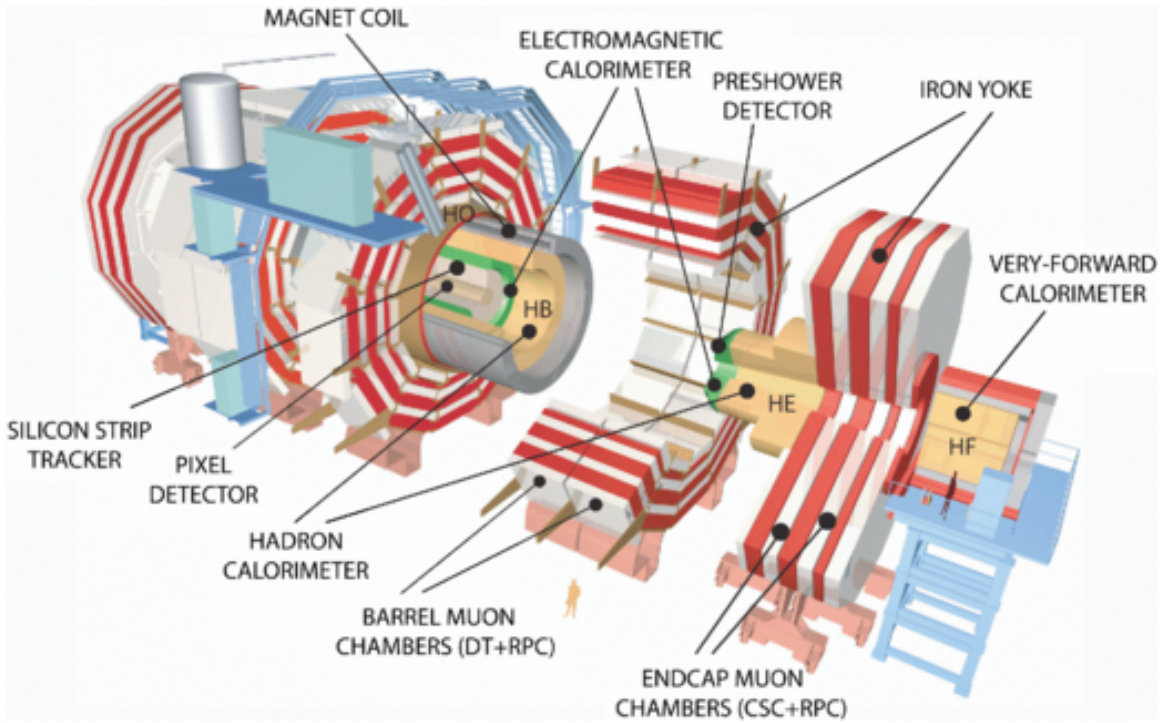


**Figure 2.9:** Layout of the CMS detector. The several subdetectors are indicated. The central region of the detector is referred as the barrel section while the endcaps are referred as the forward sections. [75].

1125        • Hadronic calorimeter.

1126        • Muon chambers (barrel and endcap)

1127        The central region of the detector is commonly referred as the barrel section while  
 1128        the endcaps are referred as the forward sections of the detector; thus, each subdetector  
 1129        is composed of a barrel section and a forward section.

1130        When a  $pp$  collision happens inside the CMS detector, many different particles are  
 1131        produced, but only some of them live long enough to be detected; they are electrons,  
 1132        photons, pions, kaons, protons, neutrons and muons; neutrinos are not detected by  
 1133        the CMS detector. Thus, the CMS detector was designed to detect those particles and  
 1134        measure their properties. Figure 2.10 shows a transverse slice of the CMS detector.  
 1135        The silicon tracker (pixel detector + strip tracker) is capable to register the track of

the charged particles traversing it, while calorimeters (electromagnetic and hadronic) measure the energy of the particles that are absorbed by their materials. Considering the detectable particles, mentioned above, emerging from the IP, a basic description of the detection process is as follows.

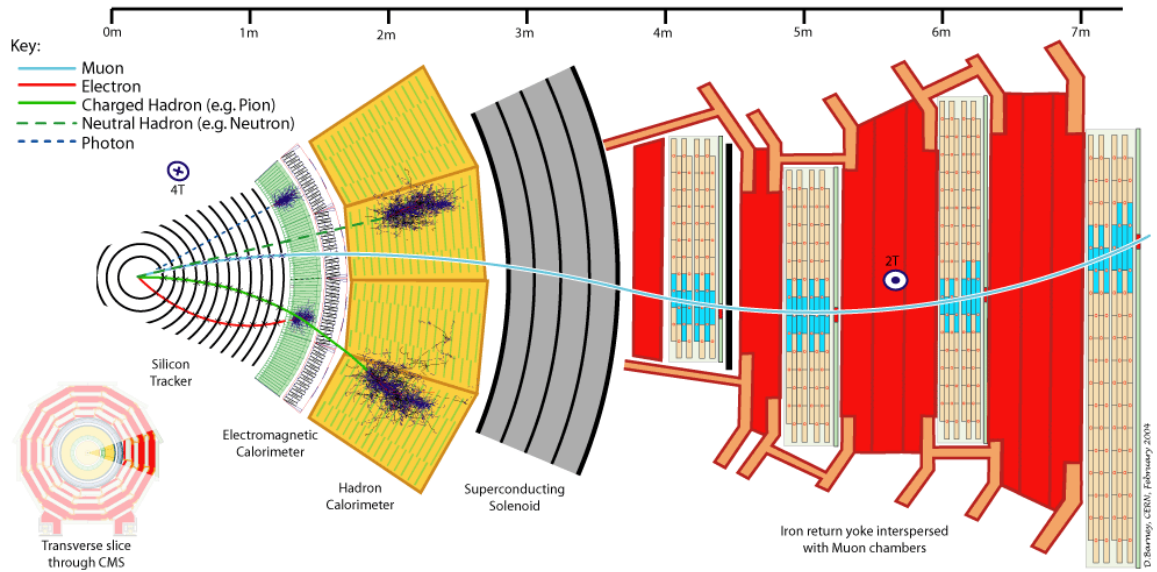


**Figure 2.10:** CMS detector transverse slice [76].

A muon emerging from the IP, will create a track on the silicon tracker and on the muon chambers. The design of the CMS detector is driven by the requirements on the identification, momentum resolution and unambiguous charge determination of the muons; therefore, a large bending power is provided by the solenoid magnet made of superconducting cable capable of generating a 3.8 T magnetic field. The muon track is bent twice since the magnetic field inside the solenoid is directed along the  $z$ -direction but outside its direction is reversed. Muons interact very weakly with the calorimeters, therefore, it is not absorbed but escape away from the detector.

An electron emerging from the IP will create a track along the tracker which will be bent due to the presence of the magnetic field, later, it will be absorbed in the electromagnetic calorimeter where its energy is measured.

1151        A photon will not leave a track because it is neutral, but it will be absorbed in  
 1152        the electromagnetic calorimeter.

1153        A neutral hadron, like the neutron, will not leave a track either but it will lose a  
 1154        small amount of its energy during its passage through the electromagnetic calorimeter  
 1155        and then it will be absorbed in the hadron calorimeter depositing the rest of its energy.

1156        A charged hadron, like the proton or  $\pi^\pm$ , will leave a curved track on the silicon  
 1157        tracker, some of its energy in the electromagnetic calorimeter and finally will be  
 1158        absorbed in the hadronic calorimeter.

1159        A more detailed description of each detection system will be presented in the  
 1160        following sections.

### 1161        2.3.1 CMS coordinate system

1162        The coordinate system used by CMS is centered on the geometrical center of the  
 1163        detector which is the nominal IP as shown in Figure 2.11<sup>1</sup>. The  $z$ -axis is parallel  
 1164        to the beam direction, while the  $Y$ -axis pointing vertically upward, and the  $X$ -axis  
 1165        pointing radially inward toward the center of the LHC.

1166        In addition to the common cartesian and cylindrical coordinate systems, two co-  
 1167        ordinates are of particular utility in particle physics: rapidity ( $y$ ) and pseudorapidity  
 1168        ( $\eta$ ), defined in connection to the polar angle  $\theta$ , energy and longitudinal momentum  
 1169        component (momentum along the  $z$ -axis) according to

$$y = \frac{1}{2} \ln \frac{E + p_z}{E - p_z} \quad \eta = -\ln \left( \tan \frac{\theta}{2} \right) \quad (2.6)$$

1170        Rapidity is related to the angle between the  $XY$ -plane and the direction in which  
 1171        the products of a collision are emitted; it has the nice property that the difference

---

<sup>1</sup> Not all the  $pp$  interaction occur at the nominal IP because of the bunch lenght, therefore, each  $pp$  collision has its own IP location

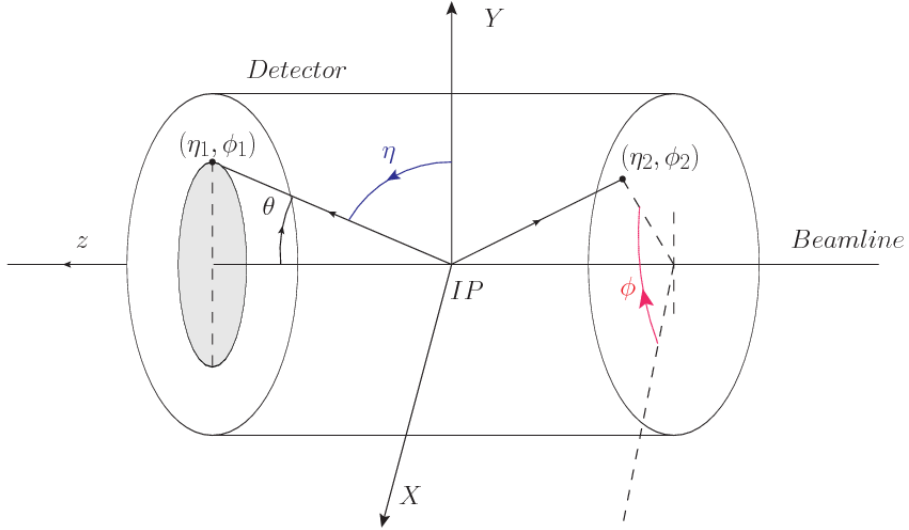


**Figure 2.11:** CMS detector coordinate system.

1172 between the rapidities of two particles is invariant with respect to Lorentz boosts  
 1173 along the  $z$ -axis, hence, data analysis becomes more simple when based on rapid-  
 1174 ity; however, it is not simple to measure the rapidity of highly relativistic particles,  
 1175 as those produced after  $pp$  collisions. Under the highly relativistic motion approxi-  
 1176 mation,  $y$  can be rewritten in terms of the polar angle, concluding that rapidity is  
 1177 approximately equal to the pseudorapidity defined above, i.e.,  $y \approx \eta$ . Note that  $\eta$   
 1178 is easier to measure than  $y$  given the direct relationship between the former and the  
 1179 polar angle.

1180       The angular distance between two objects in the detector ( $\Delta R$ ) is commonly used  
 1181 to judge the isolation of those object; it is defined in terms of their coordinates  $(\eta_1, \phi_1)$ ,  
 1182  $(\eta_2, \phi_2)$  as

$$\Delta R = \sqrt{(\Delta\eta)^2 - (\Delta\phi)^2} \quad (2.7)$$

### 1183 2.3.2 Tracking system

1184 The CMS tracking system is designed to provide a precise measurement of the trajectories (*track*) followed by the charged particles created after the  $pp$  collisions; also, the  
 1185 precise reconstruction of the primary and secondary origins of the tracks (*vertices*) is  
 1186 expected in an environment where, each 25 ns, the bunch crossing produces about 20  
 1187 inelastic collisions and about 1000 particles.  
 1188

1189 Physics requirements guiding the tracking system performance include the precise characterization of events involving gauge bosons, W and Z, and their leptonic  
 1190 decays for which an efficient isolated lepton and photon reconstruction is of capital  
 1191 importance, given that isolation is required to suppress background events to a level  
 1192 that allows observations of interesting processes like Higgs boson decays or beyond  
 1193 SM events.

1195 The ability to identify and reconstruct  $b$ -jets and B-hadrons within these jets is also  
 1196 a fundamental requirement, achieved through the ability to reconstruct accurately  
 1197 displaced vertices, given that  $b$ -jets are part of the signature of top quark physics, like  
 1198 the one treated in this thesis.

1199 An schematic view of the CMS tracking system is shown in Figure 2.12

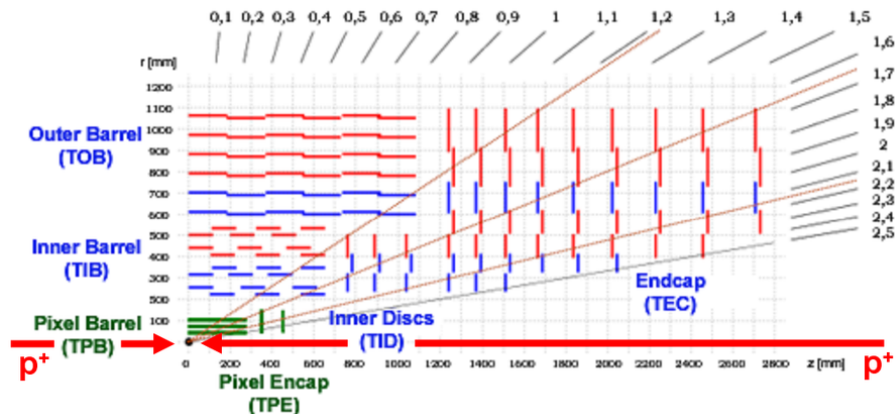


**Figure 2.12:** CMS tracking system schematic view [78].

1200 In order to satisfy these performance requirements, the tracking system uses two  
 1201 different detector subsystems arranged in concentric cylindrical volumes, the pixel  
 1202 detector and the silicon strip tracker; the pixel detector is located in the high particle  
 1203 density region ( $r < 20\text{cm}$ ) while the silicon strip tracker is located in the medium and  
 1204 lower particle density regions  $20\text{cm} < r < 116\text{cm}$ .

1205 **Pixel detector**

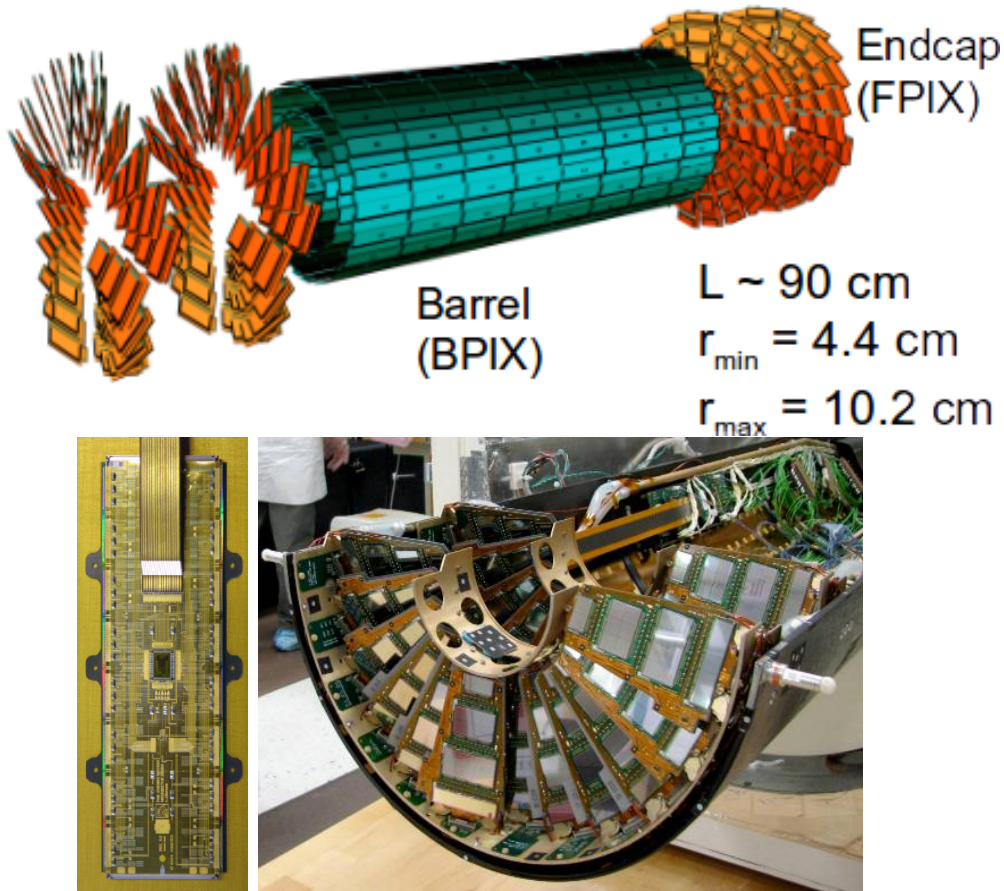


**Figure 2.13:** CMS pixel detector. Top: schematic view; Bottom: pictures of a barrel(BPIX) module(left) and forward modules(right) [74].

1206 The pixel detector was replaced during the 2016-2017 extended year-end technical  
 1207 stop, due to the increasingly challenging operating conditions like the higher particle

flux and more radiation harsh environment, among others. The new one is responding as expected, reinforcing its crucial role in the successful way to fulfill the new LHC physics objectives after the discovery of the Higgs boson. Since the data sets used in this thesis were produced using the previous version of the pixel detector, it will be the subject of the description in this section. The last chapter of this thesis is dedicated to describe my contribution to the *Forward Pixel Phase 1 upgrade*.

The pixel detector was composed of 1440 silicon pixel detector modules organized in three-barrel layers in the central region (BPix) and two disks in the forward region (FPix) as shown in the top side of Figure 2.13; it was designed to record efficiently and with high precision, up to  $20\mu\text{m}$  in the  $XY$ -plane and  $20\mu\text{m}$  in the  $z$ -direction, the first three space-points (*hits*) nearest to the IP region in the range  $|\eta| \leq 2.5$ . The first barrel layer was located at a radius of 44 mm from the beamline, while the third layer was located at a radius of 102 mm, closer to the strip tracker inner barrel layer (see Section 2.3.3) in order to reduce the rate of fake tracks. The high granularity of the detector is represented in its about 66 Mpixels, each of size  $100 \times 150\mu\text{m}^2$ . The transverse momentum resolution of tracks can be measured with a resolution of 1-2% for muons of  $p_T = 100$  GeV.

A charged particle passing through the pixel sensors produce ionization in them, giving energy for electrons to be removed from the silicon atoms, hence, creating electron-hole pairs. The collection of charges in the pixels generates an electrical signal that is read out by an electronic readout chip (ROC); each pixel has its own electronics which amplifies the signal. Combining the signal from the pixels activated by a traversing particle in the several layers of the detector allows one to reconstruct the particle's trajectory in 3D.

Commonly, the charge produced by traversing of a particle is collected by and shared among several pixels; by interpolating between pixels, the spatial resolution

is improved. In the barrel section the charge sharing in the  $r\phi$ -plane is due to the Lorentz effect. In the forward pixels the charge sharing is enhanced by arranging the blades in the turbine-like layout as shown in Figure 2.13 bottom left.

### 2.3.3 Silicon strip tracker

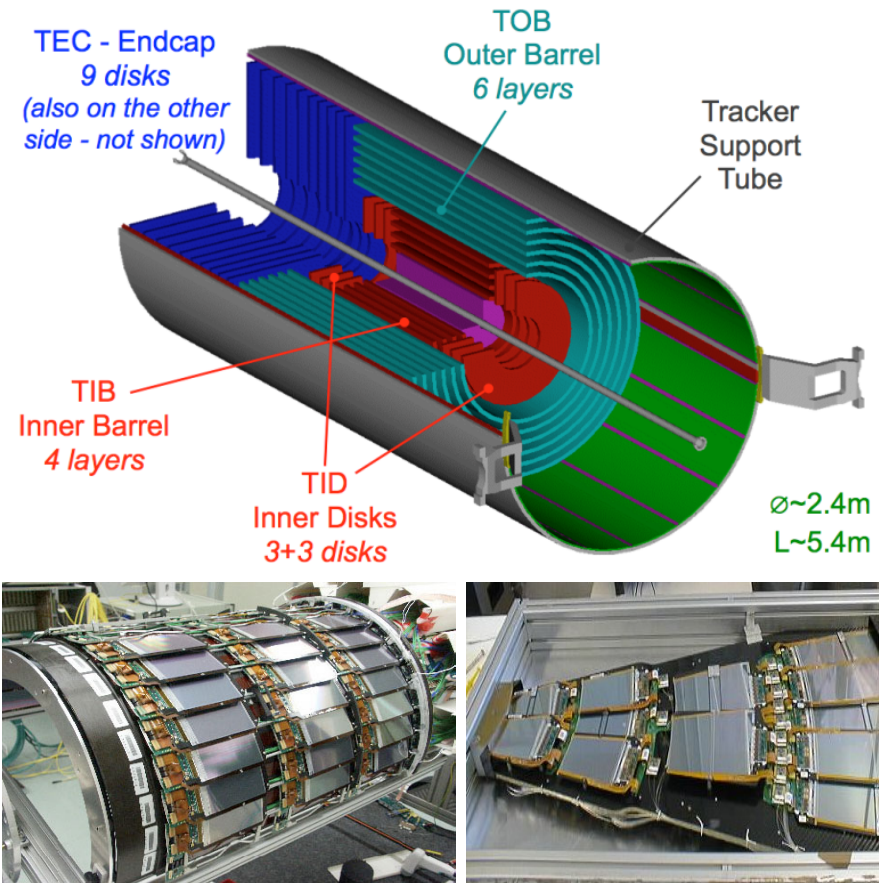


**Figure 2.14:** Top: CMS Silicon Strip Tracker (SST) schematic view. The SST is composed of the tracker inner barrel (TIB), the tracker inner disks (TID), the tracker outer barrel (TOB) and the tracker endcaps (TEC). Each part is made of silicon strip modules; the modules in blue represent two modules mounted back-to-back and rotated in the plane of the module by a stereo angle of 120 mrad in order to provide a 3-D reconstruction of the hit positions. Bottom: pictures of the TIB (left) and TEC (right) modules [80–82].

The silicon strip tracker (SST) is the second stage in the CMS tracking system. The top side of Figure 2.14 shows a schematic of the SST. The inner tracker region is

1240 composed of the tracker inner barrel (TIB) and the tracker inner disks (TID) covering  
 1241 the region  $r < 55$  cm and  $|z| < 118$  cm. The TIB is composed of 4 layers while the TID  
 1242 is composed of 3 disks at each end. The silicon sensors in the inner tracker are 320  
 1243  $\mu\text{m}$  thick, providing a resolution of about 13-38  $\mu\text{m}$  in the  $r\phi$  position measurement.

1244 The modules indicated in blue in the schematic view of Figure 2.14 are two mod-  
 1245 ules mounted back-to-back and rotated in the plane of the module by a *stereo* angle  
 1246 of 100 mrad; the hits from these two modules, known as *stereo hits*, are combined to  
 1247 provide a measurement of the second coordinate ( $z$  in the barrel and  $r$  on the disks)  
 1248 allowing the reconstruction of hit positions in 3-D.

1249 The outer tracker region is composed of the tracker outer barrel (TOB) and the  
 1250 tracker endcaps (TEC). The six layers of the TOB offer coverage in the region  $r > 55$   
 1251 cm and  $|z| < 118$  cm, while the 9 disks of the TEC cover the region  $124 < |z| < 282$   
 1252 cm. The resolution offered by the outer tracker is about 13-38  $\mu\text{m}$  in the  $r\phi$  position  
 1253 measurement. The inner four TEC disks use silicon sensors 320  $\mu\text{m}$  thick; those in  
 1254 the TOB and the outer three TEC disks use silicon sensors of 500  $\mu\text{m}$  thickness. The  
 1255 silicon strips run parallel to the  $z$ -axis and the distance between strips varies from 80  
 1256  $\mu\text{m}$  in the inner TIB layers to 183  $\mu\text{m}$  in the inner TOB layers; in the endcaps the  
 1257 wedge-shaped sensors with radial strips, whose pitch range between 81  $\mu\text{m}$  at small  
 1258 radii and 205  $\mu\text{m}$  at large radii.

1259 The whole SST has 15148 silicon modules, 9.3 million silicon strips and cover a  
 1260 total active area of about 198  $\text{m}^2$ .

### 1261 **2.3.4 Electromagnetic calorimeter**

1262 The CMS electromagnetic calorimeter (ECAL) is designed to measure the energy of  
 1263 electrons and photons. It is composed of 75848 lead tungstate crystals which have a

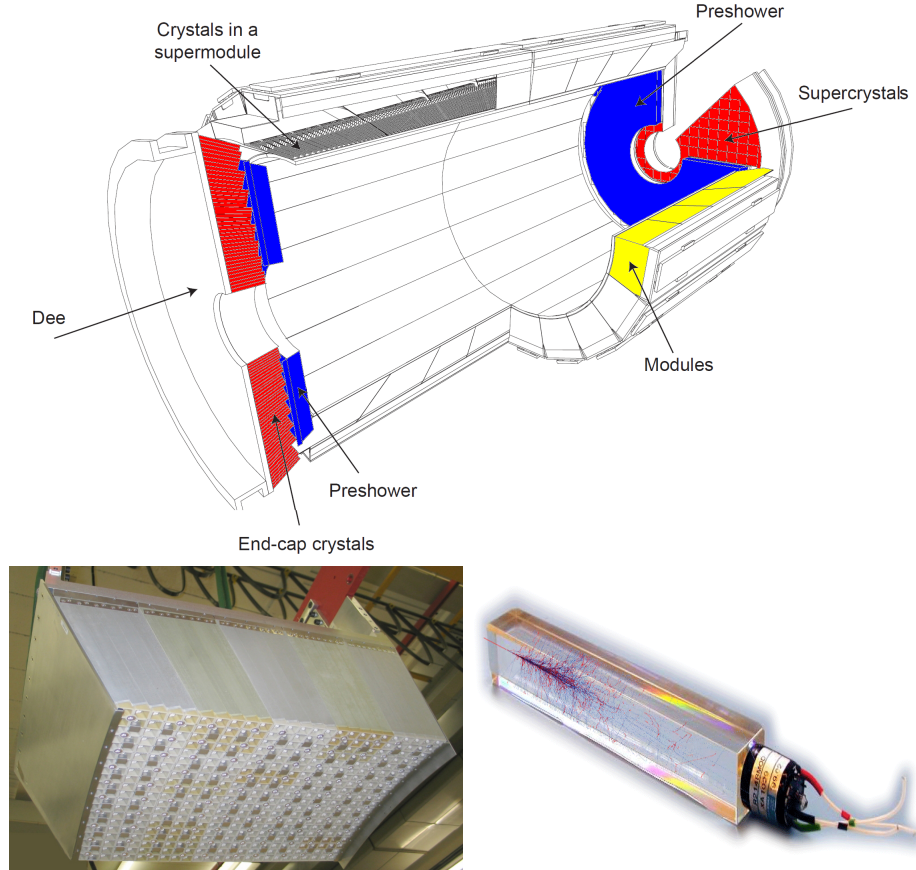


**Figure 2.15:** Top: CMS ECAL schematic view. Bottom: Module equipped with the crystals (left); ECAL crystal(right) with an artistic representation of an electromagnetic shower [74].

1264 short radiation length (0.89 cm) and fast response, since 80% of the light is emitted  
 1265 within 25 ns; however, they are combined with Avalanche photodiodes (APDs) as  
 1266 photodetectors given that crystals themselves have a low light yield ( $30\gamma/\text{MeV}$ ). A  
 1267 schematic view of the ECAL is shown in Figure 2.15.

1268 Energy is measured when electrons and photons are absorbed by the crystals  
 1269 which generates an electromagnetic *shower*, as seen in bottom right picture of the  
 1270 Figure 2.15; the shower is seen as a *cluster* of energy which depending on the amount  
 1271 of energy deposited can involve several crystals. The ECAL barrel (EB) covers the  
 1272 region  $|\eta| < 1.479$ , using crystals of depth of 23 cm and  $2.2 \times 2.2 \text{ cm}^2$  transverse

1273 section; the ECAL endcap (EE) covers the region  $1.479 < |\eta| < 3.0$  using crystals of  
 1274 depth 22 cm and transverse section of  $2.86 \times 2.86 \text{ cm}^2$ ; the photodetectors used are  
 1275 vacuum phototriodes (VPTs). Each EE is divided in two structures called *Dees*.

1276 The preshower detector (ES) is installed in front of the EE and covers the region  
 1277  $1.653 < |\eta| < 2.6$ . The ES provides a precise measurement of the position of electro-  
 1278 magnetic showers, which allows to distinguish electrons and photon signals from  $\pi^0$   
 1279 decay signals. The ES is composed of a layer of lead radiators followed by a layer of  
 1280 silicon strip sensors. The lead radiators initiate electromagnetic showers when reached  
 1281 by photons and electrons, then, the strip sensors measure the deposited energy and  
 1282 the transverse shower profiles. The full ES thickness is 20 cm.

### 1283 2.3.5 Hadronic calorimeter

1284 Hadrons are not absorbed by the ECAL<sup>2</sup> but by the hadron calorimeter (HCAL),  
 1285 which is made of a combination of alternating brass absorber layers and silicon photo-  
 1286 multiplier(SiPM) layers; therefore, particles passing through the scintillator material  
 1287 produce showers, as in the ECAL, as a result of the inelastic scattering of the hadrons  
 1288 with the detector material. Since the particles are not absorbed in the scintillator,  
 1289 their energy is sampled; therefore the total energy is not measured but estimated from  
 1290 the energy clusters, which reduces the resolution of the detector. Brass was chosen  
 1291 as the absorber material due to its short interaction length ( $\lambda_I = 16.42\text{cm}$ ) and its  
 1292 non-magnetivity. Figure 2.16 shows a schematic view of the CMS HCAL.

1293 The HCAL is divided into four sections; the Hadron Barrel (HB), the Hadron  
 1294 Outer (HO), the Hadron Endcap (HE) and the Hadron Forward (HF) sections. The  
 1295 HB covers the region  $0 < |\eta| < 1.4$ , while the HE covers the region  $1.3 < |\eta| < 3.0$ .  
 1296 The HF, made of quartz fiber scintillator and steel as absorption material, covers the

---

<sup>2</sup> Most hadrons are not absorbed, but few low-energy ones might be.

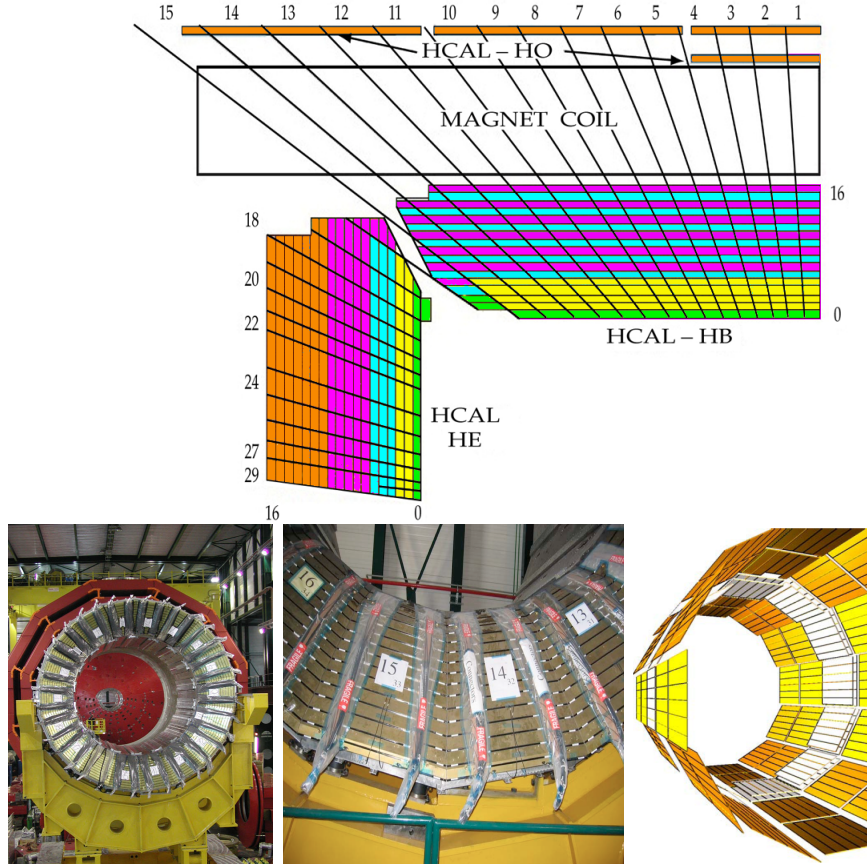


**Figure 2.16:** Top: CMS HCAL schematic view, the colors indicate the layers that are grouped into the same readout channels. Bottom: picture of a section of the HB; the absorber material is the golden region and scintillators are placed in between the absorber material (left and center). Schematic view of the HO (right). [83,84]

1297 forward region  $3.0 < |\eta| < 5.2$ . Both the HB and HF are located inside the solenoid.  
 1298 The HO is placed outside the magnet as an additional layer of scintillators with the  
 1299 purpose of measure the energy tails of particles passing through the HB and the  
 1300 magnet (see Figure 2.16 top and bottom right).

### 1301 2.3.6 Superconducting solenoid magnet

1302 The superconducting magnet installed in the CMS detector is designed to provide  
 1303 an intense and highly uniform magnetic field in the central part of the detector.

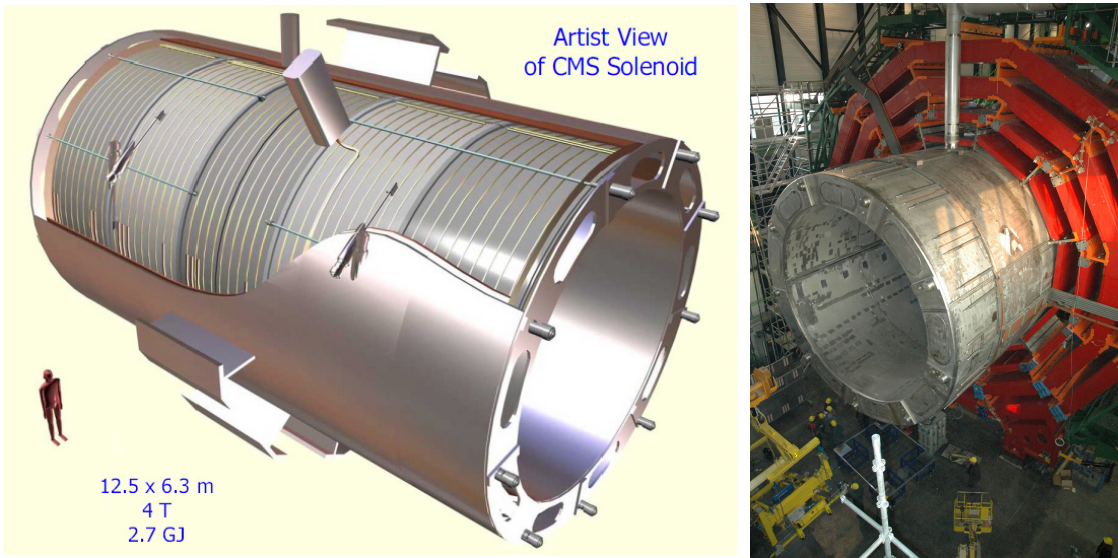


**Figure 2.17:** Artistic representation of the CMS solenoid magnet(left). The magnet is supported on an iron yoke (right) which also serves as the house of the muon detector and as mechanical support for the whole CMS detector [77].

1304 In fact, the tracking system takes advantage of the bending power of the magnetic  
 1305 field to measure with precision the momentum of the particles that traverse it; the  
 1306 unambiguous determination of the sign for high momentum muons was a driving  
 1307 principle during the design of the magnet. The magnet has a diameter of 6.3 m, a  
 1308 length of 12.5 m and a cold mass of 220 t; the generated magnetic field reaches a  
 1309 strength of 3.8T. Since it is made of Ni-Tb superconducting cable it has to operate at  
 1310 a temperature of 4.7 K by using a helium cryogenic system; the current circulating in  
 1311 the cables reaches 18800 A under normal running conditions. The left side of Figure  
 1312 2.17 shows an artistic view of the CMS magnet, while the right side shows a transverse  
 1313 view of the cold mass where the winding structure is visible.

1314 The yoke (see Figure 2.17), composed of 5 barrel wheels and 6 endcap disks made  
 1315 of iron, serves not only as the media for magnetic flux return but also provides housing  
 1316 for the muon detector system and structural stability to the full detector.

### 1317 2.3.7 Muon system

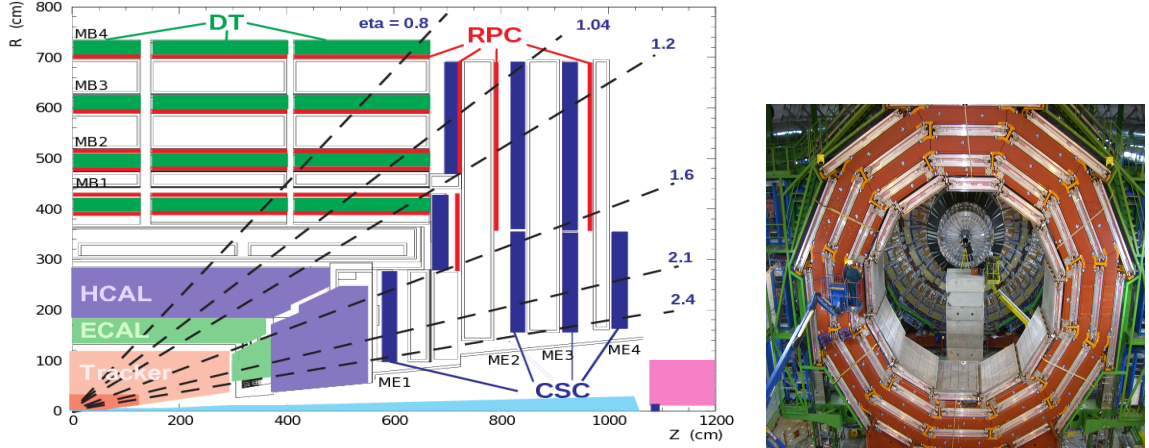


**Figure 2.18:** Left: CMS muon system schematic view; Right: one of the yoke rings with the muon DTs and RPCs installed; in the back it is possible to see the muon endcap [85].

1318 Muons are the only charged particles able to pass through all the CMS detector  
 1319 due to their low ionization energy loss; thus, muons can be separated easily from the  
 1320 high amount of particles produced in a  $pp$  collision. Also, muons are expected to be  
 1321 produced in the decay of several new particles; therefore, good detection of muons  
 1322 was one of the leading principles when designing the CMS detector.

1323 The CMS muon detection system (muon spectrometer) is embedded in the return  
 1324 yoke as seen in Figure 2.18. It is composed of three different detector types, the drift  
 1325 tube chambers (DT), cathode strip chambers (CSC), and resistive plate chambers  
 1326 (RPC); DT are located in the central region  $\eta < 1.2$  arranged in four layers of drift  
 1327 chambers filled with an Ar/CO<sub>2</sub> gas mixture.

1328 The muon endcaps are made of CSCs covering the region  $\eta < 2.4$  and filled with  
 1329 a mixture of Ar/CO<sub>2</sub>/CF<sub>4</sub>. The reason behind using a different detector type lies on  
 1330 the different conditions in the forward region like the higher muon rate and higher  
 1331 residual magnetic field compared to the central region.

1332 The third type of detector used in the muon system is a set of four disks of RPCs

1333 working in avalanche mode. The RPCs provide good spatial and time resolutions. The  
1334 track of high- $p_T$  muon candidates is built combining information from the tracking  
1335 system and the signal from up to six RPCs and four DT chambers.

1336 The muon tracks are reconstructed from the hits in the several layers of the muon  
1337 system.

### 1338 **2.3.8 CMS trigger system**

1339 CMS expects  $pp$  collisions every 25 ns, i.e., an interaction rate of 40 MHz for which  
1340 it is not possible to store the recorded data in full. In order to handle this high event  
1341 rate data, an online event selection, known as triggering, is performed; triggering  
1342 reduces the event rate to 100 Hz for storage and further offline analysis.

1343 The trigger system starts with a reduction of the event rate to 100 kHz in the  
1344 so-called *the level 1 trigger* (L1). L1 is based on dedicated programmable hardware  
1345 like Field Programmable Gate Arrays (FPGAs) and Application Specific Integrated  
1346 Circuits (ASICs), partly located in the detector itself; another portion is located in  
1347 the CMS underground cavern. Hit pattern information from the muon chambers  
1348 and the energy deposits in the calorimeter are used to decide if an event is accepted  
1349 or rejected, according to selection requirements previously defined, which reflect the  
1350 interesting physics processes. Figure 2.19 shows the L1 trigger architecture.

1351 The second stage in the trigger system is called *the high-level trigger* (HLT); events  
1352 accepted by L1 are passed to HLT in order to make an initial reconstruction of them.  
1353 HLT is software based and runs on a dedicated server farm, using selection algorithms  
1354 and high-level object definitions; the event rate at HLT is reduced to 100 Hz. The  
1355 first HLT stage takes information from the muon detectors and the calorimeters to  
1356 make the initial object reconstruction; in the next HLT stage, information from the

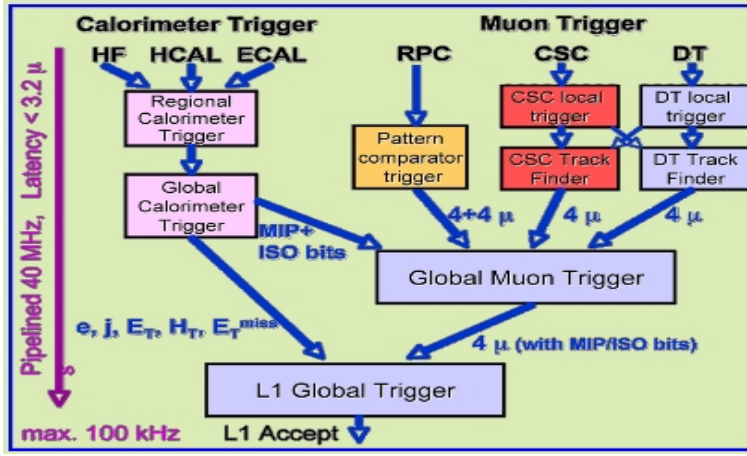


Figure 2.19: CMS Level-1 trigger architecture [86].

pixel and strip detectors is used to do first fast tracking and then full tracking online.  
This initial object reconstruction is used in further steps of the trigger system.

Events and preliminary reconstructed physics objects from HLT are sent to be fully reconstructed at the CERN computing center known also as Tier-0 facility. Again, the pixel detector information provides high-quality seeds for the track reconstruction algorithm offline, primary vertex reconstruction, electron and photon identification, muon reconstruction,  $\tau$  identification, and b-tagging. After full reconstruction, data sets are made available for offline analyses.

### 2.3.9 CMS computing

Data coming from the experiment have to be stored and made available for further analysis; in order to cope with all the tasks implied in the offline data processing, like transfer, simulation, reconstruction and reprocessing, among others, a large computing power is required. The CMS computing system is based on the distributed architecture concept, where users of the system and physical computer centers are distributed worldwide and interconnected by high-speed networks.

The worldwide LHC computing grid (WLCG) is the mechanism used to provide

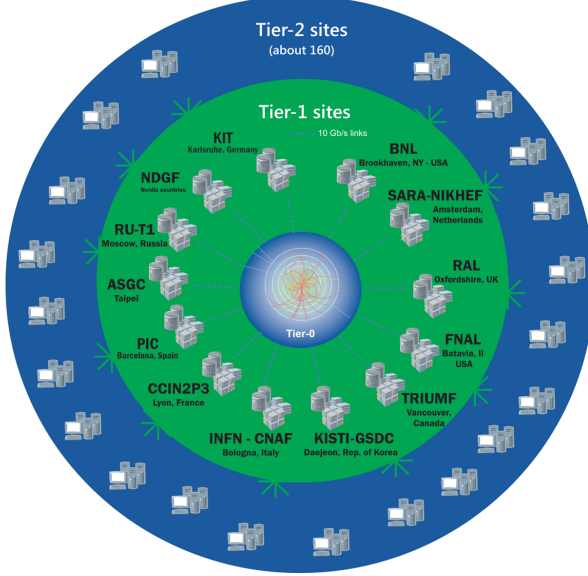


**Figure 2.20:** WLCG structure. The primary computer centers (Tier-0) are located at CERN (data center) and at the Wigner datacenter in Budapest. Tier-1 is composed of 13 centers and Tier-2 is composed of about 160 centers. [87].

1373 that distributed environment. WLCG is a tiered structure connecting computing  
 1374 centers around the world, which provides the necessary storage and computing facil-  
 1375 ities. The primary computing centers of the WLCG are located at the CERN and  
 1376 the Wigner datacenter in Budapest and are known as Tier-0 as shown in Figure 2.20.  
 1377 The main responsibilities for each tier level are [87]

- 1378     • **Tier-0:** initial reconstruction of recorded events and storage of the resulting  
       1379 datasets, the distribution of raw data to the Tier-1 centers.
- 1380     • **Tier-1:** provide storage capacity, support for the Grid, safe-keeping of a pro-  
       1381 portional share of raw and reconstructed data, large-scale reprocessing and safe-  
       1382 keeping of corresponding output, generation of simulated events, distribution  
       1383 of data to Tier 2s, safe-keeping of a share of simulated data produced at these  
       1384 Tier 2s.
- 1385     • **Tier-2:** store sufficient data and provide adequate computing power for spe-

1386       cific analysis tasks and proportional share of simulated event production and  
1387       reconstruction.

1388       Aside from the general computing strategy to manage the huge amount of data  
1389       produced by experiments, CMS uses a software framework to perform a variety of  
1390       processing, selection and analysis tasks. The central concept of the CMS data model  
1391       referred to as *event data model* (EDM) is the *Event*; therefore, an event is the unit  
1392       that contains the information from a single bunch crossing, any data derived from  
1393       that information like the reconstructed objects, and the details of the derivation.

1394       Events are passed as the input to the *physics modules* that obtain information  
1395       from them and create new information; for instance, *event data producers* add new  
1396       data into the events, *analyzers* produce an information summary from an event set,  
1397       *filters* perform selection and triggering.

1398       CMS uses several event formats with different levels of detail and precision

1399       • **Raw format:** events in this format contain the full recorded information from  
1400       the detector as well as trigger decision and other metadata. An extended version  
1401       of raw data is used to store information from the CMS Monte Carlo simulation  
1402       tools (see Chapter 3). Raw data are stored permanently, occupying about  
1403       2MB/event

1404       • **RECO format:** events in this format correspond to raw data that have been  
1405       submitted to reconstruction algorithms like primary and secondary vertex re-  
1406       construction, particle ID, and track finding. RECO events contain physics ob-  
1407       jects and all the information used to reconstruct them; average size is about 0.5  
1408       MB/event.

- 1409     • **AOD format:** Analysis Object Data (AOD) is the data format used in the  
 1410       physics analyses given that it contains the parameters describing the high-level  
 1411       physics objects in addition to enough information to allow a kinematic refitting if  
 1412       needed. AOD events are filtered versions of the RECO events to which skimming  
 1413       or other filtering have been applied, hence AOD events are subsets of RECO  
 1414       events. Requires about 100 kB/event.
- 1415     • **Non-event data** are data needed to interpret and reconstruct events. Some  
 1416       of the non-event data used by CMS contains information about the detector  
 1417       contraction and condition data like calibrations, alignment, and detector status.

1418     Figure 2.21 shows the data flow scheme between CMS detector and tiers.

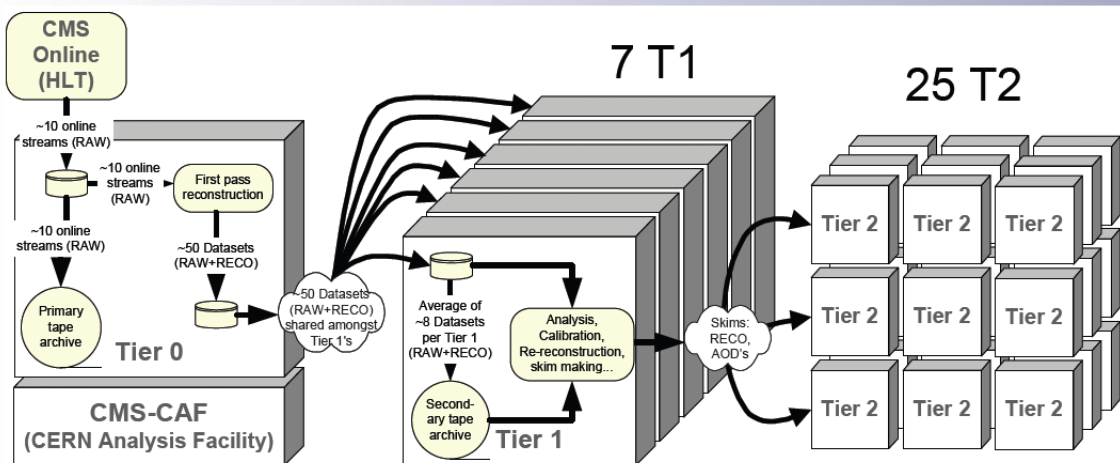


**Figure 2.21:** Data flow from CMS detector through tiers.

1419     The whole collection of software built as a framework is referred to as *CMSSW*. This  
 1420       framework provides the services needed by the simulation, calibration and alignment,  
 1421       and reconstruction modules that process event data, so that physicists can perform  
 1422       analysis. The CMSSW event processing model is composed of one executable, called  
 1423       `cmsRun`, and several plug-in modules which contains all the tools (calibration, recon-

1424 struction algorithms) needed to process an event. The same executable is used for  
1425 both detector data and Monte Carlo simulations [88].

1426 **Chapter 3**

1427 **Event generation, simulation and  
1428 reconstruction**

1429 The process of analyzing data recorded by the CMS experiment involves several stages  
1430 where the data are processed in order to interpret the information provided by all  
1431 the detection systems; in those stages, the particles produced after the  $pp$  collision  
1432 are identified by reconstructing their trajectories and measuring their features. In  
1433 addition, the SM provides a set of predictions that have to be compared with the  
1434 experimental results; however, in most of the cases, theoretical predictions are not  
1435 directly comparable to experimental results due to the diverse source of uncertainties  
1436 introduced by the experimental setup and theoretical approximations, among others.

1437

1438 The strategy to face these conditions consists in using statistical methods imple-  
1439 mented in computational algorithms to produce numerical results that can be con-  
1440 trasted with the experimental results. These computational algorithms are commonly  
1441 known as Monte Carlo (MC) methods and, in the case of particle physics, they are  
1442 designed to apply the SM rules and produce predictions about the physical observ-

ables measured in the experiments. Since particle physics is governed by quantum mechanics principles, predictions are not allowed from single events; therefore, a high number of events are *generated* and predictions are produced in the form of statistical distributions for the observables. Effects of the detector presence are included in the predictions by introducing simulations of the detector itself.

1448

1449 This chapter presents a description of the event generation strategy and the tools  
 1450 used to perform the detector simulation and physics objects reconstruction. A com-  
 1451 prehensive review of event generators for LHC physics can be found in Reference [89]  
 1452 on which this chapter is based.

### 1453 3.1 Event generation

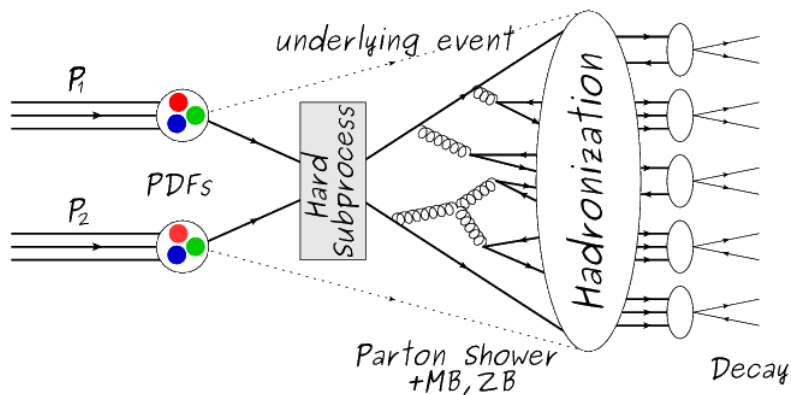


**Figure 3.1:** Event generation process. The actual interaction is generated in the hard subprocess. The parton shower describes the evolution of the partons from the hard subprocess. Modified from Reference [90].

1454 The event generation is intended to create events that mimic the behavior of ac-  
 1455 tual events produced in collisions; they obey a sequence of steps from the particles  
 1456 collision hard process to the decay process into the final state. Figure 3.1 shows a  
 1457 schematic view of the event generation process; the fact that the full process can be

1458 treated as several independent steps is motivated by the QCD factorization theorem.

1459

1460 Generation starts by taking into account the PDFs of the incoming particles.

1461 Event generators offer the option to chose from several PDF sets depending on the

1462 particular process under simulation<sup>1</sup>; in the following,  $pp$  collisions will be consid-

1463 ered. The *hard subprocess* describes the actual interaction between partons from the

1464 incoming protons; it is represented by the matrix element connecting the initial and

1465 final states of the interaction. Normally, the matrix element can be written as a sum

1466 over Feynman diagrams and consider interferences between terms in the summation.

1467 During the generation of the hard subprocess, the production cross section is calcu-

1468 lated.

1469

1470 The order to which the cross section is calculated depends on the order of the Feyn-

1471 man diagrams involved in the calculation; therefore, radiative corrections are included

1472 by considering a higher order Feynman diagrams where QCD radiation dominates.

1473 Currently, cross sections calculated to LO do not offer a satisfactory description of the

1474 processes, i.e., the results are only reliable for the shape of distributions; therefore,

1475 NLO calculations have to be performed with the implication that the computing time

1476 needed is highly increased.

1477

1478 The final parton content of the hard subprocess is subjected to the *parton shower*

1479 which generates the gluon radiation. Parton shower evolves the partons, i.e., glouns

1480 split into quark-antiquark pairs and quarks with enough energy radiate gluons giv-

1481 ing rise to further parton multiplication, following the DGLAP (Dokshitzer-Gribov-

1482 Lipatov-Altarelli-Parisi) equations. Showering continues until the energy scale is low

---

<sup>1</sup> Tool in Reference [91] allows to plot different PDF sets under customizable conditions.

1483 enough to reach the non-perturbative limit.

1484

1485 In the simulation of LHC processes that involve  $b$  quarks, like the single top quark  
 1486 or Higgs associated production, it is needed to consider that the  $b$  quark is heavier  
 1487 than the proton; hence, the QCD interaction description is made in two different  
 1488 schemes [95]

1489 • four-flavor (4F) scheme.  $b$  quarks appear only in the final state because they  
 1490 are heavier than the proton and therefore they can be produced only from the  
 1491 splitting of a gluon into pairs or singly in association with a  $t$  quark in high  
 1492 energy-scale interactions; furthermore, during the simulation, the  $b$ -PDFs are set  
 1493 to zero. Calculations in this scheme are more complicated due to the presence  
 1494 of the second  $b$  quark but the full kinematics is considered already at LO and  
 1495 therefore the accuracy of the description is better.

1496 • five-flavor (5F) scheme.  $b$  quarks are considered massless, therefore they can  
 1497 appear in both initial and final states since they can now be part of the proton;  
 1498 thus, during the simulation  $b$ -PDFs are not set to zero. In this scheme, calcu-  
 1499 lations are simpler than in the 4F scheme and possible logarithmic divergences  
 1500 are absorbed by the PDFs through the DGLAP evolution.

1501 In this thesis, the  $tHq$  events are generated using the 4F scheme in order to reduce  
 1502 uncertainties, while the  $tHW$  events are generated using the 5F scheme to eliminate  
 1503 LO interference with  $t\bar{t}H$  process [48].

1504

1505 Partons involved in the  $pp$  collision are the focus of the simulation, however, the  
 1506 rest of the partons inside the incoming protons are also affected because the remnants  
 1507 are colored objects; also, multiple parton interactions can occur. The hadronization

1508 of the remnants and multiple parton interactions are known as *underlying event* and  
 1509 it has to be included in the simulation. In addition, multiple  $pp$  collisions in the same  
 1510 bunch crossing (pile-up mentioned in 2.2) occurs, actually in two forms

- 1511       • *in-time PU* which refers to multiple  $pp$  collision in the bunch crossing but that  
 1512           are not considered as primary vertices.
- 1513       • *Out-of-time PU* which refers to overlapping  $pp$  collisions from consecutive bunch  
 1514           crossings; this can occur due to the time-delays in the detection systems where  
 1515           information from one bunch crossing is assigned to the next or previous one.

1516       While the underlying event effects are included in generation using generator-  
 1517 specific tools, PU effects are added to the generation by overlaying Minimum-bias  
 1518 (MB) and Zero-bias (ZB) events to the generated events. MB events are inelastic  
 1519 events selected by using a loose trigger with as little bias as possible, therefore ac-  
 1520 cepting a large fraction of the overall inelastic event; ZB events correspond to random  
 1521 events recorded by the detector when collisions are likely. MB models in-time PU  
 1522 and ZB models out-of-time PU.

1523

1524       The next step in the generation process is called *hadronization*. Since particles  
 1525 with a net color charge are not allowed to exits isolated, they have to recombine  
 1526 to form bound states. This is precisely the process by which the partons resulting  
 1527 from the parton shower arrange themselves as color singlets to form hadrons. At  
 1528 this step, the energy-scale is low and the strong coupling constant is large, there-  
 1529 fore hadronization process is non-perturbative and the evolution of the partons is  
 1530 described using phenomenological models. Most of the baryons and mesons produced  
 1531 in the hadronization are unstable and hence they will decay in the detector.

1532

1533        The last step in the generation process corresponds to the decay of the unstable  
 1534   particles generated during hadronization; it is also simulated in the hadronization  
 1535   step, based on the known branching ratios.

1536   **3.2 Monte Carlo Event Generators.**

1537   The event generation described in the previous section has been implemented in  
 1538   several software packages for which a brief description is given.

1539   • **PYTHIA 8.** It is a program designed to perform the generation of high energy  
 1540   physics events which describes the collisions between particles such as electrons  
 1541   and protons. Several theories and models are implemented in it, in order to  
 1542   describe physical aspects like hard and soft interaction, parton distributions,  
 1543   initial and final-state parton showers, multiple parton interactions, beam rem-  
 1544   nants, hadronization<sup>2</sup> and particle decay. Thanks to extensive testing, several  
 1545   optimized parametrizations, known as *tunings*, have been defined in order to  
 1546   improve the description of actual collisions to a high degree of precision; for  
 1547   analysis at  $\sqrt{s} = 13$  TeV, the underline event CUETP8M1 tune is employed [97].  
 1548   The calculation of the matrix element is performed at LO which is not enough  
 1549   for the current required level of precision; therefore, pythia is often used for  
 1550   parton shower, hadronization and decays, while other event generators are used  
 1551   to generate the matrix element at NLO.

1552   • **MadGraph5\_aMC@NLO.** MadGraph is a matrix element generator which  
 1553   calculates the amplitudes for all contributing Feynman diagrams of a given pro-  
 1554   cess but does not provide a parton shower while MC@NLO incorporates NLO

---

<sup>2</sup> based in the Lund string model [96]

1555 QCD matrix elements consistently into a parton shower framework; thus, Mad-  
 1556 Graph5\_aMC@NLO, as a merger of the two event generators MadGraph5 and  
 1557 aMC@NLO, is an event generator capable to calculate tree-level and NLO cross  
 1558 sections and perform the matching of those with the parton shower. It is one of  
 1559 the most frequently used matrix element generators; however, it has the partic-  
 1560 ular feature of the presence of negative event weights which reduce the number  
 1561 of events used to reproduce the properties of the objects generated [98].

1562

1563 • **POWHEG.** It is an NLO matrix element generator where the hardest emis-  
 1564 sion of color charged particles is generated in such a way that the negative event  
 1565 weights issue of MadGraph5\_aMC@NLO is overcome; however, the method re-  
 1566 quires an interface with  $p_T$ -ordered parton shower or a parton shower generator  
 1567 where this highest emission can be vetoed in order to avoid double counting of  
 1568 this highest-energetic emission. PYTHIA is a commonly matched to POWHEG  
 1569 event generator [100].

1570 Events resulting from the whole generation process are known as MC events.

### 1571 3.3 CMS detector simulation.

1572 After generation, MC events contain the physics of the collisions but they are not  
 1573 ready to be compared to the events recorded by the experiment since these recorded  
 1574 events correspond to the response of the detection systems to the interaction with  
 1575 the particles traversing them. The simulation of the CMS detector has to be applied  
 1576 on top of the event generation; it is simulated with a MC toolkit for the simulation  
 1577 of particles passing through matter called Geant4 which is also able to simulate the

1578 electronic signals that would be measured by all detectors inside CMS.

1579

1580 The simulation takes the generated particles contained in the MC events as input,  
1581 makes them pass through the simulated geometry, and models physics processes that  
1582 particles experience during their passage through matter. The full set of results from  
1583 particle-matter interactions corresponds to the simulated hit which contains informa-  
1584 tion about the energy loss, momentum and position. Particles of the input event are  
1585 called *primary*, while the particles originating from GEANT4-modeled interactions of  
1586 a primary particle with matter are called a *secondary*. Simulated hits are the input  
1587 of subsequent modules that emulate the response of the detector readout system and  
1588 triggers. The output from the emulated detection systems and triggers is known as  
1589 digitization [101, 102].

1590

1591 The modeling of the CMS detector corresponds to the accurate modeling of the  
1592 interaction among particles, the detector material, and the magnetic field. This  
1593 simulation procedure includes the following standard steps

1594 • Modeling of the Interaction Region.

1595 • Modeling of the particle passage through the hierarchy of volumes that compose  
1596 CMS detector and of the accompanying physics processes.

1597 • Modeling of the effect of multiple interactions per beam crossing and/or the  
1598 effect of events overlay ( Pile-Up simulation).

1599 • Modeling of the detector's electronics response, signal shape, noise, calibration  
1600 constants (digitization).

1601 In addition to the full simulation, i.e., a detailed detector simulation, a faster sim-  
 1602 ulation (FastSim) have been developed, that may be used where much larger statistics  
 1603 are required. In FastSim, detector material effects are parametrized and included in  
 1604 the hits; those hits are used as input of the same higher-level algorithms<sup>3</sup> used to an-  
 1605 alyze the recorded events. In this way, comparisons between fast and full simulations  
 1606 can be performed [104].

1607

1608 After the full detector simulation, the output events can be directly compared  
 1609 to events actually recorded in the CMS detector. The collection of MC events that  
 1610 reproduces the expected physics for a given process is known as MC sample.

## 1611 **3.4 Event reconstruction.**

1612 The CMS experiment use the *particle-flow event reconstruction algorithm (PF)* to do  
 1613 the reconstruction of particles produced in  $pp$  collisions. Next sections will present  
 1614 a basic description of the *Elements* used by PF (tracker tracks, energy clusters, and  
 1615 muon tracks), based in the References [105, 106] where more detailed descriptions can  
 1616 be found.

### 1617 **3.4.1 Particle-Flow Algorithm.**

1618 Each of the several sub detection systems of the CMS detector is dedicated to identify  
 1619 a specific type of particles, i.e., photons and electrons are absorbed by the ECAL  
 1620 and their reconstruction is based on ECAL information; hadrons are reconstructed  
 1621 from clusters in the HCAL while muons are reconstructed from hits in the muon

---

<sup>3</sup> track fitting, calorimeter clustering, b tagging, electron identification, jet reconstruction and calibration, trigger algorithms which will be considered in the next sections

1622 chambers. PF is designed to correlate signals from all the detector layers (tracks and  
 1623 energy clusters) in order to reconstruct and identify each final state particle and its  
 1624 properties as sketched in Figure 3.2.

1625

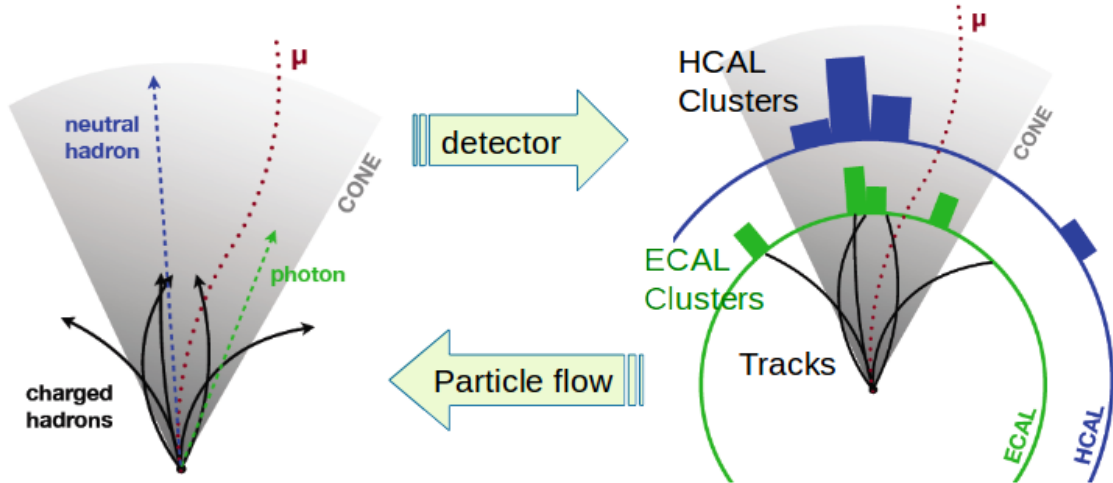


**Figure 3.2:** Particle flow algorithm. Information from the several CMS detection systems is provided as input to the algorithm which then combine it to identify and reconstruct all the particles in the final state and their properties. Reconstruction of simulated events is also performed by providing information from MC samples, detector and trigger simulation [107].

1626 For instance, a charged hadron is identified by a geometrical connection, known  
 1627 as *link*, between one or more calorimeter clusters and a track in the tracker, provided  
 1628 there are no hits in the muon system; combining several measurements allows a better  
 1629 determination of the energy and charge sign of the charged hadron.

### 1630 Charged-particle track reconstruction.

1631 The strategy used by PF in order to reconstruct tracks is called *Iterative Tracking*  
 1632 which occurs in four steps

- 1633 • Seed generation where initial track candidates are found by looking for a combi-  
 1634 nation of hits in the pixel detector, strip tracker, and muon chambers. In total

1635        ten iterations are performed, each one with a different seeding requirement.  
 1636        Seeds are used to estimate the trajectory parameters and uncertainties at the  
 1637        time of the full track reconstruction. Seeds are also considered track candidates.

- 1638        • Track finding using a tracking software known as Combinatorial Track Finder  
               (CTF) [108]. The seed trajectories are extrapolated along the expected flight  
               path of a charged particle, in agreement to the trajectory parameters obtained  
               in the first step, in an attempt to find additional hits that can be assigned to  
               the track candidates.
- 1643        • Track-fitting where the found tracks are passed as input to a module which  
               provides the best estimate of the parameters of each trajectory.
- 1645        • Track selection where track candidates are submitted to a selection which dis-  
               cards those that fail a set of defined quality criteria.

1647        Iterations differ in the seeding configuration and the final track selection as elab-  
 1648        orated in References [105, 106]. In the first iteration, high  $p_T$  tracks and tracks pro-  
 1649        duced near to the interaction region are identified and those hits are masked thereby  
 1650        reducing the combinatorial complexity. Next, iterations search for more complicated  
 1651        tracks, like low  $p_T$  tracks and tracks from b hadron decays, which tend to be displaced  
 1652        from the interaction region.

1653        **Vertex reconstruction.**

1654        During the track reconstruction, an extrapolation toward to the calorimeters is per-  
 1655        formed in order to match energy deposits; that extrapolation is performed also toward  
 1656        the beamline in order to find the origin of the track known as *vertex*. The vertex re-  
 1657        construction is performed by selecting from the available reconstructed tracks, those

1658 that are consistent with being originated in the interaction region where  $pp$  collisions  
 1659 are produced. The selection involves a requirement on the number of tracker (pixel  
 1660 and strip) hits and the goodness of the track fit.

1661

1662 Selected tracks are clustered using a *deterministic annealing algorithm (DA)*<sup>4</sup>. A  
 1663 set of candidate vertices and their associated tracks, resulting from the DA, are then  
 1664 fitted with an *adaptive vertex fitter (AVF)* to produce the best estimate of the vertices  
 1665 locations.

1666

1667 The  $p_T$  of the tracks associated to a reconstructed vertex is added, squared and  
 1668 used to organize the vertices; the vertex with the highest squared sum is designated  
 1669 as the *primary vertex (PV)* while the rest are designated as PU vertices.

## 1670 Calorimeter clustering.

1671 After traversing the CMS tracker system, electrons, photons and hadrons deposit their  
 1672 energy in the ECAL and HCAL cells. The PF clustering algorithm aims to provide  
 1673 a high detection efficiency even for low-energy particles and an efficient distinction  
 1674 between close energy deposits. The clustering runs independently in the ECAL barrel  
 1675 and endcaps, HCAL barrel and endcaps, and the two preshower layers, following two  
 1676 steps

- 1677 • cells with an energy larger than a given seed threshold and larger than the energy  
 1678 of the neighboring cells are identified as cluster seeds. The neighbor cells are  
 1679 those that either share a side with the cluster seed candidate, or the eight closest  
 1680 cells including cells that only share a corner with the seed candidate.

---

<sup>4</sup> DA algorithm and AVF are described in detail in References [110, 111]

1681       • cells with at least a corner in common with a cell already in the cluster seed  
 1682           and with an energy above a cell threshold are grouped into topological clusters.

1683       Clusters formed in this way are known as *particle-flow clusters*. With this cluster-  
 1684       ing strategy, it is possible to detect and measure the energy and direction of photons  
 1685       and neutral hadrons as well as differentiate these neutral particles from the charged  
 1686       hadron energy deposits. In cases involving charged hadrons for which the track pa-  
 1687       rameters are not determined accurately, for instance, low-quality and high- $p_T$  tracks,  
 1688       clustering helps in the energy measurements.

1689 **Electron track reconstruction.**

1690       Although the charged-particle track reconstruction described above works for elec-  
 1691       trons, they lose a significant fraction of their energy via bremsstrahlung photon radi-  
 1692       ation before reaching the ECAL; thus, the reconstruction performance depends on the  
 1693       ability to measure also the radiated energy. The reconstruction strategy, in this case,  
 1694       requires information from the tracking system and from the ECAL. Bremsstrahlung  
 1695       photons are emitted at similar  $\eta$  values to that of the electron but at different values  
 1696       of  $\phi$ ; therefore, the radiated energy can be recovered by grouping ECAL clusters in a  
 1697        $\eta$  window over a range of  $\phi$  around the electron direction. The group is called ECAL  
 1698       supercluster.

1699       Electron candidates from the track-seeding and ECAL super clustering are merged  
 1700       into a single collection which is submitted to a full electron tracking fit with a  
 1701       Gaussian-sum filter (GSF) [109]. The electron track and its associated ECAL su-  
 1702       percluster form a *particle-flow electron*.

1703 **Muon track reconstruction.**

1704 Given that the CMS detector is equipped with a muon spectrometer capable to iden-  
 1705 tify and measure the momentum of the muons traversing it, the muon reconstruction  
 1706 is not specific to PF; therefore, three different muon types are defined

- 1707     • *Standalone muon.* A clustering on the DTs or CSCs hits is performed to form  
 1708       track segments; those segments are used as seeds for the reconstruction in the  
 1709       muon spectrometer. All DTs, CSCs, and RPCs hits along the muon trajectory  
 1710       are combined and fitted to form the full track. The fitting output is called a  
 1711       *standalone-muon track*.
- 1712     • *Tracker muon.* Each track in the inner tracker with  $p_T$  larger than 0.5 GeV and  
 1713       a total momentum  $p$  larger than 2.5 GeV is extrapolated to the muon system.  
 1714       A *tracker muon track* corresponds to a extrapolated track that matches at least  
 1715       one muon segment.
- 1716     • *Global muon.* When tracks in the inner tracker (inner tracks) and standalone-  
 1717       muon tracks are matched and turn out being compatibles, their hits are com-  
 1718       bined and fitted to form a *global-muon track*.

1719 Global muons sharing the same inner track with tracker muons are merged into  
 1720 a single candidate. PF muon identification uses the muon energy deposits in ECAL,  
 1721 HCAL, and HO associated with the muon track to improve the muon identification.

1722 **Particle identification and reconstruction.**

1723 PF elements are connected by a linker algorithm that tests the connection between any  
 1724 pair of elements; if they are found to be linked, a geometrical distance that quantifies  
 1725 the quality of the link is assigned. Two elements may be linked indirectly through

1726 common elements. Linked elements form *PF blocks* and each PF block may contain  
 1727 elements originating in one or more particles. Links can be established between  
 1728 tracks, between calorimeter clusters, and between tracks and calorimeter clusters.  
 1729 The identification and reconstruction start with a PF block and proceed as follows

1730 • Muons. An *isolated global muon* is identified by evaluating the presence of  
 1731 inner track and energy deposits close to the global muon track in the  $(\eta, \phi)$   
 1732 plane, i.e., in a particular point of the global muon track, inner tracks and  
 1733 energy deposits are sought within a radius of  $\Delta R = 0.3$  (see eqn. 2.7) from the  
 1734 muon track; if they exit and the  $p_T$  of the found track added to the  $E_T$  of the  
 1735 found energy deposit does not exceed 10% of the muon  $p_T$  then the global muon  
 1736 is an isolated global muon. This isolation condition is stringent enough to reject  
 1737 hadrons misidentified as muons.

1738 *Non-isolated global muons* are identified using additional selection requirements  
 1739 on the number of track segments in the muon system and energy deposits along  
 1740 the muon track. Muons inside jets are identified with more stringent criteria  
 1741 in isolation and momentum as described in Reference [112]. The PF elements  
 1742 associated with an identified muon are masked from the PF block.

1743 • Electrons are identified and reconstructed as described above plus some addi-  
 1744 tional requirements on fourteen variables like the amount of energy radiated,  
 1745 the distance between the extrapolated track position at the ECAL and the po-  
 1746 sition of the associated ECAL supercluster, among others, which are combined  
 1747 in an specialized multivariate analysis strategy that improves the electron iden-  
 1748 tification. Tracks and clusters used to identify and reconstruct electrons are  
 1749 masked in the PF block.

- 1750     ● Isolated photons are identified from ECAL superclusters with  $E_T$  larger than 10  
 1751       GeV, for which the energy deposited at a distance of 0.15, from the supercluster  
 1752       position on the  $(\eta,\phi)$  plane, does not exceed 10% of the supercluster energy;  
 1753       note that this is an isolation requirement. In addition, there must not be links  
 1754       to tracks. Clusters involved in the identification and reconstruction are masked  
 1755       in the PF block.
  
- 1756     ● Bremsstrahlung photons and prompt photons tend to convert to electron-positron  
 1757       pairs inside the tracker, therefore, a dedicated finder algorithm is used to link  
 1758       tracks that seem to originate from a photon conversion; in case those two tracks  
 1759       are compatible with the direction of a bremsstrahlung photon, they are also  
 1760       linked to the original electron track. Photon conversion tracks are also masked  
 1761       in the PF block.
  
- 1762     ● The remaining elements in the PF block are used to identify hadrons. In the  
 1763       region  $|\eta| \leq 2.5$ , neutral hadrons are identified with HCAL clusters not linked  
 1764       to any track while photons from neutral pion decays are identified with ECAL  
 1765       clusters without links to tracks. In the region  $|\eta| > 2.5$  ECAL clusters linked to  
 1766       HCAL clusters are identified with a charged or neutral hadron shower; ECAL  
 1767       clusters with no links are identified with photons. HCAL clusters not used yet,  
 1768       are linked to one or more unlinked tracks and to an unlinked ECAL in order to  
 1769       reconstruct charged-hadrons or a combination of photons and neutral hadrons  
 1770       according to certain conditions on the calibrated calorimetric energy.
  
- 1771     ● Charged-particle tracks may be liked together when they converge to a *sec-  
 1772       ondary vertex (SV)* displaced from the IP where the PV and PU vertices are  
 1773       reconstructed; at least three tracks are needed in that case, of which at most

1774 one has to be an incoming track with hits in tracker region between a PV and  
 1775 the SV.

1776 The linker algorithm, as well as the whole PF algorithm, has been validated and  
 1777 commissioned; results from that validation are presented in the Reference [105].

1778 **Jet reconstruction.**

1779 Quarks and gluons may be produced in the  $pp$  collisions, therefore, their hadronization  
 1780 will be seen in the detector as a shower of hadrons and their decay products in the  
 1781 form of a *jet*. Two classes of clustering algorithms have been developed based in  
 1782 their jet definition [113]:

- 1783 • Iterative cone algorithms (IC). Jets are defined in terms of circles of fixed radius  
 1784  $R$  in the  $\eta\text{-}\phi$  plane, known as *stable cones*, for which the sum of the momenta  
 1785 of all the particles within the cone points in the same direction as the center  
 1786 of the circle. The seed of the iteration is the hardest non-isolated particle in  
 1787 the event, then, the resulting momentum direction is assigned as the new cone  
 1788 direction and a new iteration starts; iteration process stops when the cone is  
 1789 found to be stable.

- 1790 • Sequential recombination algorithms. The distance between non-isolated par-  
 1791 ticles is calculated; if that distance is below a threshold, these particles are  
 1792 recombined into a new object. The sequence is repeated until the separation  
 1793 between the recombined object and any other particle is above certain thresh-  
 1794 old; the recombined object is called a jet and the algorithm starts again with  
 1795 the remaining particles.

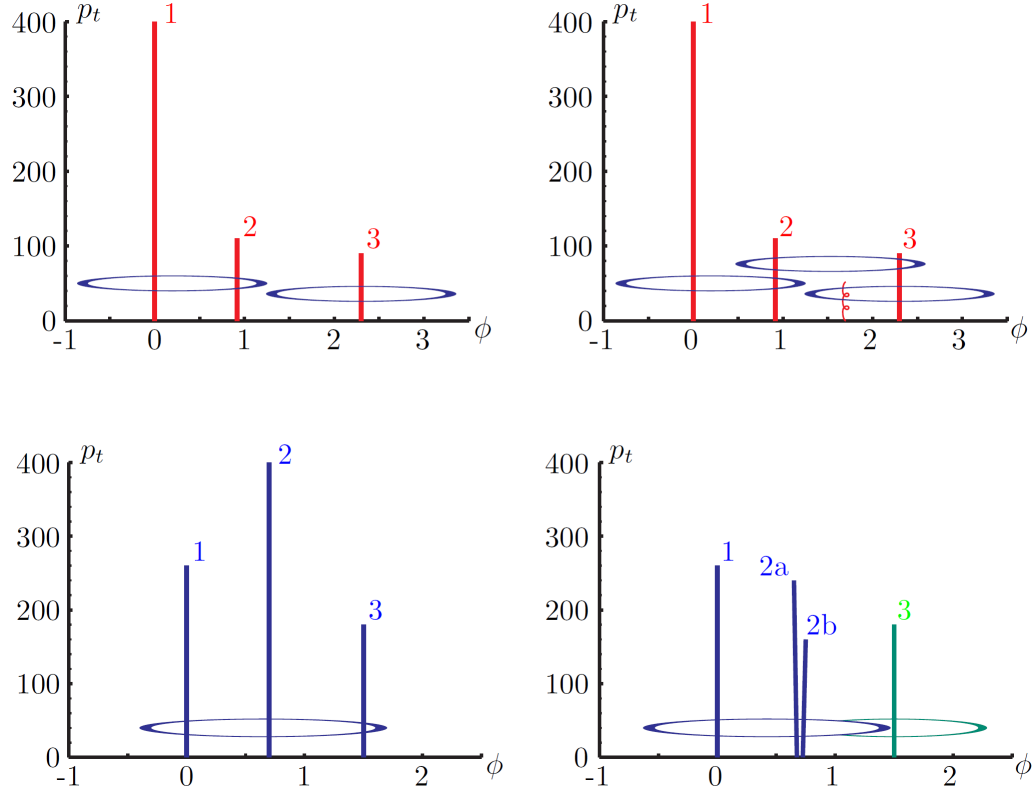


**Figure 3.3:** Stable cones identification using IC algorithms [113].

1796 Two conditions are of particular importance for the clustering algorithms, *infrared*  
 1797 *and collinear (IRC) safety*. In order to explain the concept of infrared (IR) safety,  
 1798 consider an event with three hard particles as shown in the top left side of Figure 3.3,  
 1799 two stable cones are found and then two jets are identified; if a soft gluon is added, as  
 1800 shown in the top right side of Figure 3.3, three stable cones are found and the three  
 1801 hard particles are now clustered into a single jet. If the addition of soft particles  
 1802 change the outcome of the clustering, then it is said that the algorithm is IR unsafe.  
 1803 Soft radiation is highly likely in perturbative QCD, which dominates the physics of  
 1804 the jets, and then IR unsafe effect leads to divergences [113].

1805 The concept of collinear safety can also be explained considering a three hard  
 1806 particles event, as shown in the bottom left side of Figure 3.3, where one stable cone  
 1807 containing all three particles is found and one jet is identified; if the hardest particle

1808 is split into two collinear particles (2a and 2b) in the bottom right side of Figure 3.3,  
 1809 then the clustering results in a different jet identification and the algorithm is said  
 1810 to be collinear unsafe. The collinear unsafe effect leads to divergences in jet cross  
 1811 section calculations [114].

1812 It has been determined that IC algorithms are IRC unsafe, and therefore, they  
 1813 have to be replaced by algorithms that not only provide the finite perturbative results  
 1814 from theoretical computations, but also that are not highly dependent on underlying  
 1815 event and pileup effects which leads to significant corrections [113].

1816 The sequential recombination algorithms arise as the IRC safe alternative used by  
 1817 the CMS experiment; in particular the anti- $k_t$  algorithm which is a generalization of  
 1818 the previously existing  $k_t$  [115] and Cambridge/Aachen [116] jet clustering algorithms.

1819 The anti- $k_t$  algorithm is used to perform the jet reconstruction by clustering those  
 1820 PF particles within a cone (see Figure 3.4); previously, isolated electrons, isolated  
 1821 muons, and charged particles associated with other interaction vertices are excluded  
 1822 from the clustering.

1823 The anti- $k_t$  algorithm proceeds in a sequential recombination of PF particles; the  
 1824 distance between particles  $i$  and  $j$  ( $d_{ij}$ ) and the distance between particles and the  
 1825 beam are defined as

$$d_{ij} = \min \left( \frac{1}{k_{ti}^2}, \frac{1}{k_{tj}^2} \right) \frac{\Delta_{ij}^2}{R^2}$$

$$d_{iB} = \frac{1}{k_{ti}^2} \quad (3.1)$$

1826 where  $\Delta_{ij}^2 = (y_i - y_j)^2 + (\phi_i - \phi_j)^2$ ,  $k_{ti}$ ,  $y_i$  and  $\phi_i$  are the transverse momentum, ra-  
 1827 pidity and azimuth of particle  $i$  respectively and  $R$  is the called jet radius. For all  
 1828 the remaining PF particles, after removing the isolated ones,  $d_{ij}$  and  $d_{iB}$  are calcu-

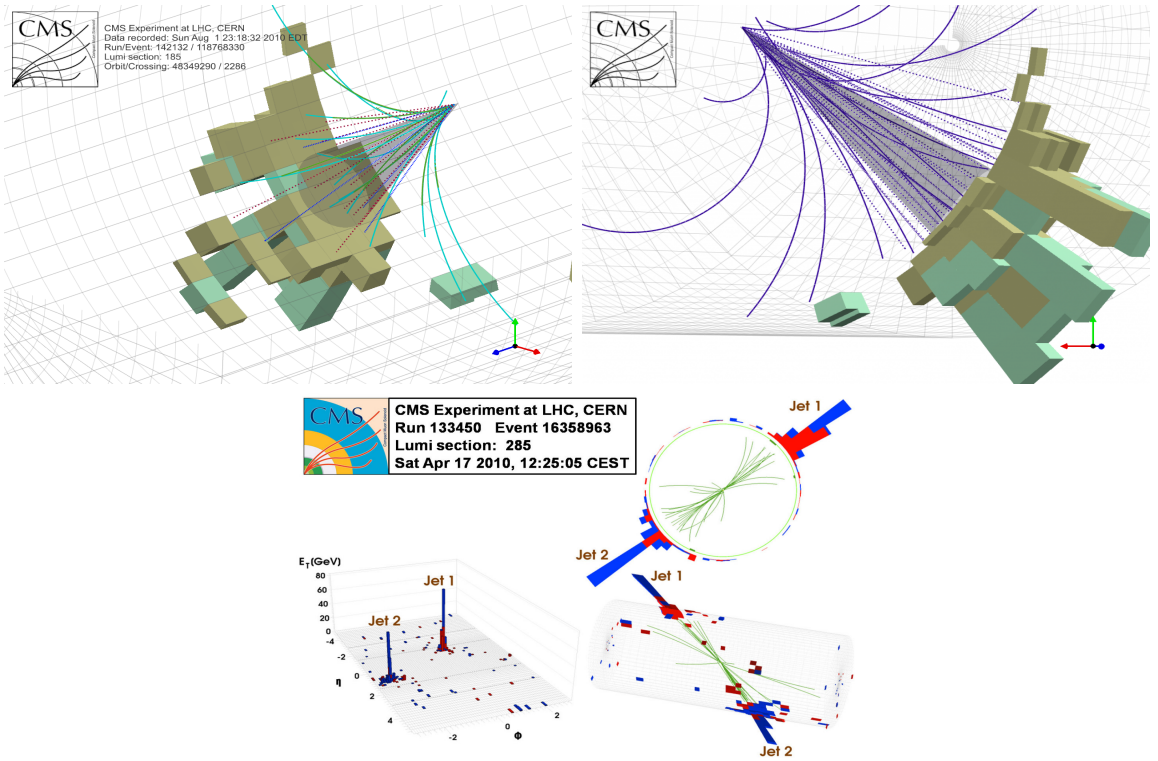


**Figure 3.4:** Jet reconstruction performed by the anti- $k_t$  algorithm. Top: Two different views of a CMS recorded event are presented. Continuous lines correspond to tracks left by charged particles in the tracker while dotted lines are the imaginary paths followed by neutral particles. The green cubes represent the ECAL cells while the blue ones represent the HCAL cells; in both cases, the height of the cube represent the amount of energy deposited in the cells [117]. Bottom: Reconstruction of a recorded event with two jets [118].

lated<sup>5</sup> and the smallest is identified; if it is a  $d_{ij}$ , particles  $i$  and  $j$  are replaced with a new object whose momentum is the vectorial sum of the combined particles. If the smallest distance is a  $d_{iB}$  the clustering process ends, the object  $i$  (which at this stage should be a combination of several PF particles) is declared as a *Particle-flow-jet* (PF jet) and all the associated PF particles are removed from the detector. The clustering process is repeated until no PF particles remain.  $R$  is a free parameter that can be adjusted according to the specific analysis conditions; usually, two values are used,  $R=0.4$  and  $R=0.5$ , giving the name to the so-called AK4-jet and AK5-jet respectively.

<sup>5</sup> Notice that this is a combinatorial calculation.

An advantage of the anti- $k_t$  algorithm over other clustering algorithms is the regularity of the boundaries of the resulting jets. For all known IRC safe algorithms, soft radiation can introduce irregularities in the boundaries of the final jets; however, anti- $k_t$  algorithm is soft-resilient, meaning that jets shape is not affected by soft radiation, which is a valuable property considering that knowing the typical shape of jets makes experimental calibration of jets more simple. In addition, that soft-resilience is expected to simplify certain theoretical calculations and reduce the momentum-resolution loss caused by underlying-event (UE) and pileup contamination [114].

The effect of the UE and pileup contamination over a jet identification, can be seen as if soft events are added to the jet; for instance, if a soft event representing UE or pileup is added to an event for which a set of jets  $J$  have been identified, and the clustering is rerun on that new extended event, the outcome will be different in two aspects: jets will contain some additional soft energy and the distribution of particles in jets may have change; that effect is called *back-reaction*. The back-reaction effect in the anti- $k_t$  algorithm is suppressed not by the amount of momentum added to the jet but by the jet transverse momentum  $p_{T,J}$ , which means that this strong suppression leads to a smaller correction due to EU and pileup effect [114].

1854 Jet energy Corrections

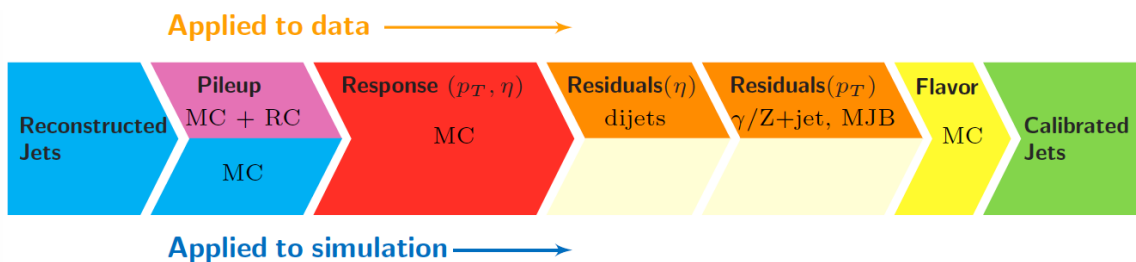


**Figure 3.5:** Jet energy correction diagram. Correction levels are applied sequentially in the indicated fixed order [120].

1855        Even though jets can be reconstructed efficiently, there are some effects that are  
 1856        not included in the reconstruction and that lead to discrepancies between the re-  
 1857        constructed results and the predicted results; in order to overcome these discrep-  
 1858        ancies, a factorized model has been designed in the form of jet energy corrections  
 1859        (JEC) [119,120] applied sequentially as shown in the diagram of Figure 3.5.

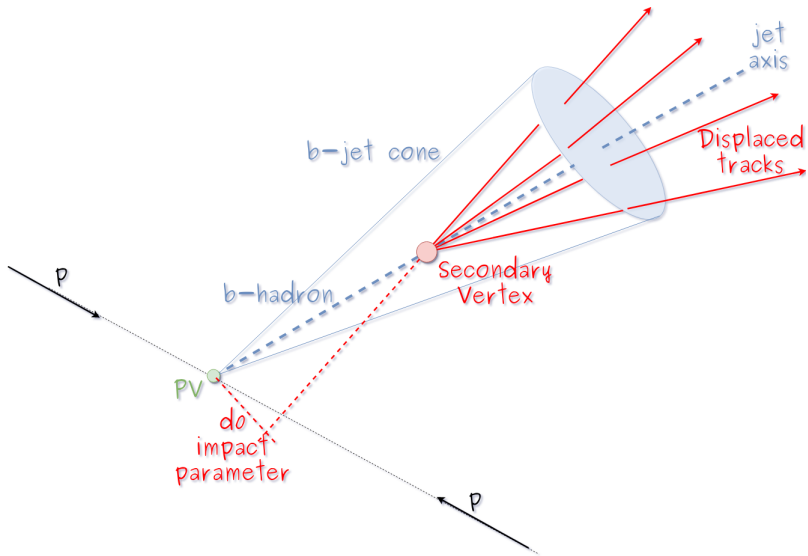
1860        At each level, the jet four-momentum is multiplied by a scaling factor based on  
 1861        jet properties, i.e.,  $\eta$ , flavor, etc.

- 1862        • Level 1 correction removes the energy coming from pile-up. The scale factor is  
               determined using a MC sample of QCD dijet (2 jets) events with and without  
               pileup overlay; it is parametrized in terms of the offset energy density  $\rho$ , jet  
               area A, jet  $\eta$  and jet  $p_T$ . Different corrections are applied to data and MC due  
               to the detector simulation.
- 1867        • MC-truth correction accounts for differences between the reconstructed jet en-  
               ergy and the MC particle-level energy. The correction is determined on a QCD  
               dijet MC sample and is parametrized in terms of the jet  $p_T$  and  $\eta$ .
- 1870        • Residuals correct remaining small differences within jet response in data and  
               MC. The Residuals  $\eta$ -dependent correction compares jets of similar  $p_T$  in the  
               barrel reference region. The Residuals  $p_T$ -dependent correct the jet absolute  
               scale (JES vs  $p_T$ ).
- 1874        • Jet-flavor corrections are derived in the same way as MC-truth corrections but  
               using QCD pure flavor samples.

1876 ***b*-tagging of jets.**

1877 A particular feature of the hadrons containing bottom quarks (*b*-hadrons) is that  
 1878 their lifetime is long enough to travel some distance before decaying, but it is not as  
 1879 long as those of light quark hadrons; therefore, when looking at the hadrons produced  
 1880 in  $p\bar{p}$  collisions, *b*-hadrons decay typically inside the tracker rather than reaching the  
 1881 calorimeters as some light-hadrons do. As a result, a *b*-hadron decay gives rise to a  
 1882 displaced vertex (secondary vertex) with respect to the primary vertex as shown in  
 1883 Figure 3.6; the SV displacement is in the order of a few millimeters. A jet resulting  
 1884 from the decay of a *b*-hadron is called *b* jet; other jets are called light jets.

1885

**Figure 3.6:** Secondary vertex in a *b*-hadron decay.

1886 Several methods to identify *b*-jets (*b*-tagging) have been developed; the method  
 1887 used in this thesis is known as *Combined Secondary Vertex* algorithm in its second  
 1888 version (CSVv2) [121]. By using information of the impact parameter, the recon-  
 1889 structed secondary vertices, and the jet kinematics as input in a multivariate analysis  
 1890 that combines the discrimination power of each variable in one global discrimina-

1891 tor variable, three working points (references): loose, medium and tight, are defined  
 1892 which quantify the probabilities of mistag jets from light quarks as jets from  $b$  quarks;  
 1893 10, 1 and 0.1 % respectively. Although the mistagging probability decreases with the  
 1894 working point strength, the efficiency to correctly tag  $b$ -jets also decreases as 83, 69  
 1895 and 49 % for the respective working point; therefore, a balance needs to be achieved  
 1896 according to the specific requirements of the analysis.

1897 **3.4.1.1 Missing transverse energy.**

1898 The fact that proton bunches carry momentum along the  $z$ -axis implies that for each  
 1899 event it is expected that the momentum in the transverse plane is balanced. Imbal-  
 1900 ances are quantified by the missing transverse energy (MET) and are attributed to  
 1901 several sources including particles escaping undetected through the beam pipe, neu-  
 1902 trinos produced in weak interactions processes which do not interact with the detector  
 1903 and thus escaping without leaving a sign, or even undiscovered particles predicted by  
 1904 models beyond the SM.

1905

1906 The PF algorithm assigns the negative sum of the momenta of all reconstructed  
 1907 PF particles to the *particle-flow MET* according to

$$\vec{E}_T = - \sum_i \vec{p}_{T,i} \quad (3.2)$$

1908 JEC are propagated to the calculation of the  $\vec{E}_T$  as described in the Reference [122].

1909

1910 **3.4.2 Event reconstruction examples**

1911 Figures 3.7-3.9 show the results of the reconstruction performed on 3 recorded events.

1912 Descriptions are taken directly from the source.

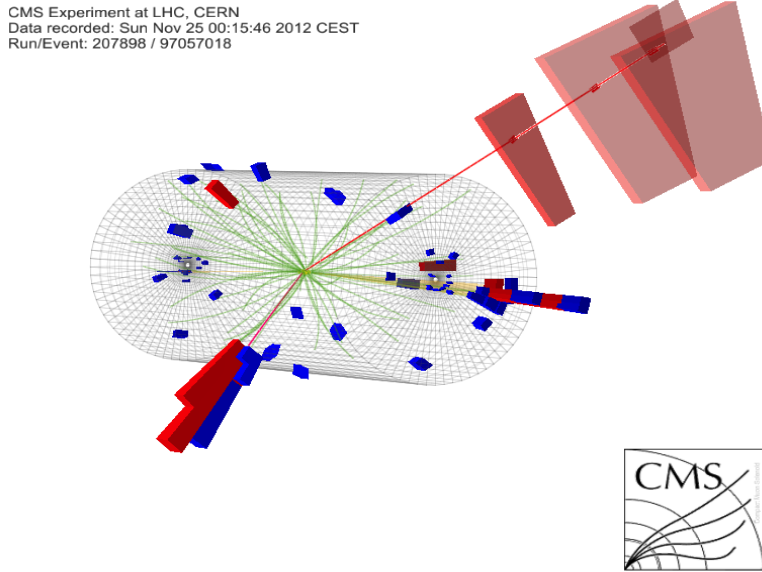


**Figure 3.7:** HIG-13-004 Event 1 reconstruction results; “HIG-13-004 Event 1: Event recorded with the CMS detector in 2012 at a proton-proton center-of-mass energy of 8 TeV. The event shows characteristics expected from the decay of the SM Higgs boson to a pair of  $\tau$  leptons. Such an event is characterized by the production of two forward-going jets, seen here in opposite endcaps. One of the  $\tau$  decays to a muon (red lines on the right) and neutrinos, while the other  $\tau$  decays into a charged hadron and a neutrino.” [123].

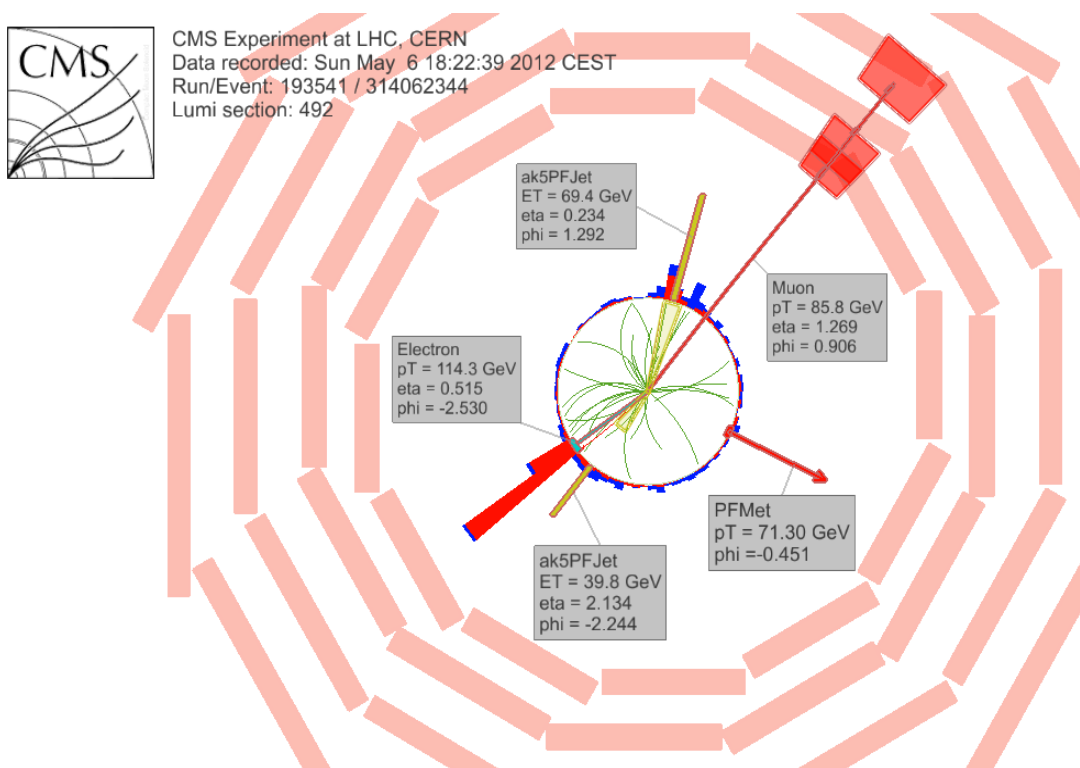


**Figure 3.8:**  $e\mu$  event reconstruction results; “An  $e\mu$  event candidate selected in 8 TeV data, as seen from the direction of the proton beams. The kinematics of the main objects used in the event selection are highlighted: two isolated leptons and two particle-flow jets. The reconstructed missing transverse energy is also displayed for reference” [124].

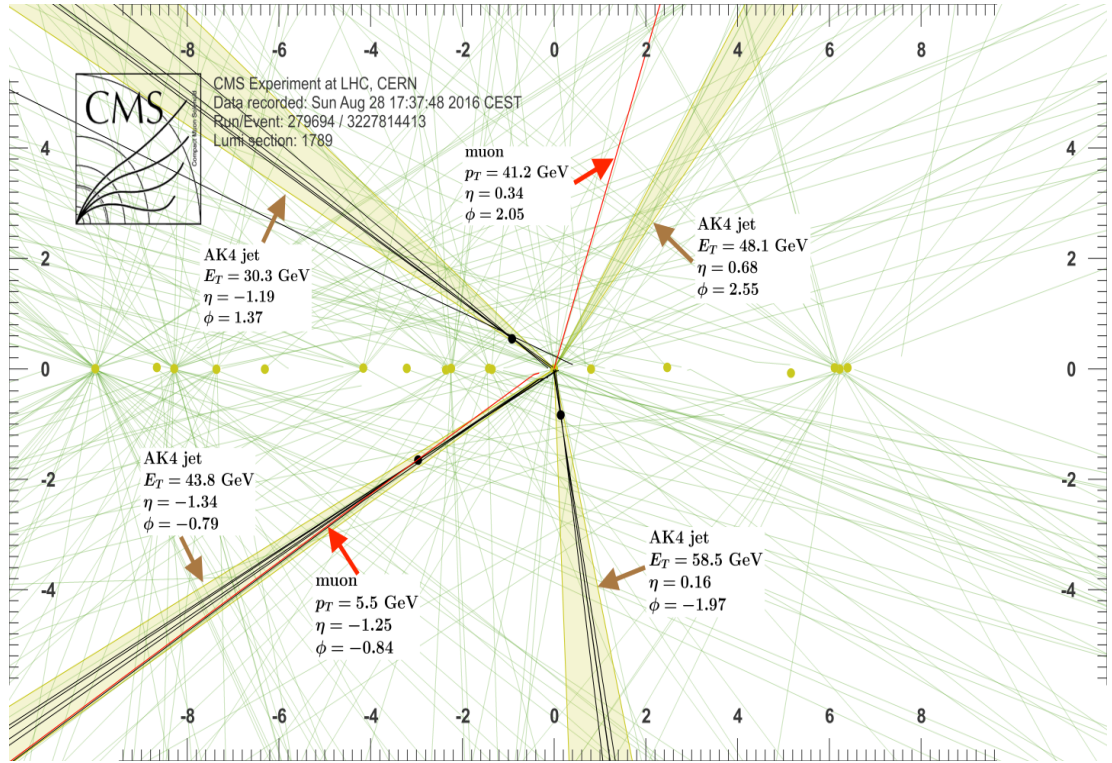


**Figure 3.9:** Recorded event reconstruction results; “Recorded event ( $\rho$ - $z$  projection) with three jets with  $p_T > 30$  GeV with one displaced muon track in 2016 data collected at 13 TeV. Each of the three jets has a displaced reconstructed vertex. The jet with  $p_T(j) = 43.8$  GeV,  $\eta(j) = -1.34$ ,  $\phi(j) = -0.79$  contains muon with  $p_T(\mu) = 5.5$  GeV,  $\eta(\mu) = -1.25$ ,  $\phi(\mu) = -0.84$ . Event contains reconstructed isolated muon with  $p_T(\mu) = 41.2$  GeV,  $\eta(\mu) = 0.34$ ,  $\phi(\mu) = 2.05$  and MET with  $p_T = 72.5$  GeV,  $\phi = -0.32$ . Jet candidates for a  $b$ -jet from top quark leptonic and hadronic decays are tagged by CSVv2T algorithm. One of the other two jets is tagged by CharmT algorithm. Tracks with  $p_T > 0.5$  GeV are shown. The number of reconstructed primary vertices is 18. Reconstructed  $m_T(W)$  is 101.8 GeV. Beam spot position correction is applied. Reconstructed primary vertices are shown in yellow color, while reconstructed displaced vertices and associated tracks are presented in black color. Dimensions are given in cm” [125].

<sub>1913</sub> **Chapter 5**

<sub>1914</sub> **Statistical methods**

<sub>1915</sub> In the course of analyzing the data sets provided by the CMS experiment and used in  
<sub>1916</sub> this thesis, several statistical tools have been employed; in this chapter, a description  
<sub>1917</sub> of these tools will be presented, starting with the general statement of the multivariate  
<sub>1918</sub> analysis methods, followed by the particularities of the Boosted Decision Trees (BDT)  
<sub>1919</sub> method and its application to the classification problem. Statistical inference methods  
<sub>1920</sub> used will also be presented. This chapter is based mainly on References [126–128].

<sub>1921</sub> **5.1 Multivariate analysis**

<sub>1922</sub> Multivariate data analysis (MVA) makes use of the statistical techniques developed  
<sub>1923</sub> to analyze more than one variable at once, taking into account all the correlations  
<sub>1924</sub> among variables. MVA is employed in a variety of fields like consumer and market  
<sub>1925</sub> researches, quality control and process optimization. Using MVA it is possible to  
<sub>1926</sub> identify the dominant patterns in a data sample, like groups, outliers and trends, and  
<sub>1927</sub> determine to which group a set of values belong; in the particle physics context, MVA  
<sub>1928</sub> methods are used to perform the selection of certain type of events from a large data

1929 set, e.g., a raw data input.

1930 Processes with small cross section, such as the  $tHq$  process, are hard to detect  
 1931 in the presence of the processes with larger cross sections; therefore, only a small  
 1932 fraction of the data contains events of interest (signal), the major part is signal-like  
 1933 events, which mimic signal characteristics but belong to different process, so they are  
 1934 a background to the process of interest. This implies that it is not possible to say  
 1935 with certainty that a given event is a signal or a background and statistical methods  
 1936 should be involved. In that sense, the challenge can be formulated as one where a  
 1937 set of events have to be classified according to certain special features; these features  
 1938 correspond to the measurements of several parameters like energy or momentum,  
 1939 organized in a set of *input variables*. The measurements for each event can be written  
 1940 in a vector  $\mathbf{x} = (x_1, \dots, x_n)$  for which

1941 •  $f(\mathbf{x}|s)$  is the probability density (*likelihood function*) that  $\mathbf{x}$  is the set of mea-  
 1942 sured values given that the event is a signal event (signal hypothesis).

1943 •  $f(\mathbf{x}|b)$  is the probability density (*likelihood function*) that  $\mathbf{x}$  is the set of mea-  
 1944 sured values given that the event is a background event (background hypothe-  
 1945 sis).

1946 Figure 5.1 shows three ways to perform a classification of events for which mea-  
 1947 surements of two properties, i.e., two input variables  $x_1$  and  $x_2$ , have been performed;  
 1948 blue circles represent signal events while red triangles represent background events.  
 1949 The classification on the left is *cut-based* requiring  $x_1 < c_1$  and  $x_2 < c_2$ ; usually the cut  
 1950 values ( $c_1$  and  $c_2$ ) are chosen according to some knowledge about the event process.  
 1951 In the middle plot, the classification is performed using a linear function of the input  
 1952 variables, hence the boundary is a line, while in the right plot the the relationship  
 1953 between input variables is not linear thus the boundary is not linear either.

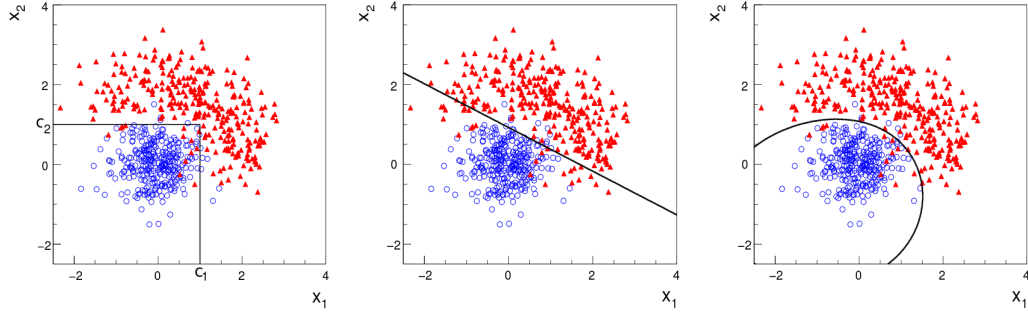


**Figure 5.1:** Scatter plots-MVA event classification. Distribution of two input variables  $x_1$  and  $x_2$  measured for a set of events; blue circles represent signal events and red triangles represent background events. The classification is based on cuts (left), linear boundary (center), and nonlinear boundary (right) [126]

1954        In general, the boundary can be parametrized in terms of the input variables such  
 1955      that the cut is set on the parametrization instead of on the variables, i.e.,  $y(\mathbf{x}) = y_{cut}$   
 1956      with  $y_{cut}$  being a constant; thus, the acceptance or rejection of an event is based on  
 1957      which side of the boundary the event is located. If  $y(\mathbf{x})$ , usually called *test statistic*,  
 1958      has functional form, it can be used to determine the probability distribution functions  
 1959       $p(y|s)$  and  $p(y|b)$  and then perform a scalar test statistic with a single cut on the scalar  
 1960      variable  $y$ .

1961        Figure 5.2 illustrates what would be the probability distribution functions under  
 1962      the signal and background hypotheses for a scalar test statistic with a cut on the  
 1963      classifier  $y$ . Note that the tails of the distributions indicate that some signal events  
 1964      fall on the rejection region and some background events fall on the acceptance region;  
 1965      therefore, it is convenient to define the *efficiency* with which events of a given type  
 1966      are accepted. The signal and background efficiencies are given by

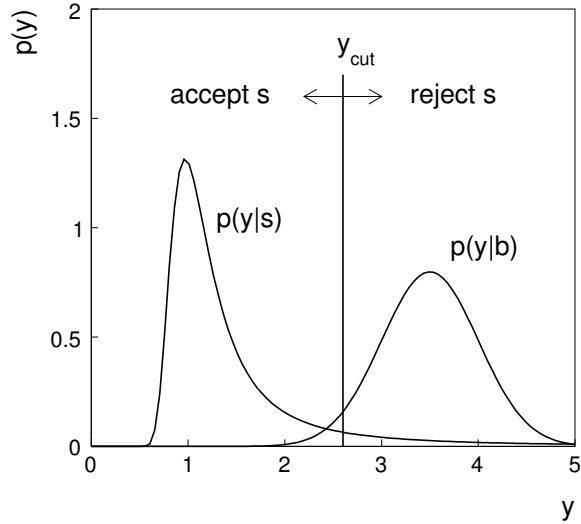


**Figure 5.2:** Distributions of the scalar test statistic  $y(\mathbf{x})$  under the signal and background hypotheses. [126]

$$\varepsilon_s = P(\text{accept event}|s) = \int_A f(\mathbf{x}|s) d\mathbf{x} = \int_{-\infty}^{y_{cut}} p(y|s) dy , \quad (5.1)$$

$$\varepsilon_b = P(\text{accept event}|b) = \int_A f(\mathbf{x}|b) d\mathbf{x} = \int_{-\infty}^{y_{cut}} p(y|b) dy , \quad (5.2)$$

1967 where  $A$  is the acceptance region. If the background hypothesis is the *null hypothesis*  
 1968 ( $H_0$ ), the signal hypothesis would be *alternative hypothesis* ( $H_1$ ); in this context, the  
 1969 background efficiency corresponds to the significance level of the test ( $\alpha$ ) and describes  
 1970 the misidentification probability, while the signal efficiency corresponds to the power  
 1971 of the test ( $1-\beta$ ) and describes the probability of rejecting the background hypothesis  
 1972 if the signal hypothesis is true. What is sought in an analysis is to maximize the  
 1973 power of the test relative to the significance level, i.e., set a selection with the largest  
 1974 possible selection efficiency and the smallest possible misidentification probability.

### 1975 5.1.1 Decision trees

1976 For this thesis, the implementation of the MVA strategy, described above, is per-  
 1977 formed through decision trees by using the TMVA software package [127] included in  
 1978 the the ROOT analysis framework [129]. In a simple picture, a decision tree classifies  
 1979 events according to their input variables values by setting a cut on each input variable  
 1980 and checking which events are on which side of the cut, just as proposed in the MVA  
 1981 strategy, but in addition, as a machine learning algorithm, decision trees offer the  
 1982 possibility to be trained and then perform the classification efficiently.

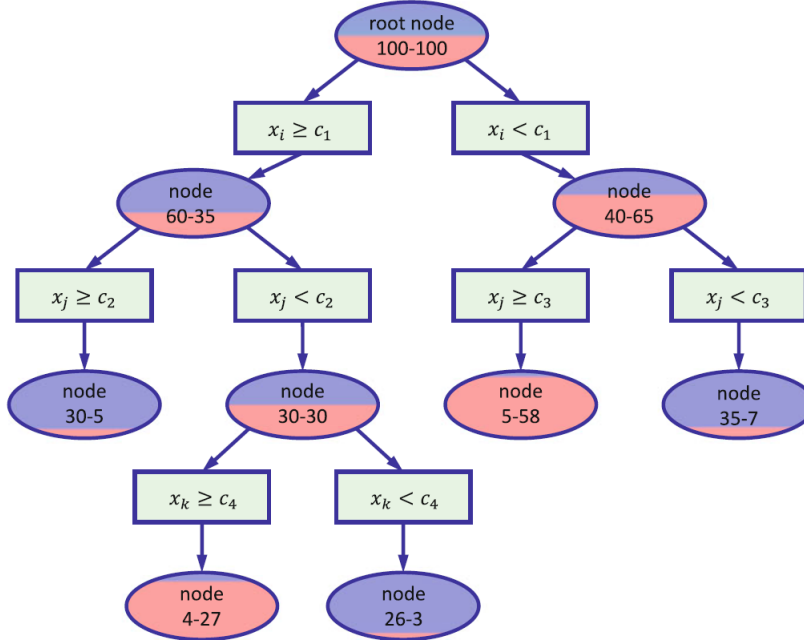


**Figure 5.3:** Example of a decision tree. Each node is fed with a MC sample mixing signal and background events (left-right numbers); nodes colors represent the relative number of signal/background events [128].

1983 The training or growing of a decision tree is the process where the rules for clas-  
 1984 sifying events are defined; this process is represented in Figure 5.3 and consists of  
 1985 several steps:

- 1986 • take MC samples of signal and background events and split them into two parts

1987 each; first parts will be used in the decision tree training, while the second parts  
 1988 will be used for testing the final classifier obtained from the training. Each event  
 1989 has associated a set of input variables  $\mathbf{x} = (x_1, \dots, x_n)$  which serve to distinguish  
 1990 between signal and background events. The training sample is taken in at the  
 1991 root *node*.

- 1992     • pick one variable, say  $x_i$
- 1993     • pick one value of  $x_i$ , each event has its own value of  $x_i$ , and split the training  
     1994      sample into two subsamples  $B_1$  and  $B_2$ ;  $B_1$  contains events for which  $x_i < c_1$   
     1995      while  $B_2$  contains the rest of the training events;
- 1996     • scan all possible values of  $x_i$  and find the splitting value that provides the *best*  
     1997      classification<sup>1</sup>, i.e.,  $B_1$  is mostly made of signal events while  $B_2$  is mostly made  
     1998      of background events.
- 1999     • It is possible that variables other than the picked one produce a better classi-  
     2000      fication, hence, all the variables have to be evaluated. Pick the next variable,  
     2001      say  $x_j$ , and repeat the scan over its possible values.
- 2002     • At the end, all the variables and their values will have been scanned, the *best*  
     2003      variable and splitting value will have been identified, say  $x_1, c_1$ , and there will  
     2004      be two nodes fed with the subsamples  $B_1$  and  $B_2$ .

2005       Nodes are further split by repeating the decision process until a given number of  
 2006      final nodes is obtained, nodes are largely dominated by either signal or background  
 2007      events, or nodes have too few events to continue. Final nodes are called *leaves* and  
 2008      they are classified as signal or background leaves according to the class of the majority  
 2009      of events in them. Each *branch* in the tree corresponds to a sequence of cuts.

---

<sup>1</sup> Quality of the classification will be treated in the next paragraph.

2010        The quality of the classification at each node is evaluated through a separation  
 2011 criteria; there are several of them but the *Gini Index* ( $G$ ) is the one used in the  
 2012 decision trees trained for the analysis in this thesis.  $G$  is written in terms of the  
 2013 purity ( $P$ ), i.e., the fraction of signal events in the samples after the separation is  
 2014 made; it is given by

$$G = P(1 - P) \quad (5.3)$$

2015 note that  $P=0.5$  at the root node while  $G=0$  for pure leaves. For a node  $A$  split into  
 2016 two nodes  $B_1$  and  $B_2$  the  $G$  gain is

$$\Delta G = G(A) - G(B_1) - G(B_2) \quad (5.4)$$

2017 the *best* classification corresponds to that for which the gain of  $G$  is maximized; hence,  
 2018 the scanning over all the variables in an event and their values is of great importance.

2019        In order to provide a numerical output for the classification, events in a sig-  
 2020 nal(background) leaf are assigned a score of 1(-1) each, defining in this way the  
 2021 decision tree *classifier/weak learner* as

$$f(\mathbf{x}) = \begin{cases} 1 & \mathbf{x} \text{ in signal region,} \\ -1 & \mathbf{x} \text{ in background region.} \end{cases}$$

2022        Figure 5.4 shows an example of the classification of a sample of events, containing  
 2023 two variables, performed by a decision tree.

### 2024 **5.1.2 Boosted decision trees (BDT).**

2025 Event misclassification occurs when a training event ends up in the wrong leaf, i.e., a  
 2026 signal event ends up in a background leaf or a background event ends up in a signal

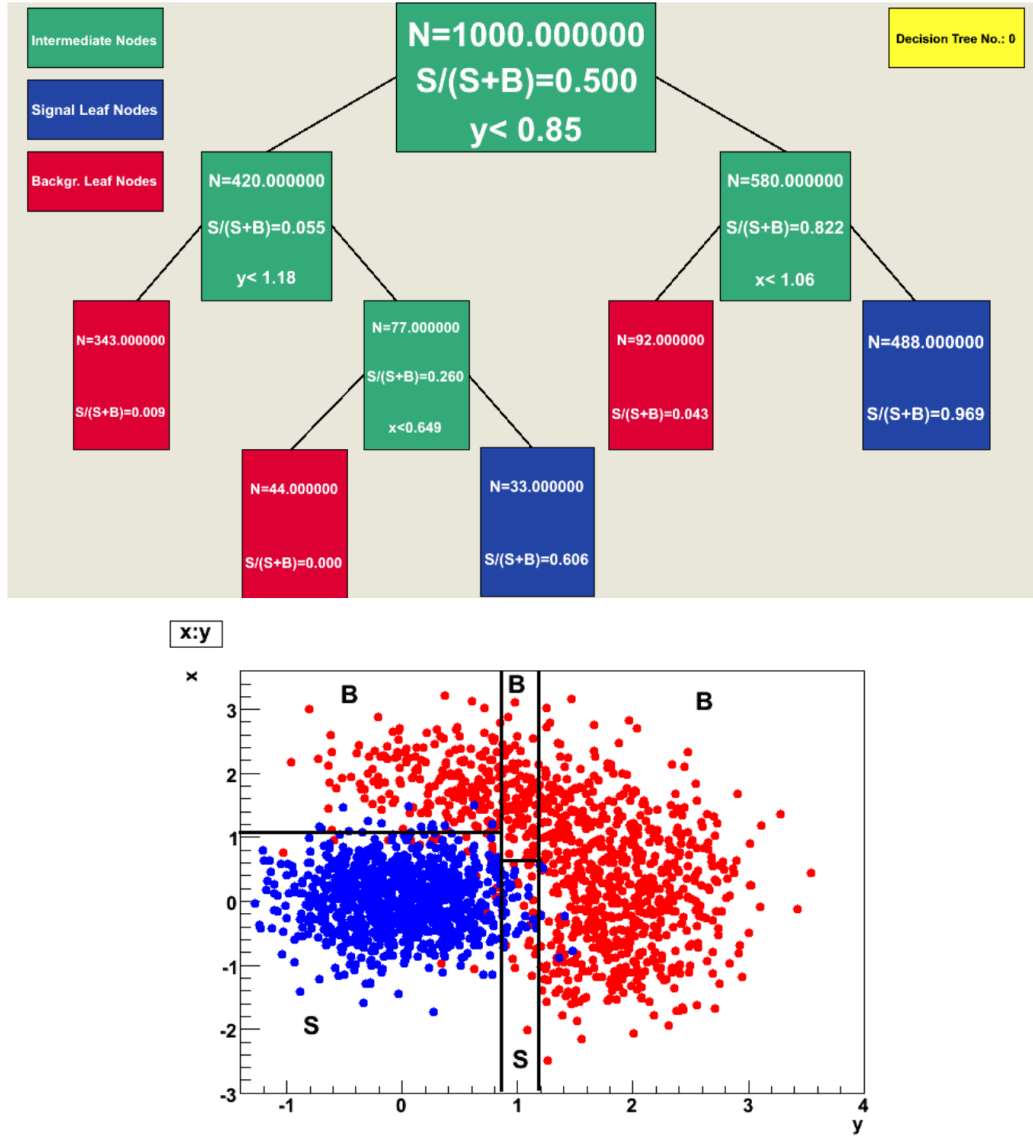


**Figure 5.4:** Example of a decision tree output. Each leaf, blue for signal events and red for background events, is represented by a region in the variables phase space [130].

leaf. A way to correct it is to assign a weight to the misclassified events and train a second tree using the reweighted events; the event reweighting is performed by a boosting algorithm in such a way that when used in the training of a new decision tree the *boosted events* get correctly classified. The process is repeated iteratively adding a new tree to the forest and creating a set of classifiers, which are combined

2032 to create the next classifier; the final classifier offers more stability<sup>2</sup> and has a smaller  
 2033 misclassification rate than any individual ones. The resulting tree collection is known  
 2034 as a *boosted decision tree (BDT)*.

2035 Thus, purity of the sample is generalized to

$$P = \frac{\sum_s w_s}{\sum_s w_s + \sum_b w_b} \quad (5.5)$$

2036 where  $w_s$  and  $w_b$  are the weights of the signal and background events respectively;  
 2037 the Gini index is also generalized

$$G = \left( \sum_i^n w_i \right) P(1 - P) \quad (5.6)$$

2038 with  $n$  the number of events in the node. The final score of an event, after pass-  
 2039 ing through the forest, is calculated as the renormalized sum of all the individual  
 2040 (possibly weighted) scores; thus, high(low) score implies that the event is most likely  
 2041 signal(background).

2042 The boosting procedure, implemented in the *Gradient boosting* algorithm used in  
 2043 this thesis, produces a classifier  $F(\mathbf{x})$  which is the weighted sum of the individual  
 2044 classifiers obtained after each iteration, i.e.,

$$F(\mathbf{x}) = \sum_{m=1}^M \beta_m f(\mathbf{x}; a_m) \quad (5.7)$$

2045 where  $M$  is the number of trees in the forest. The *loss function*  $L(F, y)$  represents the  
 2046 deviation between the classifier  $F(\mathbf{x})$  response and the true value  $y$  obtained from the  
 2047 training sample (1 for signal events and -1 for background event), according to

---

<sup>2</sup> Decision trees suffer from sensitivity to statistical fluctuations in the training sample which may lead to very different results with a small change in the training samples.

$$L(F, y) = \ln(1 + e^{-2F(\mathbf{x})y}) \quad (5.8)$$

thus, the reweighting is employed to ensure the minimization of the loss function; a more detailed description of the minimization procedure can be found in Reference [131]. The final classifier output is later used as a final discrimination variable, labeled as *BDT output/response*.

### 5.1.3 Overtraining

Decision trees offer the possibility to have as many nodes as wished in order to reduce the misclassification to zero (in theory); however, when a classifier is too much adjusted to a particular training sample, the classifier's response to a slightly different sample may leads to a completely different classification results; this effect is known as *overtraining*.

An alternative to reduce the overtraining in BDTs consists in pruning the tree by removing statistically insignificant nodes after the tree growing is completed but this option is not available for BDTs with gradient boosting in the TMVA-toolkit, therefore, the overtraining has to be reduced by tuning the algorithm, number of nodes, minimum number of events in the leaves, etc. The overtraining can be evaluated by comparing the responses of the classifier when running over the training and test samples.

### 5.1.4 Variable ranking

BDTs have a couple of particular advantages related to the input variables; on one side, they are relatively insensitive to the number of input variables used in the vector  $\mathbf{x}$ . The ranking of the BDT input variables is determined by counting the number of

times a variable is used to split decision tree nodes; in addition, the separation gain-squared achieved in the splitting and the number of events in the node are accounted by applying a weighting to that number. Thus, those variables with small or no power to separate signal and background events are rarely chosen to split the nodes, i.e., are effectively ignored.

On the other side, variables correlations play an important role for some MVA methods like the Fisher discriminant algorithm in which the first step consist of performing a linear transformation to a phase space where the correlations between variables are removed; in the case of BDT algorithm, correlations do not affect the performance.

### 5.1.5 BDT output example.

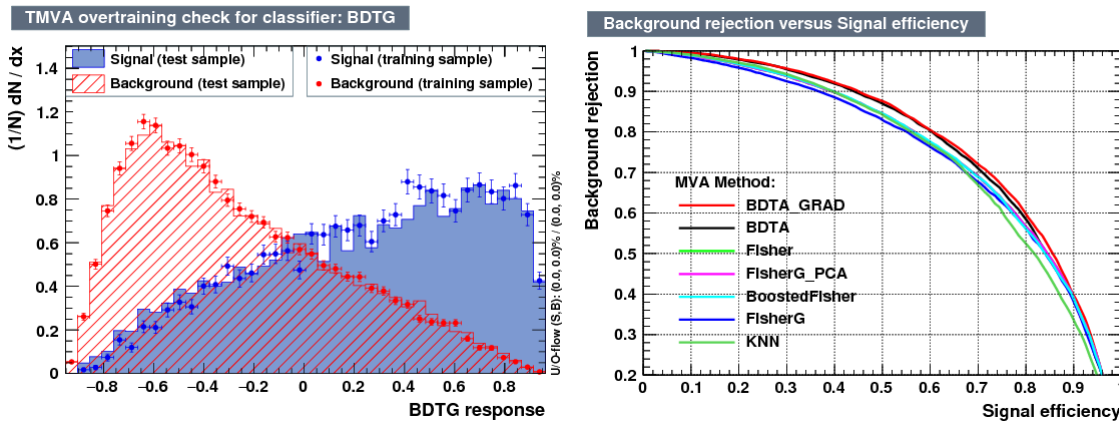


**Figure 5.5:** Left: Output distributions for the gradient boosted decision tree (BDTG) classifier using a sample of signal ( $pp \rightarrow tHq$ ) and background ( $pp \rightarrow t\bar{t}$ ) events. Right: Background rejection vs signal efficiency (ROC curves) for various MVA classifiers running over the same sample used to produce the plot on the left.

Left side of figure 5.5 shows the BDT output distributions for signal ( $pp \rightarrow tHq$ ) and background ( $pp \rightarrow t\bar{t}$ ) events; this plot is the equivalent to the one showed in Figure 5.2. A forest with 800 trees, maximum depth per tree = 3, and gradient

2083 boosting have been used as training parameters. The BDTG classifier offers a good  
 2084 separation power; while there is a small overtraining in the signal distribution, the  
 2085 background distribution seems to be well predicted which might indicate that the  
 2086 sample is composed of more background than signal events.

2087 Right side of figure 5.5 shows the background rejection vs signal efficiency curves  
 2088 for several combinations of MVA classifiers-boosting algorithms; these curves are  
 2089 known as ROC curves and give an indication of the performance of the classifier. The  
 2090 best performance is achieved with the BDTG classifier (BDTA\_GRAD).

## 2091 5.2 Statistical inference.

2092 Once events are classified, the next step consists in finding the parameters that define  
 2093 the likelihood functions  $f(\mathbf{x}|s), f(\mathbf{x}|b)$  for signal and background events respectively.  
 2094 In general, likelihood functions depend not only on the measurements but also on  
 2095 parameters ( $\theta_m$ ) that define their shapes; the process of estimating these *unknown*  
 2096 *parameters* and their uncertainties from the experimental data is called *inference*.

2097 The statistical inference tools used in this analysis are implemented in the RooFit  
 2098 toolkit [132] and COMBINE package [133] included in the CMSSW software frame-  
 2099 work.

### 2100 5.2.1 Nuisance parameters.

2101 The unknown parameter vector  $\boldsymbol{\theta}$  is made of two types of parameters: on one side,  
 2102 those parameters that provide information about the physical observables of interest  
 2103 for the experiment or *parameters of interest*. On the other side, the *nuisance parame-  
 2104 ters* that are not of direct interest for the experiment but that need to be included in  
 2105 the analysis in order to achieve a satisfactory description of the data; they represent

2106 effects of the detector response like the finite resolutions of the detection systems,  
 2107 miscalibrations, and in general any source of uncertainty introduced in the analysis.

2108        Nuisance parameters can be estimated from experimental data; for instance, data  
 2109 samples from a test beam are usually employed for calibration purposes. In cases  
 2110 where experimental samples are not available, the estimation of nuisance parameters  
 2111 makes use of dedicated simulation programs to provide the required samples.

2112        The estimation of the unknown parameters involves certain deviation from their  
 2113 true values, hence, the measurement of the nuisance parameter is written in terms  
 2114 of an estimated value, also called central value,  $\hat{\theta}$  and its uncertainty  $\delta\theta$  using the  
 2115 notation

$$\theta = \hat{\theta} \pm \delta\theta \quad (5.9)$$

2116 where the interval  $[\hat{\theta} - \delta\theta, \hat{\theta} + \delta\theta]$  is called *confidence interval*; it is usually interpreted,  
 2117 in the limit of infinite number of experiments, as the interval where the true value  
 2118 of the unknown parameter  $\theta$  is contained with a probability of 0.6827 (if no other  
 2119 convention is stated); this interval represents the area under a Gaussian distribution  
 2120 in the interval  $\pm 1\sigma$ .

2121        The uncertainties associated to nuisance parameters produce *systematic uncer-*  
 2122 *tainties* in the final measurement, while the uncertainties related only to fluctuations  
 2123 in data and that affect the determination of parameters of interest produce *statistical*  
 2124 *uncertainties*.

## 2125 5.2.2 Maximum likelihood estimation method

2126 The estimation of the unknown parameters that are in best agreement with the ob-  
 2127 served data is performed through a function of the data sample that return the

2128 estimate of those parameters; that function is called an *estimator*. Estimators are  
 2129 usually constructed using mathematical expressions encoded in algorithms.

2130 In this thesis, the estimator used is the likelihood function  $f(\mathbf{x}|\boldsymbol{\theta})$ <sup>3</sup> which depends  
 2131 on a set of measured variables  $\mathbf{x}$  and a set of unknown parameters  $\boldsymbol{\theta}$ . The likelihood  
 2132 function for N events in a sample is the combination of all the individual likelihoods  
 2133 functions, i.e.,

$$L(\boldsymbol{\theta}) = \prod_{i=1}^N f(\mathbf{x}^i|\boldsymbol{\theta}) = \prod_{i=1}^N f(x_1^i, \dots, x_n^i; \theta_1, \dots, \theta_m) \quad (5.10)$$

2134 and the estimation method used is the *Maximum Likelihood Estimation* method  
 2135 (MLE); it is based on the combined likelihood function defined by eqn. 5.10 and  
 2136 the procedure seeks for the parameter set that corresponds to the maximum value of  
 2137 the combined likelihood function, i.e., the *maximum likelihood estimator* of the un-  
 2138 known parameter vector  $\boldsymbol{\theta}$  is the function that produces the vector of *best estimators*  
 2139  $\hat{\boldsymbol{\theta}}$  for which the likelihood function  $L(\boldsymbol{\theta})$  evaluated at the measured  $\mathbf{x}$  is maximum.

2140 Usually, the logarithm of the likelihood function is used in numerical algorithm  
 2141 implementations in order to avoid underflow the numerical precision of the computers  
 2142 due to the product of low likelihoods. In addition, it is common to minimize the  
 2143 negative logarithm of the likelihood function, therefore, the negative log-likelihood  
 2144 function is

$$F(\boldsymbol{\theta}) = -\ln L(\boldsymbol{\theta}) = -\sum_{i=1}^N f(\mathbf{x}^i|\boldsymbol{\theta}). \quad (5.11)$$

2145 The minimization process is performed by the software MINUIT [134] imple-  
 2146 mented in the ROOT analysis framework. In case of data samples with large number  
 2147 of measurements, the computational resources necessary to calculate the likelihood  
 2148 function are too big; therefore, the parameter estimation is performed using binned

---

<sup>3</sup> analogue to the likely functions described in previous sections

2149 distributions of the variables of interest for which the *binned likelihood function* is  
 2150 given by

$$L(\mathbf{x}|r, \boldsymbol{\theta}) = \prod_{i=1} \frac{(r \cdot s_i(\boldsymbol{\theta}) + b_i(\boldsymbol{\theta}))^{n_i}}{n_i!} e^{-r \cdot s_i(\boldsymbol{\theta}) - b_i(\boldsymbol{\theta})} \prod_{j=1} \frac{1}{\sqrt{2\pi}\sigma_{\theta_j}^2} e^{-(\theta_j - \theta_{0,j})^2/2\sigma_{\theta_j}^2}, \quad (5.12)$$

2151 with  $s_i$  and  $b_i$  the expected number of signal and background yields for the bin  $i$ ,  $n_i$   
 2152 is the observed number of events in the bin  $i$  and  $r = \sigma/\sigma_{SM}$  is the signal strength.  
 2153 Note that the number of entries per bin follows a Poisson distribution. The effect  
 2154 of the nuisance parameters have been included in the likelihood function through  
 2155 the multiplication by a Gaussian distribution that models the nuisance. The three  
 2156 parameters,  $r$ ,  $s_i$  and  $b_i$  are jointly fitted to estimate the value of  $r$ .

## 2157 5.3 Upper limits

2158 In this analysis, two hypotheses are considered; the background only hypothesis  
 2159 ( $H_0(b)$ ) and the signal plus background hypothesis ( $H_1(s+b)$ ), i.e., the sample of  
 2160 events is composed of background only events ( $r=0$ ) or it is a mixture of signal plus  
 2161 background events ( $r=1$ ). The exclusion of one hypothesis against the other means  
 2162 that the observed data sample better agrees with  $H_0$  or rather with  $H_1$ . In order  
 2163 to discriminate these hypotheses, a test statistic is constructed on the basis of the  
 2164 likelihood function evaluated for each of the hypothesis.

2165 The *Neyman-Pearson* lemma [135] states that the test statistic that provide the  
 2166 maximum power for  $H_1$  for a given significance level (background misidentification  
 2167 probability  $\alpha$ ), is given by the ratio of the likelihood functions  $L(\mathbf{x}|H_1)$  and  $L(\mathbf{x}|H_0)$ ;  
 2168 however, in order to use that definition it is necessary to know the true likelihood  
 2169 functions, which in practice is not always possible. Approximate functions obtained

2170 by numerical methods, like the BDT method described above, have to be used, so  
 2171 that the *profile likelihood* test statistic is defined by

$$\lambda(\mathbf{r}) = \frac{L(\mathbf{x}|r, \hat{\boldsymbol{\theta}}(r))}{L(\mathbf{x}|\hat{r}, \hat{\boldsymbol{\theta}})}, \quad (5.13)$$

2172 where,  $\hat{r}$  and  $\hat{\boldsymbol{\theta}}$  maximize the likelihood function, and  $\hat{\boldsymbol{\theta}}$  maximize the likelihood  
 2173 function for a given value of the signal strength modifier  $r$ . In practice, the test  
 2174 statistic  $t_r$

$$t_r = -2\ln\lambda(r) \quad (5.14)$$

2175 is used to evaluate the presence of signal in the sample, since the minimum of  $t_r$  at  
 2176  $r = \hat{r}$  suggest the presence of signal with signal strength  $\hat{r}$ . The uncertainty interval  
 2177 for  $r$  is determined by the values of  $r$  for which  $t_r = 1$ .

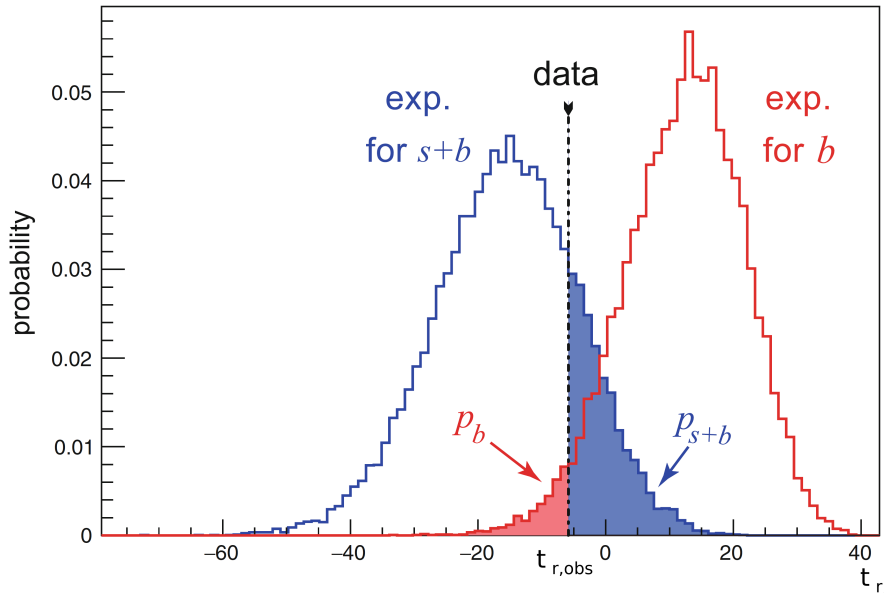


**Figure 5.6:**  $t_r$  p.d.f. from MC pseudo experiments assuming  $H_0$  (red) and  $H_1$  (blue). The black dashed line shows the value of the test statistic as measured from data. Adapted from Reference [128].

2178 The expected probability density function (p.d.f)  $f(t_r|r, \boldsymbol{\theta})$  of the test statistic  $t_r$

2179 can be obtained numerically by generating MC pseudo-experiments assuming each  
 2180  $H_0(b)$  and  $H_1(s+b)$  as shown in Figure 5.6. The probability that  $t_r$  takes a value  
 2181 equal or greater than the observed value ( $t_{r,obs}$ ) when a signal with a signal modifier  $r$   
 2182 is present in the data sample, is called *p-value* of the observation; it can be calculated  
 2183 using

$$p_r = \int_{t_{r,obs}}^{\infty} f(t'_r|r, \boldsymbol{\theta}) dt'_r, \quad (5.15)$$

2184 thus,  $p_r < 0.05$  means that, for that particular value of  $r$ ,  $H_1$  could be excluded at  
 2185 95% Confidence Level (CL). The corresponding background-only p-value is given by

$$1 - p_b = \int_{t_{r,obs}}^{\infty} f(t'_r|0, \boldsymbol{\theta}) dt'_r, \quad (5.16)$$

2186 If the  $t_r$  p.d.f. for both hypotheses are well separated, as shown in the top side  
 2187 of Figure 5.7, the experiment is sensitive to the presence of signal in the sample. If  
 2188 the signal presence is small, both p.d.f. will be largely overlapped (bottom of Figure  
 2189 ??) and either the signal hypothesis could be rejected with not enough justification  
 2190 because experiment is not sensitive to the signal or a fluctuation of the background  
 2191 could be misinterpreted as presence of signal with the corresponding rejection of  
 2192 the background-only hypothesis. These issues are corrected by using the modified  
 2193 p-value [136]

$$p'_r = \frac{p_r}{1 - p_b} \equiv CL_s. \quad (5.17)$$

2194 If  $H_1$  is true, then  $p_b$  is small,  $CL_s \simeq p_r$  and  $H_0$  is rejected; if there is large  
 2195 overlap and an statistical fluctuation cause that  $p_b$  is large, then both numerator and  
 2196 denominator in Eqn. 5.17 become small but  $CL_s$  would allow the rejection of  $H_1$

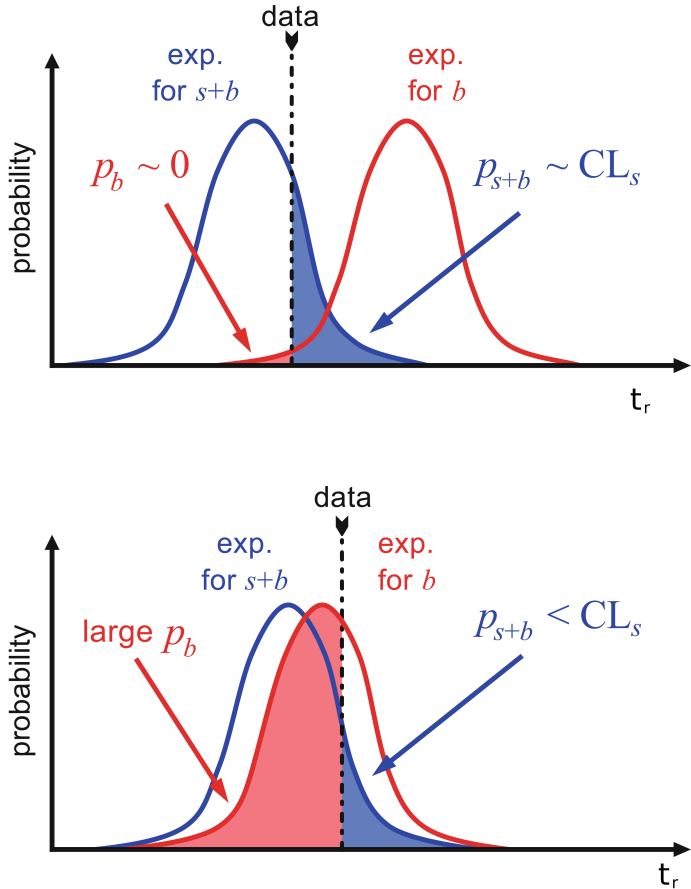


**Figure 5.7:**  $CL_s$  limit illustration. When the test statistic p.d.f. for the two hypotheses  $H_0$  and  $H_1$  are well separated (top) and when they are largely overlapped (bottom). Adapted from Reference [128].

2197 even if there is poor sensitivity to signal.

2198 The upper limit of the parameter of interest  $r^{up}$  is determined by excluding the  
 2199 range of values of  $r$  for which  $CL_s(r, \theta)$  is lower than the confidence level desired,  
 2200 normally 90% or 95%, e.g., scanning over  $r$  and finding the value for which  $p_r'^{up} =$   
 2201 0.05. The expected upper limit can be calculated using pseudo-experiments based on  
 2202 the background-only hypothesis and obtaining a distribution for  $r_{ps}^{up}$ ; the median of  
 2203 that distribution corresponds to the expected upper limit, while the  $\pm 1\sigma$  and  $\pm 2\sigma$   
 2204 deviations correspond to the values of the distribution that defines the 68% and 95%

of the area under the distribution centered in the median. It is usual to present all the information about the expected and observed limits in the so-called *Brazilian-flag plot* as the one showed in Figure 5.8.

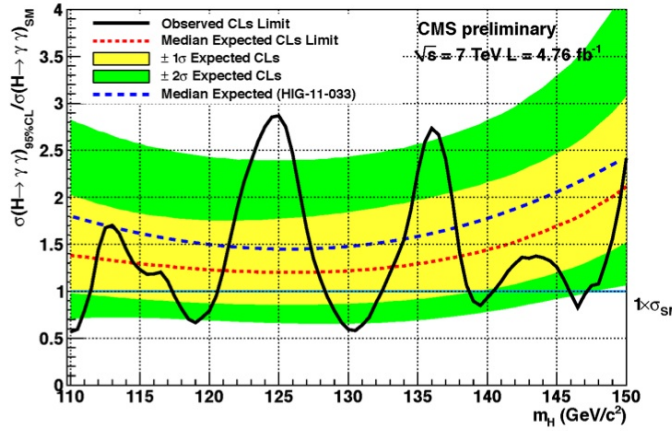


**Figure 5.8:** Brazilian flag plot of CMS experiment limits for Higgs boson decaying to photons [137].

## 5.4 Asymptotic limits

As said before, the complexity of the likelihood functions, the construction of test statistics, and the calculation of the limits and their uncertainties is not always manageable and requires extensive computational resources; in order to overcome those issues, asymptotic approximations for likelihood-based test statistics, like the ones described in previous sections, have been developed [138, 139] using Wilks' theorem. Asymptotic approximations replace the construction of the test statistics p.d.f.s using MC pseudo-experiments, with the approximate calculation of the test statistics p.d.f.s by employing the so-called *Asimov dataset*.

The Asimov dataset is defined as the dataset that produce the true values of the nuisance parameters when it is used to evaluate the estimators for all the parameters;

2219 it is obtained by setting the values of the variables in the dataset to their expected  
2220 values [139].

2221 Limits calculated by using the asymptotic approximation and the Asimov dataset  
2222 are known as *asymptotic limits*.

2223 **Chapter 6**

2224 **Search for production of a Higgs**

2225 **boson and a single top quark in**

2226 **multilepton final states in pp**

2227 **collisions at  $\sqrt{s} = 13$  TeV**

2228 **6.1 Introduction**

2229 The Higgs boson discovery, supported on experimental observations and theoretical  
2230 predictions made about the SM, gives the clue of the way in that elementary particles  
2231 acquire mass through the Higgs mechanism; therefore, knowing the Higgs mass, the  
2232 Higgs-vector boson and Higgs-fermion couplings can be determined. In order to test  
2233 the Higgs-top coupling, several measurements have been performed, as stated in the  
2234 chapter 1, but they are limited in sensitivity to measure the square of the coupling;  
2235 the production of a Higgs boson in association with a single top quark ( $tH$ ) not  
2236 only offers access to the sign of the coupling, but also, to the CP phase of the Higgs

2237 couplings.

2238 This chapter presents the search for the associated production of a Higgs boson  
 2239 and a single top quark events, focusing on leptonic signatures provided by the Higgs  
 2240 decay modes to  $WW$ ,  $ZZ$ , and  $\tau\tau$ ; the 13 TeV dataset produced in 2016, which  
 2241 corresponds to an integrated luminosity of  $35.9\text{fb}^{-1}$ , is used.

2242 As shown in section 1.5, the SM cross section of the associated production of  
 2243 a Higgs boson and a single top quark ( $tHq$ ) process is driven by a destructive in-  
 2244 terference between two contributions (see Figure 1.15), where the Higgs couples to  
 2245 either the W boson or the top quark; however, if the sign of the Higgs-top coupling  
 2246 is flipped with respect to the SM prediction, a large enhancement of the cross section  
 2247 occurs, making this analysis sensitive to such deviation. A second process, where the  
 2248 Higgs boson and top quark are accompanied by a W boson ( $tHW$ ) has similar be-  
 2249 havior, albeit with a weaker interference pattern and lower contribution to the cross  
 2250 section, therefore, a combination of both processes would increase the sensitivity; in  
 2251 this analysis both contributions are combined and referred as  $tH$ channel. A third  
 2252 contribution comes from  $t\bar{t}H$  process. The purpose of this analysis is to investigate  
 2253 the exclusion of the presence of the  $tH + t\bar{t}H$  processes under the assumption of the  
 2254 anomalous Higgs-top coupling modifier ( $\kappa_t = -1$ ). The analysis exploits signatures  
 2255 with two leptons of the same sign (*2lss channel*) and three leptons (*3l channel*) in  
 2256 the final state.

2257 Constraints on the sign of the Higgs-top coupling ( $y_t$ ) have been derived from the  
 2258 decay rate of Higgs boson to photon pairs [50] and from the cross section for associated  
 2259 production of Higgs and Z bosons via gluon fusion [141], with recent results disfavoring  
 2260 negative signs of the coupling [44, 59, 142], although the negative sign coupling have  
 2261 not been completely excluded.

2262 The analysis presented here, expands previous analyses performed at 8 TeV [143,

2263 144] and searches for associated production of  $t\bar{t}$  pair and a Higgs boson in the multi-  
 2264 lepton final state channel [145]; it also complements searches in other decay channels  
 2265 targeting  $H \rightarrow b\bar{b}$  [146].

2266 The first sections present the characteristic  $tHq$  signature as well as the expected  
 2267 backgrounds. The MC samples, data sets, and the physics object definitions are  
 2268 then defined. Following, the background predictions, the signal extraction, and the  
 2269 statistical treatment of the selected events as well as the systematic uncertainties are  
 2270 described. The final section present the results for the exclusion limits as a function  
 2271 of the ratio of  $\kappa_t$  and the dimensionless modifier of the Higgs-vector boson coupling  
 2272  $\kappa_V$ .

## 2273 **6.2 $tHq$ signature**

2274 In order to select events of  $tHq$  process, its features are translated into a set of  
 2275 selection rules; figure 6.1 shows the Feynman diagram and an schematic view of the  
 2276  $tHq$  process from the  $pp$  collision to the final state configuration. A single top quark  
 2277 is produced accompanied by a light quark, denoted as  $q$ ; this light quark is produced  
 2278 predominantly in the forward region of the detector. The Higgs boson which can  
 2279 be either emitted by the exchanged W boson or directly by the singly produced top  
 2280 quark.

2281 The top quark and Higgs boson decay after their production in the detector due to  
 2282 their high masses/low lifetimes. The Higgs boson is required to decay into a W boson  
 2283 pair<sup>1</sup>. The top quark almost always decays into a bottom quark and a W boson, as  
 2284 encoded in the CMK matrix. The W bosons are required to decay hadronically in  
 2285 the 2lss channel case and leptonically in the 3l channel case, while  $\tau$  leptons are not

---

<sup>1</sup> ZZ and  $\tau\tau$  decays are also include in the analysis but they are not separately reconstructed

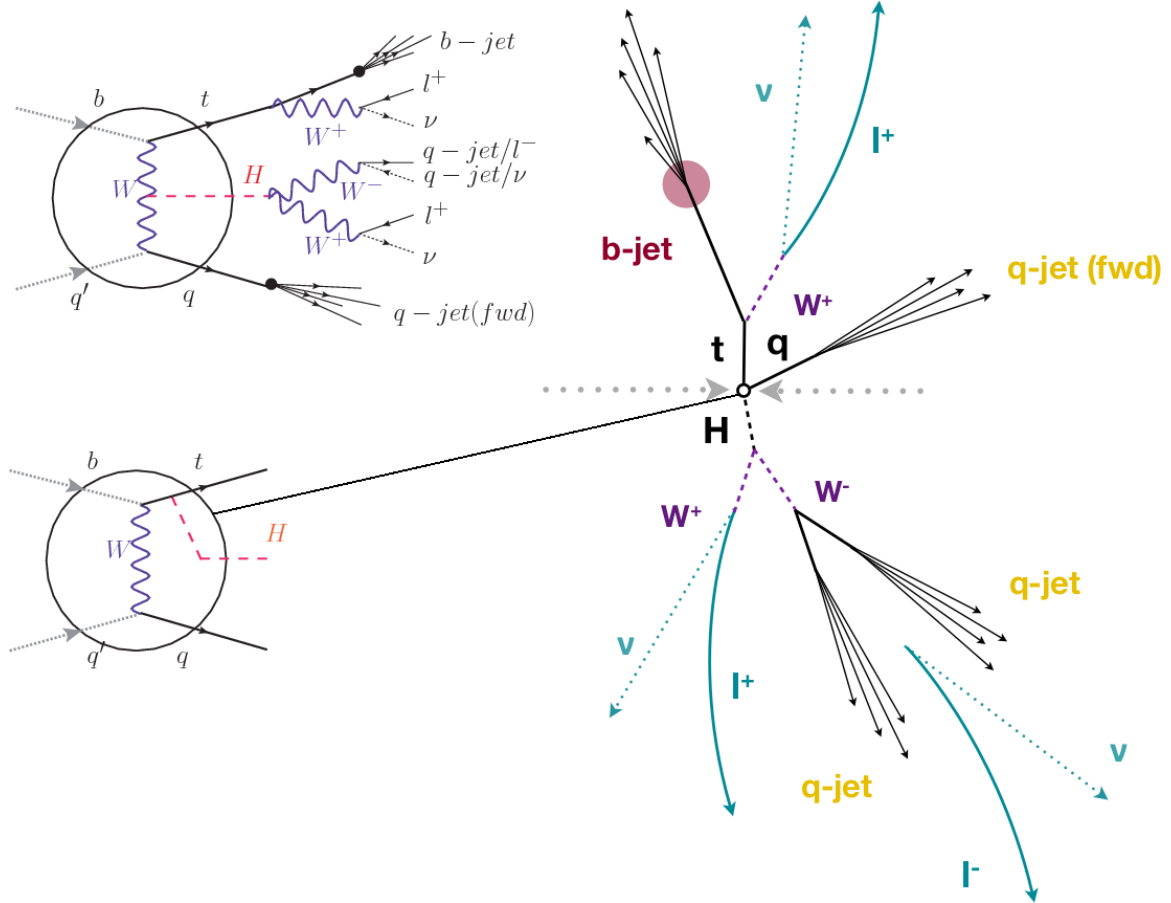


**Figure 6.1:**  $tHq$  event signature. Left: Feynman diagram including the whole evolution up to the final state for the case of the Higgs boson emitted by the  $W$  boson (top); Feynman diagram for the case where the Higgs boson is emitted by the top quark. Right: Schematic view as it would be seen in the detector; the circle in the Feynman diagrams on the left corresponds to the circle in the center of the schematic view as indicated by the line connecting them. In the 2lss channel, one of the  $W$  bosons from the Higgs boson decays to two light-quark jets while in the 3l channel both  $W$  bosons decays to leptons.

2286 reconstructed separately and only their leptonic decays into either electrons or muons  
 2287 are considered in this analysis.

2288 In summary, the signal process is characterized by a the final state with

- 2289 • one light-flavored forward jet,
- 2290 • one central b-jet,

- 2291     • 2lss channel → two leptons of the same sign, two neutrinos and two light (often  
 2292               soft) jets,
- 2293     • 3l channel → three leptons, three neutrinos and no central light-flavored jets,
- 2294     The presence of neutrinos is inferred from the presence of MET. The analysis has  
 2295     been made public by CMS as a Physics Analysis Summary [147] combining the result  
 2296     for the three lepton and two lepton same-sign channels. Currently, an effort to turn  
 2297     the analysis into a paper is ongoing.

2298 **6.3 Background processes**

2299 The background processes are those that can mimic the signal signature or at least  
 2300 can be reconstructed as that as a result of certain circumstances. The backgrounds  
 2301 can be classified as

- 2302     • Irreducible backgrounds where genuine prompt leptons are produced in on-  
 2303               shell W and Z boson decays; they can be reliably estimated directly from MC  
 2304               simulated events, using higher-order cross sections or data control regions for  
 2305               the overall normalization.
- 2306     • Reducible backgrounds where at least one of the leptons is *non-prompt*, i.e., pro-  
 2307               duced within a hadronic jet, either a genuine lepton from heavy flavor decays.  
 2308               misreconstructed jets, also known as *mis-ID leptons* or *fake leptons*, are consid-  
 2309               ered non-prompt leptons as well. These non-prompt leptons leave tracks and  
 2310               hits in the detection systems as would a prompt lepton, but correlating those  
 2311               hits with nearby jets could be a way of removing them. Reducible backgrounds  
 2312               are not well predicted by simulation, and are estimated using data-driven meth-  
 2313               ods.

2314 The main sources of background events in the case of  $tHq$  process are  $t\bar{t}$  process  
 2315 and  $t\bar{t} + X(X = W, Z, \gamma)$  processes, here represented together as  $t\bar{t}V$  process. Figure  
 2316 6.2 shows the signature for  $t\bar{t}$  and  $t\bar{t}W$  processes;

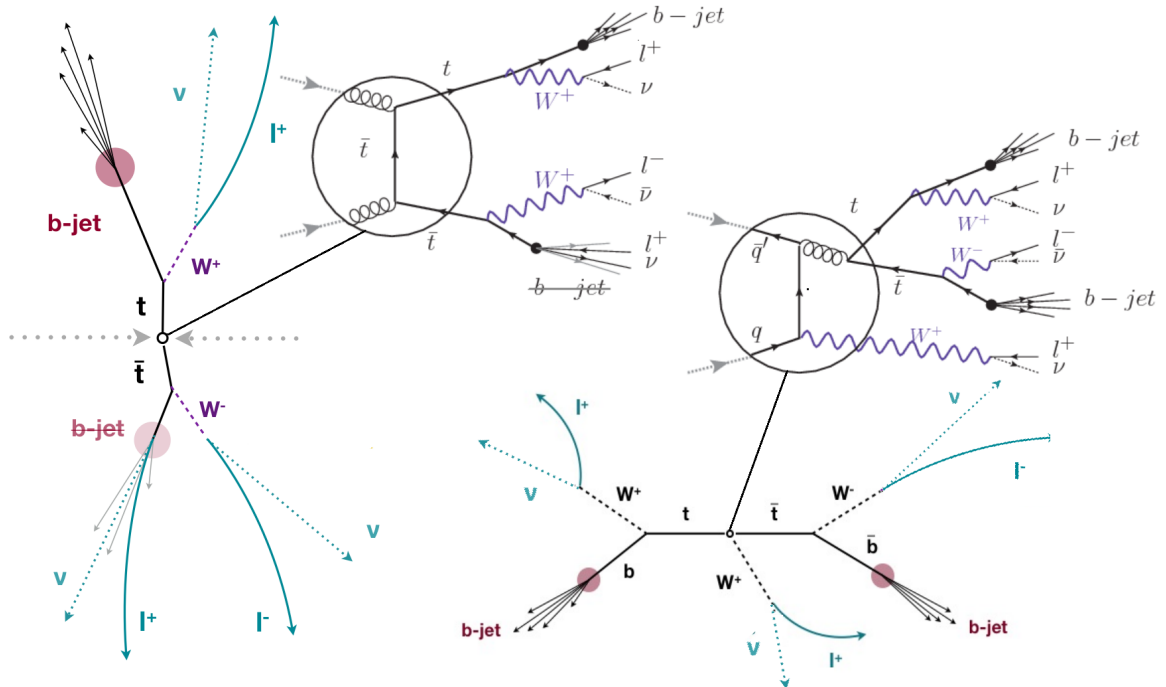


**Figure 6.2:**  $t\bar{t}$  (left) and  $t\bar{t}W$  (right) events signature as they would be seen in the detector; the Feynman diagrams including the whole evolution up to the final state are also showed. The  $t\bar{t}$  process signature is very similar to that of the signal process with one fake lepton and non forward activity. The  $t\bar{t}W$  process present a higher b-jet multiplicity compared to the signal process, a prompt lepton and no forward activity.

2317 The largest contribution to irreducible backgrounds involving prompt leptons  
 2318 comes from  $t\bar{t}W$ ,  $t\bar{t}Z$ , processes for which the number of ( $b-$ )jets (( $b-$ )jet multiplicity)  
 2319 is higher than that of the signal events, while for other contributing background  
 2320 events,  $WZ$ ,  $ZZ$ , and rare SM processes like  $W^\pm W^\pm qq$ ,  $t\bar{t}t\bar{t}$ ,  $tZq$ ,  $tZW$ ,  $WWW$ ,  
 2321  $WWZ$ ,  $WZZ$ ,  $ZZZ$ , the ( $b-$ )jet multiplicity is lower compared to that of the signal  
 2322 events. None of the irreducible backgrounds present activity in the forward region of  
 2323 the detector.

2324 On the side of the reducible backgrounds, the largest contribution comes from the

2325  $t\bar{t}$  events which have a very similar signature to the signal events but does no present  
 2326 activity in the forward region of the detector either; A particular feature of the  $t\bar{t}$   
 2327 events is their charge-symmetry which is also a difference with the signal events.

2328       The charge misidentification plays an important role in the the 2lss channel since  
 2329 leptons in processes like  $t\bar{t} + \text{jets}$  or  $Z + \text{jets}$  can be charge misidentified, leading to  
 2330 backgrounds increments. An identification variable have been designed in order to  
 2331 reject this type of background events.

## 2332 **6.4 Data and MC Samples**

2333 Technical developments on the event generator side allow for an event-wise reweight-  
 2334 ing that can change the event kinematics based on specific generation parameters.  
 2335 This way not only the case of  $\kappa_t = -1$ , but a whole range of  $\kappa_t$  and  $\kappa_V$  values can be  
 2336 investigated.

2337       The data considered in this analysis were collected by the CMS experiment dur-  
 2338 ing 2016 and correspond to a total integrated luminosity of  $35.9 fb^{-1}$ . Only periods  
 2339 when the CMS magnet was on were considered when selecting the data samples, that  
 2340 corresponds to the 23 Sep 2016 (Run B to G) and PromptReco (Run H) versions  
 2341 of the datasets. The MC samples used in this analysis correspond to the RunI-  
 2342 ISummer16MiniAODv2 campaign produced with CMSSW 80X. The two signal sam-  
 2343 ples (for  $tHq$  and  $tHW$ ) were produced with MG5\_aMC@NLO (version 5.222), in  
 2344 leading-order order mode, and are normalized to next-to-leading-order cross sections,  
 2345 see Tab. 6.1. Each sample is generated with a set of event weights corresponding to  
 2346 different values of  $\kappa_t$  and  $\kappa_V$  couplings as shown in Tab. 6.2.

Sample	$\sigma$ [pb]	BF
/THQ_Hincl_13TeV-madgraph-pythia8_TuneCUETP8M1/	0.7927	0.324
/THW_Hincl_13TeV-madgraph-pythia8_TuneCUETP8M1/	0.1472	1.0

**Table 6.1:** Signal samples and their cross section and branching fraction used in this analysis. See Ref. [156] for more details.

### 2347 6.4.1 Full 2016 dataset and MC samples

2348 Different MC generators were used to generate the background processes. The dom-  
 2349 inant sources ( $t\bar{t}$ ,  $t\bar{t}W$ ,  $t\bar{t}Z$ ,  $t\bar{t}H$ ) were produced using AMC@NLO interfaced to  
 2350 PYTHIA8, and are scaled to NLO cross sections. Other processes are simulated us-  
 2351 ing POWHEG interfaced to PYTHIA, or bare PYTHIA (see table 6.3 and [145] for  
 2352 more details).

### 2353 6.4.2 Triggers

2354 We consider online-reconstructed events triggered by one, two, or three leptons.  
 2355 Single-lepton triggers are included to boost the acceptance of events where the  $p_T$  of  
 2356 the sub-leading lepton falls below the threshold of the double-lepton triggers. Ad-  
 2357 ditionally, by including double-lepton triggers in the  $\geq 3$  lepton category, as well  
 2358 as single-lepton triggers in all categories, we increase the efficiency, considering the  
 2359 logical “or” of the trigger decisions of all the individual triggers in a given category.  
 2360 Tab. 6.5 shows the lowest-threshold non-prescaled triggers present in the High-Level  
 2361 Trigger (HLT) menus for both Monte-Carlo and data in 2016.

### 2362 Trigger efficiency scale factors

2363 The efficiency of events to pass the trigger is measured in simulation (trivially using  
 2364 generator information) and in the data (using event collected by an uncorrelated  
 2365 MET trigger). Small differences between the data and MC efficiencies are corrected

		<i>tHq</i>		<i>tHW</i>		
$\kappa_V$	$\kappa_t$	sum of weights	cross section [pb]	sum of weights	cross section [pb]	LHE weights
1.0	-3.0	35.700022	2.991	11.030445	0.6409	LHEweight_wgt[446]
1.0	-2.0	20.124298	1.706	5.967205	0.3458	LHEweight_wgt[447]
1.0	-1.5	14.043198	1.205	4.029093	0.2353	LHEweight_wgt[448]
1.0	-1.25	11.429338	0.9869	3.208415	0.1876	LHEweight_wgt[449]
1.0	-1.0		0.7927		0.1472	
1.0	-0.75	7.054998	0.6212	1.863811	0.1102	LHEweight_wgt[450]
1.0	-0.5	5.294518	0.4723	1.339886	0.07979	LHEweight_wgt[451]
1.0	-0.25	3.818499	0.3505	0.914880	0.05518	LHEweight_wgt[452]
1.0	0.0	2.627360	0.2482	0.588902	0.03881	LHEweight_wgt[453]
1.0	0.25	1.719841	0.1694	0.361621	0.02226	LHEweight_wgt[454]
1.0	0.5	1.097202	0.1133	0.233368	0.01444	LHEweight_wgt[455]
1.0	0.75	0.759024	0.08059	0.204034	0.01222	LHEweight_wgt[456]
1.0	1.0	0.705305	0.07096	0.273617	0.01561	LHEweight_wgt[457]
1.0	1.25	0.936047	0.0839	0.442119	0.02481	LHEweight_wgt[458]
1.0	1.5	1.451249	0.1199	0.709538	0.03935	LHEweight_wgt[459]
1.0	2.0	3.335034	0.2602	1.541132	0.08605	LHEweight_wgt[460]
1.0	3.0	10.516125	0.8210	4.391335	0.2465	LHEweight_wgt[461]
1.5	-3.0	45.281492	3.845	13.426212	0.7825	LHEweight_wgt[462]
1.5	-2.0	27.606715	2.371	7.809713	0.4574	LHEweight_wgt[463]
1.5	-1.5	20.476088	1.784	5.594971	0.3290	LHEweight_wgt[464]
1.5	-1.25	17.337465	1.518	4.635978	0.2749	LHEweight_wgt[465]
1.5	-1.0	14.483302	1.287	3.775902	0.2244	LHEweight_wgt[466]
1.5	-0.75	11.913599	1.067	3.014744	0.1799	LHEweight_wgt[467]
1.5	-0.5	9.628357	0.874	2.352505	0.1410	LHEweight_wgt[468]
1.5	-0.25	7.627574	0.702	1.789184	0.1081	LHEweight_wgt[469]
1.5	0.0	5.911882	0.5577	1.324946	0.08056	LHEweight_wgt[470]
1.5	0.25	4.479390	0.4365	0.959295	0.05893	LHEweight_wgt[471]
1.5	0.5	3.331988	0.3343	0.692727	0.04277	LHEweight_wgt[472]
1.5	0.75	2.469046	0.2558	0.525078	0.03263	LHEweight_wgt[473]
1.5	1.0	1.890565	0.2003	0.456347	0.02768	LHEweight_wgt[474]
1.5	1.25	1.596544	0.1689	0.486534	0.02864	LHEweight_wgt[475]
1.5	1.5	1.586983	0.1594	0.615638	0.03509	LHEweight_wgt[476]
1.5	2.0	2.421241	0.2105	1.170602	0.06515	LHEweight_wgt[477]
1.5	3.0	7.503280	0.5889	3.467546	0.1930	LHEweight_wgt[478]
0.5	-3.0	27.432685	2.260	8.929074	0.5136	LHEweight_wgt[479]
0.5	-2.0	13.956013	1.160	4.419093	0.2547	LHEweight_wgt[480]
0.5	-1.5	8.924438	0.7478	2.757611	0.1591	LHEweight_wgt[481]
0.5	-1.25	6.835341	0.5726	2.075247	0.1204	LHEweight_wgt[482]
0.5	-1.0	5.030704	0.4273	1.491801	0.08696	LHEweight_wgt[483]
0.5	-0.75	3.510528	0.2999	1.007273	0.05885	LHEweight_wgt[484]
0.5	-0.5	2.274811	0.1982	0.621663	0.03658	LHEweight_wgt[485]
0.5	-0.25	1.323555	0.1189	0.334972	0.01996	LHEweight_wgt[486]
0.5	0.0	0.656969	0.06223	0.147253	0.008986	LHEweight_wgt[487]
0.5	0.25	0.274423	0.02830	0.058342	0.003608	LHEweight_wgt[488]
0.5	0.5	0.176548	0.01778	0.068404	0.003902	LHEweight_wgt[489]
0.5	0.75	0.363132	0.03008	0.177385	0.009854	LHEweight_wgt[490]
0.5	1.0	0.834177	0.06550	0.385283	0.02145	LHEweight_wgt[491]
0.5	1.25	1.589682	0.1241	0.692099	0.03848	LHEweight_wgt[492]
0.5	1.5	2.629647	0.2047	1.097834	0.06136	LHEweight_wgt[493]
0.5	2.0	5.562958	0.4358	2.206057	0.1246	LHEweight_wgt[494]
0.5	3.0	14.843102	1.177	5.609519	0.3172	LHEweight_wgt[495]

**Table 6.2:**  $\kappa_V$  and  $\kappa_t$  combinations generated for the two signal samples and their NLO cross sections. The *tHq* cross section is multiplied by the branching fraction of the enforced leptonic decay of the top quark (0.324). See also Ref. [156].

Sample	$\sigma$ [pb]
TTWJetsToLNu_TuneCUETP8M1_13TeV-amcatnloFXFX-madspin-pythia8	0.2043
TTZToLLNuNu_M-10_TuneCUETP8M1_13TeV-amcatnlo-pythia8	0.2529
ttHJetToNonbb_M125_13TeV_amcatnloFXFX_madspin_pythia8_mWCutfix /store/cmst3/group/susy/gpetrucc/13TeV/u/TTLL_m1to10_LO_NoMS_for76X/	0.2151 0.0283
WGToLNuG_TuneCUETP8M1_13TeV-madgraphMLM-pythia8	585.8
ZGTo2LG_TuneCUETP8M1_13TeV-amcatnloFXFX-pythia8	131.3
TGJets_TuneCUETP8M1_13TeV_amcatnlo_madspin_pythia8	2.967
TGJets_TuneCUETP8M1_13TeV_amcatnlo_madspin_pythia8	2.967
TTGJets_TuneCUETP8M1_13TeV-amcatnloFXFX-madspin-pythia8	3.697
WpWpJJ_EWK-QCD_TuneCUETP8M1_13TeV-madgraph-pythia8	0.03711
ZZZ_TuneCUETP8M1_13TeV-amcatnlo-pythia8	0.01398
WWZ_TuneCUETP8M1_13TeV-amcatnlo-pythia8	0.1651
WZZ_TuneCUETP8M1_13TeV-amcatnlo-pythia8	0.05565
WW_DoubleScattering_13TeV-pythia8	1.64
tZq_ll_4f_13TeV-amcatnlo-pythia8_TuneCUETP8M1	0.0758
ST_tWll_5f_LO_13TeV-MadGraph-pythia8	0.01123
TTTT_TuneCUETP8M1_13TeV-amcatnlo-pythia8	0.009103
WZTo3LNu_TuneCUETP8M1_13TeV-powheg-pythia8	4.4296
ZZTo4L_13TeV_powheg_pythia8	1.256
TTJets_SingleLeptFromTbar_TuneCUETP8M1_13TeV-madgraphMLM-pythia8	182.1754
TTJets_SingleLeptFromT_TuneCUETP8M1_13TeV-madgraphMLM-pythia8	182.1754
TTJets_DiLept_TuneCUETP8M1_13TeV-madgraphMLM-pythia8	87.3
DYJetsToLL_M-10to50_TuneCUETP8M1_13TeV-amcatnloFXFX-pythia8	18610
DYJetsToLL_M-50_TuneCUETP8M1_13TeV-madgraphMLM-pythia8	6024
WJetsToLNu_TuneCUETP8M1_13TeV-amcatnloFXFX-pythia8	61526.7
ST_tW_top_5f_inclusiveDecays_13TeV-powheg-pythia8_TuneCUETP8M1	35.6
ST_tW_antitop_5f_inclusiveDecays_13TeV-powheg-pythia8_TuneCUETP8M1	35.6
ST_t-channel_4f_leptonDecays_13TeV-amcatnlo-pythia8_TuneCUETP8M1	70.3144
ST_t-channel_antitop_4f_leptonDecays_13TeV-powheg-pythia8_TuneCUETP8M1	26.2278
ST_s-channel_4f_leptonDecays_13TeV-amcatnlo-pythia8_TuneCUETP8M1	3.68064
WWTo2L2Nu_13TeV-powheg	10.481

**Table 6.3:** List of background samples used in this analysis (CMSSW 80X). In the first section of the table are listed the samples of the processes for which we use the simulation to extract the final yields and shapes, in the second section the samples of the processes we will estimate from data. The MC simulation is used to design the data driven methods and derive the associated systematics.

Sample	$\sigma$ [pb]
ttWJets_13TeV_madgraphMLM	0.6105
ttZJets_13TeV_madgraphMLM	0.5297/0.692

**Table 6.4:** Leading-order  $t\bar{t}W$  and  $t\bar{t}Z$  samples used in the signal BDT training.

Same-sign dilepton (==2 muons)
HLT_Mu17_TrkIsoVVL_Mu8_TrkIsoVVL_DZ_v*
HLT_Mu17_TrkIsoVVL_TkMu8_TrkIsoVVL_DZ_v*
HLT_IsoMu22_v*
HLT_IsoTkMu22_v*
HLT_IsoMu22_eta2p1_v*
HLT_IsoTkMu22_eta2p1_v*
HLT_IsoMu24_v*
HLT_IsoTkMu24_v*
Same-sign dilepton (==2 electrons)
HLT_Ele23_Ele12_CaloIdL_TrackIdL_IsoVL_DZ_v*
HLT_Ele27_eta2p1_WP Loose_Gsf_v*
HLT_Ele27_WPTight_Gsf_v*
HLT_Ele25_eta2p1_WPTight_Gsf_v*
Same-sign dilepton (==1 muon, ==1 electron)
HLT_Mu23_TrkIsoVVL_Ele8_CaloIdL_TrackIdL_IsoVL_v*
HLT_Mu8_TrkIsoVVL_Ele23_CaloIdL_TrackIdL_IsoVL_v*
HLT_Mu23_TrkIsoVVL_Ele8_CaloIdL_TrackIdL_IsoVL_DZ_v*
HLT_Mu8_TrkIsoVVL_Ele23_CaloIdL_TrackIdL_IsoVL_DZ_v*
HLT_IsoMu22_v*
HLT_IsoTkMu22_v*
HLT_IsoMu22_eta2p1_v*
HLT_IsoTkMu22_eta2p1_v*
HLT_IsoMu24_v*
HLT_IsoTkMu24_v*
HLT_Ele27_WPTight_Gsf_v*
HLT_Ele25_eta2p1_WPTight_Gsf_v*
HLT_Ele27_eta2p1_WP Loose_Gsf_v*
Three lepton and Four lepton
HLT_DiMu9_Ele9_CaloIdL_TrackIdL_v*
HLT_Mu8_DiEle12_CaloIdL_TrackIdL_v*
HLT_TripleMu_12_10_5_v*
HLT_Ele16_Ele12_Ele8_CaloIdL_TrackIdL_v*
HLT_Mu23_TrkIsoVVL_Ele8_CaloIdL_TrackIdL_IsoVL_v*
HLT_Mu23_TrkIsoVVL_Ele8_CaloIdL_TrackIdL_IsoVL_DZ_v*
HLT_Mu8_TrkIsoVVL_Ele23_CaloIdL_TrackIdL_IsoVL_v*
HLT_Mu8_TrkIsoVVL_Ele23_CaloIdL_TrackIdL_IsoVL_DZ_v*
HLT_Ele23_Ele12_CaloIdL_TrackIdL_IsoVL_DZ_v*
HLT_Mu17_TrkIsoVVL_Mu8_TrkIsoVVL_DZ_v*
HLT_Mu17_TrkIsoVVL_TkMu8_TrkIsoVVL_DZ_v*
HLT_IsoMu22_v*
HLT_IsoTkMu22_v*
HLT_IsoMu22_eta2p1_v*
HLT_IsoTkMu22_eta2p1_v*
HLT_IsoMu24_v*
HLT_IsoTkMu24_v*
HLT_Ele27_WPTight_Gsf_v*
HLT_Ele25_eta2p1_WPTight_Gsf_v*
HLT_Ele27_eta2p1_WP Loose_Gsf_v*

**Table 6.5:** Table of high-level triggers that we consider in the analysis.

Category	Scale Factor
ee	$1.01 \pm 0.02$
e $\mu$	$1.01 \pm 0.01$
$\mu\mu$	$1.00 \pm 0.01$
3l	$1.00 \pm 0.03$

**Table 6.6:** Trigger efficiency scale factors and associated uncertainties, shown here rounded to the nearest percent.

2366 by applying scale factors as shown in Tab. 6.6. The exact procedure and control plots  
 2367 are documented in [150] for the current analysis.

## 2368 6.5 Object Identification

2369 In this section, the specific definitions of the physical objects in terms of the numerical  
 2370 values assigned to the reconstruction parameters are presented; thus, the provided  
 2371 details summarize and complement the descriptions presented in previous chapters.  
 2372 The object reconstruction and selection strategy used in this thesis is inherited from  
 2373 the analyses in references [145, 150], thus, the information provided in this section is  
 2374 extracted from those documents unless other references are stated.

### 2375 6.5.1 Jets and $b$ -jet tagging.

2376 In this analysis, jets are reconstructed by clustering PF candidates using the anti- $k_t$   
 2377 algorithm with parameter distance  $\Delta R = 0.4$ ; those charged hadrons that are not  
 2378 consistent with the selected primary vertex are discarded from the clustering. The  
 2379 jet energy is then corrected for the varying response of the detector as a function  
 2380 of transverse momentum  $p_T$  and pseudorapidity  $\eta$ . Jets are selected for use in the  
 2381 analysis only if they have  $p_T > 25$  GeV and are separated from any selected leptons  
 2382 by  $\Delta R > 0.4$ .

2383        Jets coming from the primary vertex and jets coming from pile-up vertices are  
 2384        distinguished using a MVA discriminator based on the differences in the jet shapes,  
 2385        in the relative multiplicity of charged and neutral components, and in the different  
 2386        fraction of transverse momentum which is carried by the hardest components. Jet  
 2387        tracks are also required to be compatible with the primary vertex.

2388        Jets originated from the hadronization of a  $b$  quark are selected using a MVA  
 2389        likelihood discriminant which uses track-based lifetime information and reconstructed  
 2390        secondary vertices (CSV algorithm). Only jets within the CMS tracker acceptance  
 2391        ( $\eta < 2.4$ ) are identified with this tool. Data samples are used to measure the efficiency  
 2392        of the  $b$ -jet tagging and the probability to misidentify jets from light quarks or gluons;  
 2393        in both cases the measurements are parametrized as a function of the jet  $p_T$  and  $\eta$   
 2394        and later used to correct differences between the data and MC simulation in the  $b$   
 2395        tagging performance, by applying per-jet weights to the simulation, dependent on  
 2396        the jet  $p_T$ ,  $\eta$ ,  $b$  tagging discriminator, and flavor (from simulation truth) [148]. The  
 2397        per-event weight is taken as the product of the per-jet weights, including those of the  
 2398        jets associated to the leptons. The weights are derived on  $t\bar{t}$  and Z+jets events.

2399        Two working points are defined, based on the CSV algorithm output: *loose*' work-  
 2400        ing point (CSV>0.46) with a  $b$  signal tagging efficiency of about 83% and a mistagging  
 2401        rate of about 8%; and *medium* working point (CSV>0.80) with  $b$ -tagging efficiency of  
 2402        about 69% and mistagging rate of order 1% [149]. Tagging of jets from charm quarks  
 2403        have efficiencies of about 40% and 18% for loose and medium working points re-  
 2404        spectively. Separate scale factors are applied to jets originating from bottom/charm  
 2405        quarks and from light quarks in simulated events to match the tagging efficiencies  
 2406        measured in the data.

2407 **6.5.2 Missing Energy MET.**

2408 As stated in section 3.4.1.1, the MET vector is calculated as the negative of the vector  
 2409 sum of transverse momenta of all PF candidates in the event and its magnitude is  
 2410 referred to as  $E_T^{miss}$ . Due to pile-up interactions, the performance in determining  
 2411 MET is degraded; in order to correct for that, the energy from the selected jets and  
 2412 leptons that compose the event is assigned to the variable  $H_T^{miss}$ . It is calculated in  
 2413 the same way as  $E_T^{miss}$  and although it has worse resolution than  $E_T^{miss}$ , it is more  
 2414 robust in the sense that it does not rely on the soft part of the event. The event  
 2415 selection uses a linear discriminator based on the two variables given by

$$E_T^{miss} LD = 0.00397 * E_T^{miss} + 0.00265 * H_T^{miss} \quad (6.1)$$

2416 taking advantage of the fact that the correlation between  $E_T^{miss}$  and  $H_T^{miss}$  is less  
 2417 for events with instrumental missing energy than for events with real missing energy.  
 2418 The working point  $E_T^{miss} LD > 0.2$  was chosen to ensure a good signal efficiency while  
 2419 keeping a good background rejection.

2420 **6.5.3 Lepton reconstruction and identification**

2421 Two types of leptons are defined in this analysis: *signal leptons* are those coming from  
 2422  $W, Z$  and  $\tau$  decays which usually are isolated from other particles; *background leptons*  
 2423 are defined as leptons produced in  $b$ -jet hadron decays, light-jets misidentification,  
 2424 and photon conversions.

2425 The process of reconstruction and identification of electron and muon candidates  
 2426 was described in chapter3, hence, the identification variables used in order to retain  
 2427 the highest possible efficiency for signal leptons while maximizing the rejection of

2428 background leptons are listed and described in the following sections <sup>2</sup>.

2429 The identification variables include not only observables related directly to the re-  
 2430 constructed leptons themselves, but also to the clustered energy deposits and charged  
 2431 particles in a cone around the lepton direction (jet-related variables); an initial loose  
 2432 preselection of leptons candidates is performed and then an MVA discriminator, re-  
 2433 ferred to as *lepton MVA* discriminator, is used to distinguish signal leptons from  
 2434 background leptons.

2435 **Muons.**

2436 The Physics Objects Groups (POG) at CMS, are in charge of studying and defining  
 2437 the set of selection criteria applied on the course of reconstruction and identification  
 2438 of particles. These selection criteria are implemented in the CMS framework in the  
 2439 form of several object identification working points according to the strength of the  
 2440 requirements.

2441 The muon candidates are reconstructed by combining information from the tracker  
 2442 system and the muon detection system of CMS detector and the POG defined three  
 2443 working points for muon identification *MuonID* [151];

- 2444 • *POG Loose Muon ID* is a particle identified as a muon by the PF event re-  
 2445 construction and also reconstructed either as a global-muon or as an arbitrated  
 2446 tracker-muon. This identification criteria is designed to be highly efficient for  
 2447 prompt muons and for muons from heavy and light quark decays; it can be com-  
 2448 plemented by applying impact parameter cuts in analyses with prompt muon  
 2449 signals.

---

<sup>2</sup> the studies performed to optimize the identification are far from the scope of this thesis, therefore, only general descriptions are provided

- 2450     • *POG Medium Muon ID* is a Loose muon with additional track-quality and  
 2451       muon-quality (spatial matching between the individual measurements in the  
 2452       tracker and the muon system) requirements. This identification criteria is de-  
 2453       signed to be highly efficient in the separation of the muons coming from decay  
 2454       in flight of heavy quarks and muons coming from B meson decays as well as  
 2455       prompt muons. An additional category *MVA Prompt ID* is defined in this iden-  
 2456       tification criteria directed to discriminated muons from B mesons and prompt  
 2457       muons (from W,Z and  $\tau$  decays). The Medium ID provides the same fake rate as  
 2458       the Tight Muon ID but a higher efficiency on prompt and B-decays muons. [152]
- 2459     • *POG Tight Muon ID* is a global muon with additional muon-quality require-  
 2460       ments Tight Muon ID selects a subset of the PF muons.

2461       Only muons within the muon system acceptance  $|\eta| < 2.4$  and minimum  $p_T$  of 5  
 2462       GeV are considered.

### 2463     **Electrons.**

2464       Electrons are reconstructed using information from the tracker and from the electro-  
 2465       magnetic calorimeter and identified by an MVA algorithm (*MVA eID* discriminant)  
 2466       using the shape of the calorimetric shower variables like the shape in  $\eta$  and  $\phi$ , the clus-  
 2467       ter circularity, widths along  $\eta$  and  $\phi$ ; track-cluster matching variables like  $E_{tot}/p_{in}$ ,  
 2468        $E_{Ele}/p_{out}$ ,  $\Delta\eta_{in}$ ,  $\Delta\eta_{out}$ ,  $\Delta\phi_{in}$ ,  $1/E - 1/p$ ; and track quality variables like  $\xi^2$  of the  
 2469       GSF tracks, the number of hits used by the GSF filter [153].

2470       A loose selection based on  $\eta$ -dependent cuts on this discriminant is used to prese-  
 2471       lect electron candidates, the full shape of the discriminant is used in the lepton MVA  
 2472       selection to separate signal leptons from background leptons (described in section  
 2473       6.5.3).

2474 In order to reject electrons from photon conversions, electron candidates with  
 2475 missing hits in the pixel tracker layers or matched to a conversion secondary vertex  
 2476 are discarded. Electrons are selected for the analysis if they have  $p_T > 7$  GeV and  
 2477 are located within the tracker system acceptance region ( $|\eta| < 2.5$ ).

2478 **Lepton vertexing and pile-up rejection.**

2479 The impact parameter in the transverse plane  $d_0$ , impact parameter along the z  
 2480 axis  $d_z$ , and the impact parameter significance in the detector space  $SIP_{3D}$ , are  
 2481 considered to perform the identification and rejection of pile-up, misreconstructed  
 2482 tracks, and background leptons from b-hadron decays; pile-up and misreconstructed  
 2483 track mitigation is achieved by imposing loose cuts on the impact parameter variables.  
 2484 The full shape of those variables is used in a lepton MVA classifier to achieve the  
 2485 best separation between the signal and the background leptons.

2486 **Lepton isolation.**

2487 PF is able to recognize leptons from two different sources: on one side, leptons from  
 2488 the decays of heavy particles, such as W and Z bosons, which are normally isolated  
 2489 in space from the hadronic activity in the event; on the other side, leptons from the  
 2490 decays of hadrons and jets misidentified as leptons, which are not isolated as the  
 2491 former. For highly boosted systems, like the lepton and the  $b$ -jet generated in the  
 2492 semileptonic decay of a boosted top, the decay products tend to be more closer and  
 2493 sometimes they even overlap; thus, the PF standard definition of isolation in terms of  
 2494 the separation between the lepton candidates and other PF objects in the  $\eta$ - $\phi$  plane,

$$\Delta R = \sqrt{(\eta^l - \eta^i)^2 + (\phi^l - \phi^i)^2} < 0.3 \quad (6.2)$$

which considers all the neutral, charged hadrons and photons in a cone around the leptons, is refocused to the local isolation of the leptons through the mini-isolation  $I_{mini}$  [154] defined as the sum of particle flow candidates  $p_T$  within a cone around the lepton, corrected for the effects of pileup and divided by the lepton  $p_T$

$$I_{mini} = \frac{\sum_R p_T(h^\pm) - \max\left(0, \sum_R p_T(h^0) + p_T(\gamma) - \rho \mathcal{A}\left(\frac{R}{0.3}\right)^2\right)}{p_T(l)} \quad (6.3)$$

where  $\rho$  is the pileup energy density,  $h^\pm, h^0, \gamma, l$ , represent the charged hadron, neutral hadrons, photons, and the lepton, respectively. The radius  $R$  of the cone depends on the  $p_T$  of the lepton according to

$$R = \frac{10\text{GeV}}{\min(\max(p_T(l), 50\text{GeV}), 200\text{GeV})}, \quad (6.4)$$

The  $p_T$  dependence of the cone size allows for greater signal efficiency. Setting a cut on  $I_{mini}$  below a given threshold ensures that the lepton is locally isolated, even in boosted systems. The effect of pileup is mitigated using the so-called effective area correction  $\mathcal{A}$  listed in Table 6.7.

$ \eta $ range	$\mathcal{A}(e)$ neutral/charged	$\mathcal{A}(\mu)$ neutral/charged
0.0 - 0.8	0.1607 / 0.0188	0.1322 / 0.0191
0.8 - 1.3	0.1579 / 0.0188	0.1137 / 0.0170
1.3 - 2.0	0.1120 / 0.0135	0.0883 / 0.0146
2.0 - 2.2	0.1228 / 0.0135	0.0865 / 0.0111
2.2 - 2.5	0.2156 / 0.0105	0.1214 / 0.0091

**Table 6.7:** Effective areas, for electrons and muons used to mitigate the effect of pileup by using the so-called effective area correction.

A loose cut on  $I_{mini}$  is applied to pre-select the muon and electron candidates; however, the full shape is used in the lepton MVA discriminator when performing the signal lepton selection.

2509 **Jet-related variables.**

2510 In order to reject misidentified leptons from  $b$ -jets, mostly coming from  $t\bar{t}$ +jets,  
 2511 Drell-Yan+jets, and W+jets events, the vertexing and isolation described in previous  
 2512 sections are complemented with additional variables related to the closest recon-  
 2513 structed jet to the lepton, i.e., the PF jets reconstructed<sup>3</sup> around the leptons with  
 2514  $\Delta R = \sqrt{(\eta^l - \eta^{jet})^2 + (\phi^l - \phi^{jet})^2} < 0.5$ . The identification variables used in the lep-  
 2515 ton MVA discriminator are the ratio  $p_T^l/p_T^{jet}$ , the CSV b-tagging discriminator value  
 2516 of the jet, the number of charged tracks of the jet, and the relative  $p_T$  given by

$$p_T^{rel} = \frac{(\vec{p}_{jet} - \vec{p}_l) \cdot \vec{p}_l}{\|\vec{p}_{jet} - \vec{p}_l\|}. \quad (6.5)$$

2517 **LeptonMVA discriminator.**

2518 Electrons and muons passing the basic selection process described above are referred  
 2519 to as *loose leptons*. Additional discrimination between signal leptons and background  
 2520 leptons is crucial considering that the rate of  $t\bar{t}$  production is much larger than the  
 2521 signal, hence, an overwhelming background from  $t\bar{t}$  production. To maximally ex-  
 2522 ploit the available information in each event to that end, the dedicated lepton MVA  
 2523 discriminator, based on a boosted decision tree (BDT) algorithm, has been built so  
 2524 that all the identification variables can be used together.

2525 The lepton MVA discriminator training is performed using simulated signal Loose  
 2526 leptons from the  $t\bar{t}H$  MC sample and fake leptons from the  $t\bar{t}$  +jets MC sample,  
 2527 separately for muons and electrons. The input variables used include vertexing, iso-  
 2528 lation and jet-related variables, the  $p_T$  and  $\eta$  of the lepton, the electron MVA eID  
 2529 discriminator and the muon segment-compatibility variables. An additional require-  
 2530 ment known as *tight-charge* requirement, is imposed by comparing two independent

---

<sup>3</sup> charged hadrons from PU vertices are not removed prior to the jet clustering.

measurement of the charge, one from the ECAL supercluster and the other from the tracker; thus, the consistency in the measurements of the electron charge is ensured so that events with a wrong electron charge assignment are rejected; this variable is particularly used in the 2lss channel to suppress opposite-sign events for which the charge of one of the leptons has been mismeasured. The tight-charge requirement for muons is represented by the requirement of a consistently well measured track transverse momentum given by  $\Delta p_T/p_T < 0.2$ . Leptons are selected for the final analysis if they pass a given threshold of the BDT output, and are referred to as *tight leptons* in the following.

The validation of the lepton MVA algorithm and the lepton identification variables is performed using data in various control regions; the details about that validation are not discussed here but can be found in Reference [150].

### Selection definitions

Electron and muon object identification is defined in three different sets of selections criteria; the *Loose*, *Fakeable Object*, and *Tight* selection. These three levels of selection are designed to serve for event level vetoes, the fake rate estimation application region, and the final signal selection, respectively. The  $p_T$  of fakeable objects is defined as  $0.85 \times p_T(\text{jet})$ , where the jet is the one associated to the lepton object. This mitigates the dependence of the fake rate on the momentum of the fakeable object and thereby improves the precision of the method.

Tables 6.8 and 6.9 list the full criteria for the different selections of muons and electrons.

In addition to the previously defined requirements for jets, they are required to be separated from any lepton candidates passing the fakeable object selections by  $\Delta R > 0.4$ .

Cut	Loose	Fakeable object	Tight
$ \eta  < 2.4$	✓	✓	✓
$p_T$	$> 5\text{GeV}$	$> 15\text{GeV}$	$> 15\text{GeV}$
$ d_{xy}  < 0.05$ (cm)	✓	✓	✓
$ d_z  < 0.1$ (cm)	✓	✓	✓
$\text{SIP}_{3D} < 8$	✓	✓	✓
$I_{\text{mini}} < 0.4$	✓	✓	✓
is Loose Muon	✓	✓	✓
jet CSV	—	$< 0.8484$	$< 0.8484$
is Medium Muon	—	—	✓
tight-charge	—	—	✓
lepMVA $> 0.90$	—	—	✓

**Table 6.8:** Requirements on each of the three muon selections. In the cases where the cut values change between the selections, those values are listed in the table. Otherwise, whether the cut is applied is indicated.

Cut	Loose	Fakeable Object	Tight
$ \eta  < 2.5$	✓	✓	✓
$p_T$	$> 7\text{GeV}$	$> 15\text{GeV}$	$> 15\text{GeV}$
$ d_{xy}  < 0.05$ (cm)	✓	✓	✓
$ d_z  < 0.1$ (cm)	✓	✓	✓
$\text{SIP}_{3D} < 8$	✓	✓	✓
$I_{\text{mini}} < 0.4$	✓	✓	✓
MVA eID $> (0.0, 0.0, 0.7)$	✓	✓	✓
$\sigma_{in\eta} < (0.011, 0.011, 0.030)$	—	✓	✓
H/E $< (0.10, 0.10, 0.07)$	—	✓	✓
$\Delta\eta_{in} < (0.01, 0.01, 0.008)$	—	✓	✓
$\Delta\phi_{in} < (0.04, 0.04, 0.07)$	—	✓	✓
$-0.05 < 1/E - 1/p < (0.010, 0.010, 0.005)$	—	✓	✓
$p_T^{\text{ratio}}$	—	$> 0.5^\dagger / -$	—
jet CSV	—	$< 0.3^\dagger / < 0.8484$	$< 0.8484$
tight-charge	—	—	✓
conversion rejection	—	—	✓
Number of missing hits	$< 2$	$= 0$	$= 0$
lepton MVA $> 0.90$	—	—	✓

**Table 6.9:** Criteria for each of the three electron selections. In cases where the cut values change between selections, those values are listed in the table. Otherwise, whether the cut is applied is indicated. In some cases, the cut values change for different  $\eta$  ranges. These ranges are  $0 < |\eta| < 0.8$ ,  $0.8 < |\eta| < 1.479$ , and  $1.479 < |\eta| < 2.5$  and the respective cut values are given in the form (value<sub>1</sub>, value<sub>2</sub>, value<sub>3</sub>). For the two  $p_T^{\text{ratio}}$  and CSV rows, the cuts marked with a  $\dagger$  are applied to leptons that fail the lepton MVA cut, while the loose cut value is applied to those that pass the lepton MVA cut.

### 2556 6.5.4 Lepton selection efficiency

2557 Efficiencies of reconstruction and selecting loose leptons are measured both for muons  
 2558 and electrons using a tag and probe method on both data and MC, using  $Z \rightarrow \ell^+ \ell^-$   
 2559 [155]. The scale factors are derived from the ratio of efficiencies  $\varepsilon_i(p_T, \eta)$  measured  
 2560 for a given lepton in data/MC, according to

$$\rho(p_T, \eta) = \frac{\varepsilon_{\text{data}}(p_T, \eta)}{\varepsilon_{\text{MC}}(p_T, \eta)}. \quad (6.6)$$

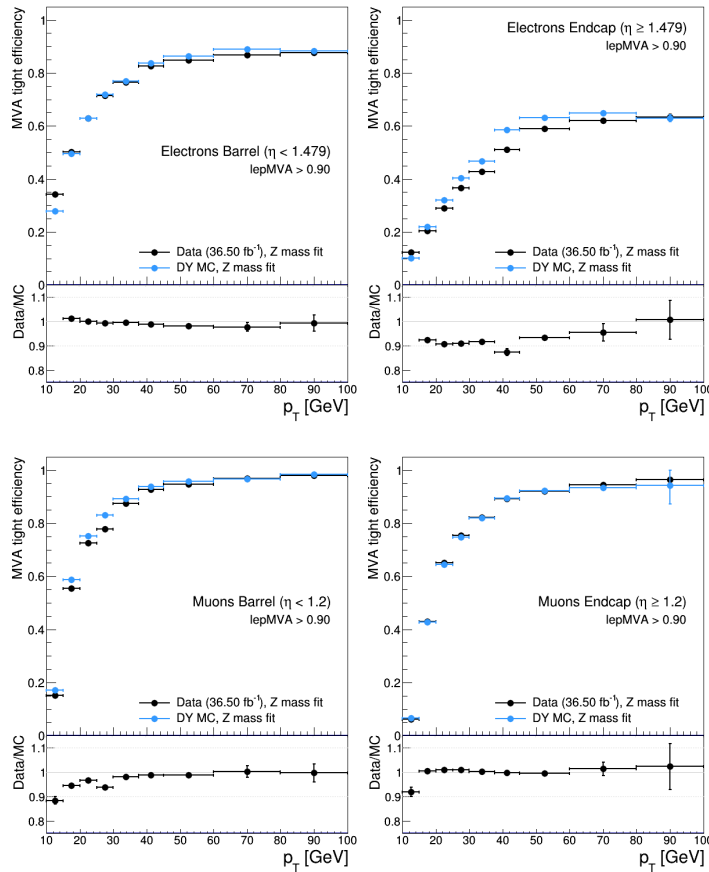


**Figure 6.3:** Tight vs loose selection efficiencies for electrons (top), and muons (bottom), for the 2lss definition, i.e., including the tight-charge requirement.

2561 The scale factor for each event is used to correct the weight of the event in the

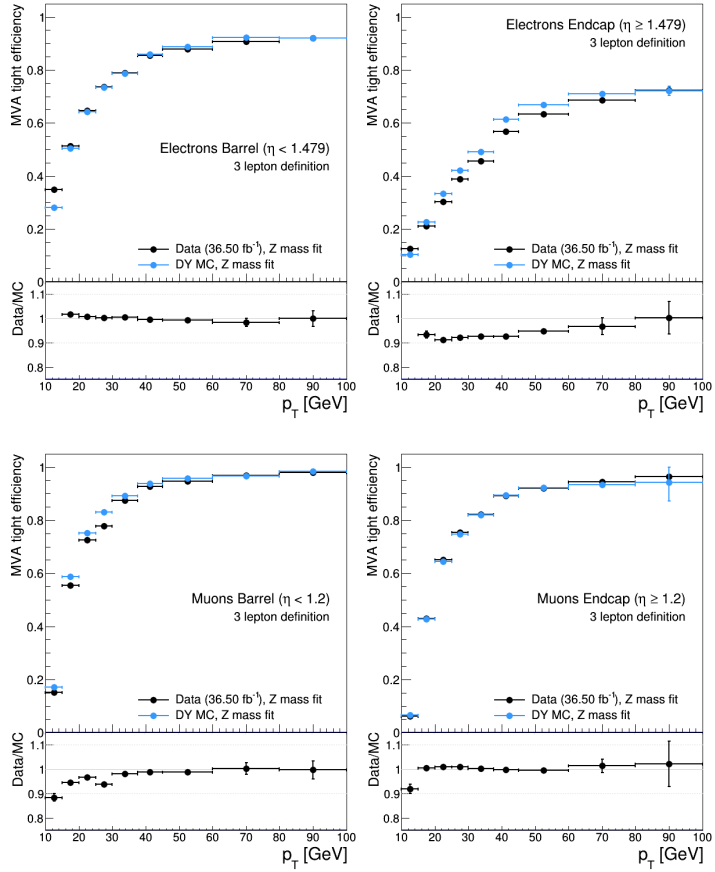


**Figure 6.4:** Tight vs loose selection efficiencies for electrons (top), and muons (bottom), for the 3l channel not including the tight-charge requirement.

2562 full sample; therefore, the full simulation correction is given by the product of all  
 2563 the individual scale factors. The scale factors used in this thesis are inherited from  
 2564 the reference [150] which in turns inherited them from leptonic SUSY analyses using  
 2565 equivalent lepton selections.

2566 The efficiency of applying the tight selection as defined in Tables 6.8 and 6.9, on the  
 2567 loose leptons are determined by using a tag and probe method on a sample of Drell-  
 2568 Yan enriched events. Figures 6.3 and 6.4 show the efficiencies for the 2lss channel and  
 2569 3l channel respectively. Efficiencies in the 2lss channel have been produced including  
 2570 the tight-charge requirement, while for the 3l channel it is not included. Number

2571 of passed and failed probes are determined from a fit to the invariant mass of the  
 2572 dilepton system.

2573 Simulation is corrected using these scale factors; note that they depends on  $\eta$  and  
 2574  $p_T$ .

2575 **6.6 Event selection**

2576 .

2577 .

2578 .

2579 .

2580 .

2581 .

2582 .

2583 .

2584 .

2585 . . .

2586 The analysis is designed to efficiently identify and select prompt leptons from  
 2587 on-shell W and

2588 Z boson decays and to reject non-prompt leptons from b quark decays and spurious  
 2589 lepton

2590 signatures from hadronic jets. Events are then selected in the various lepton  
 2591 channels, and are

2592 required to contain hadronic jets, some of which must be consistent with b quark  
 2593 hadronization. Finally, the signal yield is extracted by simultaneously fitting the  
 2594 output of two dedicated

2595 multivariate discriminants (trained to separate the  $tHq$  signal from the two dom-  
 2596 inant backgrounds) in all categories

2597 . Multivariate techniques are used to discriminate the signal from the dominant  
 2598 backgrounds. The analysis yields a 95% confidence level (C.L.) upper limit on the  
 2599 combined  $tH + ttH$  production cross section times branching ratio of 0.64 pb, with  
 2600 an expected limit of 0.32 pb, for a scenario with  $kt = \sqrt{1.0}$  and  $kV = 1.0$ . Values  
 2601 of  $kt$  outside the range of  $\sqrt{1.25}$  to  $\sqrt{1.60}$  are excluded at 95% C.L., assuming  $kV$   
 2602  $= 1.0$ .

2603 Dont forget to mention previous constrains to ct check reference ?? and references  
 2604 <https://link.springer.com/content/pdf/10.1007%2FJHEP01%282013%29088.pdf> (para-  
 2605 graph after eq 2)

2606 We selects events with three leptons and a  $b$ -jet tagged jet in the final state. The  $tHq$   
 2607 signal contribution is then determined in a fit of the observed data to two multivariate  
 2608 classifier outputs, each trained to discriminate against one of the two dominant back-  
 2609 grounds of events with non-prompt leptons from  $t\bar{t}$  and of associated production of  $t\bar{t}$   
 2610 and vector bosons ( $t\bar{t}W$ ,  $t\bar{t}Z$ ). The fit result is then used to set an upper limit on the  
 2611 combined  $t\bar{t}H$ ,  $tHq$  and  $tHW$  production cross section, as a function of the relative  
 2612 coupling strengths of Higgs and top quark and Higgs and W boson, respectively.

## 2613 6.7 Background predictions

2614 The modeling of reducible and irreducible backgrounds in this analysis uses the exact  
 2615 methods, analysis code, and ROOT trees used for the  $t\bar{t}H$  multilepton analysis. We  
 2616 give a brief description of the methods and refer to the documentation of that analysis  
 2617 in Refs. [145, 150] for any details.

2618 The backgrounds in three-lepton final states can be split in two broad categories:

irreducible backgrounds with genuine prompt leptons (i.e. from on-shell W and Z boson decays); and reducible backgrounds where at least one of the leptons is “non-prompt”, i.e. produced within a hadronic jet, either a genuine lepton from heavy flavor decays, or simply mis-reconstructed jets.

Irreducible backgrounds can be reliably estimated directly from Monte-Carlo simulated events, using higher-order cross sections or data control regions for the overall normalization. This is done in this analysis for all backgrounds involving prompt leptons:  $t\bar{t}W$ ,  $t\bar{t}Z$ ,  $t\bar{t}H$ ,  $WZ$ ,  $ZZ$ ,  $W^\pm W^\pm qq$ ,  $t\bar{t}t\bar{t}$ ,  $tZq$ ,  $tZW$ ,  $WWW$ ,  $WWZ$ ,  $WZZ$ ,  $ZZZ$ .

Reducible backgrounds, on the other hand, are not well predicted by simulation, and are estimated using data-driven methods. In the case of non-prompt leptons, a fake rate method is used,

Additional identification criteria are applied for electrons with  $p_T$  greater than 30 GeV to mimic the identification applied at trigger level in order to ensure consistency between the measurement region and application region of the fake-rate.

where the contribution to the final selection is estimated by extrapolating from a sideband (or “application region”) with a looser lepton definition (the fakeable object definitions in Tabs. 6.8 and 6.9) to the signal selection. The tight-to-loose ratios (or “fake rates”) are measured in several background dominated data events with dedicated triggers, subtracting the residual prompt lepton contribution using MC. Non-prompt leptons in our signal regions are predominantly produced in  $t\bar{t}$  events, with a much smaller contribution, from Drell–Yan production. The systematic uncertainty on the normalization of the non-prompt background estimation is on the order of 50%, and thereby one of the dominant limitations on the performance of multilepton analyses in general and this analysis in particular. It consists of several individual sources, such as the result of closure tests of the method using simulated

2645 events, limited statistics in the data control regions due to necessary prescaling of  
 2646 lepton triggers, and the uncertainty in the subtraction of residual prompt leptons  
 2647 from the control region.

2648 The fake background where the leptons pass the looser selection are weighted  
 2649 according to how many of them fail the tight criteria. Events with a single failing  
 2650 lepton are weighted with the factor  $f/(1-f)$  for the estimate to the tight selection  
 2651 region, where  $f$  is the fake rate. Events with two failing leptons are given the negative  
 2652 weight  $-f_i f_j / (1-f_i)(1-f_j)$ , and for three leptons the weight is positive and equal  
 2653 to the product of  $f/(1-f)$  factor evaluated for each failing lepton.

2654 Figures 6.5 show the distributions of some relevant kinematic variables, normalized  
 2655 to the cross section of the respective processes and to the integrated luminosity.

## 2656 6.8 Signal discrimination

2657 The  $tHq$  signal is separated from the main backgrounds using a boosted decision  
 2658 tree (BDT) classifier, trained on simulated signal and background events. A set  
 2659 of discriminating variables are given as input to the BDT which produces a output  
 2660 distribution maximizing the discrimination power. Table 6.10 lists the input variables  
 2661 used while Figures 6.6 show their distributions for the relevant signal and background  
 2662 samples, for the three lepton channel. Two BDT classifiers are trained for the two  
 2663 main backgrounds expected in the analysis: events with prompt leptons from  $t\bar{t}W$  and  
 2664  $t\bar{t}Z$  (also referred to as  $t\bar{t}V$ ), and events with non-prompt leptons from  $t\bar{t}$ . The datasets  
 2665 used in the training are the  $tHq$  signal (see Tab. 6.1), and LO MADGRAPH samples  
 2666 of  $t\bar{t}W$  and  $t\bar{t}Z$ , in an admixture proportional to their respective cross sections (see  
 2667 Tab. 6.4).

2668 The MVA analysis consist of two stages: first a “training” where the MVA method

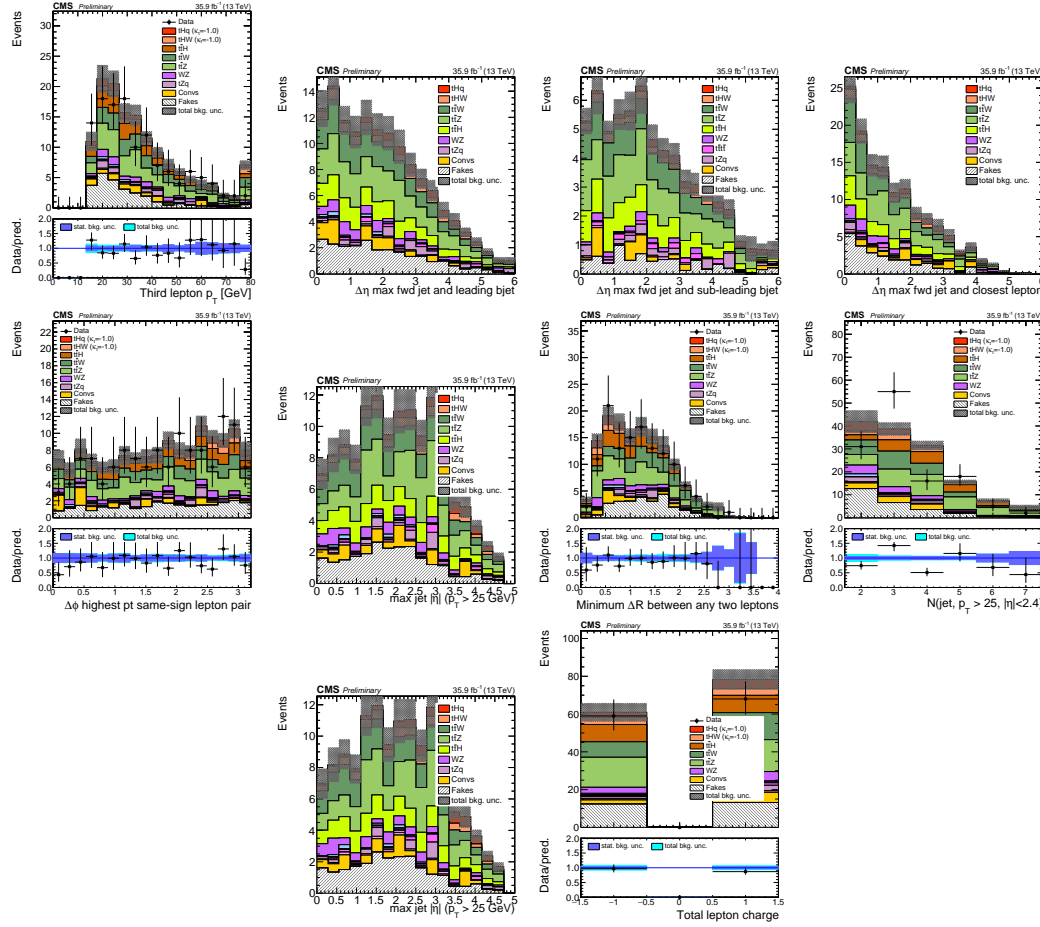


**Figure 6.5:** Distributions of input variables to the BDT for signal discrimination, three lepton channel, normalized to their cross section and to  $35.9\text{fb}^{-1}$ .

is trained to discriminate between simulated signal and background events, then a “test” stage where the trained algorithm is used to classify different events from the samples. The sample is obtained from a pre-selection (see Tab. ?? with pre-selection cuts). Figures 6.7 show the input variables distributions as seen by the MVA algorithm. Note that in contrast to the distributions in Fig. 6.6 only the main backgrounds ( $t\bar{t}$  from simulation,  $t\bar{t}V$ ) are included.

Note that splitting the training in two groups reveals that some variables show opposite behavior for the two background sources; potentially screening the discrimination power if they were to be used in a single discriminant. For some other variables

Variable name	Description
nJet25	Number of jets with $p_T > 25$ GeV, $ \eta  < 2.4$
MaxEtaJet25	Maximum $ \eta $ of any (non-CSV-loose) jet with $p_T > 25$ GeV
totCharge	Sum of lepton charges
nJetEta1	Number of jets with $ \eta  > 1.0$ , non-CSV-loose
detaFwdJetBJet	$\Delta\eta$ between forward light jet and hardest CSV loose jet
detaFwdJet2BJet	$\Delta\eta$ between forward light jet and second hardest CSV loose jet (defaults to -1 in events with only one CSV loose jet)
detaFwdJetClosestLep	$\Delta\eta$ between forward light jet and closest lepton
dphiHighestPtSSPair	$\Delta\phi$ of highest $p_T$ same-sign lepton pair
minDRll	minimum $\Delta R$ between any two leptons
Lep3Pt/Lep2Pt	$p_T$ of the 3 <sup>rd</sup> lepton (2 <sup>nd</sup> for ss2l)

**Table 6.10:** MVA input discriminating variables

2678 the distributions are similar in both background cases.

2679 From table 6.10, it is clear that the input variables are correlated to some extend.  
 2680 These correlations play an important role for some MVA methods like the Fisher  
 2681 discriminant method in which the first step consist of performing a linear transfor-  
 2682 mation to an phase space where the correlations between variables are removed. In  
 2683 case a boosted decision tree (BDT) method however, correlations do not affect the  
 2684 performance. Figure 6.9 show the linear correlation coefficients for signal and back-  
 2685 ground for the two training cases (the signal values are identical by construction). As  
 2686 expected, strong correlations appears for variables related to the forward jet activity.  
 2687 Same trend is seen in case of the same sign dilepton channel in Figure ??.

### 2688 6.8.1 Classifiers response

2689 Several MVA algorithms were evaluated to determine the most appropriate method  
 2690 for this analysis. The plots in Fig. 6.10 (top) show the background rejection as a  
 2691 function of the signal efficiency for  $t\bar{t}$  and  $t\bar{t}V$  trainings (ROC curves) for the different

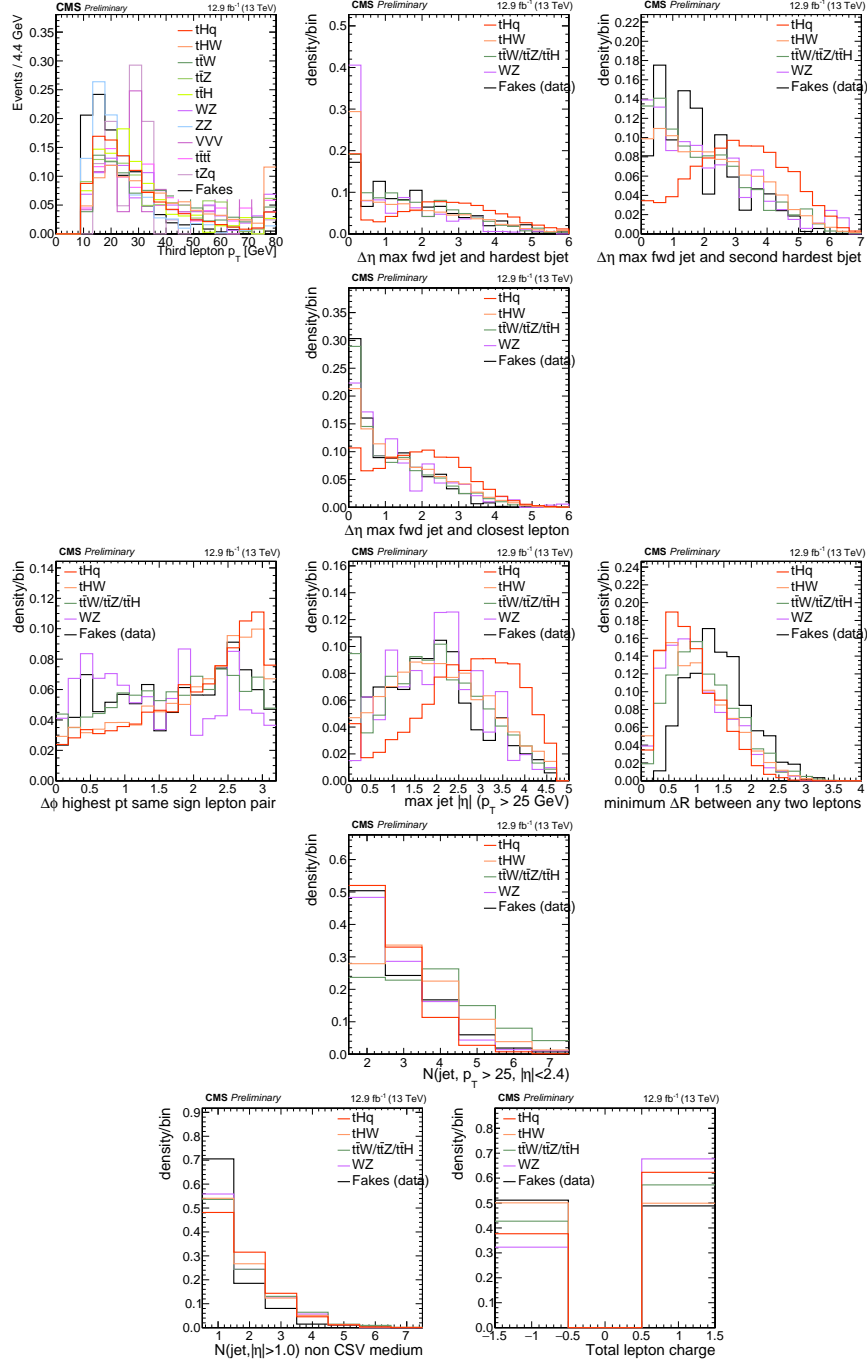


**Figure 6.6:** Distributions of input variables to the BDT for signal discrimination, three lepton channel.

algorithms that were evaluated.

In both cases the gradient boosted decision tree (“BDTA\_GRAD”) classifier offers

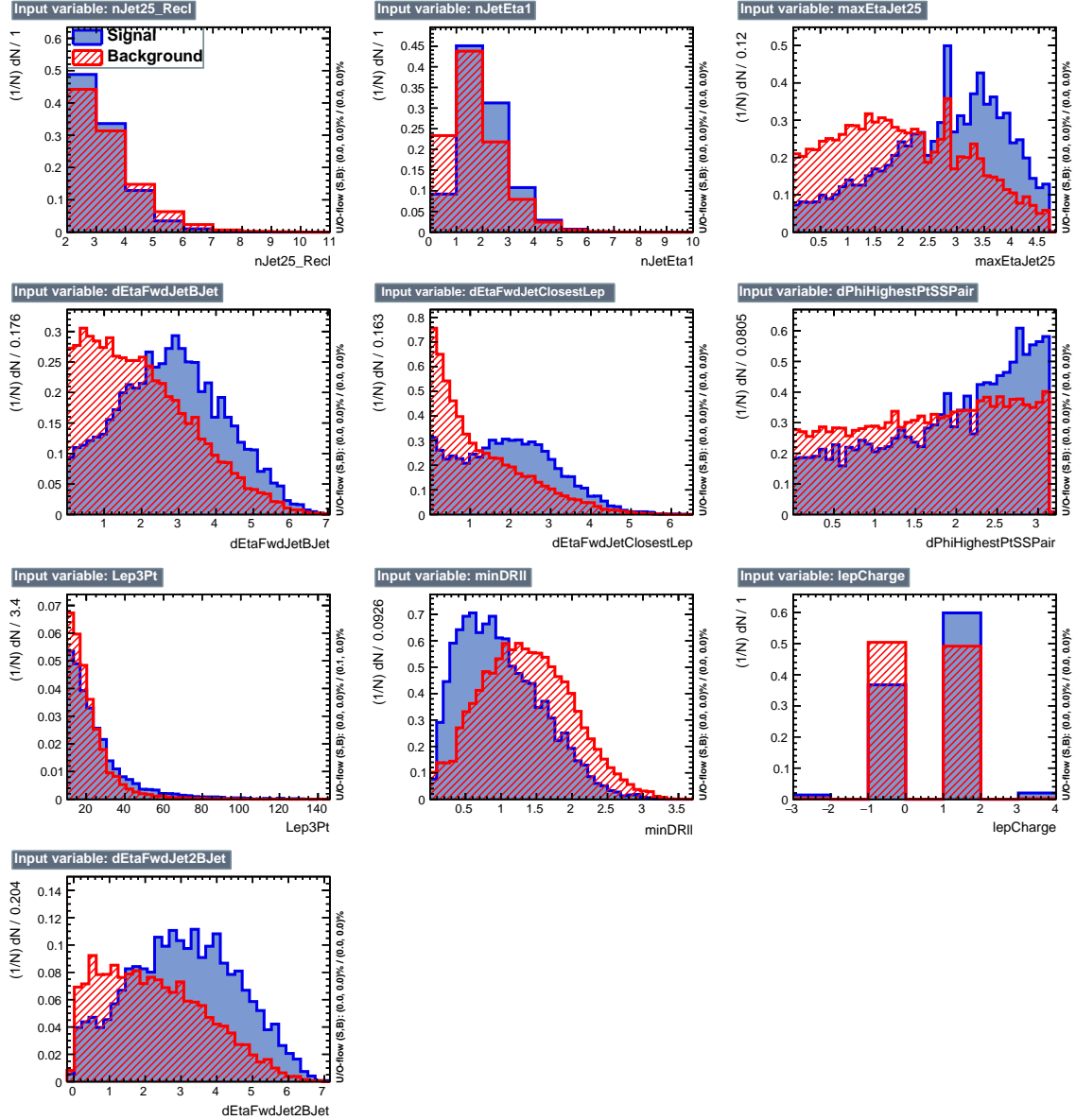


**Figure 6.7:** BDT inputs as seen by TMVA (signal, in blue, is  $tHq$ , background, in red, is  $t\bar{t}$ ) for the three lepton channel, discriminated against  $t\bar{t}$  (fakes) background.

the best results, followed by an adaptive BDT classifier (“BDTA”). The BDTA\_GRAD classifier output distributions for signal and backgrounds are shown on the bottom of Fig. 6.10. As expected, a good discrimination power is obtained using default discriminator parameter values, with minimal overtraining. TMVA provides a ranking of the input variables by their importance in the classification process, shown in Tab. 6.11.

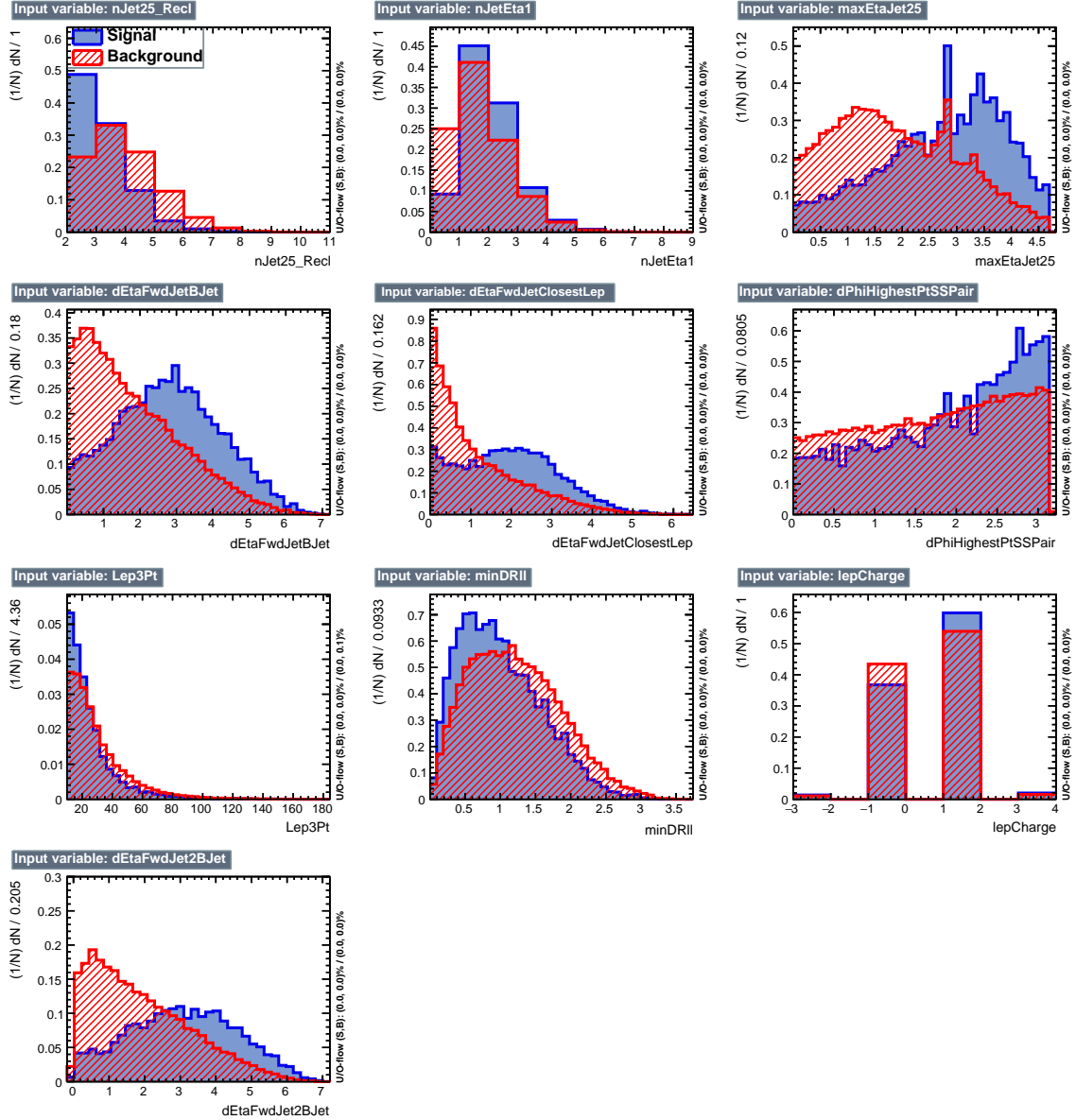


**Figure 6.8:** BDT inputs as seen by TMVA (signal, in blue, is  $tHq$ , background, in red, is  $t\bar{t}W+t\bar{t}Z$ ) for the three lepton channel, discriminated against  $t\bar{t}V$  background.

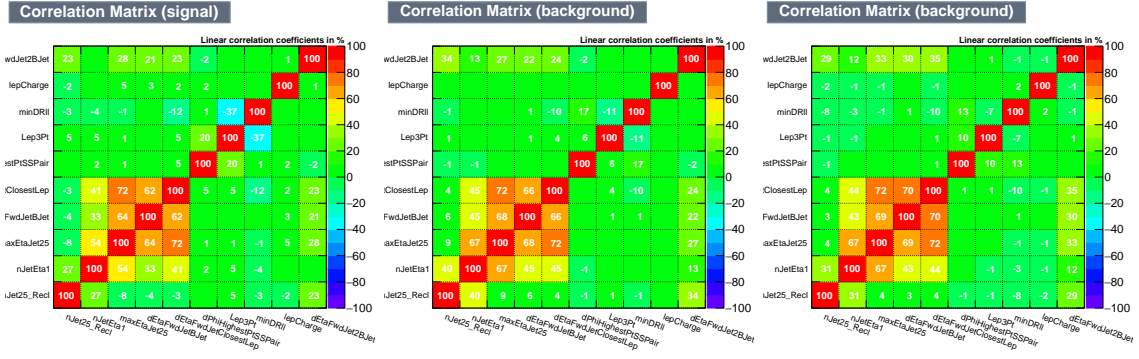


**Figure 6.9:** Signal (left),  $t\bar{t}$  background (middle), and  $t\bar{t}V$  background (right.) correlation matrices for the input variables in the TMVA analysis for the three lepton channel.

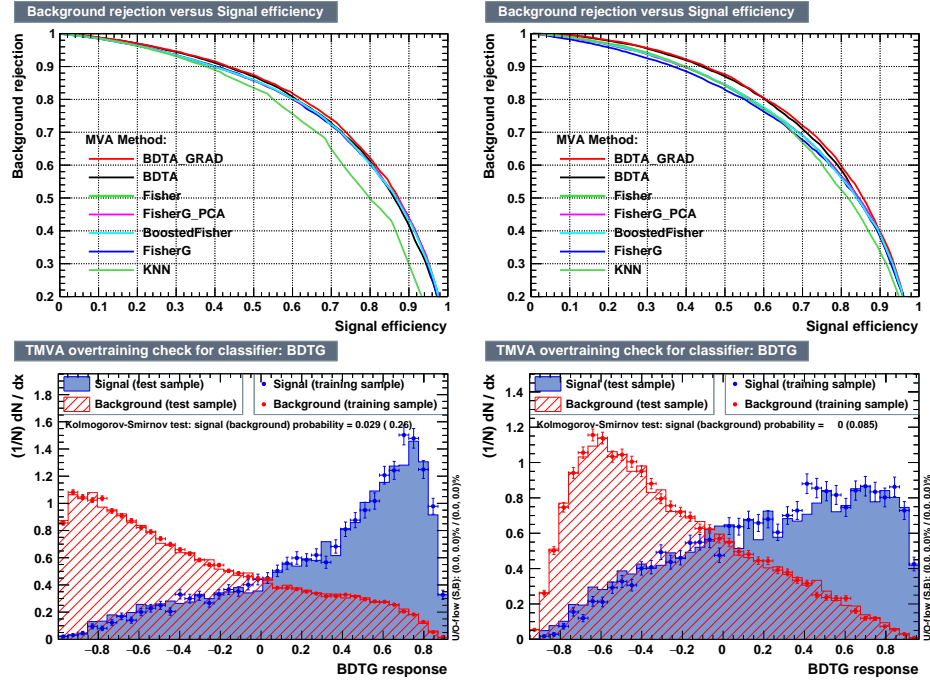


**Figure 6.10:** Top: background rejection vs signal efficiency (ROC curves) for various MVA classifiers (top) in the three lepton channel against  $t\bar{t}V$  (left) and  $t\bar{t}$  (right). Bottom: classifier output distributions for the gradient boosted decision trees, for training against  $t\bar{t}V$  (left) and against  $t\bar{t}$  (right).

## 2700 6.9 Additional discriminating variables

2701 Two additional discriminating variables were tested considering the fact that the  
 2702 forward jet in the background could come from the pileup; since we have a real forward

ttbar training			ttV training		
Rank	Variable	Importance	Variable	Importance	
1	minDRll	1.329e-01	dEtaFwdJetBJet	1.264e-01	
2	dEtaFwdJetClosestLep	1.294e-01	Lep3Pt	1.224e-01	
3	dEtaFwdJetBJet	1.209e-01	maxEtaJet25	1.221e-01	
4	dPhiHighestPtSSPair	1.192e-01	dEtaFwdJet2BJet	1.204e-01	
5	Lep3Pt	1.158e-01	dEtaFwdJetClosestLep	1.177e-01	
6	maxEtaJet25	1.121e-01	minDRll	1.143e-01	
7	dEtaFwdJet2BJet	9.363e-02	dPhiHighestPtSSPair	9.777e-02	
8	nJetEta1	6.730e-02	nJet25_Recl	9.034e-02	
9	nJet25_Recl	6.178e-02	nJetEta1	4.749e-02	
10	lepCharge	4.701e-02	lepCharge	4.116e-02	

**Table 6.11:** TMVA input variables ranking for BDTA\_GRAD method for the trainings in the three lepton channel. For both trainings the rankings show almost the same 5 variables in the first places.

---

```
TMVA.Types.kBDT
NTrees=800
BoostType=Grad
Shrinkage=0.10
!UseBaggedGrad
nCuts=50
MaxDepth=3
NegWeightTreatment=PairNegWeightsGlobal
CreateMVAPdfs
```

---

**Table 6.12:** TMVA configuration used in the BDT training.

2703 jet in the signal, it could give some improvement in the discriminating power. The  
 2704 additional variables describe the forward jet momentum (fwdJetPt25) and the forward  
 2705 jet identification(fwdJetPUID). Distributions for these variables in the three lepton  
 2706 channel are shown in the figure 6.11. The forward jet identification distribution show  
 2707 that for both, signal and background, jets are mostly real jets.

2708 The testing was made including in the MVA input one variable at a time, so we  
 2709 can evaluate the dicrimination power of each variable, and then both simultaneously.  
 2710 fwdJetPUID was ranked in the last place in importance (11) in both training (ttV  
 2711 and tt) while fwdJetPt25 was ranked 3 in the ttV training and 7 in the tt training.  
 2712 When training using 12 variables, fwdJetPt25 was ranked 5 and 7 in the ttV and tt

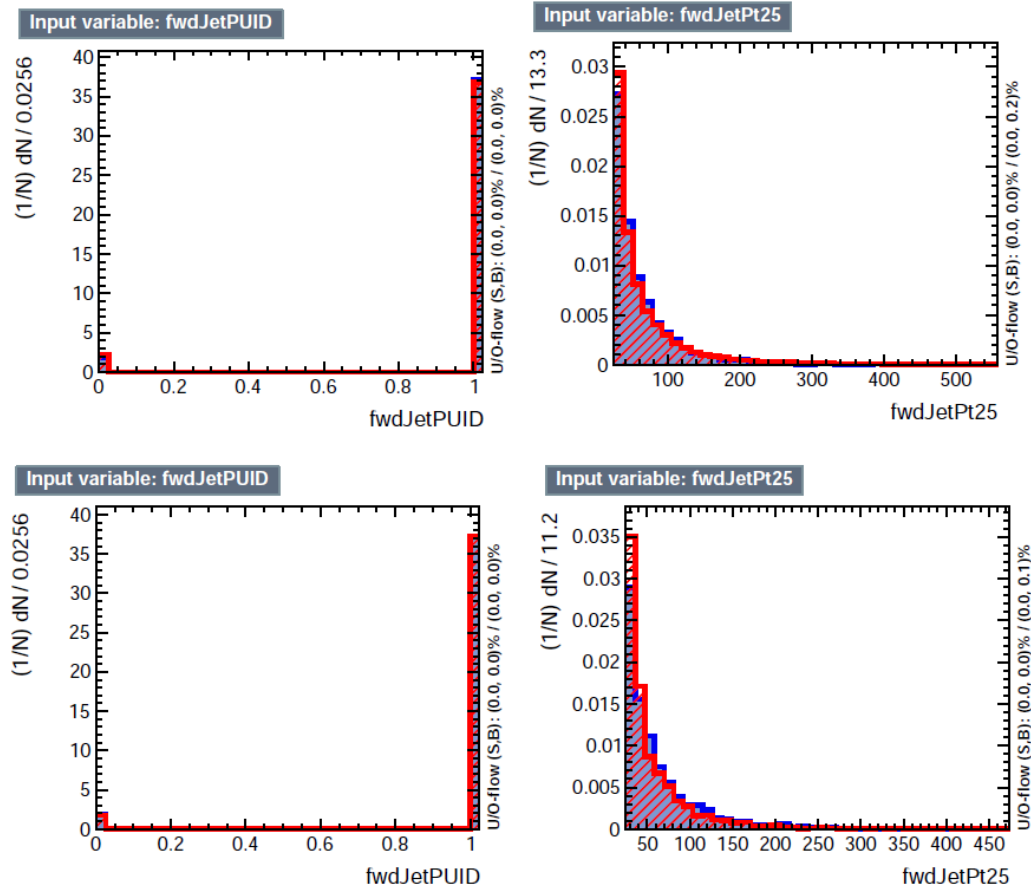


**Figure 6.11:** Additional discriminating variables distributions for ttv training (Top row) and tt training (bottom row) in the three lepton channel. The origin of the jets in the forward jet identification distribution is tagged as 0 for “pileup jets” while “real jets” are tagged as 1.

2713 trainings respectively, while `fwdJetPUID` was ranked 12 in both cases.

2714 The improvement in the discrimination performance provided by the additional  
 2715 variables is about 1%, so it was decided not to include them in the procedure. Table  
 2716 6.13 show the ROC-integral for all the testing cases we made.

ROC-integral	
base 10 var ttv	0.848
+ fwdJetPUID ttv	0.849
+ fwdJetPt25 ttv	0.856
12 var ttv	0.856
<hr/>	
base 10 var tt	0.777
+ fwdJetPUID tt	0.777
+ fwdJetPt25 tt	0.787
12 var	0.787

**Table 6.13:** ROC-integral for all the testing cases we made in the evaluation of the additional variables discriminating power. The improvement in the discrimination performance provided by the additional variables is about 1%

2717 

## References

- 2718 [1] J. Schwinger. "Quantum Electrodynamics. I. A Covariant Formulation". Phys-  
2719       ical Review. 74 (10): 1439-61, (1948). <https://doi.org/10.1103/PhysRev.74.1439>
- 2721 [2] R. P. Feynman. "Space-Time Approach to Quantum Electrodynamics". Physical  
2722       Review. 76 (6): 769-89, (1949). <https://doi.org/10.1103/PhysRev.76.769>
- 2723 [3] S. Tomonaga. "On a Relativistically Invariant Formulation of the Quantum  
2724       Theory of Wave Fields". Progress of Theoretical Physics. 1 (2): 27-42, (1946).  
2725       <https://doi.org/10.1143/PTP.1.27>
- 2726 [4] D.J. Griffiths, "Introduction to electrodynamics". 4th ed. Pearson, (2013).
- 2727 [5] F. Mandl, G. Shaw. "Quantum field theory." Chichester, Wiley (2009).
- 2728 [6] F. Halzen, and A.D. Martin, "Quarks and leptons: An introductory course in  
2729       modern particle physics". New York: Wiley, (1984) .
- 2730 [7] File: Standard\_Model\_of\_Elementary\_Particle\_dark.svg. (2017, June 12)  
2731       Wikimedia Commons, the free media repository. Retrieved November 27, 2017  
2732       from <https://www.collegiate-advanced-electricity.com/single-post/2017/04/10/The-Standard-Model-of-Particle-Physics>.

- 2734 [8] E. Noether, "Invariante Variationsprobleme", Nachrichten von der Gesellschaft  
 2735 der Wissenschaften zu Göttingen, mathematisch-physikalische Klasse, vol. 1918,  
 2736 pp. 235-257, (1918).
- 2737 [9] C. Patrignani et al. (Particle Data Group), Chin. Phys. C, 40, 100001 (2016)  
 2738 and 2017 update.
- 2739 [10] M. Goldhaber, L. Grodzins, A.W. Sunyar "Helicity of Neutrinos", Phys. Rev.  
 2740 109, 1015 (1958).
- 2741 [11] Palanque-Delabrouille N et al. "Neutrino masses and cosmology with Lyman-  
 2742 alpha forest power spectrum", JCAP 11 011 (2015).
- 2743 [12] M. Gell-Mann. "A Schematic Model of Baryons and Mesons". Physics Letters.  
 2744 8 (3): 214-215 (1964).
- 2745 [13] G. Zweig. "An SU(3) Model for Strong Interaction Symmetry and its Breaking"  
 2746 (PDF). CERN Report No.8182/TH.401 (1964).
- 2747 [14] G. Zweig. "An SU(3) Model for Strong Interaction Symmetry and its Breaking:  
 2748 II" (PDF). CERN Report No.8419/TH.412(1964).
- 2749 [15] M. Gell-Mann. "The Interpretation of the New Particles as Displaced Charged  
 2750 Multiplets". Il Nuovo Cimento 4: 848. (1956).
- 2751 [16] T. Nakano, K. Nishijima. "Charge Independence for V-particles". Progress of  
 2752 Theoretical Physics 10 (5): 581-582. (1953).
- 2753 [17] N. Cabibbo, "Unitary symmetry and leptonic decays" Physical Review Letters,  
 2754 vol. 10, no. 12, p. 531, (1963).

- 2755 [18] M.Kobayashi, T.Maskawa, “CP-violation in the renormalizable theory of weak  
2756 interaction,” Progress of Theoretical Physics, vol. 49, no. 2, pp. 652-657, (1973).
- 2757 [19] File: Weak Decay (flipped).svg. (2017, June 12). Wikimedia Com-  
2758 mons, the free media repository. Retrieved November 27, 2017  
2759 from [https://commons.wikimedia.org/w/index.php?title=File:  
2760 Weak\\_Decay\\_\(flipped\)\.svg&oldid=247498592](https://commons.wikimedia.org/w/index.php?title=File:Weak_Decay_(flipped)\.svg&oldid=247498592).
- 2761 [20] Georgia Tech University. Coupling Constants for the Fundamental Forces(2005).  
2762 Retrieved January 10, 2018, from [http://hyperphysics.phy-astr.gsu.edu/  
2763 hbase/Forces/couple.html#c2](http://hyperphysics.phy-astr.gsu.edu/hbase/Forces/couple.html#c2)
- 2764 [21] M. Strassler. (May 31, 2013).The Strengths of the Known Forces. Retrieved Jan-  
2765 uary 10, 2018, from [https://profmattstrassler.com/articles-and-posts/  
2766 particle-physics-basics/the-known-forces-of-nature/  
2767 the-strength-of-the-known-forces/](https://profmattstrassler.com/articles-and-posts/particle-physics-basics/the-known-forces-of-nature/the-strength-of-the-known-forces/)
- 2768 [22] S.L. Glashow. “Partial symmetries of weak interactions”, Nucl. Phys. 22 579-  
2769 588, (1961).
- 2770 [23] A. Salam, J.C. Ward. “Electromagnetic and weak interactions”, Physics Letters  
2771 13 168-171, (1964).
- 2772 [24] S. Weinberg, “A model of leptons”, Physical Review Letters, vol. 19, no. 21, p.  
2773 1264, (1967).
- 2774 [25] M. Peskin, D. Schroeder, “An introduction to quantum field theory”. Perseus  
2775 Books Publishing L.L.C., (1995).
- 2776 [26] A. Pich. “The Standard Model of Electroweak Interactions” <https://arxiv.org/abs/1201.0537>

- 2778 [27] G. Arnison et al. (UA1 Collaboration), Phys. Lett. B 122, 103 (1983).
- 2779 [28] M. Banner et al. (UA2 Collaboration), Phys. Lett. B 122, 476 (1983).
- 2780 [29] G. Arnison et al. (UA1 Collaboration), Phys. Lett. B 126, 398 (1983).
- 2781 [30] P. Bagnaia et al. (UA2 Collaboration), Phys. Lett. B 129, 130 (1983).
- 2782 [31] F.Bellaiche. (2012, 2 September). “What’s this Higgs boson anyway?”. Retrieved  
2783 from: <https://www.quantum-bits.org/?p=233>
- 2784 [32] M. Endres et al. Nature 487, 454-458 (2012) doi:10.1038/nature11255
- 2785 [33] F. Englert, R. Brout. “Broken Symmetry and the Mass of Gauge  
2786 Vector Mesons”. Physical Review Letters. 13 (9): 321-23.(1964)  
2787 doi:10.1103/PhysRevLett.13.321
- 2788 [34] P.Higgs. “Broken Symmetries and the Masses of Gauge Bosons”. Physical Re-  
2789 view Letters. 13 (16): 508-509,(1964). doi:10.1103/PhysRevLett.13.508.
- 2790 [35] G.Guralnik, C.R. Hagen and T.W.B. Kibble. “Global Conservation Laws  
2791 and Massless Particles”. Physical Review Letters. 13 (20): 585-587, (1964).  
2792 doi:10.1103/PhysRevLett.13.585.
- 2793 [36] CMS collaboration. “Observation of a new boson at a mass of 125 GeV with  
2794 the CMS experiment at the LHC”. Physics Letters B. 716 (1): 30-61 (2012).  
2795 arXiv:1207.7235. doi:10.1016/j.physletb.2012.08.021
- 2796 [37] ATLAS collaboration. “Observation of a New Particle in the Search for the Stan-  
2797 dard Model Higgs Boson with the ATLAS Detector at the LHC”. Physics Letters  
2798 B. 716 (1): 1-29 (2012). arXiv:1207.7214. doi:10.1016/j.physletb.2012.08.020.

- 2799 [38] ATLAS collaboration; CMS collaboration (26 March 2015). “Combined Mea-  
 2800 surement of the Higgs Boson Mass in pp Collisions at  $\sqrt{s}=7$  and 8 TeV with  
 2801 the ATLAS and CMS Experiments”. Physical Review Letters. 114 (19): 191803.  
 2802 arXiv:1503.07589. doi:10.1103/PhysRevLett.114.191803.
- 2803 [39] LHC InternationalMasterclasses“When protons collide”. Retrieved from [http://atlas.physicsmasterclasses.org/en/zpath\\_protoncollisions.htm](http://atlas.physicsmasterclasses.org/en/zpath_protoncollisions.htm)
- 2805 [40] CMS Collaboration, “SM Higgs Branching Ratios and Total Decay Widths (up-  
 2806 date in CERN Report4 2016)”. <https://twiki.cern.ch/twiki/bin/view/LHCPhysics/CERNYellowReportPageBR> , last accessed on 17.12.2017.
- 2808 [41] R.Grant V. “Determination of Higgs branching ratios in  $H \rightarrow W^+W^- \rightarrow l\nu jj$   
 2809 and  $H \rightarrow ZZ \rightarrow l^+l^-jj$  channels”. Physics Department, University of Ten-  
 2810 nessee (Dated: October 31, 2012). Retrieved from <http://aesop.phys.utk.edu/ph611/2012/projects/Riley.pdf>
- 2812 [42] LHC Higgs Cross Section Working Group, Denner, A., Heinemeyer, S. et al.  
 2813 “Standard model Higgs-boson branching ratios with uncertainties”. Eur. Phys.  
 2814 J. C (2011) 71: 1753. <https://doi.org/10.1140/epjc/s10052-011-1753-8>
- 2815 [43] D. de Florian et al., LHC Higgs Cross Section Working Group,  
 2816 CERNâš2017âš002-M, arXiv:1610.07922[hep-ph] (2016).
- 2817 [44] ATLAS and CMS Collaborations, “Measurements of the Higgs boson produc-  
 2818 tion and decay rates and constraints on its couplings from a combined ATLAS  
 2819 and CMS analysis of the LHC pp collision data at  $\sqrt{s} = 7$  and 8 TeV,” (2016).  
 2820 CERN-EP-2016-100, ATLAS-HIGG-2015-07, CMS-HIG-15-002.

- 2821 [45] J. A. Aguilar-Saavedra, R. Benbrik, S. Heinemeyer, and M. Perez-Victoria,  
 2822 “Handbook of vector-like quarks: Mixing and single production”, Phys. Rev. D  
 2823 88 (2013) 094010, doi:10.1103/PhysRevD.88.094010, arXiv:1306.0572.
- 2824 [46] A. Greljo, J. F. Kamenik, and J. Kopp, “Disentangling flavor vio-  
 2825 lation in the top-Higgs sector at the LHC”, JHEP 07 (2014) 046,  
 2826 doi:10.1007/JHEP07(2014)046, arXiv:1404.1278.
- 2827 [47] F. Demartin, F. Maltoni, K. Mawatari, and M. Zaro, “Higgs production in  
 2828 association with a single top quark at the LHC,” European Physical Journal C,  
 2829 vol. 75, p. 267, (2015). doi:10.1140/epjc/s10052-015-3475-9, arXiv:1504.00611.
- 2830 [48] F. Demartin, B. Maier, F. Maltoni, K. Mawatari, and M. Zaro, “tWH associated  
 2831 production at the LHC”, European Physical Journal C, vol. 77, p. 34, (2017).  
 2832 arXiv:1607.05862
- 2833 [49] F. Maltoni, K. Paul, T. Stelzer, and S. Willenbrock, “Associated production  
 2834 of Higgs and single top at hadron colliders”, Phys.Rev. D64 (2001) 094023,  
 2835 [hep-ph/0106293].
- 2836 [50] S. Biswas, E. Gabrielli, F. Margaroli, and B. Mele, “Direct constraints on the  
 2837 top-Higgs coupling from the 8 TeV LHC data,” Journal of High Energy Physics,  
 2838 vol. 07, p. 073, (2013).
- 2839 [51] M. Farina, C. Grojean, F. Maltoni, E. Salvioni, and A. Thamm, “Lifting de-  
 2840 generacies in Higgs couplings using single top production in association with a  
 2841 Higgs boson,” Journal of High Energy Physics, vol. 05, p. 022, (2013).
- 2842 [52] T.M. Tait and C.-P. Yuan, “Single top quark production as a window to physics  
 2843 beyond the standard model”, Phys. Rev. D 63 (2000) 014018 [hep-ph/0007298].

- 2844 [53] CMS Collaboration, “Modelling of the single top-quark production in associa-  
2845 tion with the Higgs boson at 13 TeV.” <https://twiki.cern.ch/twiki/bin/viewauth/CMS/SingleTopHiggsGeneration13TeV>, last accessed on 16.01.2018.  
2846
- 2847 [54] CMS Collaboration, “SM Higgs production cross sections at  $\sqrt{s} =$   
2848 13 TeV.” <https://twiki.cern.ch/twiki/bin/view/LHCPhysics/CERNYellowReportPageAt13TeV>, last accessed on 16.01.2018.  
2849
- 2850 [55] S. Dawson, The effective W approximation, Nucl. Phys. B 249 (1985) 42.
- 2851 [56] S. Biswas, E. Gabrielli and B. Mele, JHEP 1301 (2013) 088 [arXiv:1211.0499  
2852 [hep-ph]].
- 2853 [57] LHC Higgs Cross Section Working Group, “Handbook of LHC Higgs Cross  
2854 Sections: 4.Deciphering the Nature of the Higgs Sector”, arXiv:1610.07922.
- 2855 [58] J. Ellis, D. S. Hwang, K. Sakurai, and M. Takeuchi.“Disentangling Higgs-Top  
2856 Couplings in Associated Production”, JHEP 1404 (2014) 004, [arXiv:1312.5736].
- 2857 [59] CMS Collaboration, V. Khachatryan et al., “Precise determination of the mass  
2858 of the Higgs boson and tests of compatibility of its couplings with the standard  
2859 model predictions using proton collisions at 7 and 8 TeV,” arXiv:1412.8662.
- 2860 [60] ATLAS Collaboration, G. Aad et al., “Updated coupling measurements of the  
2861 Higgs boson with the ATLAS detector using up to  $25 \text{ fb}^{-1}$  of proton-proton  
2862 collision data”, ATLAS-CONF-2014-009.
- 2863 [61] File:Cern-accelerator-complex.svg. Wikimedia Commons, the free media repos-  
2864 itory. Retrieved January, 2018 from <https://commons.wikimedia.org/wiki/File:Cern-accelerator-complex.svg>  
2865

- 2866 [62] J.L. Caron , “Layout of the LEP tunnel including future LHC infrastructures.”,  
2867 (Nov, 1993). A C Collection. Legacy of AC. Pictures from 1992 to 2002. Re-  
2868 trieved from <https://cds.cern.ch/record/841542>
- 2869 [63] M. Vretenar, “The radio-frequency quadrupole”. CERN Yellow Report CERN-  
2870 2013-001, pp.207-223 DOI:10.5170/CERN-2013-001.207. arXiv:1303.6762
- 2871 [64] L.Evans. P. Bryant (editors). “LHC Machine”. JINST 3 S08001 (2008).
- 2872 [65] CERN Photographic Service.“Radio-frequency quadrupole, RFQ-1”, March  
2873 1983, CERN-AC-8303511. Retrieved from <https://cds.cern.ch/record/615852>.
- 2875 [66] CERN Photographic Service “Animation of CERN’s accelerator network”, 14  
2876 October 2013. DOI: 10.17181/cds.1610170 Retrieved from <https://videos.cern.ch/record/1610170>
- 2878 [67] C.Sutton. “Particle accelerator”.Encyclopedia Britannica. July 17,  
2879 2013. Retrieved from <https://www.britannica.com/technology/particle-accelerator>.
- 2881 [68] L.Guiraud. “Installation of LHC cavity in vacuum tank.”. July 27 2000. CERN-  
2882 AC-0007016. Retrieved from <https://cds.cern.ch/record/41567>.
- 2883 [69] J.L. Caron, “Magnetic field induced by the LHC dipole’s superconducting coils”.  
2884 March 1998. AC Collection. Legacy of AC. Pictures from 1992 to 2002. LHC-  
2885 PHO-1998-325. Retrieved from <https://cds.cern.ch/record/841511>.
- 2886 [70] AC Team. “Diagram of an LHC dipole magnet”. June 1999. CERN-DI-9906025  
2887 retrieved from <https://cds.cern.ch/record/40524>.

- 2888 [71] CMS Collaboration “Public CMS Luminosity Information”. [https://twiki.cern.ch/twiki/bin/view/CMSPublic/LumiPublicResults#2016\\\_\\\_proton\\_proton\\_13\\_TeV\\_collis](https://twiki.cern.ch/twiki/bin/view/CMSPublic/LumiPublicResults#2016\_\_proton_proton_13_TeV_collis), last accessed 24.01.2018
- 2891 [72] J.L Caron. “LHC Layout” AC Collection. Legacy of AC. Pictures from 1992  
2892 to 2002. September 1997, LHC-PHO-1997-060. Retrieved from <https://cds.cern.ch/record/841573>.
- 2894 [73] J.A. Coarasa. “The CMS Online Cluster:Setup, Operation and Maintenance  
2895 of an Evolving Cluster”. ISGC 2012, 26 February - 2 March 2012, Academia  
2896 Sinica, Taipei, Taiwan.
- 2897 [74] CMS Collaboration. “The CMS experiment at the CERN LHC” JINST 3 S08004  
2898 (2008).
- 2899 [75] CMS Collaboration. “CMS detector drawings 2012” CMS-PHO-GEN-2012-002.  
2900 Retrieved from <http://cds.cern.ch/record/1433717>.
- 2901 [76] Davis, Siona Ruth. “Interactive Slice of the CMS detector”, Aug. 2016,  
2902 CMS-OUTREACH-2016-027, retrieved from <https://cds.cern.ch/record/2205172>
- 2904 [77] R. Breedon. “View through the CMS detector during the cooldown of the  
2905 solenoid on February 2006. CMS Collection”, February 2006, CMS-PHO-  
2906 OREACH-2005-004, Retrieved from <https://cds.cern.ch/record/930094>.
- 2907 [78] Halyo, V. and LeGresley, P. and Lujan, P. “Massively Parallel Computing and  
2908 the Search for Jets and Black Holes at the LHC”, Nucl.Instrum.Meth. A744  
2909 (2014) 54-60, DOI: 10.1016/j.nima.2014.01.038”

- 2910 [79] A. Dominguez et. al. “CMS Technical Design Report for the Pixel Detector  
2911 Upgrade”, CERN-LHCC-2012-016. CMS-TDR-11.
- 2912 [80] CMS Collaboration. “Description and performance of track and primary-vertex  
2913 reconstruction with the CMS tracker,” Journal of Instrumentation, vol. 9, no.  
2914 10, p. P10009,(2014).
- 2915 [81] CMS Collaboration and M. Brice. “Images of the CMS Tracker Inner Bar-  
2916 rel”, November 2008, CMS-PHO-TRACKER-2008-002. Retrieved from <https://cds.cern.ch/record/1431467>.
- 2918 [82] M. Weber. “The CMS tracker”. 6th international conference on hyperons, charm  
2919 and beauty hadrons Chicago, June 28-July 3 2004.
- 2920 [83] CMS Collaboration. “Projected Performance of an Upgraded CMS Detector at  
2921 the LHC and HL-LHC: Contribution to the Snowmass Process”. Jul 26, 2013.  
2922 arXiv:1307.7135
- 2923 [84] L. Veillet. “End assembly of HB with EB rails and rotation inside SX ”,Jan-  
2924 uary 2002. CMS-PHO-HCAL-2002-002. Retrieved from <https://cds.cern.ch/record/42594>.
- 2926 [85] J. Puerta-Pelayo.“First DT+RPC chambers installation round in the UX5 cav-  
2927 ern.”. January 2007, CMS-PHO-OREACH-2007-001. Retrieved from <https://cds.cern.ch/record/1019185>
- 2929 [86] X. Cid Vidal and R. Cid Manzano. “CMS Global Muon Trigger” web site:  
2930 Taking a closer look at LHC. Retrieved from [https://www.lhc-closer.es/taking\\_a\\_closer\\_look\\_at\\_lhc/0.lhc\\_trigger](https://www.lhc-closer.es/taking_a_closer_look_at_lhc/0.lhc_trigger)

- 2932 [87] WLCG Project Office, “Documents & Reference - Tiers - Structure,”  
 2933 (2014). <http://wlcg.web.cern.ch/documents-reference> , last accessed on  
 2934 30.01.2018.
- 2935 [88] CMS Collaboration. “CMSSW Application Framework”, <https://twiki.cern.ch/twiki/bin/view/CMSPublic/WorkBookCMSSWFramework>,  
 2936 last accesses 06.02.2018
- 2938 [89] A. Buckleya, J. Butterworthb, S. Giesekec, et. al. “General-purpose event gen-  
 2939 erators for LHC physics”. arXiv:1101.2599v1 [hep-ph] 13 Jan 2011
- 2940 [90] A. Quadt. “Top Quark Physics at Hadron Colliders”. Advances in the Physics  
 2941 of Particles and Nuclei. Springer-Verlag Berlin Heidelberg. DOI: 10.1007/978-  
 2942 3-540-71060-8 (2007)
- 2943 [91] DurhamHep Data Project, “The Durham HepData Project - PDF Plotter.”  
 2944 <http://hepdata.cedar.ac.uk/pdf/pdf3.html> , last accessed on 02.02.2018.
- 2945 [92] G. Altarelli and G. Parisi. “ASYMPTOTIC FREEDOM IN PARTON LAN-  
 2946 GUAGE”, Nucl.Phys. B126:298 (1977).
- 2947 [93] Yu.L. Dokshitzer. Sov.Phys. JETP 46:641 (1977)
- 2948 [94] V.N. Gribov, L.N. Lipatov. “Deep inelastic e p scattering in perturbation the-  
 2949 ory”, Sov.J.Nucl.Phys. 15:438 (1972)
- 2950 [95] F. Maltoni, G. Ridolfi, and M. Ubiali, “b-initiated processes at the LHC: a  
 2951 reappraisal,” Journal of High Energy Physics, vol. 07, p. 022, (2012).
- 2952 [96] B. Andersson, G. Gustafson, G. Ingelman and T. Sjostrand, “Parton fragmen-  
 2953 tation and string dynamics”, Physics Reports, Vol. 97, No. 2-3, pp. 31-145,  
 2954 1983.

- 2955 [97] CMS Collaboration, “Event generator tunes obtained from underlying event  
 2956 and multiparton scattering measurements;” European Physical Journal C, vol.  
 2957 76, no. 3, p. 155, (2016).
- 2958 [98] J. Alwall et. al., “The automated computation of tree-level and next-to-leading  
 2959 order differential cross sections, and their matching to parton shower simula-  
 2960 tions,” Journal of High Energy Physics, vol. 07, p. 079, (2014).
- 2961 [99] T. Sjöstrand and P. Z. Skands, “Transverse-momentum-ordered showers and  
 2962 interleaved multiple interactions,” European Physical Journal C, vol. 39, pp.  
 2963 129–154, (2005).
- 2964 [100] S. Frixione, P. Nason, and C. Oleari, “Matching NLO QCD computations with  
 2965 Parton Shower simulations: the POWHEG method,” Journal of High Energy  
 2966 Physics, vol. 11, p. 070, (2007).
- 2967 [101] S. Agostinelli et al., “GEANT4: A Simulation toolkit,” Nuclear Instruments  
 2968 and Methods in Physics, vol. A506, pp. 250–303, (2003).
- 2969 [102] J.Allison et.al.,“Recent developments in Geant4”, Nuclear Instruments and  
 2970 Methods in Physics Research A 835 (2016) 186-225.
- 2971 [103] CMS Collaboration “Full Simulation Offline Guide”, <https://twiki.cern.ch/twiki/bin/view/CMSPublic/SWGuideSimulation>, last accessed 04.02.2018
- 2973 [104] A. Giammanco. “The Fast Simulation of the CMS Experiment” J. Phys.: Conf.  
 2974 Ser. 513 022012 (2014)
- 2975 [105] A.M. Sirunyan et. al. “Particle-flow reconstruction and global event description  
 2976 with the CMS detector”, JINST 12 P10003 (2017) <https://doi.org/10.1088/1748-0221/12/10/P10003>.

- 2978 [106] The CMS Collaboration. “ Description and performance of track and pri-  
2979 mary vertex reconstruction with the CMS tracker”. JINST 9 P10009 (2014).  
2980 doi:10.1088/1748-0221/9/10/P10009
- 2981 [107] J. Incandela. “Status of the CMS SM Higgs Search” July 4, 2012. Pdf slides.  
2982 Retrieved from [https://indico.cern.ch/event/197461/contributions/1478917/attachments/290954/406673/CMS\\_4July2012\\_Final.pdf](https://indico.cern.ch/event/197461/contributions/1478917/attachments/290954/406673/CMS_4July2012_Final.pdf)
- 2984 [108] P. Billoir and S. Qian, “Simultaneous pattern recognition and track fitting by  
2985 the Kalman filtering method”, Nucl. Instrum. Meth. A 294 219. (1990).
- 2986 [109] W. Adam, R. Fruhwirth, A. Strandlie and T. Todorov, “Reconstruction of  
2987 electrons with the Gaussian sum filter in the CMS tracker at LHC”, eConf  
2988 C 0303241 (2003) TULT009 [physics/0306087].
- 2989 [110] K. Rose, “Deterministic Annealing for Clustering, Compression, Classification,  
2990 Regression and related Optimisation Problems”, Proc. IEEE 86 (1998) 2210.
- 2991 [111] R. Fruhwirth, W. Waltenberger and P. Vanlaer, “ Adaptive Vertex Fitting”,  
2992 CMS Note 2007-008 (2007).
- 2993 [112] CMS collaboration, “Performance of CMS muon reconstruction in pp collision  
2994 events at  $\sqrt{s} = 7 \text{ TeV}$ ”, JINST 7 P10002 2012, [arXiv:1206.4071].
- 2995 [113] Coco, Victor and Delsart, Pierre-Antoine and Rojo-Chacon, Juan and Soyez,  
2996 Gregory and Sander, Christian, “Jets and jet algorithms”, Proceedings,  
2997 HERA and the LHC Workshop Series on the implications of HERA for LHC  
2998 physics: 2006-2008, pag. 182-204. <http://inspirehep.net/record/866539/files/access.pdf>, (2009), doi:10.3204/DESY-PROC-2009-02/54

- 3000 [114] M. Cacciari, G. P. Salam, and G. Soyez, “The anti- $k_t$  jet clustering algorithm,”  
3001 Journal of High Energy Physics, vol. 04, p. 063, (2008).
- 3002 [115] S. Catani, Y. L. Dokshitzer, M. H. Seymour, and B. R. Webber, “Longitudi-  
3003 nally invariant  $K_t$  clustering algorithms for hadron hadron collisions”, Nuclear  
3004 Physics B, vol. 406, pp. 187–224, (1993).
- 3005 [116] Y.L. Dokshitzer, G.D. Leder, S.Moretti, and B.R. Webber, “Better jet clustering  
3006 algorithms,” Journal of High Energy Physics, vol. 08, p. 001, (1997).
- 3007 [117] B. Dorney. “Anatomy of a Jet in CMS”. Quantum Diaries. June  
3008 1st, 2011. Retrieved from [https://www.quantumdiaries.org/2011/06/01/  
3009 anatomy-of-a-jet-in-cms/](https://www.quantumdiaries.org/2011/06/01/anatomy-of-a-jet-in-cms/)
- 3010 [118] The CMS Collaboration.“Event Displays from the high-energy collisions at 7  
3011 TeV”, May 2010, CMS-PHO-EVENTS-2010-007, Retrieved from [https://cds.  
3012 cern.ch/record/1429614.](https://cds.cern.ch/record/1429614)
- 3013 [119] The CMS collaboration. “Determination of jet energy calibration and transverse  
3014 momentum resolution in CMS”. JINST 6 P11002 (2011). [http://dx.doi.org/  
3015 10.1088/1748-0221/6/11/P11002](http://dx.doi.org/10.1088/1748-0221/6/11/P11002)
- 3016 [120] The CMS Collaboration, “Introduction to Jet Energy Corrections at  
3017 CMS.”. <https://twiki.cern.ch/twiki/bin/view/CMS/IntroToJEC>, last ac-  
3018 cessed 10.02.2018.
- 3019 [121] CMS Collaboration Collaboration. “Identification of b quark jets at the CMS  
3020 Experiment in the LHC Run 2”. Tech. rep. CMS-PAS-BTV-15-001. Geneva:  
3021 CERN, (2016). [https://cds.cern.ch/record/2138504.](https://cds.cern.ch/record/2138504)

- 3022 [122] CMS Collaboration Collaboration. “Performance of missing energy reconstruction  
3023 in 13 TeV pp collision data using the CMS detector”. Tech. rep. CMS-PAS-  
3024 JME16-004. Geneva: CERN, 2016. <https://cds.cern.ch/record/2205284>.
- 3025 [123] CMS Collaboration, “New CMS results at Moriond (Electroweak) 2013”,  
3026 Retrieved from [http://cms.web.cern.ch/sites/cms.web.cern.ch/files/styles/large/public/field/image/HIG13004\\_Event01\\_0.png?itok=LAWZzPHR](http://cms.web.cern.ch/sites/cms.web.cern.ch/files/styles/large/public/field/image/HIG13004_Event01_0.png?itok=LAWZzPHR)
- 3029 [124] CMS Collaboration, “New CMS results at Moriond (Electroweak) 2013”,  
3030 Retrieved from [http://cms.web.cern.ch/sites/cms.web.cern.ch/files/styles/large/public/field/image/TOP12035\\_Event01.png?itok=uMdnSqzC](http://cms.web.cern.ch/sites/cms.web.cern.ch/files/styles/large/public/field/image/TOP12035_Event01.png?itok=uMdnSqzC)
- 3033 [125] K. Skovpen. “Event displays highlighting the main properties of heavy flavour  
3034 jets in the CMS Experiment”, Aug 2017, CMS-PHO-EVENTS-2017-006. Re-  
3035 trieval from <https://cds.cern.ch/record/2280025>.
- 3036 [126] G. Cowan. “Topics in statistical data analysis for high-energy physics”.  
3037 arXiv:1012.3589v1
- 3038 [127] A. Hoecker et al., “TMVA-Toolkit for multivariate data analysis”  
3039 arXiv:physics/0703039v5 (2009)
- 3040 [128] L. Lista. “Statistical Methods for Data Analysis in Particle Physics”, 2nd  
3041 ed. Springer International Publishing. (2017) <https://dx.doi.org/10.1007/978-3-319-62840-0>

- 3043 [129] I. Antcheva et al., “ROOT-A C++ framework for petabyte data storage, sta-  
3044 tistical analysis and visualization ,” Computer Physics Communications, vol.  
3045 182, no. 6, pp. 1384â€¢1385, (2011).
- 3046 [130] Y. Coadou. “Boosted decision trees”, ESIPAP, Archamps, 9 Febru-  
3047 ary 2016. Lecture. Retrieved from [https://indico.cern.ch/event/472305/contributions/1982360/attachments/1224979/1792797/ESIPAP\\_MVA160208-BDT.pdf](https://indico.cern.ch/event/472305/contributions/1982360/attachments/1224979/1792797/ESIPAP_MVA160208-BDT.pdf)
- 3049
- 3050 [131] J.H. Friedman. “Greedy function approximation: A gradient boosting ma-  
3051 chine”. Ann. Statist. Volume 29, Number 5 (2001), 1189-1232. [https://projecteuclid.org/download/pdf\\_1/euclid-aos/1013203451](https://projecteuclid.org/download/pdf_1/euclid-aos/1013203451).
- 3052
- 3053 [132] W. Verkerke and D. Kirkby, “The RooFit toolkit for data modeling,” arXiv  
3054 preprint physics, (2003).
- 3055 [133] CMS Collaboration, “Documentation of the RooStats-based statistics  
3056 tools for Higgs PAG”. <https://twiki.cern.ch/twiki/bin/view/CMS/SWGuideHiggsAnalysisCombinedLimit>, last accessed on 08.04.2018.
- 3057
- 3058 [134] F. James, M. Roos, “MINUIT: Function minimization and error analysis”. Cern  
3059 Computer Centre Program Library, Geneve Long Write-up No. D506, 1989
- 3060
- 3061 [135] J. Neyman and E. S. Pearson, “On the problem of the most efficient tests of  
statistical hypotheses”. Springer-Verlag, (1992).
- 3062
- 3063 [136] A.L. Read. “Modified frequentist analysis of search results (the  $CL_s$  method),”  
(2000). CERN-OPEN-2000-205.
- 3064
- 3065 [137] C. Palmer. “Searches for a Light Higgs with CMS”, CMS-CR-2012-215. <https://cds.cern.ch/record/1560435>.

- 3066 [138] A. Wald, “Tests of statistical hypotheses concerning several parameters when  
 3067 the number of observations is large”, Transactions of the American Mathematical  
 3068 society, vol. 54, no. 3, pp. 426–482, (1943).
- 3069 [139] G. Cowan, K. Cranmer, E. Gross, and O. Vitells, “Asymptotic formulae for  
 3070 likelihood-based tests of new physics”, European Physical Journal C, vol. 71,  
 3071 p. 1554, (2011).
- 3072 [140] S. S. Wilks, “The Large-Sample Distribution of the Likelihood Ratio for Testing  
 3073 Composite Hypotheses”, Annals of Mathematical Statistics, vol. 9, pp. 60–62,  
 3074 (03, 1938).
- 3075 [141] B. Hespel, F. Maltoni, and E. Vryonidou, “Higgs and Z boson associated pro-  
 3076 duction via gluon fusion in the SM and the 2HDM”, JHEP 06 (2015) 065,  
 3077 [https://dx.doi.org/10.1007/JHEP06\(2015\)065](https://dx.doi.org/10.1007/JHEP06(2015)065), arXiv:1503.01656.
- 3078 [142] ATLAS Collaboration, “Measurements of Higgs boson pro-  
 3079 duction and couplings in diboson final states with the AT-  
 3080 LAS detector at the LHC”, Phys. Lett. B726 (2013) 88–119,  
 3081 doi:10.1016/j.physletb.2014.05.011, 10.1016/j.physletb.2013.08.010,  
 3082 arXiv:1307.1427. [Erratum: Phys. Lett.B734,406(2014)].
- 3083 [143] CMS Collaboration, “Search for the associated production of a Higgs boson  
 3084 with a single top quark in proton-proton collisions at  $\sqrt{s} = 8$  TeV”, JHEP 06  
 3085 (2016) 177, doi:10.1007/JHEP06(2016)177, arXiv:1509.08159.
- 3086 [144] B. Stieger, C. Jorda Lope et al., “Search for Associated Production of a Single  
 3087 Top Quark and a Higgs Boson in Leptonic Channels”, CMS Analysis Note CMS  
 3088 AN-14-140, 2014.

- 3089 [145] M. Peruzzi, C. Mueller, B. Stieger et al., “Search for ttH in multilepton final  
3090 states at  $\sqrt{s} = 13$  TeV”, CMS Analysis Note CMS AN-16-211, 2016.
- 3091 [146] CMS Collaboration, “Search for H to bbar in association with a single top quark  
3092 as a test of Higgs boson couplings at  $\sqrt{s} = 13$  TeV”, CMS Physics Analysis  
3093 Summary CMS-PAS-HIG-16-019, 2016.
- 3094 [147] CMS Collaboration, “Search for production of a Higgs boson and a single top  
3095 quark in multilepton final states in proton collisions at  $\sqrt{s} = 13$  TeV”, CMS  
3096 Physics Analysis Summary CMS-PAS-HIG-17-005, 2016.
- 3097 [148] B. WG, “BtagRecommendation80XReReco”, February, 2017. <https://twiki.cern.ch/twiki/bin/view/CMS/BtagRecommendation80XReReco>.
- 3099 [149] CMS Collaboration, “Identification of b quark jets at the CMS Experiment  
3100 in the LHC Run 2”, CMS Physics Analysis Summary CMS-PAS-BTV-15-001,  
3101 2016.
- 3102 [150] M. Peruzzi, F. Romeo, B. Stieger et al., “Search for ttH in multilepton final1  
3103 states at  $\sqrt{s} = 13$  TeV”, CMS Analysis Note CMS AN-17-029, 2017.
- 3104 [151] CMS Collaboration, “Baseline muon selections for Run-II.” <https://twiki.cern.ch/twiki/bin/view/CMSPublic/SWGuideMuonIdRun2>, last accessed on  
3105 24.02.2018.
- 3107 [152] G. Petrucciani and C. Botta, “Two step prompt muon identification”, January,  
3108 2015. <https://indico.cern.ch/event/368007/contribution/2/material/slides/0.pdf>.

- 3110 [153] H. Brun and C. Ochando, “Updated Results on MVA eID with 13 TeV samples”,  
3111 October, 2014. [https://indico.cern.ch/event/298249/contribution/3/  
3112 material/slides/0.pdf](https://indico.cern.ch/event/298249/contribution/3/material/slides/0.pdf).
- 3113 [154] K. Rehermann and B. Tweedie, “Efficient Identification of Boosted Semileptonic  
3114 Top Quarks at the LHC”, JHEP 03 (2011) 059, [https://dx.doi:10.1007/  
3115 JHEP03\(2011\)059](https://dx.doi.org/10.1007/JHEP03(2011)059), arXiv:1007.2221.
- 3116 [155] CMS Collaboration. “Tag and Probe”, [https://twiki.cern.ch/twiki/bin/  
view/CMSPublic/TagAndProbe](https://twiki.cern.ch/twiki/bin/<br/>3117 view/CMSPublic/TagAndProbe), last accessed on 02.03.2018.
- 3118 [156] B. Maier, “SingleTopHiggProduction13TeV”, February, 2016. [https://twiki.cern.ch/twiki/bin/  
viewauth/CMS/SingleTopHiggsGeneration13TeV](https://twiki.<br/>3119 cern.ch/twiki/bin/viewauth/CMS/SingleTopHiggsGeneration13TeV).